sfa

EURATOM-MESCS

Slovenska Fuzijska Asociacija
Slovenian Fusion Association

Association EURATOM – MESCS
ANNUAL REPORT 2012

Ljubljana, November 2013

Slovenska Fuzijska Asociacija
Slovenian Fusion Association

EURATOM-MESCS

Association EURATOM – MESCS
ANNUAL REPORT 2012

Ljubljana, November 2013

Figure on the front cover:
    Tokamaks enclosed. ASDEX UPGRADE coils, vessel, limiter, magdiag
    and edge simulation inside JET and ITER vessel composite - visualization
    with VisIt.
    Courtesy Leon Kos, H.-J. Klingshirn and EFDA ITM contributors.
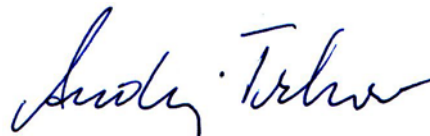
CONTENTS

FOREWORD

Nuclear fusion represents a viable option for solving the world's future energy needs. However, due to mostly technological issues, there is still quite a way to go. With the silhouette of ITER rising in Cadarache and detailed DEMO specifications coming out of the shadows, it is clear that, magnetic confinement fusion is becoming one of the largest scientific and technological projects of our time. Thus, each year individually, we are proud to be a part of this community that has embarked on such a journey. In front of you now stands a sum up of EURATOM-MESCS (Slovenian Fusion Association) contributions to European fusion programme in the year of 2012. Since the beginnings of our Association, the number of people doing R&D in the field of fusion had steadily been growing and most of the included research groups now focus their work primarily on fusion. These reinforcements come in handy, as there are still many issues that need to be addressed. New questions are arising with the onset of the dedicated DEMO unit in EFDA - the Power Plant Physics and Technology Department. With newly established problems, new approaches are developed, which is exactly why e.g. two research groups under SFA have joined their knowledge in coupling the fields of thermohydraulics and neutronics, to investigate the heat generation and removal in the Helium Cooled Pebble Bed Test Blanket Module. It is collaborations like this, where many different physical processes have to be addressed simultaneously, as part of a larger system, that are showing we are indeed getting closer to a working fusion power plant.

Our activities in the year 2012 were included in the following EFDA coordinated structures:

- **ITER Physics**, where our effort was strongest in the Plasma Wall Interaction (PWI) Task Force, encompassing studies of various plasma surface processes like particle removal, deposition and retention, as well as improving of the edge plasma diagnostics. Inside ITM Task Force visualization tools for common ITM platform were developed.
- Neutron transport studies remain a part of **JET** programme, including upgrading JET MCNP models, further work on neutron yield calibration and gamma ray camera study of neutron attenuation.
- In **emerging technologies** the work is divided between dedicated the DEMO tasks (helium cooled divertor design, neutronic studies, blanket test case) and more general tasks (development of ceramic based materials for various application in fusion power plants).
- The **Public information** programme under SFA does not only service domestic needs for education and information on magnetic confinement fusion, but also continues to successfully run the international Fusion Expo itinerant exhibition, the work, which has been rewarded with an extension of the operation until the end of the year 2013.

In the first year of running with the new leadership, our Association has proved to be a well-oiled machine which, continues to integrate and contribute valuably into the European fusion programme. That could, of course, not be possible without excellent support from all included individuals and institutions in Slovenia and EU. To them we wish to express our greatest thanks.

Dr. Andrej Trkov
Head of Research Unit

EXECUTIVE SUMMARY

1   ITER Physics Basis

1.1   Improvement of diagnostics in edge plasma of fusion devices

We took part in two PS tasks related to probe measurements which has shifted the reserch focus from the predictions in our EFDA work plan set for 2012.

In the first task we were dealing with the feasibility of emissive probe use inside tokamaks, mostly contributing theoretical support. We focused on studying the case for high emission but also high temperature ratio between the emitted electrons and bulk electrons. It was shown, that the floating potential of a highly emissive probe could indeed reach the plasma potential. This is in reality however not possible, as the emitted electrons have a significantly lower temperature than the bulk electrons, so the probe potential would remain roughly 1.7 kTe below the plasma potential. The task is expected to move into design phase in 2013 where we will again provide support with calculation and construction design.

The other task was focused on the relation between the fluid and kinetic boundary conditions in magnetized plasma. A comprehensive study was made on the formation of potential regions in front of boundary wall inside magnetized plasma. This is important both in plasma diagnostic as well as in general boundary plasma physics, since improved boundary conditions help in understanding and accuracy of parameter calculations. We made calculations of polytropic function γ depending on the ratios of finite length scales and the angle of magnetic field.

In 2013 we plan to extend our work to the use of alternative probe measurement techniques in COMPASS-D tokamak with INRNE.BG and provide theoretical support for them.

1.2   Processes with neutral hydrogen atoms and molecules

The goal of this project under IPH BS/PS tasks was to contribute to understanding and to provide quantitative data for processes with neutral hydrogen atoms and molecules relevant to the fusion development program in particular to the field of plasma surface interaction.

In 2012 we continued the study of H and D retention in ITER grade tungsten in particular the influence of the neutron induced type damage to the retention in collaboration with IPP Garching. The damaged samples were produced by high energy W-ion irradiation (simulating n-irradiation) by exposing them to a well characterised beam of thermal deuterium atoms produced by the flow of hydrogen gas through a hot tungsten capillary. Study of deuterium retention after long-term D exposure of undamaged and damaged samples at different sample temperatures was performed *ex-situ* by [3]He Nuclear Reaction Analysis (NRA) and Thermal Desorption Spectroscopy (TDS). It was shown that D atoms do decorate the radiation-induced damage and that the rate decoration of defects depends on temperature. The D saturation concentration decreases with temperatures; namely, D is de-trapped from low energy traps and

radiation damage is partly annealed at temperatures above 500 K. In this year a new set up for *in situ* NRA studies was completed at JSI that will enable acquiring new information on the dynamics of D diffusion in damaged and undamaged W.

Another important activity has been started on the problem of the efficiency and technological applicability of methods for fuel removal on tungsten in collaboration with CEA Cadarache and the Laboratory for Physics of Interactions of Ions and Molecules (PIIM), University of Provence (Aix-Marseille. We have focused on the determination of deuterium release and re-absorption in W surfaces treated by RF discharges. The main part of the activity was conducted at PIIM during nine month post-doc stay of S. Markelj. This comprised the development and calibration of a set-up for TDS, with doubly differentially pumped mass spectrometer, and sample preparation by analysing the W sample by surface science analytical techniques. First data on D retention by TDS on W sample with controlled submonolayer oxygen contamination were obtained and quantified. Within the JSI part of the task we completed and tested the broad beam NRA for future studies of samples which will be produced at CEA/PIIM by D ion/plasma exposure and TDS analyses.

Spectrometer for vibrational diagnostics of hydrogen molecules based on the properties of low energy dissociative electron attachment was modified. Differential pumping of reaction and detection region is achieved by an addition of turbomolecular pump so that important enhancement of instrument's performance was insured.

1.3   Removal of deposits by neutral oxygen and nitrogen atoms

Research on the removal of deposits by neutral oxygen and nitrogen atoms is performed at the plasma laboratory of the Department of Surface Engineering and Optoelectronics at the Jožef Stefan Institute. The neutral atomic species can either come from the fusion plasma – hydrogen atoms in the divertor area and the plasma-shadowed areas – or could be created with remote sources, such as neutral oxygen and nitrogen atoms.

Since carbon-based materials have not yet been eliminated from the list of possible candidates for first-wall materials in ITER the problem of amorphous hydrogenated carbon (a-C:H) deposit formation must still be properly addressed. Experiments with atomic oxygen have so far yielded promising results and continue to be in the close focus of our research activities. However, indications that use of atomic oxygen may not be compatible with in-vessel reactor components force us to search for alternative routes, namely removal by nitrogen-based plasma species. Since tungsten was introduced as a possible plasma facing material for ITER, the interaction of tungsten and neutral hydrogen atoms has also become the subject of our research.

In 2012, we continued the research of removal of a-C:H layers by neutral oxygen atoms. We achieved very favourable erosion rates. Similar erosion rates were achieved with two different plasma systems that were used as atomic oxygen sources. This further reaffirms our interpretation that the erosion takes place only due to interaction with neutral oxygen atoms, not other plasma species or phenomena that are characteristic to either of the types of discharges used in the experiments.

We performed experiments in removal of a-C:H layers by RF plasma of ammonia, in close collaboration with CIEMAT, Madrid. We achieved relatively good erosion rates, as well as explored the impact of the E – H mode transition on the erosion

efficiency of the plasma, and identified the plasma species that contribute the most to the a-C:H erosion.

In order to assess the production of dust during such methods of fuel removal, we developed a process of deposition of a-C:H layers that are prone to dust production during interaction with plasma. In collaboration with LAPLACE, Toulouse we are also working to develop a method of dust detection which will assist us in further experiments of dust generation assessment.

To verify the compatibility of tungsten with the chemically reactive environment of weakly ionised, highly dissociated hydrogen plasma, we performed experiments of interaction between a tungsten surface and neutral hydrogen atoms at CNRS Font-Romeu.

1.4 Application of ion beam analytical methods to the studies of plasma-wall interaction in tokamaks (IBAF)

In 2012, we concentrated our efforts in the development and application of a broad ^{3}He-beam Nuclear Reaction Analysis (NRA) for deuterium depth profiling with varying impact beam energy. Thick implanted Si particle detector, acquired within an earlier EFDA PS project, was installed in the RBS/ERDA chamber at an angle of 135° with respect to the beam direction.

NRA with ^{3}He was used in 2012 to analysing samples with multi element composition provided by Association MEdC according to the IPH task (WP12-IPH-A01-3-10/BS-01/MHEST). Two kinds of samples were prepared by TVA technique: samples with single, approximately homogeneous, mixed layer and samples with multi layered structure. Used materials were W, C and Al as a substitute for Be. Certain samples were prepared in the presence of deuterium gas in plasma reactor so that deuterium was co-deposited in the mixed material layers. Besides these samples from MEdC some samples provided by CEA were also studied by NRA during 2012.

Two important enhancements of the accelerator facility were done during 2012 enabling efficient forthcoming fusion related studies. The first is the modification of the gas handling system at the duoplasmatron ion source so to allow easy switch from ^{4}He to ^{3}He operation and also the operation with two-isotope mixture as a plasma sustaining gas. This modification greatly reduced the consumption of precious ^{3}He gas.

The second and major enhancement was the installation of the new multicusp H⁻ source at our tandem accelerator done during November 2012. The installation of multicusp ion source is primarily intended to increase brightness of injected H⁻ beam with the goal to drastically increase the intensity of the proton microbeam. The existing duoplasmatron ion source is now permanently configured for positive extraction, required for the helium beam in particular for ^{3}He beam needed for NRA. These improvements enable our laboratory to serve fusion research with significantly higher efficiency.

1.5 Deuterium interaction kinetics with Be, W and mixtures relevant to ITER and DEMO

Knowledge of the properties of diffusion and potential retention of hydrogen isotopes in Be/W mixed materials and alloys is still rather poor today and further research is definitely required. Since both W and Be films were rarely measured in

relation to fusion, we have an advantage that we have more than 3 years of collecting our own experimental data on both material in form of films, Be and W, both relevant to ITER. It is thus important to determine first the parameters that govern the permeation process at known film structure and composition and achieve proper understanding of the influence of material morphology, structure and high temperature loads on H/D/T retention in films made of Be/W alloys with different Be/W ratio.

Besides this knowledge, our data may contribute complementary data to predict the upper limit for D/T accumulation in Be/W deposits or dust formed in JET or ITER. Permeation properties of nano-crystalline W films on Eurofer, produced by different techniques, exhibit substantial differences. The aim of further study is to determine primarily the permeation properties of Be/W films, which may give a satisfactory explanation when results will be outside the expected range. So far, Be reactivity with traces of water at the upstream side may result in BeO formation whose role is still not well resolved from pure Be properties. This detail will have to be carefully investigated and some improvements of the experimental setup will be done.

1.6   Plasma deposition of C:H-metal coatings

Our investigations were focused on three topics:

a)   Deposition and characterization of carbon based coatings (a-C:H, Me-C:H, a-CN) by different deposition techniques (sputter deposition with thermionic arc, magnetron sputtering and anode layer source). Using the anode layer source we deposited a series of diamond-like carbon films, where we varied the discharge voltage and N_2-to-C_2H_2 ratio. Sputter deposition system with thermionic arc was used for preparation of W-C:H films on stainless steel substrates, while unbalanced magnetron sources were used for preparation of a-CN films.

b)   For removal rate measurements of deposits by neutral oxygen and nitrogen atoms (1.4.2 project) two set of samples coated with Cr/W/W-C/a-C:H multilayer were prepared.

c)   The OES (optical emission spectroscopy) measurements were conducted in three deposition systems: Balzers Sputron, Balzers BAI730 and CemeCon CC800/9. We tried to determine the influence of different deposition parameters on degree of ionization of different species. In each machine, a series of experiments was made, where in each experiment only one parameter was varied at a time. We varied the process parameters, like partial pressure of acetylene, axial magnetic field, bias voltage etc.

1.7   ITM advanced visualization tools

ISIP (Infrastructure and Software Integration Project) is in charge of developing and maintaining the Integrated Tokamak Modeling Task Force (ITM-TF) simulation infrastructure. Our work within ISIP »Advanced visualization tools« consists of extension of the visualization capabilities for the ITM-TF platform that provides developer tools for (automated) creation of specialized plots for Kepler workflows and sophisticated interactive data analysis tools for end users.

Custom visualizations for specific physics problems/workflows are readily available with the ITM Python visualization library ITMvis - a structured repository for code fragments that performs the processing and simplifies reuse of common and

specialized data processing for various target visualization tools. We demonstrate such use for native Matplotlib as well as embedded within VisIt and Kepler, where specialized plugins/actors have been developed for accessing CPOs in the ITM-TF database.

2   JET Programme

2.1   JET neutron calculations

In 2010/2011 the carbon plasma-facing wall in JET has been replaced with a configuration consistent with the ITER design (Beryllium/Tungsten/Carbon). One of the resulting changes due to JET upgrade is also the change in the neutron field, which is affected by altered materials of some of the new components. Since the last calibration of the neutron diagnostic system has been performed almost 30 years ago, computational support for calculation of the experimental corrections, uncertainties and determination of biases is, indeed, needed. Calibration of external fission chambers will be provided by direct measurements using a calibrated point ^{252}Cf neutron source deployed by the in-vessel remote handling system. Neutronic calculations, using advanced transport codes (MCNP), are required to support the physics, safety and engineering efforts.

We performed four major tasks regarding the neutronic calculations in JET:

a) The 3D MCNP model of JET was further upgraded to optimize the calculations of correction factors needed for the point neutron source calibration. Code was modified to track real 3D locations of particles. The modifications were verified with different approaches and a manual describing the modifications was written.

b) Calculations to support neutron yield calibration were made to study the effect of the JET remote handling system on the external neutron monitor responses during the calibration measurements with a simplified model. This calibration will provide first direct calibration of the JET activation system inside torus as well as absolute calibration of external neutron monitors with at least 10% accuracy.

c) The MCNP model of the Octant 1 was upgraded (geometry and material) to be optimized for calculation and of shutdown doses. This provides essential data needed for the dose measurements off-operational period and estimation of shutdown dose rate following hypothetical DT irradiations in preparation of the future tritium experiments.

d) For the gamma ray camera a study of the attenuation factors for neutrons was performed.

3   Emerging Technology Programme

3.1   Development of SiC-based material for structural parts in fusion reactors

The main objective of the work aimed at development of a SiC-based composite for use at extremely severe environment in structural part of future fusion reactors is full

impregnation of 3D woven stoichiometric SiC-fiber preform with a low activation SiC matrix. The work has followed rather tough requirements for the material: The composite must possess high mechanical strength and reliability at temperatures up to 1100 °C, gas impermeability and high through-thickness thermal conductivity. Low neutron-activation is expected in order to minimise production of radioactive wastes. The presently available techniques CVI and PIP offer the production of high purity material with high mechanical strength, however, the hermeticity cannot be achieved due to specific limitation of both processes. Furthermore large voids within the microstructure of such composites limit its through thickness thermal conductivity. On the other hand, the NITE process, enables fabrication of dense material with good mechanical properties, however, it possesses secondary phase which lower the thermal conductivity and degrade the low-activation properties of pure SiC. In our work we make an attempt to verify a process for production of low-activation SiC-based material for fusion application by an alternative ceramic processing as a possible route to prepare a dense low-activation material. A new, so called "SITE" process has been developed. The process comprises a combination of electrophoretic (infiltration) deposition (EP(I)D) and polymer infiltration and pyrolysis (PIP). The resulting composite material exhibits homogeneous microstructure with a more favourable pore size and porosity distribution in comparison to other state-of-art materials (e.g. CVI). The SITE-SiC$_f$/SiC composite is predominantly composed of crystalline β-SiC and was characterised with high thermal conductivity. To further improve the properties (e.g. thermal conductivity) and insure materials hermeticity incorporation of some metallic elements (W, CrSi$_2$, etc.) into the composite matrix or as a coating layer is also investigated.

3.2   Thermal-hydraulic analyses of alternative He-cooled divertor concepts

Our research was focused on investigation of alternative He-cooled divertor target concepts for updated design requirements in an early DEMO. The research activities in 2012 were carried out in the framework of the PPP&T programme, workpackage Design Assessment Studies (DAS), Task DAS02-T06. The main objective of the task was to perform thermal-hydraulic analyses of alternative cooling finger designs in terms of material choice and geometry of the tile. Two possible incident heat flux conditions were studied, 10 MW/m2 and 8.7 MW/m2, where the lower heat flux value is based on the relaxed parameters of the "early-DEMO". The scoping analyses were carried out in two directions. In the first case the alternative material (T-111) for the thimble with a much lower DBTT was investigated that allow a reduction of the coolant temperature and a better operational temperature window of the materials (e.g. steel). Thermal loading of the finger structures and pressure drop in the cooling channel are compared with the reference design at high helium temperature. In the second case, the alternative finger geometries (the hexagonal finger being the reference) at high helium outlet temperature were investigated. These analyses were performed as a cross-border activity with DAS-02-T05 from the perspective of shadowing of the target plate edges against damage caused by the incident particles. The work was carried out in cooperation with the Karlsruhe Institute of Technology (KIT) - Institute for Applied Materials-Materials Processing Technology.

3.3 Interface assessment between MCNP and ANSYS CFX for the blanket test case

The development of the DEMO fusion power plant blanket is a complex task, because it is necessary to take into account several branches of physics, including fluid dynamics, volumetric heat generation due to neutrons, heat transfer etc. Therefore, in order to support the development of the DEMO breeding blanket it is important to develop a computational model, which will take into account all the relevant data and physical processes. In 2012, the volumetric heat generation in a Helium Cooled Pebble Bed Test Blanket Module due to neutrons, together with the surface heating from the plasma and the removal of heat by the helium coolant was investigated. The main objective of the work was to test the possibilities for data transfer from the MCNP neutronic analysis to the ANSYS CFX thermo-hydraulic analysis. The assessment of the data transfer was performed for the Blanket Test Case, defined by the Karlsruhe Institute of Technology, which provided also the nuclear heating data, calculated with MCNP. It was demonstrated that the inclusion of nuclear heating in the CFX model is straightforward. The heat source can be defined by a user function, which can be a table of nuclear heating data provided for different locations in 3D. MCNP has the ability to define a mesh, superimposed over the problem geometry for tallying purposes. Within each cell of this 3D mesh the nuclear heating may be calculated and provided in form of a table, which may be directly imported into CFX after some basic editing. The Blanket Test Case was successfully simulated with ANSYS CFX, considering the provided 3D nuclear heating data. It turned out that the loading time of the nuclear heating data significantly depends on the size of the data files, thus the density of the nuclear heating data points should be optimized.

3.4 Neutronic studies for DEMO

DEMO, the future nuclear fusion power plant, is intended to be build upon the expected success of the ITER experimental nuclear fusion reactor. DEMO is still in the design phase and the results of the present work are a major design driver for the tokamak architecture and most tokamak components.

JSI collaborated on the study of DEMO characteristics by performing neutron transport calculations with the MCNP code. One study was related to the helium production in the upper vertical port and in the blanket cooling pipes. It was essential to first study the provided MCNP model since it was very complex, it comprised over 14000 cells. It was examined on lost particles but the main part of the task was devoted to variance reduction since the flux is strongly attenuated before reaching the vertical port. It was found that the helium production amounted between 0.4 appm and 2.5 appm for 5 years of operation for the vertical port and pipes. It was dependent on the boron concentration in the material.

Further JSI collaborated on testing the conversion software from CAD to MCNP. The McCad program, developed by KIT, was tested, first on the difficulty of its installation and then on the conversion properties. The CAD model of DEMO was again very complex, including more than 13000 cells. The correctness of the resulting MCNP model tested was by comparing the cell volumes with the CAD cell volumes and by calculation of wall loading.

4   Public Infromation

4.1   Public information activities at the association

Public information remains an important task inside Slovenian Fusion Associaton. The highlights for 2012 were:

- Permanent fusion exhibition at Nuclear training centre (7264 visitors),
- 21 lectures on Fusion technology,
- 24 lectures on Radioactivity and radioactive waste,
- 118 lectures on Nuclear energy and electricity (sustainable, safe energy sources),
- open day at Jožed Stefan Institute with Fusion Expo exhibition,
- articles in local and national media.

A major part of work performed under PI is also the continuation of the Fusion Expo project.

4.2   Fusion Expo Support Action

Slovenian Fusion Association (SFA) EURATOM – MESCS has taken over responsibility to run the Fusion Expo from 6th October 2008. The first Fusion Expo Support Action (WP08-PIN-FUSEX) has finished on 31st July 2010. The new support action WP10-PIN-FUSEX started on 1st August 2010 and was extended in 2012 until the end of year 2013. The main goal and intention of this project remain the same since beginning of our task agreement: to run the Fusion Expo in the most efficient way possible and to follow our tasks, which needs to be fulfilled: scheduling the exhibition, supervising the local organization, graphical work and printing Fusion Expo panels, moving the exhibits, assembling/disassembling Fusion Expo, maintenance, continuous report to EFDA, organization of a supporting participation in international events for young generations and providing the Fusion Expo with Fusion Show for larger events.

Fusion Expo is an itinerant exhibition presenting various aspects of fusion research such as: fusion as a natural phenomenon and energy source science, fusion as a European research project, history of fusion research, European research facilities, ITER, future plans toward a power plant, technological, environmental and sociological aspects of this energy source etc.

During 2012 eleven events were organized: five Maxi Fusion Expos, one Mini Fusion Expo, four events with some parts of expo and additionally one internal event (during PIN meeting in Culham). The main target venues in 2013 are science festivals, science centers and also energy related events.

IMPROVEMENT OF DIAGNOSTICS IN EDGE PLASMAS OF FUSION DEVICES

[1,2]Tomaž Gyergyek, [1]Jernej Kovačič, [2]Milan Čerček

[1]University of Ljubljana, Faculty of Electrical Engineering, Tržaška 25, SI-1000, Ljubljana, Slovenia

[2]»Jožef Stefan« Institute, Jamova 39, SI-1000, Ljubljana Slovenia
tomaz.gyergyek@fe.uni-lj.si

1 INTRODUCTION

Our collaboration in fusion programme remains oriented in plasma diagnostic improvement, specifically, diagnostic with electrical probes. Electrical probes can provide measurements of various plasma parameters with an excellent temporal and spatial resolution; however they will most likely not be included in large machine diagnostics due to the hostility of environment. Even though they are of a very simple construction, the theory behind the measurement methods is rather involved and is in general also. There are several types of probes currently being used in various fusion devices. Our interest is being focused on the understanding of operation of Langmuir and emissive probes inside smaller and mid-sized tokamaks, especially in the field of potential formation in front of plasma boundaries. Formation of different structure e.g. virtual cathodes (potential dips) or magnetic presheath has a big influence on the particle and momentum transport, therefore the results from probe theory can partly also be transferred to the physics of the SOL layer in tokamaks.

We have been a part of two tasks coordinated under EFDA, both connected to probe measurements, namely the projects WP12-IPH-A06-1-1-07/PS-01/MESCS and WP12-IPH-A06-2-05/PS-01/MHEST and project WP-IPH-A08(-2-12/PS-01/MHEST). Our main collaborators in these undertakings are ÖAW-P1, UIBK Innsbruck and ÖAW-P5, UIBK Innsbruck and also INRNE.BG, USK Sofia. Due to the fact that we have had obtained two PS projects for 2012, the milestones for our scheduled work for 2012 were partly changed or postponed until 2013.

2 WORK PERFORMED IN 2012

We have studied the operational regime of a floating emissive probe for high emission currents and high temperatures of the emitted electrons. We have shown that even for very high emission current the expected plasma potential measurement will underestimate the real plasma potential.

We have also completed the assignment regarding the kinetic boundary conditions in edge plasma with oblique magnetic field present. Simulations were run, to check the dependence of the plasma flow parameters on the magnetic field.

We are also continuing our collaboration with on alternative methods for measuring plasma parameters via Langmuir probes using detailed electron energy distribution function.

2.1 Emissive probe measurements

An emissive probe is usually a simple wired loop which is heated by a current passing through it. The probe is heated by the current, and thermionic emission of electrons begins for high enough temperatures. The emission from the emissive probe is usually described by the highly non-linear Richardson-Dushman law where the most important parameter for material selection is the work function of the electrons. The favourites chosen among the materials considered for a tokamak probe are CeB_6, LaB_6 and graphite. The former two have a lower work function, while the uniqueness of the graphite lies in the negative temperature coefficient of its resistivity. The latter provides a more suitable regulation of emission via a constant current source. The potential of a floating emissive probes at high electron emission can, ideally, become equal to the plasma potential, which was confirmed by a couple of experiments. However, several experiments, as well as theoretical approaches showed, that this was not true for plasmas with higher electron temperatures. Nevertheless, there has lately been a revived interest in such a probe being used in smaller tokamaks e.g. COMPASS-D and medium sized tokamaks, e.g. ASDEX-UPGRADE (AUG) due to probe measurement's definitely decreased dependence on the electron temperature fluctuations in comparison to standard cold probes. The main goal of this task was to evaluate the feasibility of emissive probe use in tokamaks and provide design basis for construction. An extension of the task leads to actual construction of the probe head and providing measurements in AUG. Our group partly worked in support of the ÖAW-P5 on material selection and probe design, but for the most part we were focused on the emissive probe theory. Our research was aimed at explaining the dependence of the floating emissive probe measurements on ratios of electron temperatures.

We again started with a well established 1d model of collisionless plasma, where the plasma is bounded by two perfectly absorbing parallel electrodes. Two particle species, positive ions and electrons, are injected from right electrode with half-maxwellian velocity distribution function (VDF). We also inject electrons with half-maxwellian VDF from left electrode, which acts as our emissive probe. In front of the right source electrode forms a source sheath, which is effectively our ionization presheath, followed by a quasi-neutral region. A Debye sheath is then formed in front of the left electrode. Since the plasma-sheath transition is well defined, such a model is very suitable for mathematical modelling and shows an excellent agreement with the results obtained by particle-in-cell (PIC) codes, another tool used in this research.

When thermionic emission is increasing with temperature it is said to be temperature limited. However, when negative charge collected in front of electrode starts inhibiting electron emission the process moves to space-charge limited emission, which is governed by the Child-Langmuir law. The point of transition between regimes is called critical emission and is defined by the zero electric field at the boundary

electrode. With increased emission a potential well forms in front of the probe which acts as a virtual cathode.

We can separate our results into two groups based on the amount of electron emission from the surface. We did a number of simulations with increasing emission also for increasing temperature ratio of emitted electrons to bulk electron temperature.
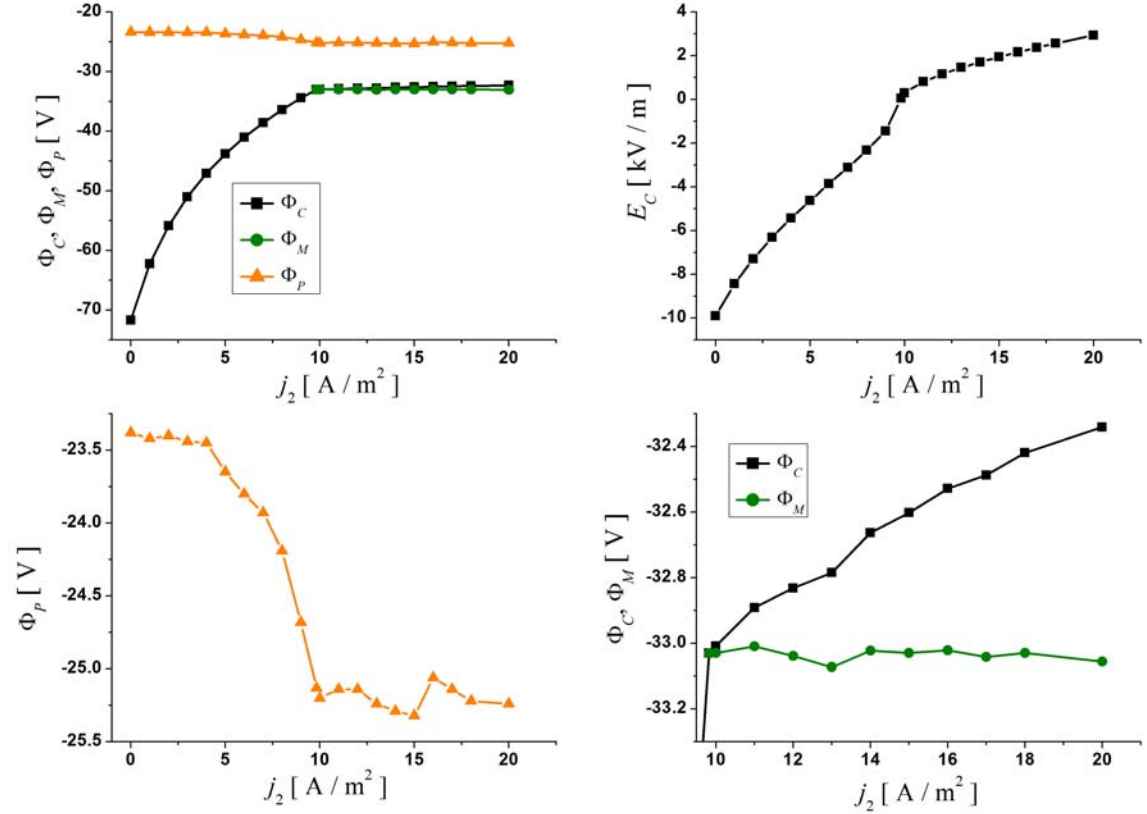

Figure 1: (In top left graph) potentials Φ_C, Φ_M, Φ_P are plotted versus emissive current j_2 and (in the top right graph) the electric field EC is plotted versus emissive current j_2. The bottom graphs show the same case on an expanded scale. The electron temperature is $kT_1=20$ eV and the emitted electrons temperature is $kT_2=1$ eV.

Figure 1 shows the three relevant potentials Φ_C of the collector (emissive probe), Φ_M of the virtual cathode on the collector and the plasma potential Φ_P versus the emitted current j_2. Figure shows the increase of the collector potential Φ_C (floating potential of an emissive probe) for increasing electron emission. This behaviour is well known in certain realistic cases: as we increase the current thorough an emissive probe, the emission increases resulting in the increasing collector floating potential Φ_C which, when critical emission is reached, appears to become saturated and almost does not change. A closer inspection of the potential profile shows, that a potential well does indeed form. The combined potential drop across the presheath and sheath amounts to about 1.7 ot 1.8 kT_e, which is a severe underestimation of plasma potential.

The extended part of work was focused on cases where beside the high emission also the temperature ratio between emitted electrons and bulk electrons would be high. Again the temperature of bulk electrons is $kT_1=20$ eV, while we varied the emitted electron temperature from 0.5 eV to 5 eV and more, as presented in Figure 2. Again the rise of emission current density results in the increase of Φ_P, Φ_M and Φ_C. A potential

13

well is again formed in between the sheath entrance and the collector. Potential Φ_C is increased much faster than the first two and even shows the tendency to surpass the potential of the source, which is the desired operational regime for an emissive probe. However, in simulation this is not possible due to the 1d3v geometry of the PIC code used, as the strength of the "probe" source can be on par with the "real" source, thus "driving" the plasma. Such is not the case in realistic setting. What happens in the simulation is, that when the collector potential goes beyond the source potential the ions emitted from the source are prevented from reaching the collector since they do not have enough energy. The simulations become unstable afterwards.
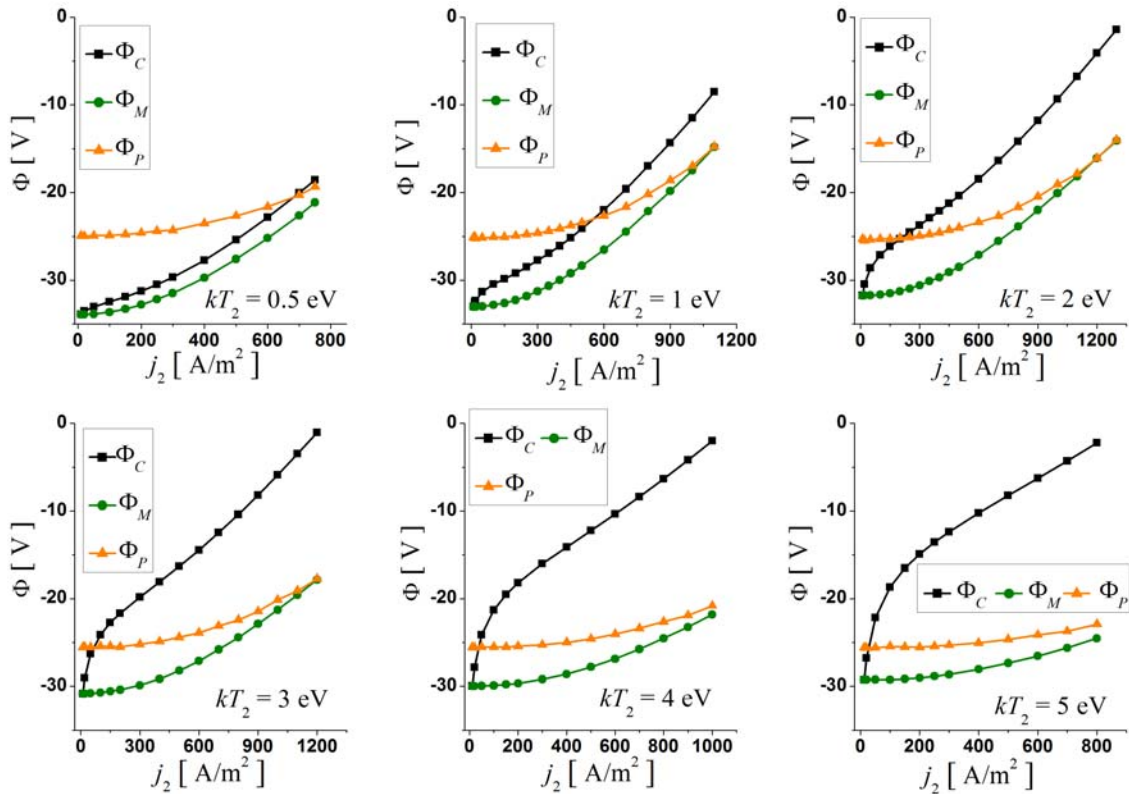

Figure 2: Potentials Φ_C, Φ_M, Φ_P are plotted versus emissive current j_2 for six different temperatures of the emitted electrons. The electron temperature is kT_1=20 eV and the emitted electrons temperature are kT_2=0.5 eV, 1 eV, 2 eV, 3 eV, 4 eV and 5 eV, respectively.

The results show a possible explanation for some experiments in which a floating potential of a highly emissive probe would go above the plasma potential. However, since this principle is shown to be possible on comparable temperature of the emitted and bulk electrons (and at very high emission) it is unfortunately not possible to achieve such measurements inside tokamaks. Therefore, an emissive probe is still predicted to measure roughly 1.7 to 1.8 kT_e below the plasma potential. A possible extension to this research could be in employing a 2d code, where ratio of collector to source area could be changed. A more detailed description of our work on this subject along with normalization procedures and result matching procedures can also be found in [1, 2].

2.2   Boundary conditions in magnetized edge plasma

When it comes to SOL or tokamak modelling in general, fluid approach is favoured over more detailed kinetic plasma description due to the complicated and time-consuming nature of calculation of distribution function development. However, the problems outside thermodynamic equilibrium or containing multiple specific particle-particle or particle-surface interactions still require kinetic approach to set the boundary conditions for the fluid modelling. As we have already reported in the Annual report of 2010, our task was to evaluate the influence of oblique magnetic field on the flow conditions of individual particle species. We have made calculations of the spatial profiles of the polytropic function for collisionless plasma with finite length scale ratios. Only recently has it been shown, that polytropic function in front of a boundary is indeed not a constant value, as being portrayed in literature until now. This is an important fact, since calculations of exact values of the polytropic can provide improvements in calculation of quantities that include it, e.g. ion sound speed, and adds to the general understanding of plasma flow conditions.

The classical approach in fluid model of warm plasma the value of the polytropic function is taken to be e.g. $\gamma=1, 3, 5/3$ for isothermal, 1D adiabatic and 3D adiabatic flow, respectively. We first opted to improve this predictions by recognizing the tensorial nature of the pressure component in the ion equation of motion and extracted the value of the polytropic coefficient from the energy conservation equation. The derivation reveals the cosinusoidal term in the $\gamma_\parallel$ calculation.

$$\frac{1}{2}\left(\vec{u}\cdot\vec{\nabla}\right)p+\frac{1}{2}p\left(\vec{\nabla}\cdot\vec{u}\right)+\left(\vec{\vec{p}}\cdot\vec{\nabla}\right)\cdot\vec{u})=0 \qquad \vec{\vec{p}}\left(\parallel,z,\perp\right)=\begin{pmatrix} p_\parallel & 0 & 0 \\ 0 & y & 0 \\ 0 & 0 & p_\perp \end{pmatrix} \text{(1.1)}$$

$$\frac{\nabla_x p_\parallel}{p_\parallel}=\left(1+2\cos\alpha\right)\frac{\nabla_x n_i}{n_i} \qquad \gamma_\parallel=1+\frac{n_i}{\nabla_x n_i}\frac{\nabla_x T_\parallel}{T_\parallel} \qquad \nabla_x p_\parallel=\gamma_\parallel k T_\parallel \nabla_x n_i$$

However, this simplistic approach neglects the effects of the finite Larmor radius, which is very important in the fusion device aspect of the ratio $\lambda_D \ll r_{Li} \ll L_i$. Therefore, we have decided to use particle-in-cell simulations to simulate a classical Tonks-Langmuir (TL) model with an applied external magnetic field. Beside the polytropic function calculation, a comprehensive study of the magnetic presheath formation was made. In this way we establishing, among other things, the fact, that for finite ratios of length scales the magnetic presheath is not a quasi-neutral region.

The simulations were made using 1d3v massively-parallel fully-kinetic code BIT1 [3], which amongst others enables maintaining of the maxwellian distribution in bulk plasma, a fact crucial for TL model.

Such plasma model can be defined via ratios of three main parameters, namely Debye length λ_D, ion Larmor radius r_{li} and ionization length L_i; $\varepsilon=\lambda_D/L_i$, $\varepsilon_{Dm}=\lambda_D/r_{li}$, $\varepsilon_{mi}=r_{li}/Li$. In asymptotic three scale limit these ratios approach 0, which produces three distinctive regions, i.e. Debye sheath, magnetic presheath and ionization presheath. In our case we chose a finite, constant ratio of $\varepsilon=\lambda_D/L_i=2\cdot10^{-4}$ and studied the cases for varying $\varepsilon_{Dm}=\lambda_D/r_{li}$ from unmagnetized to strongly magnetized ions.
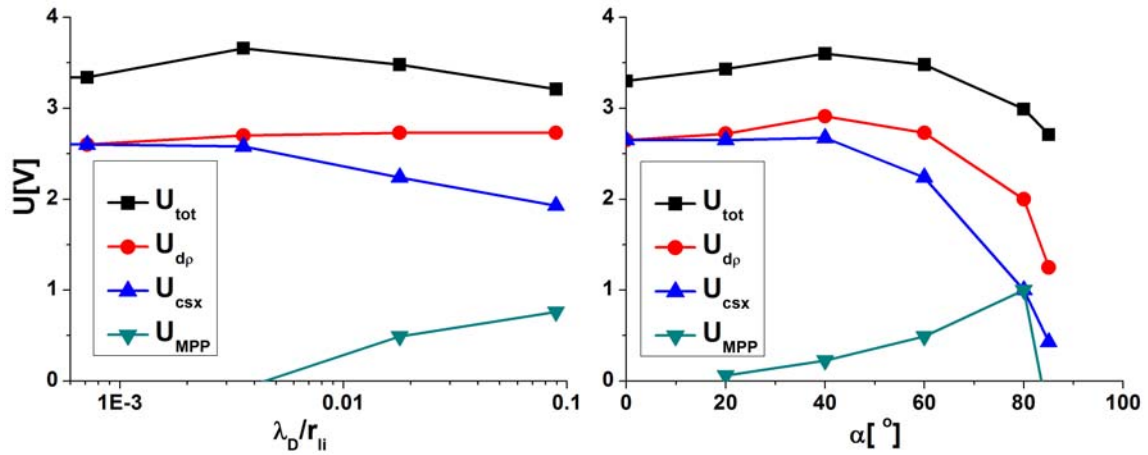
Figure 3: Potential drops in designated regions depending on the magnetization parameter ε_{Dm} at constant magnetic field angle $\alpha=60^{\circ}$ (left) and at constant $\varepsilon_{Dm}=1.8e-2$ with the angle of magnetic field varying (right) $\alpha=0-85^{\circ}$. (U_{tot} - total potential drop, $U_{d\rho}$ - drop in space-charge region, U_{csx} - drop inside region declared by Bohm acoustic velocity criterion, U_{MPP}, drop in region declared by Bohm-Chodura criterion).

The formation of individual potential regions in front of the wall is shown in Figure 3. In the top graph, dependence on the magnetic field density, or better yet, on the ratio between the Debye length and the Larmor radius, is shown for a constant magnetic field angle. The unchanged position of the entrance into space-charge region confirms the fact, that ions have no information on the nature of the presheath/sheath that they are entering. It is also to be noted, that the existence of the magnetic presheath is not only dependent on the ratios of length scales but also on the angle of the magnetic field. The maximum in the profiles of total potential drops proves to be a consequence of altering transport mechanisms to the boundary surface. In Figure 4 we present the dependence of the value of the parallel polytropic function and the normal polytropic function at the space-charge region entrance on the angle of the magnetic field and on the magnetic field density.
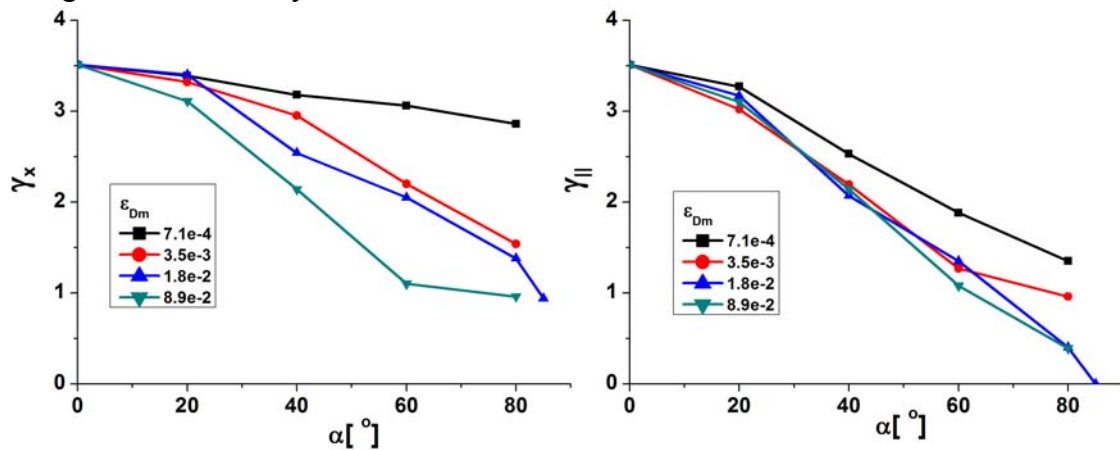

Figure 4: Values of the ion polytropic function (normal γ_x (left) and parallel $\gamma_{\parallel}$ (right)) at the entrance to the space-charge region depending on the magnetization parameter and the angle of magnetic field.

16

As predicted by the energy equation derivation, for parallel polytropic function, the dependence follows cosinusoidal function, but is also dependent on the degree of magnetization. I must also be noted, that the values are "offset" by the general plasma parameter of the ratio between the Debye length and the ionization length.

The same approach was applied also on the electron fluid. Here the model assumption was that electrons follow the Boltzmann relationship. This proved to be a good estimate, however the strong electric field produces a non-negligible cut-off of the distribution function, effectively changing the flow conditions. Since the electrons are practically fully magnetized until the entrance to the sheath, the flow is isothermal, characterized by the value $\gamma_x=1$. It is however increased inside the sheath and can reach the values of up to 2.
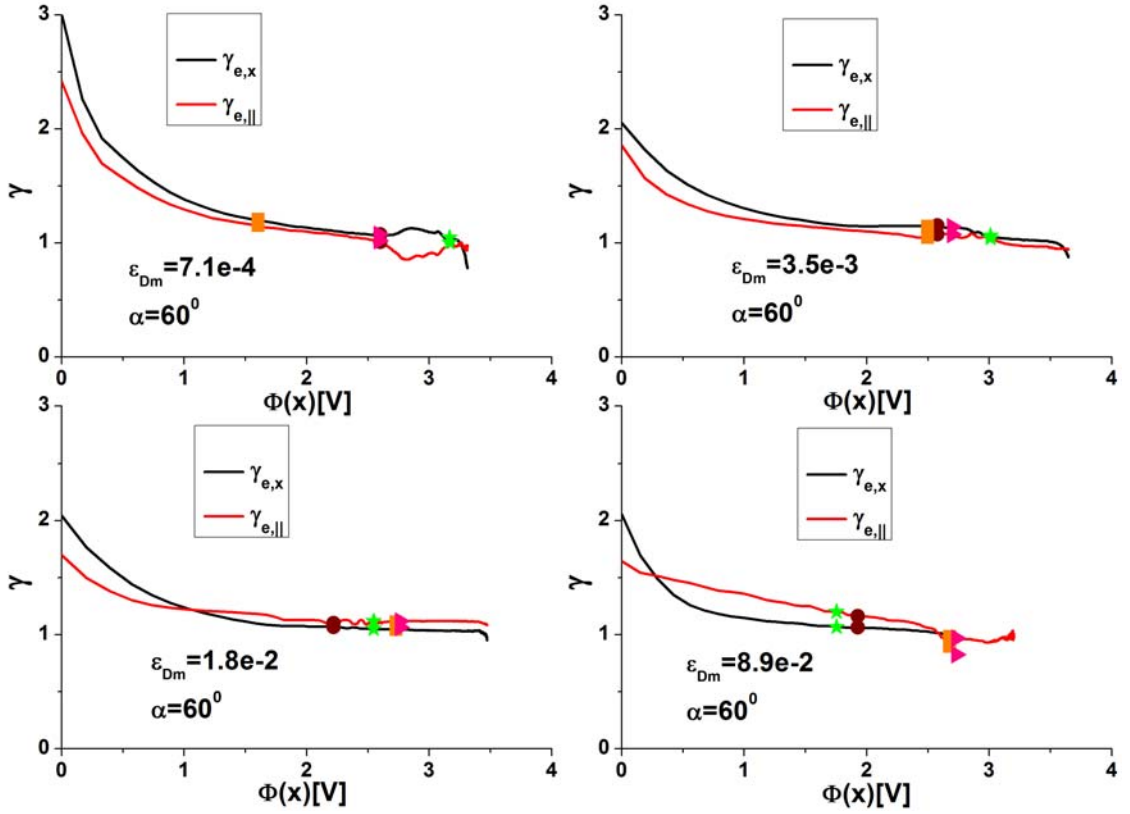

Figure 5: Profiles of polytropic functions (normal $\gamma_{e,x}$ (black) and parallel $\gamma_{e,\parallel}$ (right)) of the electrons for different magnetization parameters ε_{Dm}.

3 CONCLUSIONS AND OUTLOOK FOR 2013

We have further expanded theory on the use of emissive probes and reached a conclusion that the floating potential method of a highly emissive probe is not suitable for use in larger tokamaks. However, we do recommend a further pursuit of emissive probe installation in smaller tokamaks for SOL measurements, due to a reduced influence of electron temperature fluctuations in comparison to standard Langmuir probes. Also the effects of recently reported self-emissive probes have to be verified against an externally heated probe to understand the mechanisms. We are in talks with

ÖAW-P5 on the construction of such probe in 2013 to be possibly used in 2014 in ASDEX-UPGRADE.

We have also completed the study on the ion and electron polytropic function dependence on the angle and density of the magnetic field. The polytropic function proves to be highly dependent on this two parameters and can be estimated via simple MHD approach, as long as a reference value at zero magnetic field is known.

Also our work on other fields of plasma research is becoming more and more important in our involvement in the fusion research movement. We have continued our research collaboration on the alternative measurement methods with Langmuir probes with the Bulgarian association INRNE (prof. Tsv. Popov) [4]. Furthermore, beside the fruitful work regarding the second-derivative method used in weakly to intermediately magnetized plasmas it is planned to extend this to the first-derivative method used in strongly magnetized plasmas, specifically COMPASS-D tokamak, in 2013. Beside the evaluation of the measurements, our party is expected to also provide theoretical support and kinetic simulations of the COMPASS-D SOL region. We have also expanded our knowledge of kinetic simulations for probe measurements support with simulations of a synthetic probe inside our linear plasma device [5], which will be useful for the work on COMPASS-D simulations.

4   REFERENCES

1   T. Gyergyek, J. Kovačič, Floating potential of an electron emitting collector that terminates a bounded plasma system, Contrib. plasma phys., 52 (2012), 699-721.

2   T. Gyergyek, J. Kovačič, Potential formation in a bounded plasma system which is terminated by an electron emitting floating collector studied by a particle-in-cell computer simulation, Contrib. plasma phys., 53 (2013), 189-201.

3   D. Tskhakaya, A. Soba, R. Schneider, M. Borchardt, E. Yurtesen, J.Westerholm, PIC/MC code BIT1 for plasma simulations on HPC, Proceedings of the 18th Euromicro Conference on Parallel, Distributed, and Network-based Processing, IEEE, (2010), 476-481

4   Tsv. Popov, P. Ivanova, M. Dimitrova, J. Kovačič, T. Gyergyek, M. Čerček, Langmuir probe measurements of the electron energy distribution function on magnetized gas discgarge plasmas, Plasma sources sci. technol., 21 (2012), 1-10

5   J. Gruenwald, D. Tskhakaya, J. Kovačič, T. Gyergyek, C. Ionita, R. Schrittwieser, Comparison of measured and simulated electron energy distribution functions in low-pressure helium plasmas, Plasma sources sci. technol., 22 (2013), 1-7

PROCESSES WITH NEUTRAL HYDROGEN ATOMS AND MOLECULES

Iztok Čadež[1], Zvone Grabnar[1], Sabina Markelj[1], Primož Pelicon[1], Zdravko Rupnik[1], and Vida Žigman[2]

[1]Department for Low and Medium Energy Physics, "Jožef Stefan" Institute, Jamova cesta 39, SI-1000 Ljubljana
[2]University of Nova Gorica, Vipavska 13, SI-5000 Nova Gorica, Slovenia
iztok.cadez@ijs.si

1   INTRODUCTION

The main goal of this project is to contribute to understanding and to provide quantitative data for processes with neutral hydrogen atoms and molecules which are relevant for the current efforts in EU towards developing the magnetically confined fusion. Processes on the surface as well as collision processes in the gas phase are both of our concern. However, the emphasis is on the surface processes which are recognized as most urgent regarding the ITER physics (IPH).

In 2012 we continued the study of H and D retention in ITER grade tungsten with the goal to understand the influence of the neutron induced damage to the retention. To simulate n-irradiation, damaged samples are in our case produced by high energy W-ion irradiation, the so-called self-implantation. This work is conducted in collaboration with Max-Planck Institute für Plasmaphysik (IPP), Garching, Germany and is the subject of a task agreement within EFDA IPH WP2012. The samples were exposed to a well characterised beam of thermal deuterium atoms (~0.2 eV) produced by the flow of hydrogen gas through a hot tungsten capillary. Study of deuterium retention after long-term D exposure of undamaged and damaged samples at different sample temperatures was performed *ex-situ* by ^{3}He Nuclear Reaction Analysis (NRA) and Thermal Desorption Spectroscopy (TDS) providing new results on D retention in damaged W. In this year a new set up for *in situ* NRA studies was completed that will enable acquiring new information on the dynamics of D diffusion in damaged and undamaged W.

Another important activity has been started in 2012 where the aim is to study the efficiency and technological applicability of methods for fuel removal on tungsten. Most of these procedures work either by isotope exchange with hydrogen or deuterium or by producing volatile gas species by some kind of low temperature plasma or baking in vacuum. In collaboration with CEA, Cadarache, France and Laboratory for Physics of Interactions of Ions and Molecules (PIIM), University of Provence (Aix-Marseille), Marseille, France, we have concentrated on determination of deuterium release and re-absorption in W surfaces treated by RF discharges. This task is also a subject of a task agreement within EFDA IPH WP2012. The aim is to develop a well-controlled step-by-

step procedure for in-depth understanding of the adsorption, diffusion and desorption of D from W, and also of formation of the defects by D removal techniques and their impacts on the re-adsorption process. The JSI part of the task was to prepare and perform NRA analyses of the exposed samples whereas the CEA/PIIM part of the task was to perform D ion/plasma exposure and TDS experiments.

Spectrometer for vibrational diagnostics of hydrogen molecules based on the properties of low energy dissociative electron attachment was modified. Differential pumping of reaction and detection region is achieved by an addition of turbomolecular pump so that important enhancement of instrument's performance was insured.

2   WORK PERFORMED IN 2012

Research activities in 2012 are described below following the specific objectives as given in the work plan for 2012. Efforts were focused to the problems clearly identified in EFDA tasks within Topical Research Area 3.2 and 3.3. Part of the activity within WP2012 of the present project and also described below is a part of another task in A1.3 whose main body is described in the report of the Project 1.4.3.

2.1   Study of H/D retention, surface recycling and isotope exchange on W pre-irradiated by high energy W ions

The prediction of hydrogen isotope retention in undamaged and n-irradiated W is an important issue for edge plasma research as it has significant implications for the operation of ITER and future fusion reactors. In particular this issue is important for DEMO where more important n-damage will occur. The self-implantation of W (self-damage) is the most adequate approach for simulation of n-irradiation because it generates dense cascade with large clusters which are typical for n-irradiation and any chemical effects are avoided. The aim of our work is to determine the influence of self-damage on hydrogenic retention in different grade tungsten materials exposed to thermal hydrogen atoms.

The study of D retention in damaged W exposed to thermal D atoms was for the first time started in 2011. We performed *in situ* study by Elastic Recoil Detection Analysis (ERDA) (JSI), where undamaged and damaged W samples were exposed to thermal D. The exposed samples were after the *in situ* study analysed *ex situ* by NRA (at IPP). We have observed that D is retained in W. Both methods gave similar results in the ERDA depth range, up to 400 nm. The retention was higher in damaged W, with D being

Figure 1: D depth profile in damaged W at 600 K for two different D fluences and at 700 K and 800 K.

retained down to the depth range of damage profile, but D retention was observed also in undamaged W down to 1 μm. This work was presented at the PSI conference and will be published in Journal Nuclear Materials (2013) [1].
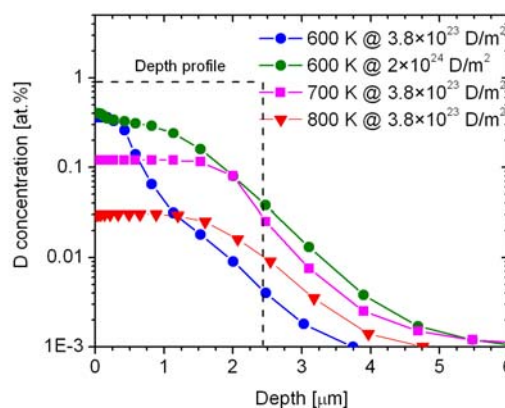
20

In 2012 we continued this work by exposure of damaged and undamaged W to thermal D at different D fluences and temperatures (from 500 K to 900 K) and the exposed samples were then *ex situ* analysed by NRA and TDS. Damaged samples were obtained by irradiation at different ion energies creating a flat damage distribution with 0.89 dpa damage concentration. The sample temperature during damaging was room temperature. The thickness of the damaged layer was 2.4 μm. D depth profile at 600 K sample temperature for two different fluences is shown in Fig. 1.

One can observe that by increasing the fluence, D saturates the traps created by W ions, so that the D-depth profile is similar to the depth profile of the damage created by W ions. D-depth profile obtained at temperatures 700 K and 800 K is also shown in Fig. 1. The fluence needed to obtain the D saturation in the traps, is lower in this case. It is lower at higher temperatures, due to faster diffusion at higher temperatures. The D saturation concentration as a function of sample temperature is shown in Fig. 2. One can also observe that the D saturation

Figure 2: D saturation concentration in the in damaged W as a function of sample temperature.

concentration decreases with temperatures; namely, D is de-trapped from low energy traps and radiation damage is partly annealed at temperatures above 500 K. The D
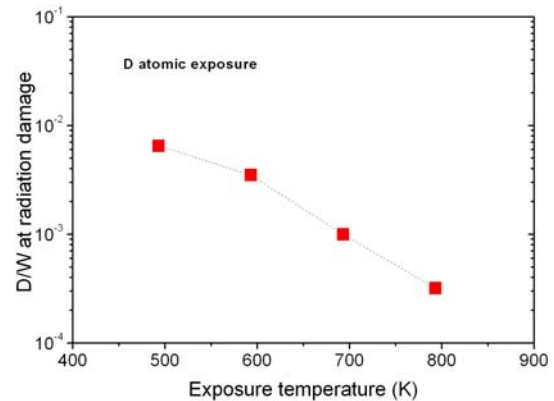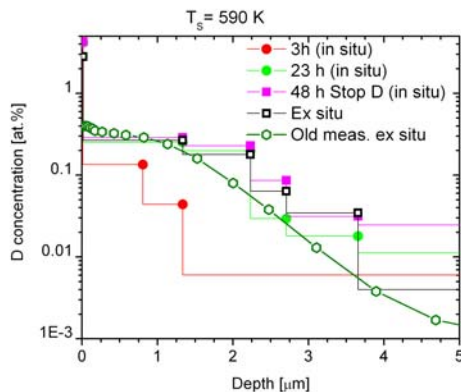

Figure 3: D depth profile measured during the exposure and after exposure ex situ by NRA. Fo comparison also old measurement of depth profile obtained at the same temperature at ex situ measurement.

retention was studied also at 900 K where we applied different cooling rates after stop of D atom exposure. The D retention in the sample with slower cooling rate was smaller indicating that D desorbed during the cooling. The influence of the sample temperature (600 K) during damaging by W ions and damaging level on D retention in W exposed to D atoms was also studied. The thermodesorption spectroscopy was also performed after the exposure and NRA and spectra are under evaluation.

New broad beam NRA set up was completed at JSI (with 1500 μm thick proton detector at 135° and an α detector at 102°) and calibration measurements were done on a standard a-C:D samples. First *in situ* NRA measurements on damaged and undamaged W exposed to D atoms at 590 K sample temperature was performed at the end of 2012, with experimental procedure similar to *in situ* ERDA measurements [1], [2]. The depth profiling was performed during the exposure and after stop of D atom exposure. This was the first time that D depth profiles were measured simultaneously during the exposure enabling a deeper insight into the D diffusion in W

bulk. The same sample was after *in-situ* experiment also analysed *ex situ* by NRA at IPP and similar depth profile was obtained as after the end of exposure. The obtained depth profiles are shown in Fig. 3, where, for comparison, the depth profile of the old measurement at the same temperature is shown. From these depth profiles obtained at different exposure times, more detailed information on the diffusion dynamics of D in W will be obtained.

This work is conducted within EFDA PWI WP12-IPH-A03-1-13/PS&BS-01/MHEST entitled: "Atomic and low-energy hydrogenic plasma interaction with damaged tungsten" in collaboration with IPP, Garching. Results were presented at 21st PSI in Aachen, 21-15 May, 2012 in the contribution: "Study of Thermal Hydrogen Atom Interaction with Undamaged and Self-Damaged Tungsten", by S. Markelj et al.

2.2   Deuterium desorption from tungsten and deuterium re-adsorption on fuel depleted samples.

The main goal of this part of the project is to study thermal desorption (TD) of deuterium from W exposed to well defined deuterium ion beam or plasma. The purpose of this is to develop a well-controlled step-by-step procedure aimed to facilitate in-depth understanding the of adsorption, diffusion and desorption of D at/in/from W, and the formation of defects by D removal techniques and their impacts on the re-adsorption. The work presented here has been performed at CEA, Cadarache and PIIM laboratory, University Aix-Marseille, within the postdoctoral visit of Sabina Markelj from JSI (9 month EURATOM mobility scheme). The exposure and the TD spectroscopy will be made at the PIIM laboratory and the depth profiling of D in the exposed samples will be preformed by NRA at JSI.

In the frame of this work the system of doubly differentially pumped mass spectrometer was installed at the PIIM laboratory in order to be able to do *in situ* TD spectroscopy (the CAMITER set up). Beside the mass spectrometer two ion guns are mounted, ion energy range 200 eV – 5 keV, with typical ion current of few µA, on the ultra high vacuum chamber, background pressure 5×10^{-10} Torr. The experiment is designed to provide sample cleaning, well defined exposure to chosen ions and recording thermo-desorption spectra without breaking vacuum. A second high vacuum chamber where samples are exposed to plasma is connected to TD chamber so that samples can be transferred between the chambers without exposure to air.

Before starting deuterium retention studies by temperature programmed desorption (TPD) we studied W cleaning procedures in order to obtain well characterized and clean W surface. Recrystallized W samples from A.L.M.T. Corp., Japan were purchased for this project. The W sample properties and cleaning procedure were studied in detail first by Secondary Electron Microscopy (SEM) before and after electropolishing and then by Auger Electron Spectroscopy (AES) and High Resolution Electron Energy Loss Spectroscopy (HREELS).

Since we studied the sample cleaning procedure step by step, it took longer time than planned and also in order to achieve sub-monolayer oxygen contamination, we tried several annealing/flashing procedures to obtain such clean surface. The *in situ* cleaning procedure on freshly polished polycrystalline W samples was optimized and proved to be reproducible in attaining sub-monolayer ($\sim10^{18}$ atom.m^{-2}) impurity concentration.

Namely, we have managed to efficiently clean the surface by sample flashing to 2000 K with remaining only low sub-monolayer oxygen contamination and no
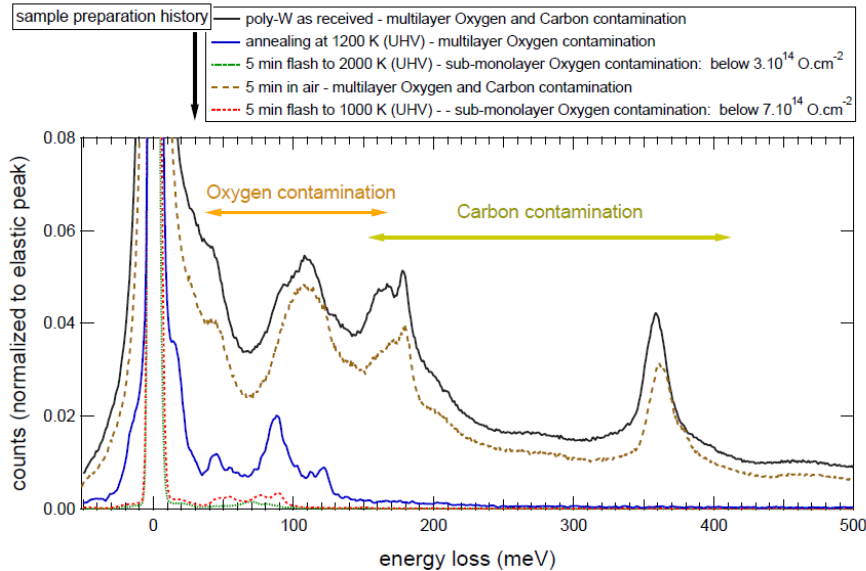

Figure 4: HRLEES spectrum obtained after flashing the sample up to 2000 K. The surface contamination and their cleaning after putting the sample for 5 min in air is also shown.

hydrocarbon contamination, shown in Fig. 4. Adsorption of impurities after exposing such clean W sample to air for 5 min was also studied. As can be seen in Fig. 4 the sample had slightly lower surface contamination as on the pristine sample, but still on the same level. When flashing such sample only to 1000 K, we have again obtained clean surface with only sub-monolayer oxygen contamination.

In order to obtain reliable TPD spectra on the new doubly differentially pumped mass spectrometer system, it first needed to be calibrated, optimized and checked for sensitivity. Beside this, before the ion implantation could be performed we optimized also the ion gun set up by observing the ion beam size and position by quartz plate, placed at the sample position. We started to analyze the sensitivity of the new system on HOPG sample, which is well studied material in surface science. The effect of Ar bombardment on its retention in Highly Oriented Pyrolyic Graphite (HOPG) has been studied for a large range of fluence (10^{18}-10^{20} Ar m^{-2}) and at three Ar ion energies and interesting effect of TPD signal as a function of implantation dose has been found. Namely, the desorption signal was steadily increasing with the exposure dose up to 1 monolayer (ML) (1 ML $=3.8\times10^{15}$ C/cm^2). The signal at 2 ML was similar to the one at 1 ML, indicating stabilization of the integrated signal. But when the dose was further increased the signal drastically increased and broadened and at 8 ML an indication of two desorption peaks appeared. The TDS spectra of Ar desorbed from HOPG after Ar bombardment at different doses are shown in Fig. 5. Furthermore, to estimate the effect of the 2 min annealing at 1300 K after each TPD ramp on the ion induced damage in HOPG, the sample was then again bombarded sequentially to increasing doses of Ar ions. It was observed, that the shape of the thermodesorption signal stayed similar as the one obtained at the highest dose, only the intensity of the peak was smaller at the smaller dose. Still, the intensity of the signal at small implantation dose was much

higher as compared to the one obtained on freshly cleaved sample. This clearly showed the effect of surface damage due to ion irradiation on the retention and shape of the
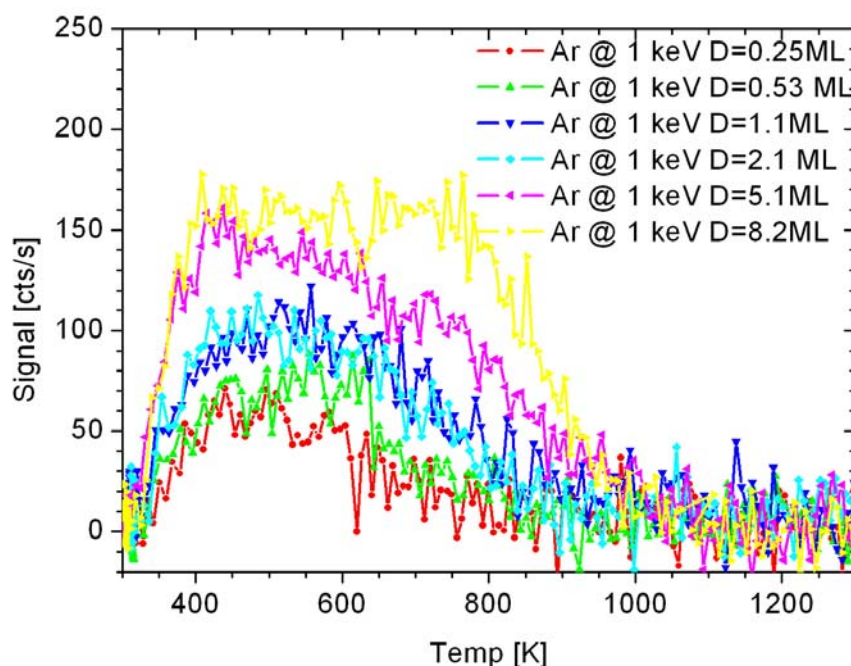

Figure 5: Ar TDS spectra obtained after Ar ion bombardment of HOPG at 1 keV ion energy for different ion doses.

TPD signal indicating on new type of trapping sites and provides means for quantitative estimate of damage influence on retention. The effect of HOPG annealing up to 1300 K on the re-saturation of Ar ions gave us some indication how the damaging of the material by ion exposure could be observed also at the D re-saturation in W.

After the study on HOPG we switched to tungsten, where we started to study D retention on well defined – clean sample surface in UHV system with the doubly differentially pumped mass spectrometer system. As presented above, we have obtained a good procedure how to efficiently clean the W samples after exposure to air for subsequent studies of hydrogenic retention in W. Namely, this sample that was first efficiently cleaned and analysed by HREELS was then transferred to CAMITER set up and cleaned by annealing to 1300 K in UHV for further TPD studies. After annealing it was exposed to D_2^+ ions with energy 250 eV/D to a fluence 18.8×10^{20} D_2^+/m^2. We have performed first study of implanted D ions in tungsten samples with controlled submonolayer impurity content. Our measurement extended existing dataset from the literature to the lower fluence and result is shown in Fig. 6. The sample was also exposed to D_2 molecules at the same exposure conditions as for ions, gas flowing through the ion gun, but without the accelerating voltage. No desorption signal was detected in that case. On the other hand when the sample was exposed to D atoms from separate atom source, a small peak was observed, at slightly higher temperature. Still, due to low D retention in W the obtained signal was on the detection limit of the present set up.

First data on W sample with controlled submonolayer oxygen contamination were obtained and quantified. In order to improve the error bars and extend the retention plots to two orders of magnitude lower fluence the setup is now being modified to a singly differential pumping configuration. The NRA depth profiling of D-ion exposed samples was not performed yet, since we wanted first to have well controlled TPD system with reproducible results on W. Both set-ups at JSI and at PIIM are now

Figure 6: D retention obtained for the present exposure at low fluence is compared to the literature.

ready for gathering data on efficiency of D removal by thermal treatment and D re-saturation in such material and then further to study the efficiency of removal by helium RF-discharge.

This work is conducted within EFDA PWI WP12-IPH-A03-2-06/PS&BS-01/MHEST entitled: "D re-adsorption/re-saturation of W surfaces subjected to helium RF-discharge as a fuel removal technique" in collaboration with CEA, Cadarche and PIIM, Marseille, France.

2.3 Interaction of hydrogen, small hydrocarbons and nitrogen with high Z materials.

Study of surface reactions at elevated temperature is of our constant interest. By using vibrational spectrometer for hydrogen molecules (DTVE) [3] we studied the influence of the flow of small hydrocarbons over the hot tungsten on the production of hydrogen atoms and vibrationally excited hydrogen molecules [4]. A very specific abrupt desorption of hydrogen atoms was observed during tungsten filament heating after being subjected to the flow of ethylene [5]. This desorption occurred in the narrow temperature range between 940-980°C during continuous filament heating from room temperature as shown in Fig. 7. The observed phenomenon resembles to a "volcano" effect previously observed in gas desorption from water ice at low temperature (e.g. [6]). In this case a pre-absorbed gas is abruptly released when the transition of solid water from crystalline to amorphous phase occurs. In the present case, the observed desorption occurs close to the critical temperature where the carbon diffuses in the bulk of tungsten and W_2C carbide is formed [7]. This characteristic temperature together with relatively abrupt nature of desorption, lasting some $10 - 12$ s, suggests that we are dealing with similar, "volcano" stile, desorption mechanism. In present case, hydrogen which was previously trapped in hydrogenated carbon deposit on tungsten is being released.
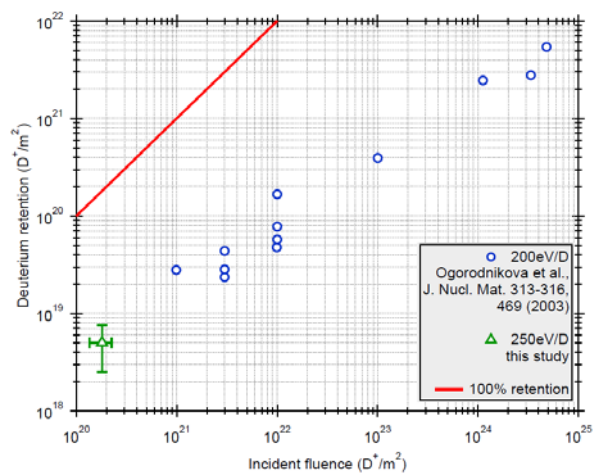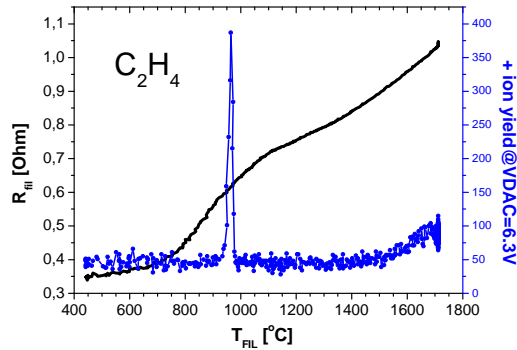
Figure 7: The proton yield as a function of filament temperature. The rate of the temperature change is about $4^oC/s$. The variation of the filament resistance is also shown.

The amount of the released hydrogen is relatively small so that no change of the ionization gauge reading could be observed. By repeating desorption under background vacuum a weak increase of background pressure simultaneous with desorption peak allowed an estimate of the amount of desorbed gas to be made and it is of the order of few monolayers of hydrogenated carbon deposit.

The observed desorption process might be quite general mechanism at the temperature where mixed materials can undergo phase transition. It can influence transient gas release to the edge plasma when temperature of the plasma facing component is increasing.

We plan to continue this work in order to confirm the observed phenomenon and also in order to fully rationalize the conditions which lead to such desorption.

2.4   Other activities.

Some other works within the project which were not included in EFDA IPH tasks but are of constant interest in our project were done in 2012. Some of these works were planned in previous years but had to be postponed due to the priority of EFDA supported projects and restricted manpower. These other activities performed in 2012 are the following:

- The modification of spectrometer for vibrational diagnostics of hydrogen molecules created by atom recombination on surface was completed so to allow single-stage differential pumping of detector and reaction chamber. An additional turbomolecular pump was mounted horizontally and connected to the detector chamber. The detector and recombination zone are now connected only through a narrow slit allowing molecules emitted from the sample surface to be directly observed by spectrometer while keeping high ratio between pressures in the two zones and thus lower detection background. First experiments in this new geometry are planned in early 2013.

- Modelling of the gas cell containing vibrationally excited hydrogen molecules and hydrogen atoms was continued in 2012 in collaboration with University of Nova Gorica. A kinetic model was upgraded so to include molecules in all vibrational states (ground and 14 excited states), dissociated atoms and atoms adsorbed on the wall. An initial set of state specific transition probabilities for the interaction of hydrogen atoms and molecules with both cold metallic walls (300 K), and hot filament ($\approx$2000 K) (molecular vibrational excitation and deexcitation, thermodissociation and atom recombination) was put forward using the available literature data. Volume processes are ignored due to the low gas pressure in the experimental cell which is the target of modelling. To allow for the recombination via Eley-Rideal mechanism, hydrogen atoms adsorbed at the cold surface have been taken into account so that the model is now

considering 17 species ($H_2(v)$, v=0 to 14, free and adsorbed atoms). The testing of the numeric program was started.

- Part of the activity in 2012 was devoted to the data on dissociative electron attachment (DEA) to molecules present in the edge plasmas. In collaboration with The Open University, Milton Keynes, UK we initiated detailed study of negative ion production by electron impact in two important small unsaturated hydrocarbons, C_2H_2 and C_2H_4 by velocity map imaging technique. A detailed overview of the current status of DEA data was prepared for and presented at the regional meeting of VAMDC data portal [8] in Belgrade, Serbia. The ion pair formation, often called dipolar ionization, is another important mechanism for anion production by electron impact. For modelling anion reaction this process is often neglected as it occurs at higher electron energies where electron population is often small. However this can be compensated by much broader energy range of this non resonant process, from the threshold upwards.

3   CONCLUSIONS AND OUTLOOK FOR 2013

In 2012 we had two EFDA tasks. In collaboration with IPP we had a task entitled "Atomic and low-energy hydrogenic plasma interaction with damaged tungsten", Garching - EFDA PWI WP12-IPH-A03-1-13/PS&BS-01/MHEST with dr. Sabina Markelj as the responsible researcher. Results were presented at 21st PSI in Aachen, 21-15 May, 2012 in the contribution: "Study of Thermal Hydrogen Atom Interaction with Undamaged and Self-Damaged Tungsten", by S. Markelj et al. and the conference paper is under publication in JNM (2013) [1]. This is also the first of specific objectives "Study of H/D retention, surface recycling and isotope exchange on W pre-irradiated by high energy W ions" from WP2012 for our project. All expected milestones were achieved and a paper studying deuterium adsorption on undamaged polycrystalline W is prepared for publication. It was shown that neutral D atoms do decorate the radiation-induced damage and since neutrals are present in the tokamaks it is crucial to know their contribution to retention. Additionally a paper entitled "In situ study of erosion and deposition of amorphous hydrogenated carbon films by exposure to a hydrogen atom beam" was published in 2012 [2], where the procedure for the *in situ* ERDA studies with hydrogen atom beam was described in detail for the first time.

In collaboration with CEA, Cadarache and PIIM, Marseille, France we had a task entitled: "D re-adsorption/re-saturation of W surfaces subjected to helium RF-discharge as a fuel removal technique" - PWI WP12-IPH-A03-2-06/PS&BS-01/MHEST with dr. Sabina Markelj as the responsible researcher. This is also the second of specific objectives "Deuterium desorption from tungsten" from WP2012 for our project. In this year we have obtained and quantified first data on D retention by TDS on W sample with controlled submonolayer oxygen contamination and NRA&RBS setup at the broad ion beam experimental station has been completed, tested and detectors calibrated. Both set-ups at JSI and at PIIM are now prepared for gathering data on efficiency of D removal by thermal treatment and D re-saturation in such material and then further to study the efficiency of removal by helium RF-discharge.

In 2013 we shall continue with the collaboration within the EFDA IPH tasks and study the D retention in W from different perspectives. Special emphasis will be given on the *in situ* studies by NRA, first time started in 2012, on damaged and undamaged W. The diffusion dynamics will be studied at different sample temperatures and by TDS

and NRA of W samples exposed to D ions and plasma with well controlled surface contamination. We will also further continue with the study of D atom recombination with new improved differentially pumped vibrational spectrometer.

4   REFERENCES

1   S. Markelj, O. Ogorodnikova, P. Pelicon, K. Sugiyama, I. Čadež, PSI 2012, J. Nucl. Material (2013) accepted for publication.

2   S. Markelj, P. Pelicon, I. Čadež, T. Schwarz-Selinger, W. Jacob, *In situ* study of erosion and deposition of amorphous hydrogenated carbon films by exposure to a hydrogen atom beam, J.Vac. Sci. Tech. A, 30 (2012), 041601-1

3   S. Markelj, I. Čadež, Production of vibrationally excited hydrogen molecules by atom recombination on Cu and W materials, J. Chem. Phys., 134 (2011), 124707-1-17.

4   I. Čadež, S. Markelj, A. R. Milosavljević, Influence of hydrocarbons on vibrational excitation of H2 molecules Nucl. Eng. Des., 241 (2011), 1267-1271.

5   I. Čadež, S. Markelj, Hydrogen Desorption from Hydrogenated Carbon on Tungsten, 21st International Conference Nuclear Energy for New Europe, Ljubljana, Slovenia, 5 – 7 September 2012 – Proceedings, Eds. T. Žagar and S. Furst, Nucl.Soc. of Slovenia, 1113.1-7.

6   M. P. Collings, J. W. Dever, H. J. Fraser, M. R. S. McCoustra, D. A. Williams, Carbon monoxide entrapment in interstellar ice analogues, Astrophys. J., 583 (2003), 1058-1062.

7   Ch. Linsmeier, M. Reinelt, K. Schmid, Surface chemistry of first wall materials – From fundamental data to modelling, J. Nucl. Mater., 415 (2011), S212-S218.

8   http://www.vamdc.org/

REMOVAL OF DEPOSITS BY NEUTRAL OXYGEN AND NITROGEN ATOMS

Miran Mozetič, Alenka Vesel, Aleksander Drenik, Rok Zaplotnik

Plasma Laboratory at the Department of Surface Engineering and Optoelectronics of the
Jožef Stefan Institute (IJS)
miran.mozetic@ijs.si

1   INTRODUCTION

Our project is focused on the research of interaction of potential plasma facing
materials with neutral atomic species. The neutral atomic species can either come from
the fusion plasma – hydrogen atoms in the divertor area and the plasma-shadowed areas
– or could be created with remote sources, such as neutral oxygen and nitrogen atoms.

Initially, our project was aimed at developing an efficient method of removal of
amorphous hydrogenated carbon (a-C:H) deposits. As carbon fibre composites are
among the list of candidates for ITER's plasma facing material, the formation of
amorphous hydrogenated deposits (a-C:H) presents a very serious operational and
safety issue. Hydrogen species from the plasma react with carbon atoms in the plasma
facing material, forming C_xH_y complexes. These desorb from the wall and are deposited
elsewhere in the reactor, thus forming a-C:H deposits. The formation of a-C:H layers
leads to entrapment and retention of fuel within the reactor vessel. To ensure a safe and
uninterrupted operation of a fusion device, these deposits must be regularly removed
[1].

In the scope of our project, we focus on the chemical methods of fuel removal,
namely removal by neutral oxygen and hydrogen atoms. Experiments with atomic
oxygen have so far yielded promising results and continue to be in the close focus of
our research activities. However, indications that use of atomic oxygen may not be
compatible with in-vessel reactor components force us to search for alternative routes.
For that reason, we have extended the scope of our research onto the interaction of a-
C:H with neutral nitrogen species. Since tungsten was introduced as a possible plasma
facing material for ITER, the interaction of tungsten and neutral hydrogen atoms has
also become the subject of our research.

2   WORK PERFORMED IN 2012

Our work performed in 2012 can be subdivided into research and development
of fuel removal methods, and the study of the compatibility of tungsten with the highly
chemically reactive environment of cold hydrogen plasma. The experiments were

performed in close collaboration with our European partner laboratories – CNRS Font-Romeu, LAPLACE, Toulouse and CIEMAT, Madrid.

2.1 Scavenger effect research

Research so far has indicated that nitrogen containing species can react with carbon precursors, thus preventing the formation of a-C:H layers. However, in a real-life experimental setting, only the net effect of nitrogen based species is detected. In other words, the absence of deposit on the sample surface may be either due to the scavenger effect or due to the erosion of the formed a-C:H deposit by nitrogen species. In this experiment, we evaluated the efficiency of erosion of a-C:H by ammonia plasma.

We performed experiments of erosion of a-C:H deposits by reactive species produced in an inductively coupled radiofrequency discharge in pure ammonia. Samples of a-C:H were exposed to the near afterglow of ammonia plasma. The erosion process was monitored *in situ* by means of laser interferometry. The experimental set-up can be seen in Figure 1. The main part of the reactor system was a borosilicate glass tube with the inner diameter of 36 mm, which branched out into two perpendicular tubes. A 6 turn coil (2) was wound around the main tube directly next to the branching. The coil was, by means of a matching network, connected to a radiofrequency generator (1), operating at the frequency of 13.56 MHz, used to ignite and sustain the plasma in the main tube. An optical fibre, connected to an Avantes AvaSpec 3648 optical emission spectrometer, was mounted near the inductive winding. A temperature-controlled sample holder (3) was mounted in the bottom side-tube, and a pair of a laser module (6) and a laser light detector (7) was mounted above the top side-tube. The top side-tube was closed with a quartz glass window
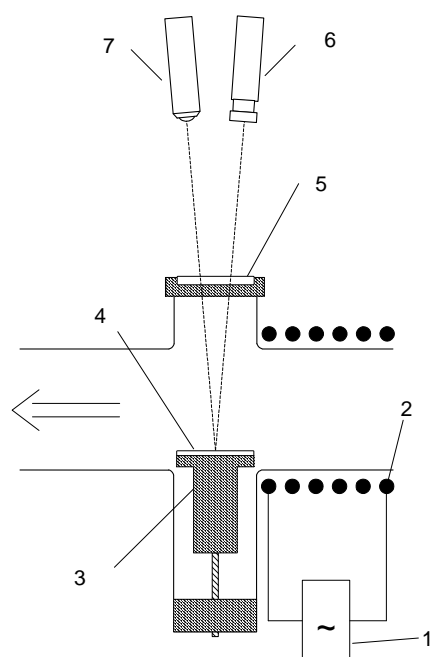

Figure 1: Schematic of the experimental set-up: 1 – RF generator, 2 – inductive winding, 3 – temperature controlled sample holder, 4 – sample, 5 – quartz window, 6 – laser module, 7 – photo detector module.

(5). Working gasses were leaked into the system through a needle valve. The pressure in the main tube was monitored with a Baratron absolute pressure gauge. The system was pumped by means of a two-stage rotary pump with the maximum pumping speed of 80 m^3/h. Prior to the erosion experiments, a characterisation of the plasma system was performed by means of optical emission spectroscopy and a double Langmuir probe.

Depending on the source gas pressure and the set forward power of the RF generator, the plasma system could operate either in E-mode or H-mode. In the E-mode, the glow region of the plasma, is spread out along the discharge tube, often reaching the metal fittings at its edges. In the H-mode, the area of extensive luminosity is localised to the volume covered by the inductive winding. Because the matching network was optimised for the H-mode the electron density was considerably higher in the H-mode than in the E-mode. The results of the measurements with the double Langmuir probe are presented as densities of charged particles versus source gas pressure, in Figure 2. Two separate branches are clearly observable. In the measurements performed in the E-mode, the density of charged particles was found to decrease at higher source gas pressures at the majority of set generator forward powers. On the contrary, in the H-mode, the density of charged particles exhibited a steep
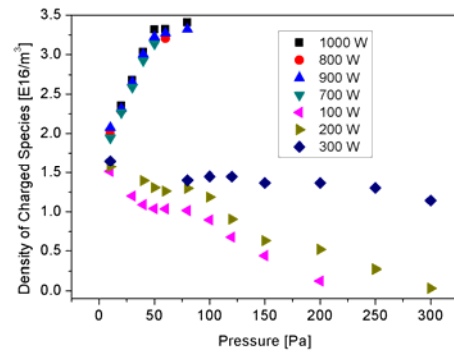

Figure 2: Double Langmuir probe measurement of charged particles density in plasma of ammonia versus source gas pressure, at different forward powers

increase for all values of the set generator forward power. Optical emission spectroscopy measurements of ammonia plasma in the E-mode and H-mode are presented in Figure 3. In the E-mode, the spectrum shows a strong NH peak and a NH_2 band, whereas in the H-mode, the NH_2 band is not present and the NH peak is strongly reduced. This suggests that there is a significant reduction of the density of NH_x species in the H-mode. The resulting plasma becomes mixed nitrogen-hydrogen plasma, rather than plasma of ammonia.
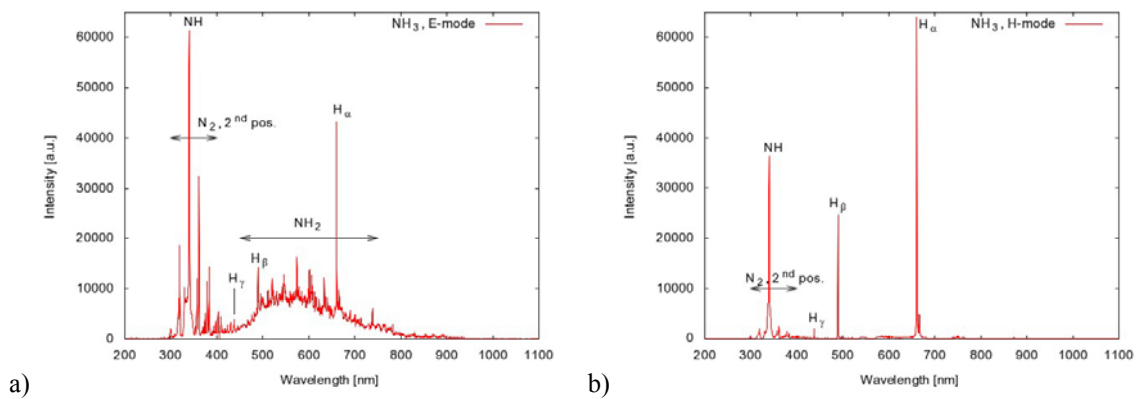

Figure 3: a) Optical emission spectrum of plasma of ammonia in E-mode, b) optical emission spectrum of plasma of ammonia in H-mode.

The erosion, as well as the growth, of the amorphous hydrogenated carbon deposits was monitored with a laser interferometry system. The system consisted of a laser module that produced laser light with the wavelength of 635 nm and the intensity

of 3 mW. The light was passed through a quartz window to the sample. The intensity of the reflected light was measured with a Hawkeye ® laser detector.

The sample material was deposited on a piece of polished silicon wafer. The silicon substrate was cut in a way to cover as much surface of the sample holder as possible. The typical dimension of the substrate was thus 15 mm across and therefore significantly larger than the diameter of the laser beam (< 3 mm). It was found that the adjusting of the laser interferometry system after mounting of the sample could not be performed without at least slightly moving the laser module and, in consequence, modifying the position of the laser spot on the sample surface. Since past experience has shown that the distribution of active species along the surface is not necessarily constant[2-6], comparable results would be best obtained by keeping the laser spot at a constant position. In order to eliminate the need for re-adjusting of the laser interferometry system, the a-C:H samples were deposited *in situ*.

The samples of a-C:H were deposited by creating an inductively coupled radiofrequency discharge in pure acetylene. The substrate was kept at room temperature. The working gas pressure was 15 Pa. The forward power of the RF generator was set at 50 W. At these conditions, the generator was operating in the E-mode. This procedure resulted in approximately 1 nm/s growth of thin a-C:H films with the refraction index of 2[7]. Typically, around 650 nm thick films were grown.

Immediately after growing, the a-C:H sample deposits were exposed to the early afterglow of ammonia plasma. The pressure of ammonia ranged from 15 Pa to 75 Pa and the forward power of the generator ranged from 100 W to 700 W. The generator was operating both in the E-mode as well as H-mode. The temperature of the sample surface ranged from room temperature to 250 °C.

The measured erosion rates depended strongly on the surface temperature and on the plasma generation mode. Without additional heating, the average erosion rate obtained in the E-mode was 0.10 nm/s ± 0.05 nm/s. The average erosion rate obtained in the H-mode was 4.0 nm/s ± 0.9 nm/s. Optical emission spectra, recorded during the erosion of a-C:H films, are presented in Figure 4. In the spectra of the E-mode plasma, the H-alpha line is clearly distinguishable and the NH_2 band is also present. In the H-mode, however, the spectrum features distinctive signatures of pure hydrogen and nitrogen species, as well as CH and CN species. Like the spectrum of pure ammonia plasma (without the a-C:H sample), this suggests a high degree of dissociation of NH_3 molecules. Moreover, the presence of CH and CN lines indicates that both hydrogen and nitrogen species are involved in the erosion process. The relatively weak signature of mixed nitrogen-hydrogen species indicates that the rates of the re-formation of the NH_3 molecule are significantly lower than those of the erosion process or the recombination of N_2 and H_2 molecules, and that the surface processes do not result in the formation of nitrogen-hydrogen species, such as the HCN molecule.
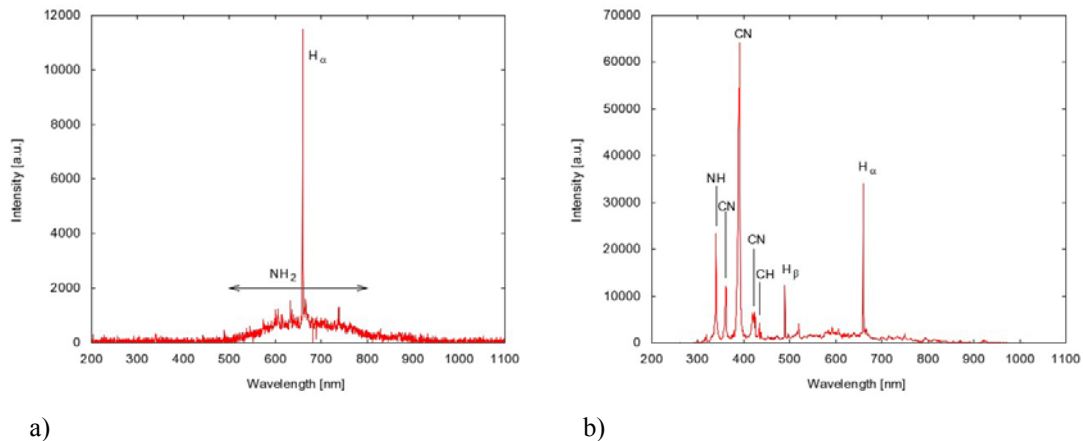
Figure 4: Optical emission spectrum recorded during the erosion of a-C:H in plasma of ammonia a) in E-mode, and b) in H-mode.

While the double Langmuir probe measurements clearly show that the density of charged species, which could directly or indirectly contribute to the erosion process, is higher in the H-mode, the OES measurements indicate that the difference in the erosion rates could be attributed to other influences beside the sheer density of active species. Namely, the high CN peak in the spectrum suggests that the key species in the erosion process are nitrogen atoms.

The effect of surface temperature was explored by varying the sample holder temperature while the plasma system was operating in the E-mode, at pressures between 15 Pa and 75 Pa , and set generator forward powers between 100 W and 300 W. Among the three parameters varied in this part of the experiments, the surface temperature exhibits the predominant influence on the erosion rates.

At the room temperature and 150 °C, the erosion rates do not change much with the increase of pressure. However, at 250 °C, the erosion rates were found to increase with pressure. This indicates that at higher pressure, more reactive species are produced. Although the density of charged particles is decreasing with pressure in this discharge regime, densities of active species, most likely neutral ammonia radicals (NH_2, NH) are higher at higher pressures.

At surface temperatures up to 150 °C, the rate of the erosion process appears to be temperature limited. Increasing the density of active species does not result in an increased erosion rate. At 250 °C, the trend of the erosion rate does not show signs of saturation. This indicates that at this temperature, the rate of the erosion process is limited by the density of active species.

2.2 Removal of a-C:H and interaction of plasma facing components with neutral oxygen atoms

Because of the very favourable erosion rates achieved in our previous experiments, we continued the research of fuel removal by atomic oxygen. We performed experiments with two different sources of atomic oxygen: inductively
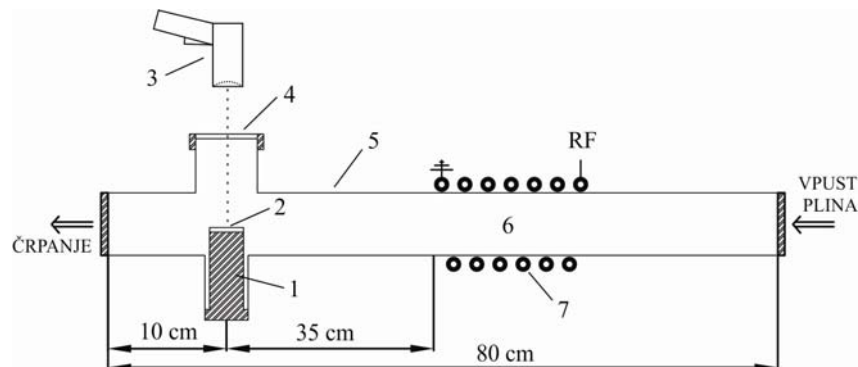
Figure 5: RF-plasma-based experimental reactor for fuel removal. 1 – Heated sample holder, 2 – sampe, 3 – pyrometer, 4 – IR transparent window, 5 – glass tube, 6 – discharge region, 7 – inductive winding.

coupled radiofrequency plasma and surface-wave microwave plasma. The experimental set-up of the radiofrequency source is shown in Figure 5. The source of atomic oxygen was weakly ionised plasma (6), created by means of an inductively coupled (7) radiofrequency generator. Pure oxygen was leaked into the reactor at pressures of 50 Pa and 100 Pa. The a-C:H samples (2) were mounted on a temperature controlled sample holder (1). The erosion process was monitored with an IR pyrometer (3). The oxygen atom densities were measured with a fibre optic catalytic probe (FOCP), and were found to range from $0.5 \times 10^{21}/m^3$ to $1.8 \times 10^{21}/m^3$. The measured erosion rates are shown in Figure 6.
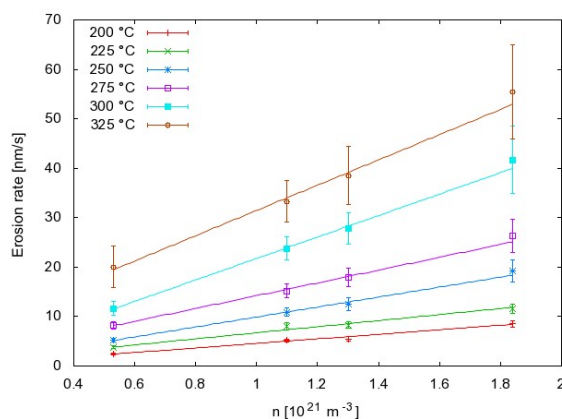

Figure 6: Rates of erosion of a-C:H achieved in the RF-based experimental system.

At the highest temperature, 325 °C, the erosion rate was as high as 50 nm/s. Moreover, the erosion rates were found to linearly increase with the density of atomic oxygen. This suggest that the saturation rate of oxidation has not been reached and that at these surface temperatures, the erosion rates could be even higher.

The microwave-powered experimental system is shown in Figure 7. The source of atomic oxygen was, in this case, weakly ionised plasma created by means of a microwave power supply connected to a surfatron (1). The mounting of the sample and monitoring of the erosion rate was the same as in the case of the RF-based experimental reactor.

The erosion rates are presented in Figure 8 where they are plotted against the atomic oxygen density. The maximum erosion rate achieved was 36 nm/s, at the surface temperature of 623 K. The source gas pressure was 200 Pa and the generator power was
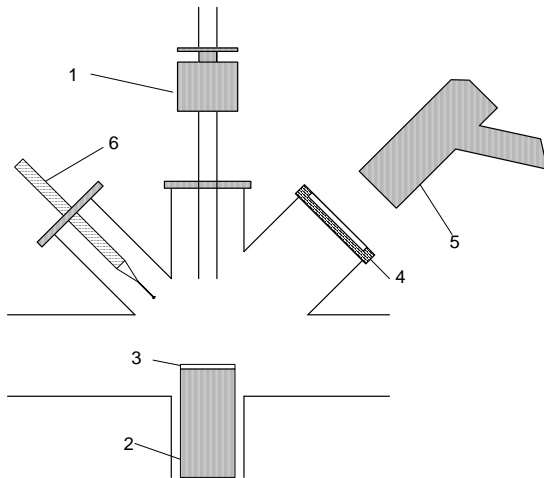
Figure 7: Microwave-plasma-based experimental reactor for fuel removal. 1 – surfatron, 2 – heated sample holder, 3 – sample, 4 – IR transparent window 5 – pyrometer, 6 – FOPCT.

been completely removed. Moreover, the plasma treatment was found to significantly decrease both the thickness of the carbon-tungsten interlayer (from 120 nm to 40 nm), as well as the carbon concentration in the interlayer (from 68 at% to 40 at%). This indicates that unlike molecular oxygen[8] the atomic oxygen species are efficient in removing carbon atoms from the mixed carbon-tungsten layer. While the primary goal of the experiment was to determine the erosion rate of the pure a-C:H layer by oxygen atoms, it is nevertheless encouraging to see that carbon atoms can be removed from mixed carbon-metallic layers by the same method. This finding could be the base of future carbon erosion experiments.

200 W. The atomic oxygen density in these conditions was $4 \cdot 10^{21}/m^3$, which corresponds to the degree of dissociation of 4 %. The erosion rates are somewhat lower than in the RF-based experimental system, with respect to the atomic oxygen density. This leads us to believe that the transport of neutral atoms to the sample surface is not as efficient in the microwave-based reactor.

Despite the difference in the erosion rates, both systems proved to be efficient in removal of the a-C:H layer. An Auger electron spectroscopy (AES) depth profile of as deposited sample is presented in Figure 9 a. The AES depth profile of a processed sample is presented in in Figure 9 b. The topmost, pure a-C:H layer has
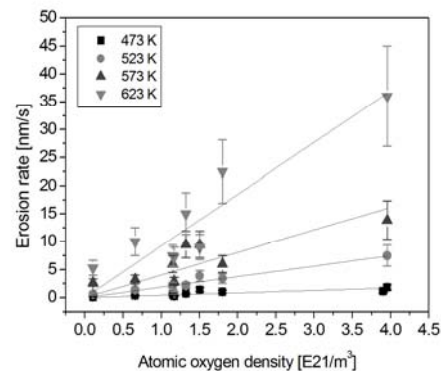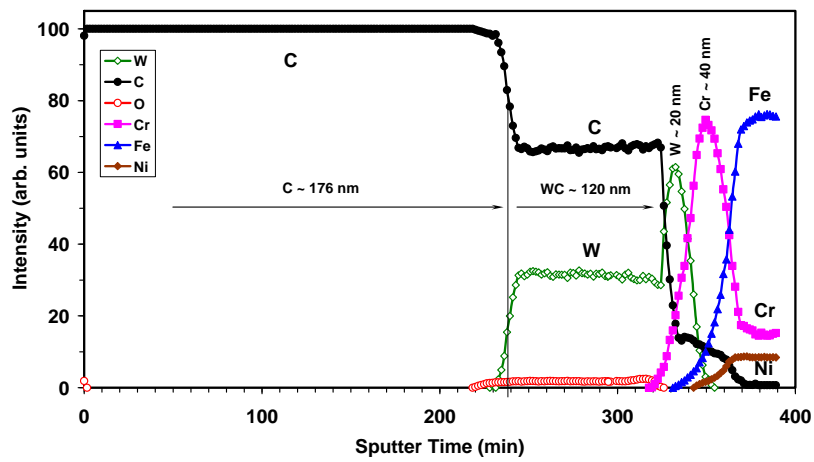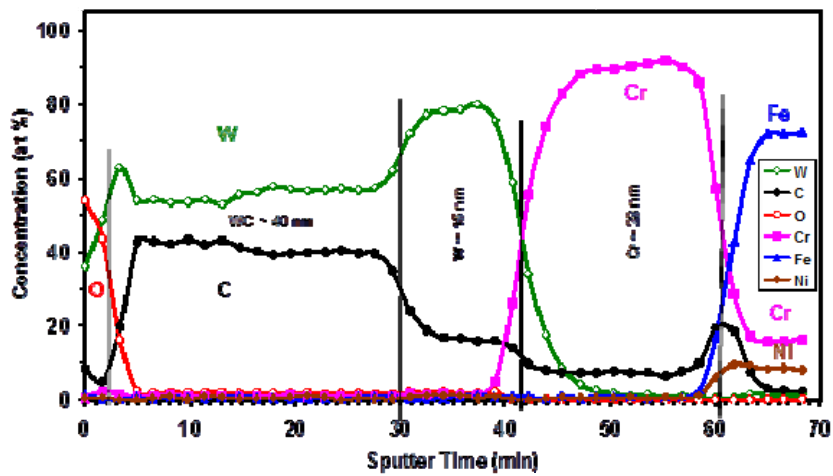

Figure 8: Rates of erosion of a-C:H achieved in the microwave-based experimental system.

a)

b)

Figure 9: AES depth profile of an unprocessed sample (a) and a sample exposed to atomic oxygen treatment (b).

2.3 Assessment of generation of dust by chemical methods for removal of co-deposits

In the past years, it has become apparent that the production of dust in fusion devices will present serious problems, both from the point of view of operation as well as safety, since dust particles may carry – and release – significant amounts of fuel. While dust may be formed by many processes in a tokamak, it is especially important that further production of dust by fuel-removal methods is avoided.

In 2012, we have started a series of experiments, dedicated to the assessment of production of dust by various chemical methods for removal of co-deposits. These experiments are performed within the EFDA Task WP12-IPH-A03-2, and in close collaboration with LAPLACE, Toulouse.

We developed a method of deposition of a large-scale model dusty deposit (MDD). The deposition

Figure 10 Top: Signature of the dusty discharge in the self-bias frequency spectrum – broad peak at 18 MHz, circled.
Bottom: The signature does not appear during removal of the a-C:H layer.

was performed in an electron cyclotron resonance (ECR) discharge, created in pure acetylene at the pressure of 0.1 Pa. The MDD is composed of graphite-like grains which are embedded in an a-C:H matrix. The grains are very mobile and in fact readily leave the surface during the deposition process. This results in very dusty plasma. The deposit itself is prone to cracking and flaking, further contributing to the dust population in the plasma.

We are also working on developing a fast and robust method of detection of dust particles in the plasma. We measured the self-bias voltage on an electrical probe inserted in the plasma reactor. In the frequency spectrum of the self-bias signal, we found a feature that is correlated to the appearance of dust in the plasma, namely a relatively broad peak in the 5 – 30 MHz range.

The MDD was exposed to removal by an ECR discharge in oxygen. In this case, no dust was observed in the volume of the reactor, neither visually nor in the self-bias frequency spectrum. This indicates that the dust particles embedded in the matrix were gradually removed while they stayed on the substrate surface the whole time, e.g. the dust particles were not mobilised during the fuel removal processing.
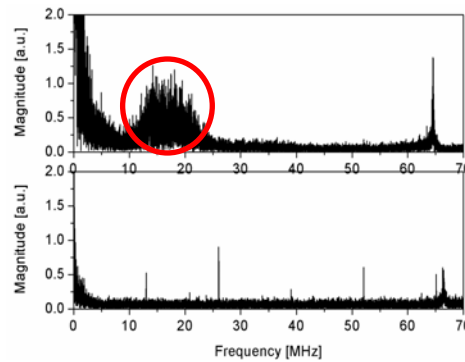
2.4 Interaction of plasma facing materials with hydrogen plasmas at extreme conditions

Exposure of metallic surfaces to high and abrupt heat loads often results in the growth of various nanostructures (nanowires, nanowebs, nanocones, in short: fuzz). The shape and dimensions of the resulting micro- and nanostructures strongly depends on the gas in the vicinity of the metallic surface during the thermal load. Exposure of metallic surfaces to plasma usually results in significantly different structures as those that appear on surfaces that have been exposed to less reactive gaseous environments. The modification of the surface topology may result in the modification of various parameters of the surface-gas (or plasma) interface; moreover, at subsequent heat loads the newly grown nanostructures can be degraded and eroded, making the nanostructured surface another source of dust production. Thus, the formation of fuzz on tungsten under high heat loads and simultaneous exposure to hydrogen plasma should be thoroughly investigated before it is used as a PFC material. The goal of this project is to determine the critical parameters at which nanostructures are produced. This project is conducted within the scope of the EFDA Task WP-12-IPH-A11-1.

In early 2012, initial experiments were performed at the solar facility at the CNRS Font-Romeu – Odeillo. A particularly suitable feature of the solar facility is that it allows for independent operation of plasma and heating to temperatures as high as 1500 K. Samples of pure tungsten were simultaneously exposed to weakly ionized hydrogen plasma and concentrated solar light which was used to heat the samples. The plasma was created by means of a microwave power supply, in pure hydrogen. The pressure of the source gas was 40 Pa and the power supply was set to operate at 500 W. The plasma exposure time was 2 minutes for all samples and the temperatures ranged from 1000 K to 1500 K. The processed samples were analysed by SEM at the Jožef Stefan Institute in Ljubljana.
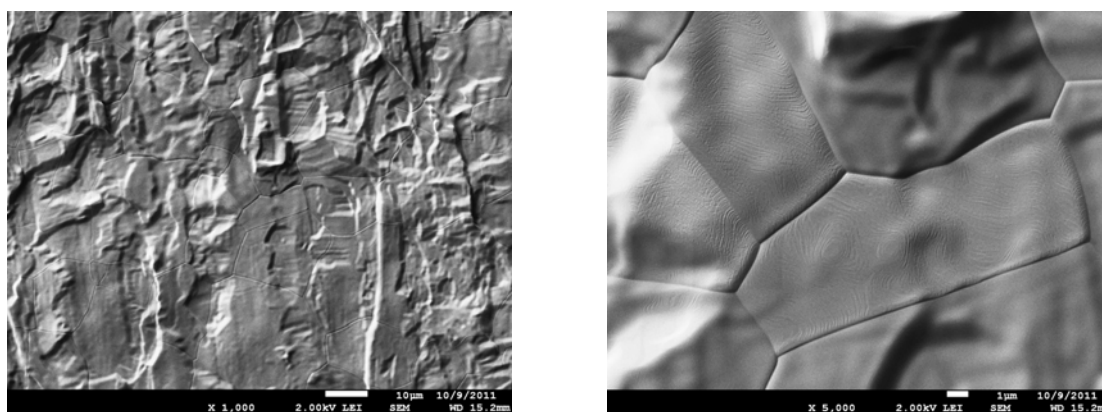
Figure 9: SEM images of W samples processed in H_2 plasma, at the temperature of 1500 K.

An example of the resulting SEM images is shown in Figure 1, which presents the sample that was heated to the highest temperature. The images do not show the presence of any sort of nanostructures. However, before we can safely conclude that exposure to H_2 plasma at high temperatures does not result in fuzz, we should take note that the samples were not processed and analysed at the same facility. Although a high

degree of attention was paid not to damage the sample surfaces during manipulation and (rather lengthy) process, we should still allow for the possibility that any nanostructures that might have been formed during the plasma processing have degraded during the transport due to "natural" processes such as aging. To verify this possibility, we are currently modifying our own plasma system at the JSI in Ljubljana, to allow for heating the samples to suitably high temperatures during H_2 plasma processing.

3   CONCLUSIONS AND OUTLOOK FOR 2013

In 2012, we continued the research of interaction of fusion-relevant surfaces with neutral atomic species. We performed experiments in removal of a-C:H layers by RF plasma of ammonia, in close collaboration with CIEMAT, Madrid. The maximum achieved erosion rate was 4 nm/s. This is lower by an order of magnitude than those achieved in oxidation experiments, however according to our past experience, higher erosion rates can be achieved by actively heating the sample surface. Moreover, we explored the impact of the E − H mode transition on the erosion efficiency of the plasma, and identified the plasma species that contribute the most to the a-C:H erosion.

In experiments with removal of a-C:H by neutral atomic oxygen we achieved very favourable erosion rates, up to 50 nm/s. Similar erosion rates were achieved with two different plasma systems that were used as atomic oxygen sources. This further reaffirms our interpretation that the erosion takes place only due to interaction with neutral oxygen atoms, not other plasma species or phenomena that are characteristic to either of the types of discharges used in the experiments.

In order to assess the production of dust during such methods of fuel removal, we developed a process of deposition of a-C:H layers with embedded graphite-like grains, and which are themselves prone to cracking, peeling, and other degrading processes which can result in the production of dust. We are also working to develop a method of dust detection which will assist us in further experiments of dust generation assessment. These experiments are performed in close collaboration with LAPLACE, Toulouse, and within the scope of the EFDA Task WP12-IPH-A03-2.

Since tungsten is being considered as another candidate for the ITER plasma-facing material, we performed experiments of interaction between a tungsten surface and neutral hydrogen atoms. The experiments were performed at CNRS Font-Romeu, France, within the scope of the EFDA Task WP-12-IPH-A11-1. The aim of the experiment is to verify the compatibility of tungsten with the chemically reactive environment of weakly ionised, highly dissociated hydrogen plasma. Primarily, we were interested in the formation of surface nanostructures which could lead to degradation of the material under fusion-relevant heat loads. Samples of tungsten surfaces were exposed to the afterglow of hydrogen plasma, created in a microwave powered plasma reactor, and to concentrated sunlight which allowed for the surface temperatures of 1500 K. The subsequent analysis of the samples by SEM revealed no nanostructures on the surface. Currently, we are upgrading our own experimental system. The upgrade will allow us to conduct such experiments on a wider scope, with more control over the plasma parameters.

Some of the research performed in 2012 was a continuation of already established experiments, and some of it are new experiments. While the new

experiments broaden our research focus with previously unexplored topics, they are nonetheless strongly connected to our past and current research. Experiments with erosion by plasma of ammonia rely heavily on the last year's study of E-H mode transition. The dusty plasma experiments will be incorporated into the already established fuel-removal experiments in the near future.

In the following year, we intend to continue the research on fuel removal methods, chiefly the removal by nitrogen-based plasma species. We will attempt to further characterise the reactions which contribute the most to the erosion process. In support of experiments of assessment of ammonia production at JET, we will investigate the production of ammonia in N_2–H_2 mixtures in laboratory plasma reactors.

Among the goals of the dusty plasma experiments started in 2012 is to produce samples of dusty deposits (or deposits prone to dust production) which will be used in already developed methods of fuel removal. These experiments are planned for early 2013. The research of fuel removal will be expanded even further – we will construct a remote source of oxygen atoms, intended for use on "real life" fusion devices. Initial experiments at COMPASS (Prague) are planned for 2013.

4 REFERENCES

1   G. Counsell, P. Coad, C. Grisola, C. Hopf, W. Jacob, A. Kirschner, A. Kreter, K. Krieger, J. Likonen, V. Philipps, J. Roth, M. Rubel, E. Salancon, A. Semerok, F.L. Tabares, and A. Widdowson, Tritium retention in next step devices and the requirements for mitigation and removal techniques, Plasma Physics and Controlled Fusion, 48 (2006), B189-B199.

2.   A. Drenik, A. Tomeljak, M. Mozetic, A. Vesel, D. Babic, and M. Balat-Pichelin, Behaviour of neutral hydrogen atom density in the presence of a sample holder in a plasma reactor, Vacuum, 84 (2009), 90-93.

3   A. Drenik, K. Elersic, M. Modic, and P. Panjan, Probability of Recombiantion and Oxidation of O Atoms on a-C:H Surface, Materiali in Tehnologije, 45 (2011), 281-285.

4   M. Balat-Pichelin, L. Bedra, O. Gerasimova, and P. Boubert, Recombination of atomic oxygen on alpha-Al2O3 at high temperature under air microwave-induced plasma, Chemical Physics, 340 (2007), 217-226.

5   M. Balat-Pichelin and E. Beche, Atomic oxygen recombination on the ODS PM 1000 at high temperature under air plasma, Applied Surface Science, 256 (2010), 4906-4914.

6   M. Balat, M. Czerniak, and J.M. Badie, Thermal and chemical approaches for oxygen catalytic recombination evaluation on ceramic materials at high temperature, Applied Surface Science, 120 (1997), 225-238.

7   F.L. Tabares, J.A. Ferreira, A. Ramos, D. Alegre, G. van Rooij, J. Westerhout, R. Al, J. Rapp, A. Drenik, and M. Mozetic, Tritium control techniques in ITER by ammonia injection, Journal of Nuclear Materials, 415 (2011), S793-S796.

8   J.W. Davis, C.G. Hamilton, A.A. Haasz, and R.G. Macaulay-Newcombe, Thermo-oxidation of hard carbon films with tungsten surface impurity, Journal of Nuclear Materials, 305 (2002), 66-69.

APPLICATION OF ION BEAM ANALYTICAL METHODS TO THE STUDIES OF PLASMA-WALL INTERACTION IN TOKAMAKS (IBAF)

Primož Pelicon, Iztok Čadež, Zdravko Rupnik, Primož Vavpetič, Sabina Markelj, Luka Jeromel, Matjaž Kavčič, Zvone Grabnar, Mirko Ribič

Department for Low and Medium Energy Physics,
Jožef Stefan Institute, Jamova 39, P.O.B. 3000, SI-1000 Ljubljana
primoz.pelicon@ijs.si

1   INTRODUCTION

The research of the fuel retention involves deuterium operation in fusion plasma reactors, as well as various simulations of physical conditions on the materials which will be exposed to plasma in the future fusion devices. The associated assay of the fate of the fusion fuel is preferentially done *in situ*, however large series of associated analyses are performed *ex situ* and in separate dedicated laboratory experiments which all contributed in the past an essential knowledge on the fuel balance in tokamaks. The results of well-defined dedicated retention experiments are extrapolated to predict the conditions of the ITER operation with tritium. The goal is to stay below the tritium inventory safety limit. Fuel retention in tokamaks with carbon walls is now better understood based on a number of experiments, including DITS project [1]. The configuration of ITER wall consisting of Be, W and CFC is under detailed consideration, as the material mixture will result in specific processes of erosion, redeposition and fuel retention.

Research on hydrogen processes in thin films and surfaces was done in the past at Jožef Stefan Institute (JSI) by Elastic Recoil Detection Analysis (ERDA) using ^{4}He and ^{7}Li [2,3] beams. The continuous efforts to upgrade the experimental facilities were in the past devoted to the introduction and application of the high-energy focused ^{3}He beam. In this way, we are capable of measuring the lateral distribution of the retained deuterium with 5 micrometer lateral resolution. After the last upgrades of the micro-NRA set up at the JSI Tandetron Accelerator Laboratory within fusion EFDA collaboration [4], the group is now providing consistent service to fusion research [5,6].

The Nuclear Reaction Analysis (NRA) is a fully-quantitative analytical technique based on a well-known cross section for $D(^{3}He,p)^{4}He$ reaction. The information on the deuterium depth concentration profiles could be obtained from the series of NRA spectra using different energy of incident ^{3}He beam [7]. As the cross section has strong energy dependence on ^{3}He ion energy, the quantitative depth concentration profiles are extracted from such measurements.

In 2012, we concentrated our efforts in the development of a broad-beam NRA for deuterium depth profiling with varying impact beam energy. In the frame of the

project 1.4.3 of the Association Euratom-MHEST (MESCS in 2012), the research has been coordinated within EFDA PWI Task Force, WP12-IPH-A01-3-10/BS-01/MHEST. In parallel, the installation of the measurement equipment at the ERDA/RBS beam-line for the implementation of the broad-beam Nuclear Reaction Analysis with ^{3}He beam, was done within the EFDA-coordinated project WP12-IPH-A03-1-13/PS+BS-01/MHEST (see report of the project 1.4.1). Thick implanted Si particle detector, acquired within an earlier EFDA PS project, was installed in the RBS/ERDA chamber at an angle of 135° with respect to the beam direction. The details and calibration of the broad-beam NRA set-up are described below.

NRA with ^{3}He was used in 2012 to analysing samples with multi element composition provided by Association MEdC according to the IPH task (WP12-IPH-A01-3-10/BS-01/MHEST). Two kinds of samples were prepared by TVA technique: samples with single, approximately homogeneous, mixed layer and samples with multi layered structure. Used materials were W, C and Al as a substitute for Be. Certain samples were prepared in the presence of deuterium gas in plasma reactor so that deuterium was co-deposited in the mixed material layers. Besides these samples from MEdC some samples provided by CEA were also studied by NRA during 2012.

Two important enhancements of the accelerator facility were done during 2012 enabling efficient forthcoming fusion related studies. The first is the modification of the gas handling system at the duoplasmatron ion source so to allow easy switch from ^{4}He to ^{3}He operation and also the operation with two-isotope mixture as a plasma sustaining gas. This modification greatly reduced the consumption of precious ^{3}He gas and enables standby operation of plasma with ^{4}He and soft gas interchanges.

The second and major enhancement was the installation of the new multicusp H$^-$ source at our tandem accelerator done during November 2012. The installation of multicusp ion source is primarily intended to increase brightness of injected H$^-$ beam with the goal to drastically increase the intensity of the proton microbeam. As multicusp ion source is dedicated exclusively for proton probing beam, the existing duoplasmatron ion source could now be permanently configured for positive extraction, required for the formation of helium beam in particular of ^{3}He beam needed for NRA. Therefore, the installation of new multicusp ion source made possible easy and prompt use of NRA without interfering with other applications running on the accelerator and needing proton beam. This, together with significant reduction of the ^{3}He gas consumption during duoplasmatron operation due to ^{3}He/^{4}He gas interchange system, enable our laboratory to serve fusion research with significantly higher efficiency.

2 WORK PERFORMED IN 2012

2.1 Development of the broad-beam Nuclear Reaction Analysis with ^{3}He beam

Thick implanted Si particle detector, acquired within earlier EFDA PS project, is transferred from microbeam to RBS/ERDA chamber and mounted on the detector holder. This detector is used to detect fast protons from D(^{3}He,p)^{4}He reaction. Besides this, two other detectors are installed, one for Rutherford Back Scattering (RBS) characterization (detects back scattered ^{3}He ions from primary beam) of the target sample and another for detection of lower energy α-particles from D(^{3}He, α)H allowing

detection of surface deuterium. A special rotatable holder for up to 20 samples is used for automated analyses of samples under static conditions at room temperature. Another sample holder is used with ceramic heater and thermocouples for in-situ dynamic studies of temperature dependent processes. In this case only single sample can be studied without opening of the chamber. The layout of detectors in the chamber is shown in figure 1.

Performances of the newly set broad beam NRA were checked and calibrated by measurements with a standard, well characterised thin layer a-C:D provided by IPP, Garching, Germany. A good agreement between D concentration provided by IPP and the concentration deduced from NRA measurements provided an additional test of determined geometrical parameters needed for NRA spectra analysis. These analyses are performed by SIMNRA [8]. Another control of the method is performed by comparing NRA signal from a-C:D thin target for different incident beam energy with literature cross section for $D(^3He,p)^4He$ nuclear reaction [9]. Result of this test is shown in figure 2 and agreement is good. The shape of the ion beam at the target is controlled by defining slit and exposure dose is measured by mesh beam intensity monitor.

Figure 1: Experimental chamber for broad-beam RBS/NRA, equipped with automated rotatable sample holder for up to 20 samples. An alternative sample holder with heater is used for in-situ studies of temperature dependent processes – adsorption, desorption isotope exchange.

The gas handling system at the duoplasmatron ion source was reconstructed during 2012 so to allow operation of the source with any of two helium isotopes and easy exchange from ordinary ^4He to ^3He gas. This proved to be very efficient in order to spare precious ^3He gas. Most of the ion source tuning and also standby operation is done with ^4He and ^3He is used only when NRA measurements are performed.

2.2 Analysis of deuterium depth profiles in mixed layers and multilayers

Work was motivated by the need for understanding and quantifying the fuel retention in mixed layers and multi-layered films. The sample layers used for the present study are expected to be similar to those deposited on the plasma wall of JET and ITER during their operation.

The materials used for the samples were W, C and Al as a mock-up for Be. Carbon is included as there is plenty of results with this material which can be used for comparison and also because its presence might be expected as an impurity.
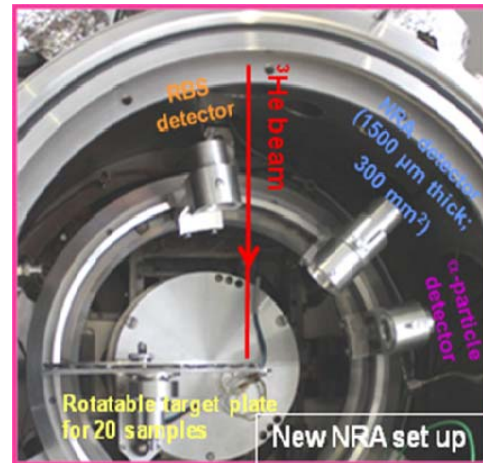
In the frame of EFDA-coordinated task WP12-IPH-A01-3-10/BS-01/MHEST in collaboration with Christian Lungu at the National Institute for Laser, Plasma and Radiation, Magurele-Bucharest, Romania, composition of the films was discussed. Set of different mixed material samples containing C, W, Al and D had been then prepared at MEdC and sent for analyses to JSI. The Thermoionic Vacuum Arc (TVA) method was used with and without deuterium introduced during deposition so that co-deposited deuterium is present in certain samples.

Representative samples of the mixed layers from MEdC were studied. The depth resolution is achieved by changing incident energy of ^{3}He beam in five values within the energy range between 0.7 and 4.5 MeV.

Experimental NRA and RBS spectra for 3 MeV energy of ^{3}He incident beam are shown in figure 3. Target sample is 1.5 micrometer thick mixed layer of C and W in approximate concentration ratio 2:1 deposited at Si substrate. Deuterium gas was present during deposition so that D is co-deposited in the layer.

The quantitative information on D concentration depth profile is obtained from NRA spectra for a set of incident energies and analysed by SIMNRA. An example of such simulation for single ion energy is shown in figure 4 and final result of depth profile in figure 5. SIMNRA is also used for RBS spectra analysis provides elemental composition profile of target sample and reflects the deposition procedure as well as possible sample modification due to thermal treatment or exposure to neutral atoms or to ions.

The deuterium depth profile as determined by NRA in another mixed material sample containing Al, W and C in about 1:1:1 ratio and also with deposition performed in the presence of D_2 gas is shown in figure 6.

Figure 2:   Comparison of the normalised NRA signal from thin standard a-D:C sample and reaction cross section for the different incident ion beam energies used for D-depth determination.
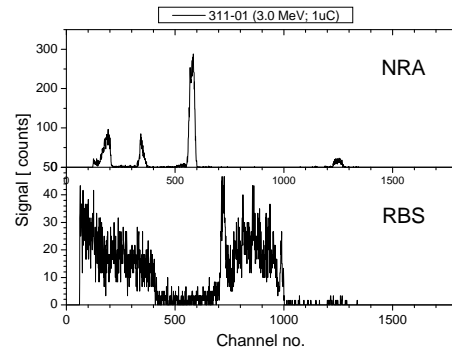
Figure 3: Experimental NRA (top) and RBS (bottom) spectra obtained with 3 MeV ^{3}He beam. The NRA signal due to D is at channel no. 1250 while the three peaks at lower energy are due to NR in ^{12}C.

We have also analysed deuterium profile in four samples of polycrystalline tungsten obtained from CEA (dr. Ch. Grisolia). These samples were exposed to deuterium RF plasma and deuterium depth profile in two samples which were treated in CASIMIR RF reactor are shown in figure 7. Strong surface peak is observed even the time between implantation and an NRA measurement was about half year.
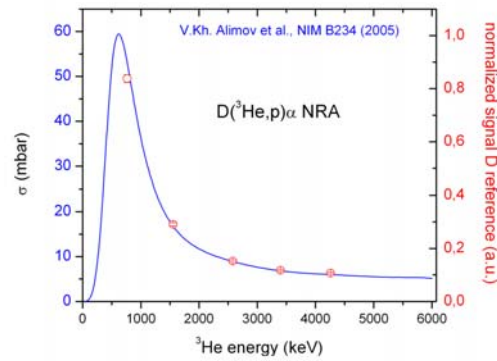
Figures 4 (left) and 5(right): left: measured and simulated NRA spectrum with deuterium peak at the C:W (2:1) layer exposed to D_2 gas during layer deposition, obtained at the ^3He ion impact energy of 1555 keV. Right: extracted deuterium depth concentration profile in the 1.5 micrometre thick mixed C:W (2:1) layer with co-deposited deuterium.

Acquired data on elemental distribution in mixed layers and multi-layered structures lead to better insight into the layer properties, co-deposition mechanisms and also layer structure changes under different treatments. Further experiments are planned in early 2013 such as thermal desorption and exposure to well-defined flux of neutral atoms and ion beam.
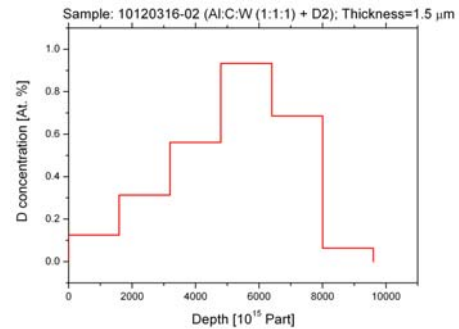
Figure 6: Extracted deuterium depth concentration profile from NRA measurements in the 1.5 micrometre thick mixed Al:C:W (1:1:1) layer with co-deposited deuterium.

3   CONCLUSIONS AND OUTLOOK FOR 2013

In 2012 we achieved important enhancements of our accelerator facility in the sense of performances for the fusion relevant IBA studies – almost 100% dedicated ion source for He operation needed for deuterium NRA and fully operational NRA at the broad beam experimental station for ERDA/RBS/NRA. Due to the extensive maintenance of the accelerator during first half of the year, installation of the new multicasp ion source, and beam line modifications we did not perform new micro-NRA measurements in 2012.

Work in 2013 will be focussed on the priorities from EFDA work plan in the field of ITER physics in particular on continuation of detailed studies of deuterium retention in mixed and multi-layered structures which are important for prediction of fuel retention and material migration in ITER.

Such studies will involve temperature dependent properties and also *in-situ* studies of thermal desorption of deuterium from complex layers as well as *in-situ* studies of deuterium absorption when layers are exposed to deuterium atoms or ions. Besides this we plan to measure deuterium in bulk tungsten subjected to the implantation. We will measure deuterium content and material distribution in detached deposit flakes and dust particle encountered in tokamak plasma reactors by using micro-beam NRA and ^{3}He-beam induced X-ray spectroscopy.
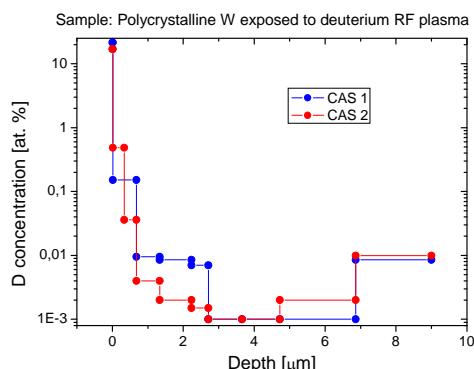

Figure 7: The depth concentration profile of deuterium implanted in CASIMIR RF reactor at CEA.

4   REFERENCES

1   E. Tsitrone et al, Deuterium inventory in Tore Supra: reconciling particle balance and post-mortem analysis, Nucl. Fusion, 49 (2009), 075011.

2   S. Markelj, P. Pelicon, I. Čadež, T. Schwarz-Selinger, W. Jacob, In situ study of erosion and deposition of amorphous hydrogenated carbon films by exposure to a hydrogen atom beam,J. Vac.Sci. Technol., A30 (2012), 041601-1-8.

3   M. Čekada, M. Kahn, P. Pelicon, Z. Siketić, I. Bogdanović Radović, W. Waldhauser, S. Paskvale, Analysis of nitrogen-doped ion-beam-deposited hydrogenated diamond-like carbon films using ERDA/RBS, TOF-ERDA and Raman spectroscopy, Surface and Coatings Technology 2012, doi:10.1016/j.surfcoat.2011.08.057.

4   P. Pelicon, P. Vavpetič, N. Grlj, I. Čadež, S. Markelj, S. Brezinsek, A. Kreter, T. Dittmar, E. Tsitrone, B. Pégourié, P. Languille, M. Rubel, T. Schwarz-Selinger, Fuel retention study in fusion reactor walls by micro-NRA deuterium mapping, Nucl. Instr. Meth., B269 (2011), 2317.B. Pégourié, S. Panayotis, P. Languille, C. Martin, T. Dittmar, l, E. Gauthier, J.-C. Hatchressian, J.-Y. Pascal, P. Roubin, R. Ruffe, E. Tsitrone, S. Vartanian, H. Wang, m, A. Beauté, J. Bouvet, C. Brosset, J. Bucalossi, M. Cabié, E. Caprin, X. Courtois, R. Dachicourt, E. Delchambre, C. Dominici, D. Douai, A. Ekedahl, J.P. Gunn, A. Hakola, W. Jacob, H. Khodja, J. Likonen, F. Linez, A. Litnovsky, Y. Marandet, S. Markelj, A. Martinez, M. Mayer, O. Meyer, P. Monier-Garbet, P. Moreau, V. Negrier, P. Oddon, C. Pardanaud, B. Pasquet, P. Pelicon, P. Petersson, V. Philipps, G. Possnert, D. Reiter, J. Roth, I. Roure, M. Rubel, F. Saint-Laurent, F. Samaille, P. Vavpetič, Deuterium inventory in Tore Supra: Coupled   carbon–deuterium   balance,   J.   Nucl.   Mater.,   (2013),   doi 10.1016/j.jnucmat.2013.01.019

5   A. Kreter, S. Brezinsek, M. Rubel, B. Emmoth, M. Freisinger, P. Pelicon, V. Philipps, O. Schmitz, P. Sundelin, G. Sergienko and TEXTOR team, Deuterium retention in different carbon materials exposed in TEXTOR, J. Phys. Conf. Series, 100 (2008), 062024.

6   M. Mayer, E. Gauthier, K. Sugiyama, U. von Toussaint, Quantitative depth profiling of deuterium up to very large depths, Nucl. Instr. Meth., B267 (2009), 506–512.

7   M. Mayer, SIMNRA User's Guide, Report No. IPP 9/113 (Max-Planck-Instutut für Plasmaphysik, Garching, Germany, 1997) and http://www.rzg.mpg.de/_mam/.

8   V.Kh. Alimov, M. Mayer, J. Roth, Differential cross-section of the D(^{3}He,p)^{4}He nuclear reaction and depth profiling of deuterium up to large depths, Nucl. Instr. and Meth., B234 (2005), 169–175.

PERMEATION MEASUREMENTS OF MIXED Be/W LAYERS ON EUROFER

Vincenc Nemanič, Bojan Zajec, Marko Žumer

Jožef Stefan Institute, Jamova 39, 1000 Ljubljana, Slovenia
vincenc.nemanic@ijs.si

1   INTRODUCTION

Beryllium and tungsten will be used for the first wall of ITER. Thermal load and ion impact will induce tritium retention in mixed deposits of tungsten and beryllium. So far, as follows from a literature survey, a few reported data on investigation of such mixed layers exist. The missing knowledge of their possible interaction with hydrogen isotopes is thus searched by using various experimental techniques.

Hydrogen in metals represents a complex two element interaction system as the lattice may have any form extending from a well structured mono-crystal to nanocrystalline metal. Accordingly, hydrogen may occupy a single-energy-type interstitial site of the monocrystal or any type of defects which represent sites for a single H atom with different binding energy. Beside single occupation interstitial or defect-induced sites, metal vacancies may be present in the disordered lattice. Each may be occupied by several H atoms and the term super-abundant vacancy (SAV) was launched in theory. Their role influencing metal properties has also been calculated. recently. Grouping of vacancies into clusters was also predicted which further complicates experimental evidence of SAV. In general, sophisticated experimental techniques are needed to determine contribution of defects and SAV on observed hydrogen mobility. Classic permeability measurement of gaseous hydrogen through bulk specimens is a suitable complementary method to determine its mobility. Unfortunately, macroscopic sizes and thicknesses of samples with low hydrogen diffusivity result in extremely low permeability which is beyond the detection limit of present day experimental technique. The same technique using a "duplex membrane" simplifies the experiments as thin W or Be/W films with desired micro-structure can be prepared on a highly permeable substrate much easier than bulk W samples [1,2,3]. Luckily, Be/W deposits will be formed as thin layers which makes our data even more relevant, initially mainly for JET as well as later on for ITER.

It 2012, precise hydrogen permeability measurements combined with long term outgassing rate measurements were realized for tungsten and Be/W films, both deposited by thermionic vacuum arc (TVA) method in the laboratory of dr. Cristian Lungu at National Institute for Laser, Plasma and Radiation Physics, NILPRP, Romania. This method gives a specific film microstructure and morphology which was characterized by various techniques, AFM, SEM, XPS and XRD. Most of experimental

data points for permeation measurements which lasted at least 24 hours were obtained at 400 °C.

2   WORK PERFORMED IN 2012

Hydrogen permeation through W films deposited by thermionic vacuum arc technique on Eurofer substrates was investigated as this data was required to get a reference in the sense of the expected range for Be/W films deposited by the same method. First, the correlation between permeation flux and W film morphology was searched. W surface was characterized by various surface sensitive techniques while the XRD was applied for determination of average grain size. The results were then applied in further studies for Be/W films, deposited by the same TVA technique. Complementary SEM, XPS, XRD, AFM methods were applied for characterization.

2.1   Experimental

Sample preparation and experimental procedure

The base material on which we applied the coating was the reduced-activation tempered martensitic steel Eurofer with the chemical composition (wt. %): 0.11 C, 8.7 Cr, 1.0 W, 0.10 Ta, 0.19 V, 0.44 Mn and 0.004 S, balance Fe. The steel was supplied in the form of a 100-mm diameter bar by Forschungszentrum Karlsruhe GmbH, Karlsruhe, Germany, in the normalized plus tempered condition, i.e., 980 °C/110 min plus tempering at 740 °C/220 min/air-cooled. The reason for selecting this special grade of steel is its well characterized interaction with hydrogen.
The disc-shaped samples for the coating experiments were cut from the 100-mm diameter bar by electro-eroding 40-mm diameter rods, which were then sliced using the same technique to produce 0.5-mm-thick discs. These discs were then ground and mechanically polished to obtain an optically flat surface, cleaned with a detergent in the ultrasonic bath, rinsed in demineralised water and dried in the air at 150 °C. First, two W coated membranes were investigated. The W films were prepared by means of TVA [??]. Figures related to the film are given below. Two equally prepared substrates were deposited in two subsequent deposition cycles lasted, 14h and 16 h for sample 1 and sample 2, respectively. Pressure in the camber was ~$1x10^{-5}$ mbar.

Coated membranes were sealed in the permeation cell by two Au 0.6 mm thick O-rings. The resulting hydrogen exposed area was 8.4 cm^2. The W film was oriented to the upstream chamber. The setup is assembled from all-metal UHV components applying gas accumulation technique described elsewhere [].
The first W film, **sample 1,** was 4.1 micrometers thick and second, termed **sample 2** was 2.7 micrometers thick. The initial phase in both measurements was a slow warm-up stage to reach 400 °C in 2 hours and the next 4 hours were allowed to expel hydrogen from the membrane and the cell. The downstream chamber was then valved-off for 10 to 30 minutes to accurately record the background pressure rise slope. Then, the upstream chamber was valved-off too and hydrogen was rapidly introduced. Accumulated gases were analyzed by the QMS in the separate chamber each time just before they were pumped out. Hydrogen represented the main species with traces of CO

and CO_2. In addition, transients of hydrogen kinetics at the downstream side after upstream pressure changes were followed directly by the QMS.

For both measuring campaigns, the time to reach a steady permeation flux was substantially longer than the time needed for uncoated membranes when it had been always achieved in less than 10 s at 400 °C at 1 bar upstream pressure.

Four next samples of Be/W films were investigated by the same hydrogen permeation technique followed, each sample required 2 days of UHV system conditioning, while the permeation evaluation lasted at least 24 h at 400°C .

Complementary sample investigation methods

The X-ray photoelectron spectroscopy (XPS) measurements were performed in the XPS spectrometer PHI-TFA XPS with monochromatic X-ray source. Survey and high energy resolution spectra were acquired on as-received sample 2 in order to identify elements on the surface and to evaluate the oxide layer thickness.

Atomic force microscopy (AFM) was conducted by the AFM microscope model Solver PRO P47 produced by the MTD-NT company. Surface morphology was recorded in semi-contact mode over an area of 5 x 5 micrometers on different locations across the same sample. After proper background subtraction the roughness parameter R_a was calculated.

Scanning electron microscope (SEM) JSM6500F was used for an additional imaging the W surface at various locations across the same sample.

2.2   Results

Results of XPS, AFM and SEM on pure W surface
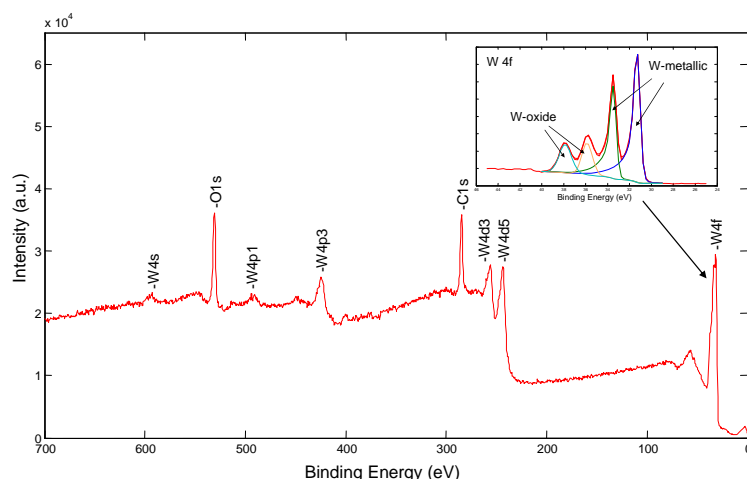
Figure 1: XPS survey spectrum of the W coating. Inset in the figure shows the W 4f peak which is composed of two doublets originating from W-oxide layer and W-metallic coating.

The XPS spectrum (Figure 1) obtained on the surface of the W-coating shows peaks of O 1s, C 1s, W 4f, W 4d and W 4p. From detected peaks the surface composition was calculated to be 46 at.% of C, 31 at.% of O and 23 at.% of W. Carbon C 1s signal originates from adsorbed carbon based contamination. Oxygen O 1s signal

49

may be also partially related with the adsorbed layer but its main origin is a thin W-oxide layer. Inset in Figure 1 shows high energy resolution spectrum of W 4f in which doublet with W $4f_{7/2}$ peak at 35.9 eV is related with W(6+)-oxide layer and a doublet at 31.3 eV is related with metallic W atoms. In order to determine the thickness of W-oxide layer we compare intensities of these two doublets using the procedure from Reference (M.S. Aouadi et al., JVST (A) 10(2), Mar/Apr 1992, p. 273). In this way we determined that the W-oxide layer is (0.4 ± 0.2) nm thick, what means that oxide layer is in the range of a monolayer.

Morphology of the W-coating deposited on the Eurofer substrate, characterized by FM and SEM show similar features. Corresponding images are shown in Figure 2. The surface is uniformly composed of small plate-like crystallites of three angular shapes. From AFM image we calculated the R_a roughness to be (30 ± 3) nm measured over area of 5 x 5 microns.
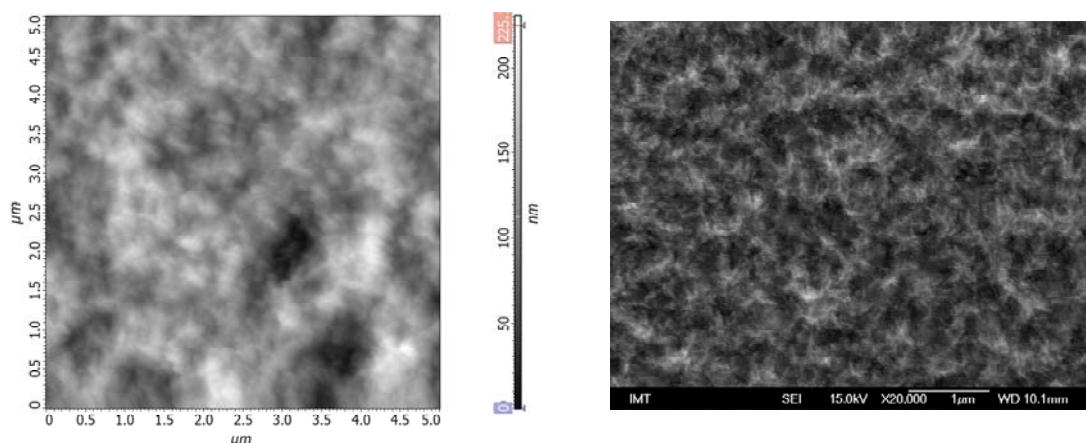

Figure 2: AFM (left) and SEM photo (right) of W surface of sample 2 show very similar texture.

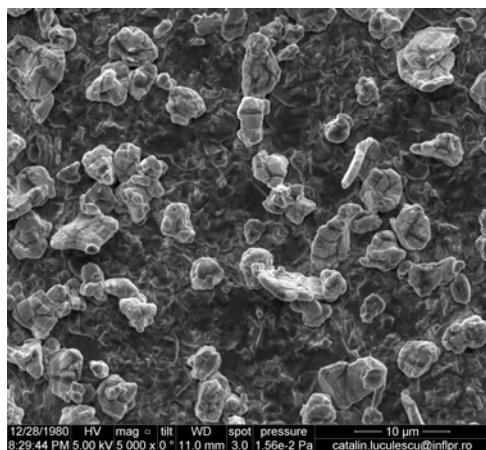*Results of XPS, AFM and SEM on Be/W surface*

Figure 3: Be/W surface exhibits different morphology than pure W in Fig. 2. The contrast on grains is related to different conductivity and does not express different composition.
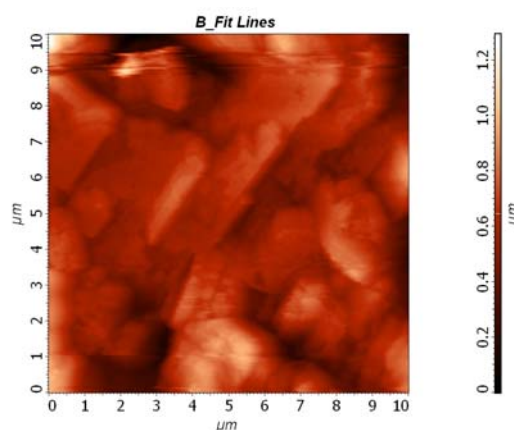
Figure 4: A detail of Be/W film on Eurofer as recorded by AFM.

Results on permeation measurements on pure W films

Identical bare 0.5 mm thick Eurofer membranes have been formerly investigated since a good reference for evaluation of W films was needed [1]. The high diffusivity and permeability of clean bare membranes is manifested in fast response to hydrogen exposure; high steady flux $\sim 1.12 \times 10^{-5}$ mol H_2/m^2s is established at 400 °C at 1 bar. This value allows evaluation of the PRF. Time–lag was ≈ 6.4 s. Both these data were recorded after the sealed membrane had been outgassing for some hours at 400 °C. The results on Sample 1 and sample 2 at 400 °C are presented in Table 1.

	thickness	*PRF*	*PRF*	P_W (24 h)*	D_W	S_W
	μm	3 h	24 h	x10^{-15} mol H_2 /(m s $Pa^{0.5}$)	x10^{-16}m^2/s	molH_2/m^3 $Pa^{0.5}$
sample 1	4.1	10.1	5.9	32	130	2.43
sample 2	2.7	91.2	96.1	1.1	6.2	1.74

*the value of the Eurofer substrate is $P_E = 1.9 \cdot 10^{-11}$ molH_2/m s Pa $^{0.5}$, [our JNM Ruset]

Table 1: Permeation reduction factors (PRF) and calculated permeability for W film achieved in 24 h. Diffusivity is calculated by using the eq. 3. From P = D.S, the solubility of tungsten is also calculated.

The only difference between two sample deposited at similar, but not identical conditions is the resulting size of micro and nano-crystallites within the film as revealed by XRD. Sample 1 has larger crystallites than Sample 2 and consequently higher permeability. This is in agreement with theoretical predictions [4] an important results detail needed also for evaluation of Be/W films.

Results on permeation measurements on Be/W films

Be/W films with stated composition (75 at.% Be, 25 at.% W) exhibit even less predictable behavior after hydrogen exposure compared to pure W films deposited by TVA method. Besides different nanostructure that is always a possible parameter influencing film properties, high Be affinity to water may results in BeO formation. It is well known that hydrogen purity is extremely important in experiments with Be, but a few ppb level purity, trusted to be maintained in present experiments, might not be enough. Moreover, the role of BeO layer on hydrogen permeability has never been reported or confirmed experimentally. Even its bulk solubility and diffusivity for hydrogen is lower than in Be and it may not suppress the permeation flux as it may have porous structure like FeO which also does not influence permeation rate through Fe. By a new campaign in 2013 we hope we could obtain more reliable and stable values. Finally, we would like to get the dependence of Be content vs. W in permeability of such films.

	thickness	*PRF*	*PRF*
	μm	1 h	24 h
sample 1	8	78	155
sample 2	8	21	21
sample 3	8	62	55
sample 4	8	84	105

Table 2: Permeation reduction factors (PRF) and calculated permeability for Be/W films achieved in 1 h and in 24 h. All numbers for 24h are approximated as all values still drift.

3   CONCLUSIONS AND OUTLOOK FOR 2013

Knowledge of the properties of diffusion of H in Be/W alloys is very poor today and further research is definitely required. Since both W and Be films were rarely measured in relation to fusion, we have an advantage that we have than 2 years of collecting our own experimental data on both material in form of films, Be and W, both relevant to ITER. It is thus important to determine first the parameters that govern the permeation process at known film structure and composition and achieve proper understanding of the influence of material morphology, structure and high temperature loads on H retention in films made of Be/W alloys with different Be/W ratio.

Besides this knowledge, our data may contribute complementary data to predict the upper limit for D/T accumulation in Be/W deposits or dust formed in JET or ITER. Permeation properties of nano-crystalline W films on Eurofer produced by different techniques exhibit substantial differences. The aim of study in 2013 is to determine primarily the permeation properties of Be/W films, which may give a satisfactory explanation when results will be outside the expected range. So far, Be reactivity with traces of water at the upstream side may result in BeO formation whose role is still not well resolved from pure Be properties. This detail requires some improvements of the experimental setup.

4   REFERENCES

1   B. Zajec, V. Nemanič and C. Ruset, Hydrogen diffusive transport parameters in W coating for fusion applications, J. Nucl. Mater., 412 (2011), 116 – 122.
2   B. Zajec, Int. J. of Hydrogen Energy, 36 (2011), 7353–7361.
3   V. Nemanič, B. Zajec, D. Dellasega, M. Passoni, Hydrogen permeation through disordered nanostructured tungsten films. J. Nucl. Mater., 429 (2012), 92-98.
4   V. Nemanič, B. Zajec, M. Žumer, C. Porosnicu, C. Lungu, Hydrogen permeability of beryllium films prepared by the thermionic vacuum arc method., Fusion eng. design, 86 (2011), 2421-2424.
5   R. Kirscheim, Solubility and diffusivity of hydrogen in complex materials, Phys. Scripta, T94 (2001), 58-67.

PLASMA DEPOSITION OF H:C-METAL COATINGS

Peter Panjan, Miha Čekada, Darinka Kek Merl, Damjan Matelič

Department for Thin Films and Surfaces, Jožef Stefan Institute, Jamova 39,
1000 Ljubljana, Slovenia
peter.panjan@ijs.si

1   INTRODUCTION

During operation the first-wall material in tokamaks and other high-temperature plasma reactors is subject to ion bombardment. The first wall material in future ITER tokamak will be beryllium, while the divertor will be constructed from carbon-fibre composite (CFC) and tungsten (W). The deposits formed in the remote parts of the divertor will therefore consist of C, H, Be and W. The sputtered material is deposited on different components of plasma reactors. In order to develop a suitable method for occasional removal deposits (to prevent hydrogen retention), a study of possible structure of model deposits has to be performed. Our study is focused on hydrogenated carbon coating. We used two different deposition techniques for preparation of hydrogenated carbon coatings (a-C:H) films on suitable substrates. Work Programme 2012 included two topics: a) deposition of multilayered a-C:H/W deposits, b) study of carbide formation at layer interfaces.

2   WORK PERFORMED IN 2012

2.1   Carbon based coatings prepared by anode layer source

Using the anode layer source we deposited a series of diamond-like carbon films, where we varied the discharge voltage and N_2-to-C_2H_2 ratio. Diamond-like carbon (DLC) is a metastable form of amorphous carbon with a significant part of sp^3 bonds. DLC coatings are typically deposited by physical vapour deposition techniques. By feeding the anode layer source with a carbon-carrying gas, e.g. acetylene, an ion beam forms. If directed to a substrate, a DLC coating starts to grow on that surface. Several process parameters can be varied: discharge voltage, total flow, gas composition (of special interest is addition of nitrogen), geometry of deposition, etc. The deposition rate is in the range 4–20 nm/min, which is acceptable for a commercial deposition. An important advantage of DLC coatings deposited by the anode layer source is an almost total absence of growth defects, which are common in coatings deposited by the classical way. This makes the technique promising for applications where smoothness and absence of defects is critical, e.g. gas permeation barriers or anticorrosion coatings. We have systematically analyzed the influence of the above mentioned deposition

parameters on the properties of the deposited coatings. Being amorphous and containing only light elements, there are not many techniques available to study their structural properties. The most convenient is the Raman spectroscopy. By a precise analysis of the Raman spectra the ordering of carbon atoms can be identified, and indirectly also the hydrogen concentration and amount of sp^3 bonds (Figure 1). The mechanical properties were analyzed the standard way: hardness evaluated by nano-indentation, adhesion (by scratch test), friction coefficient and wear rate (by pin-on-disk test), and internal stress (by measuring curvature). The general trend line is that by either increasing the discharge voltage or increasing the nitrogen flow, the coatings experience an increasing structural ordering, lower hardness and better adhesion. On the other hand, the highest hardness and the highest share of sp^3 bonds is achieved by the lowest discharge voltage using no nitrogen at all. Thus by varying the process parameters we can tune the properties of the DLC coating. There is no "optimal" set of process parameters; it rather depends on the application we are looking for.
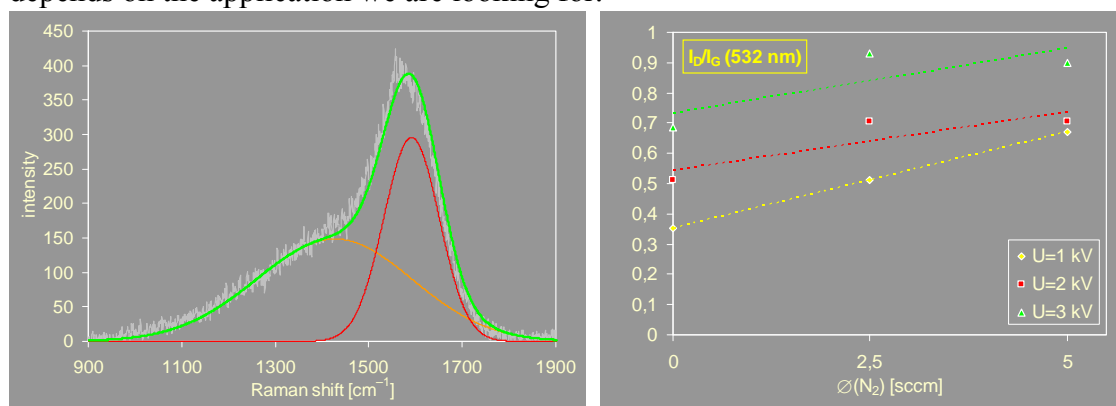

Figure 1: Raman spectroscopy is a primary tool for evaluation of carbon chemical state. The most important parameter is the peak intensity ratio (I_D/I_G) If this value is low than the film consist low percentage of sp2 and high percentage of sp3 (both C–C and C–H bonds). If this value is high than the film is composed from aromatic rings sp2 clusters. Graph on the right side shows the dependence of I_D/I_G ratio on nitrogen flow. The results of these investigations were presented at the 9. Werkstoffkongress [1].

2.2   W-C:H coatings prepared by sputtering in Sputron deposition system

Sputter deposition system with thermionic arc was used for preparation of W-C:H films on stainless steel substrates. The stainless steel samples were finally polished with diamond paste to R_a=10–14 nm, ultrasonically cleaned and degreased in bath of hot alkali solution, de-ionized water and then dried in hot air before mounting on the substrate holders. One part of substrates were in situ cleaned by ion etching prior to coating deposition. Metal interlayers (Cr, W) were used to improve the adhesion. Altogether 2 deposition runs were done using the above mentioned technique. The deposition parameters of films which compose a multilayer structure of typical sample are presented in Table 1. These samples are designed for removal test of a-C:H with neutral oxygen atoms.

	Cr	**W**	**W-C:H**
target purity	99,95	99,5	99,95
background pressure (mbar)	5×10^{-7}	5×10^{-7}	5×10^{-7}
argon pressure (mbar)	2×10^{-3}	2×10^{-3}	2×10^{-3}
flow rate C_2H_2 (a.u.)	-	-	880
target voltage (V)	1700	1700	1700
target current (A)	0.6	0.6	0.6
substrate temperature (°C)	120	120	120
Deposition time (min)	7	1	33
deposition rate (nm/min)	7	8	

Table 1: Deposition parameters of W-C:H films

Focused ion beam induced ion mixing was used for Si-C compound formation [3]

2.3 Carbon based coating prepared by magnetron sputtering

Last year Dr. Srečko Paskvale defended his PhD thesis »Carbon-based protective coatings deposited by physical vapour deposition processes« [4], where he analyzed the structural, micro structural and tribological properties of carbon based coatings, prepared by different deposition techniques. Most emphasis was given to the bi-layer coating TiAlN/a-CN$_x$, which was successfully implemented in industrial production. In his work he analyzed the dependence of friction coefficient and wear parameters on the deposition parameters (thickness, rotation rate and sample position in the chamber), and surface condition (roughness, defect density).

2.4   OES measurements

The measurements were conducted in three deposition systems: Balzers Sputron, Balzers BAI730 and CemeCon CC800/9. In each machine, a series of experiments was made, where in each experiment only one parameter was varied at a time. In most cases the spectra were recorded at the same integration time, which was selected at such a level that the number of counts never exceeded the overflow value of 65536.

The evaluation of spectra proceeded as follows:

- Each spectrum was imported into Excel, one spectrum per worksheet.
- The peaks are typically several nm apart; and for instrumental reasons, the top of a particular peak may very several tenths of nm in different spectra. For this reason the top of each spectrum was »flattened« over the width of ±1.5 nm. This simplified the comparison greatly while keeping separate peaks apart.
- The intensities were normalized on 1 ms integration time so they can be in principle compared even if different integration times were used.
- Using the Plasus software a list of candidate lines (typically 100–200 lines) was copied into Excel. The list was constant for each set of experiments.
- Using the function VLOOKUP the intensity of each line was extracted automatically for each spectrum.
- A rough evaluation was made how individual peaks (tentatively assigned to an elemental line) change with a certain parameter. If, for example the peak at around 661 nm rises with N2 flow and stays constant in other experiments, it is probably the N$^+$ line of 661.06 nm. In this way a selection of probable peak-to-line correspondences was made
- At the very end one chart per experiment was constructed while taking for each element that line which best satisfies the following conditions: high intensity,

least overlap with other elements, conforms well with the experiment expectations.

2.5 Experiments in Sputron

The spectrometer gauge was fixed on the cylinder holder, which can be put either into the »up« or »down« position. Only neutrals and single-charged ions were considered in the analysis. In the tests we used the following targets: Cr, Al, Ti, C, TiAl (50:50 alloy target), and TiV (segmental target, V in the centre).

OES characterisation of plasma was also the topic of the scientific paper published in collaboration with the research group from Institute of Physics, Prague [5]. We have carried out a systematic study of the influence of different working gases on magnetron plasma properties.

In collaboration with the scientists from Lawrence Berkeley National Laboratory (USA) we also analysed the plasma flares in high power impulse magnetron sputtering [6].

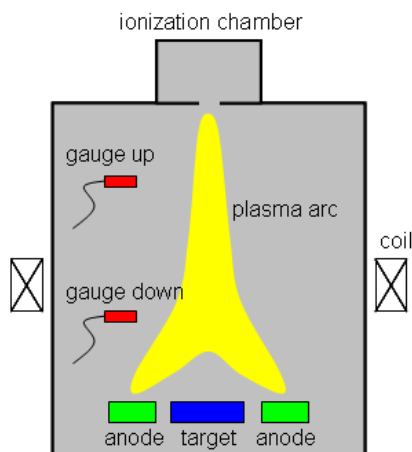*Figure 2: OES measurements conducted in sputtering system SPUTRON (Balzers) with thermionic arc - experimental set-up.*
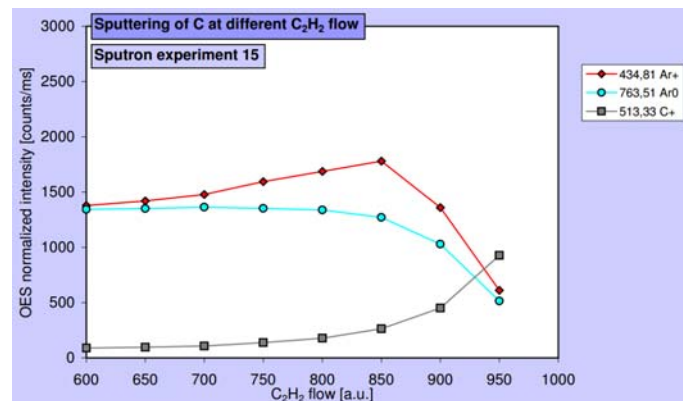
Figure 3: OES measurements during sputtering of C at different C_2H_2 flow; Graphite target DC-sputtered at different flows of C_2H_2. The units on the flow button are arbitrary from 600 to 1000, while 600 is the lowest value. Only the signal for Ar, Ar^+ and C^+ are presented.
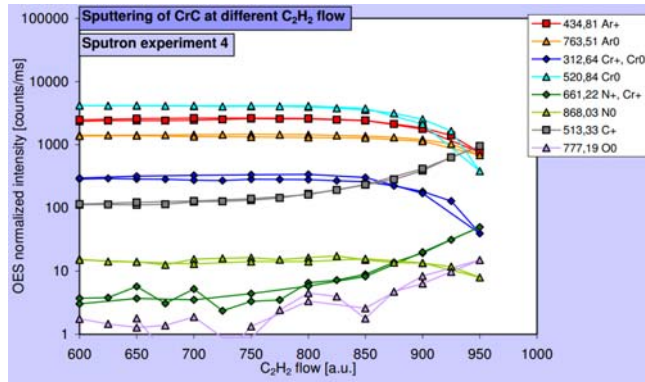
Figure 4: OES measurements during sputtering of Cr-C at different C₂H₂ flow. Standard hysteresis test of sputtering Cr in C₂H₂. The units on the flow button are arbitrary from 600 to 1000, while 600 is the lowest value. Signals for Ar, Ar⁺, Cr, Cr⁺, N, N⁺, O and C⁺ are presented.
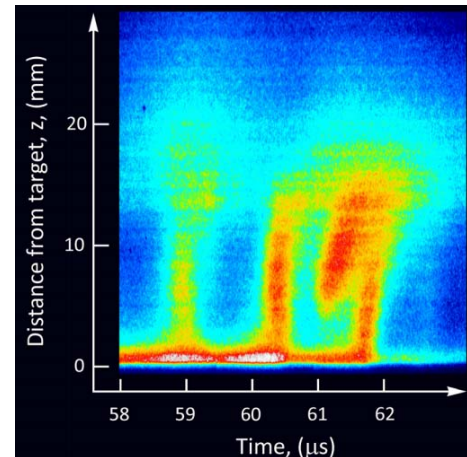
Figure 5: Streak image of plasma flares recorded in the second half of an 80 µs HIPIMS pulse [6].

3   CONCLUSIONS

Three different deposition techniques were successfully used for preparation of carbon based coatings and metal containing carbon coatings. Various deposition parameters were varied and their influence on composition, structural, mechanical, tribological properties was evaluated. We also analyzed the formation of different species in the thermionic plasma beam during the reactive sputter deposition of a-C:H films using optical emission spectroscopy. We varied the process parameters, like partial pressure of acetylene, axial magnetic field etc.

4   REFERENCES

1   M. Čekada, M. Kahn, P. Pelicon, Z. Siketić, I.Bogdanović-Radović, W. E. Waldhauser, S. Paskvale, Analysis of nitrogen-doped ion-beam-deposited hydrogenated diamond-like carbon films using ERDA/RBS, TOF-ERDA and Raman spectroscopy, Surf. coat. technol., 211 (2012), 72-75

2   M. Čekada, M. Kahn, W. E. Waldhauser, S. Paskvale, Structural and mechanical properties of ion beam deposited DLC coatings, 9. Werkstoffkongress Leoben (Austria), 28.-29. March 2012

3   A. Barna, S. Gurban, L. Kotis, J. L. Labar, A. Sulyok, A. L. Toth, M. Menyhard, J. Kovač, P. Panjan, Growth of amorphous SiC film on Si by means of ion beam induced mixing, Appl. surf. sci., 263 (2012), 367-372

4   S. Paskvale, Carbon based protective coatings prepared by physical vapour deposition technique, PhD thesis, Ljubljana (2012)

5   M. Novotny, J. Bulir, P. Pokorny, J. Lančok, L. Fekete, M. Jindrich, M. Čekada,   RF magnetron sputtering of silver thin film in Ne, Ar and Kr discharges - plasma characterisation and surface morphology, Surf. coat. technol., (2012)

6   P. A. Ni, C. Hornschuch, M. Panjan, A. Anders, Plasma flares in high power impulse magnetron sputtering, Appl. phys. lett., 101 (2012), 224102

ITM ADVANCED VISUALISATION TOOLS

Leon Kos

University of Ljubljana, Mech. Eng. LECAD laboratory
leon.kos@lecad.fs.uni-lj.si

1   INTRODUCTION

ISIP (Infrastructure and Software Integration Project) is in charge of developing and maintaining the Integrated Tokamak Modeling Task Force (ITM-TF) simulation infrastructure. The goals of the ITM-TF within the sub-project ISIP is to consolidate and extend the visualization capabilities of the ITM platform that should provide developers with tools for (automated) creation of specialized plots that can be easily distributed to end users and tools for creating plots for code/workflow development and debugging. Eventually, users will benefit easy-to use, interactive tools for data exploration, easily available custom visualizations for specific physics problems/workflows and tools that are capable of producing publication-ready plots. As a solution to the above goals we propose a structured repository for code fragments that performs the processing, and simplifies reuse of common and specialized data processing for various target visualization tools (backends).

Our work within ISIP »Advanced visualization tools« consists of extension of the visualization capabilities for the ITM-TF platform that provides developer tools for (automated) creation of specialized plots for Kepler workflows and sophisticated interactive data analysis tools for end users. Custom visualizations for specific physics problems/workflows are readily available with the ITM Python visualization library. Such approach delineates access to Consistent Physical Objects [1] (CPO), data processing and plot creation. A structured repository for code fragments that performs the processing simplifies reuse of common and specialized data processing for various target visualization tools. We demonstrate such use for native Matplotlib as well as embedded within VisIt and Kepler, where specialized plugins/actors have been developed for accessing CPOs in the ITM-TF database.

2   WORK PERFORMED IN 2012

During January – May 2012 we concentrated into upgrading UAL reader plugin as there are currently two ways to get data from the UAL into VisIt:

1. The UAL database reader plugin: builds on data mappings specified in the data structure definition (XSD files)
2. UALConnector: transforms grids and data stored in the general grid description format to VisIt

Work in April 2012 was spent for upgrading VKA to 4.10a ITM codebase. Further improvements in UAL reader plugins raised the need for rewriting XSLT

translation from CPO XSD descriptions. As we wanted for generated C++ code be easily maintained we set up build.xml procedure based on ANT make processor and it's builtin XSLT translator that embeds some EXSLT extensions but with limited output separation. For output formatting we resolved to usual piping through indent program as it is used in XSD/XML post processing of CPO descriptions.

Work in UAL reader continued from May to the end of 2012 where we introduced functional translation and support of arrays of structures. Enhancements for the largely missing representation fields that are used for standard plots were added by XSLT translation development. Such plot descriptions were collected from IMPs and automated procedure exists for generation of patches of CPO descriptions in .XSD files before CPODEF.xml generation.

Coupling of fusion codes within the European Integrated Tokamak Modeling (ITM) project is based on a careful description of Consistent Physical Objects (CPOs). CPOs are structures of data that delineate various physical aspects of a fusion experiment description into agreed pieces common to related codes used for simulations and data deriving from the experiment. Integration with CPOs thus brings a common framework to simulations that can directly compare results with experiment, use experimental data as input or mixed approaches. Contents of the CPOs have been carefully crafted and collected from previous best practices in a way that the description is general enough to cover a broad range of tokomak modeling and easy to use by most of the simulation codes that interchange input and results through CPOs. As usual, it was expected that data structure describing CPOs would improve/change during the development of the integrated tokamak modeling. Required modifications of the consented data structure are then propagated into all codes affected by the proposed change with minimal efforts among the ITM Task Force (ITM-TF). To facilitate changes and to support different programming languages, the data structure is described with XML schema definition (XSD). Rigorous validations, data binding and translations are possible/can be derived from XSD definitions of CPOs. A basic usage of data structure description is persistent storage with database. Experimental data that is already captured into scientific databases formats like MDSplus (or MDS+), HDF5 that provide data model for storing and accessing data. Further encapsulation on top of them is used ITM-TF to facilitate specifics of fusion modeling. Namely, *shot* and *run* are typical selectors for given ITM tokamak-database, while the underlying MDS+ and HDF formats follow prescribed CPOs structure. ITM-TF database access layer is modeled as library routines that help retrieving and storing CPOs in a "physical" database. This library named as *Universal Access Layer* (UAL) provides a set of routines for "middle-ware" database access tailored especially for CPO transfer. UAL is "universal" in a way that different languages use the same routine names and that data transfer is simplified without compromising efficiency when using coupled codes in a "scientific workflow" that couples different codes in a compatible way and sequence. To summarize, CPOs description together with the UAL provides a common layer for all kinds of usage within ITM modeling. A graphical inspection of stored data in variety of ways increases with data complexity. Engineering still struggles to present results in plots with a single variable dependence. As time is a key physical quantity of tokamak modeling, this quantity is included in nearly every CPO and can be assumed as an additional dimension when time-varying properties are inspected. Usually, timed

inspection is done by specifying time or selecting a cycle (frame or time-slice) from the UAL database [2]. From that point data can be retrieved and visualized in with different tools and variety of ways. Visualization tools capable of accessing UAL data directly (without exporting or converting) were developed to provide required visualizations. Three approaches are used by ITM-TF for producing visualization: (i) programming languages, (ii) general tools, and (iii) specialized tools with capabilities. Scripting languages like Python and Matlab are suited for all kinds of data processing. However, they produce specialized plots that aren't reusable and thus lack a wide use approach as every plot needs to be programmed. Non-scripting languages (C++, Java, Fortran) for producing visualizations are even less attractive. They are used for application programming and within visualization tools. In fact, there are no general purpose tools available that can cover all aspects of usage. Integrated Simulation Editor (ISE) was designed with Kepler workflow control in mind and thus giving just simple 1D signal editing and visualization. All other usages are left out. For other purposes VisIt software was selected as general visualization open-source software maintained by LLNL. VisIt is popular and extensible visualization software that provides various representation modes and data post-processing in interactive and non-interactive (batch or scripting) mode. Coupling VisIt to UAL is supported by custom database plugin *ual_reader*. In spite of many capabilities of the VisIt and other tools available within ITM-TF framework there were deficiencies spotted during everyday use.

2.1   ITM Python visualization library

VisIt and Python with the *matplotlib* library can be used for creation of 2D plots. VisIt with *ual_reader* plugin provides many "standard" 2D and 3D visualizations. During the ITM project Python was realized as a scripting language of choice for many tasks in data processing and visualization. There are many examples in ITM sub-projects (IMPs) that were developed just for plotting the results in the preferred way. If fact, there will always be requests for some kind of "specialized plots" that will not be covered under "standard" ones. Having this in mind ITM-TF aims to provide possibilities for creation of complex problem-specific visualizations as easy as possible for the developer that will; (i) enable his/her visualization to the entire ITM platform, (ii) make the visualizations readily accessible to the users, and (iii) make it possible to integrate the visualizations in different tools.

Observing visualization of various teams in the IMPs that developed a number of custom visualization scripts with Python that generally follow these steps:

1. Get CPO(s):
   - Parameters for UAL database access (run, shot, time, user, tokamak, CPO) name are hardcoded, passed as command line options or with user interaction.
   - CPOs are fetched with the Python UAL interface.
2. Data processing:
   - Compute data required for plot, possibly combining data from various CPOs.
   - Typically it uses SciPy/NumPy functionality.
3. Create plot:

- Transform data to format required for plotting library (typically matplotib)
- Set up figure (axes, labels, units), plot data.

In order to facilitate the above observer procedure in a consistent way, we proposed creation of the ITM Python visualization library (ITMvis), which provides unification of existing approaches, extensibility and different plotting tools without modification of the common (access and data processing) tasks. The ITM Python visualization library provides the following:

- A standard template script(s) covering step 1, so that all visualization scripts get a uniform user interface and capabilities.
- A structured repository for code fragments that perform the processing in step 2.
- Provides a collection of "standard" processing functions which can then be shared among multiple visualization scripts or other software.
- Collects and makes code owned/developed by specific projects available to everybody in a central place.

The proposed approach was first implemented as a set of Python routines that provide command line interface (CLI) for the plot selection. In addition to CLI, it is easy to import ITMvis library into other Python projects. Routines for accessing the UAL database (Step 1) and output (Step 3) were developed and are maintained by ITM ISIP-TF. Developers/users need to concentrate only in data processing (Step 2) and plot description by providing *metadata*.

Metadata describes the plot and verifies data availability so the user is informed if a specialized plot can be applied or not. Only if the plot contains required data, the plot with *plotdata* function can be executed. To detect extensible modules containing plots metadata and plotdata in Python search path some function naming conventions are prescribed. Listing 1 is an example of such functions. While metadata is a generic 2D-plot description, data processing in plot-data reveals complex averaging of density impurity along available species and then applying logarithmic scale to the sum. One can observer that there is no time specified. Proper CPO slice(s) specified as a function argument are retrieved by the library routines.

```
def itmvis_density_of_impurity_metadata(coreimpur):
    if field_filled(coreimpur.cpo.rho_tor) \
        and field_filled(coreimpur.cpo.nz) \
        and field_filled(coreimpur.cpo.z):
        md = dict()
        md["type"] = ITMVIS_PLOTTYPE_XY
        md["axes"] = ("$\\rho_{tor}$ [m]", "log10(nz) [m-3]")
        max_nzimp = max(coreimpur.cpo.z[0,0,:])
        legend = ["max_nzimp: " + str(max_nzimp)]
        md["legend"] = legend
        return md
    else:
        return None
def itmvis_density_of_impurity_plotdata(coreimpur):
    data = {}
    data["x"] = coreimpur.cpo.rho_tor
    nz=numpy.sum(coreimpur.cpo.nz[:,0,:],axis=1)
    data["y"] = numpy.log10(abs(nz)+1.0e-100)
    return data
```

Listing 1: Metadata and plotdata function in Python from the ITMvis library for preparation of density of impurity plot where data is averaged over the range of data to prepare a single curve in logaritmic scale.
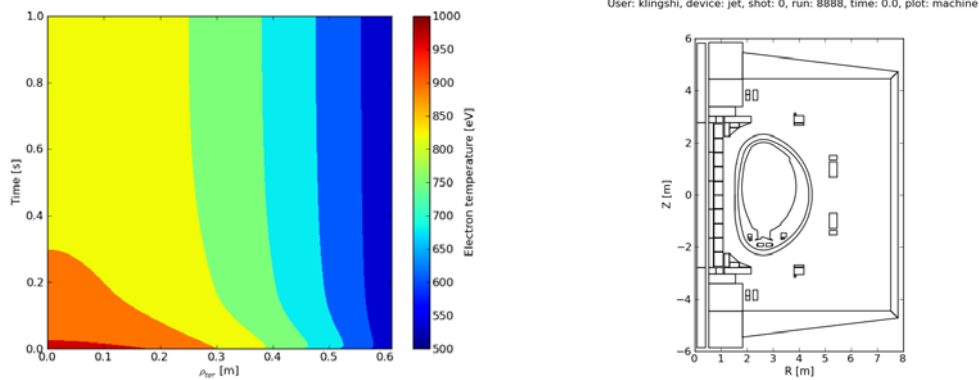

Figure 1. Electron temperature timetrace from ASDEX Upgrade coreprof CPO   (left) and JET vessel CPO (right) produced with matplotlib backend.

Plotting by different "back-ends" is then a user choice. Figure 1 show two "non-standard" examples produced with matplotlib.

2.2   ITMvis visualization with VisIt

VisIt as a general visualization tool can be used as a back-end for the ITMvis library. While VisIt itself includes Python for scripting and data processing, this processing is limited to data that have already been inserted into VisIt by a database

reader and can therefore be considered as data post-processing. To provide custom ITMvis, another Python interpreter must be included in *ual_reader*.
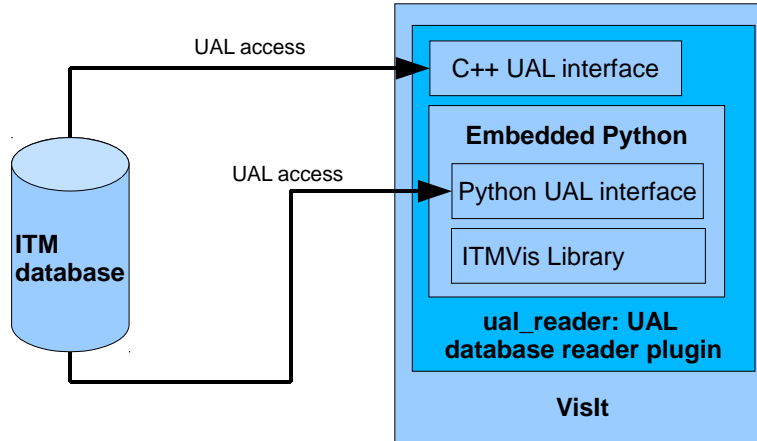

Figure 2: VisIt UAL database reader plugin provides "standard"   visualizations with C++ interface and "custom" visualizations through   embeded Python interface.

Figure 2 shows implementation layers for the proposed inclusion of the embedded Python. Passing data between Python and C++ is minimized by separating the UAL database access and providing complete ITMvis processing embedded. Similarly to the separation of the plots description is shown Listing 1.

VisIt database plugin requires the following functions to be provided by the ITMvis library:

- **PopulateDatabaseMetaData(*md);** ITMvis collects the plots from modules according to the search path and naming conventions. If the plot   is applicable and contains data filled, it appears as available under   VisIt graphical user interface (GUI) plot selector. Python returns   metadata to C++ as a custom defined list that is decoded and populated   according to C++ plugin metadata requirements. Plot name, type, topology,   data validity, labels and units are populated at this stage and returned   as a structure (*md) of all available plots (standard and ITMvis plots). \

- **GetMesh(meshname, time);** VisIt calls loaded ITMvis module with a request to provide a mesh specified with the *meshname* and   time. In order to minimize data passing complications between   Python and C++, Python is responsible to build VTK structure   as a basic visualization object on top which VisIt is built.

- **GetVar(meshname, time);** Simple 2D plots do not require any mapping of the scalar variables on the mesh as the curve suffices. This is   required only for plots with meshes [rectilinear, curvilinear, adaptive   mesh refinement

(AMR) and constructive solid geometry (CSG)]. As with GetMesh(), call-back function GetVar() returns array of data that VisIt maps on the mesh.

Above ITMvis interface for VisIt UAL plugin requires proper synchronization of objects created in memory. Referencing and dereferencing of Python and VTK objects is used for synchronization as built in *garbage collectors* needs to be informed of objects used by VisIt built in C++.
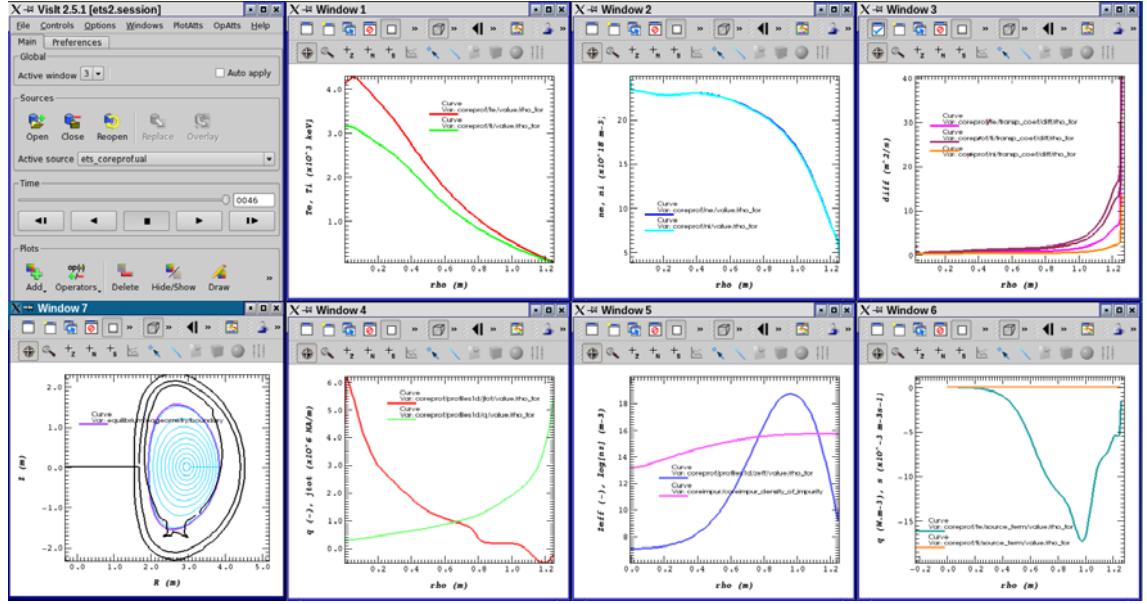

Figure 3: European Transport Solver (ETS) convergence visualization under VisIt.

Adding embedded Python to VisIt UAL plugin brought access to the Grid *service library* (GSL) that is currently implemented only for Python and FORTRAN. General Grid Library is heavily used by ITM for describing meshes of all kinds and to date could not be easily handled by VisIt UAL plugin written in C++. Standard plots can now be supplemented by custom plots from ITMvis. An example of such use is shown in Fig. 3 screen-shot of various plots required to follow *European Transport Solver* convergence. Window 5 contains ITMvis plot produced with *custom* routines in Listing 1 show together with the standard plot of effective charge profile z_{eff} in plasma core solved in the transport equation. Several CPOs were used simultaneously to produce a complete window arrangement that can be stored in a session file for reuse on similar data.

2.3   Extension of the Standard ITM VisIt visualizations

Standard visualizations provided by UAL VisIt plugin *ual_reader* are generated from CPO data structure directly with XSL transformation. This means that C++ code for each plot is generated from XSL code templates. Previously, hard to maintain XSLT

with prototype implementation was rewritten for the sake of clarity and with added EXSLT user functions provided a basis for further representations/plot types. Describing "standard" plot types is handled with *representation tags* directly in XSD description of CPO.
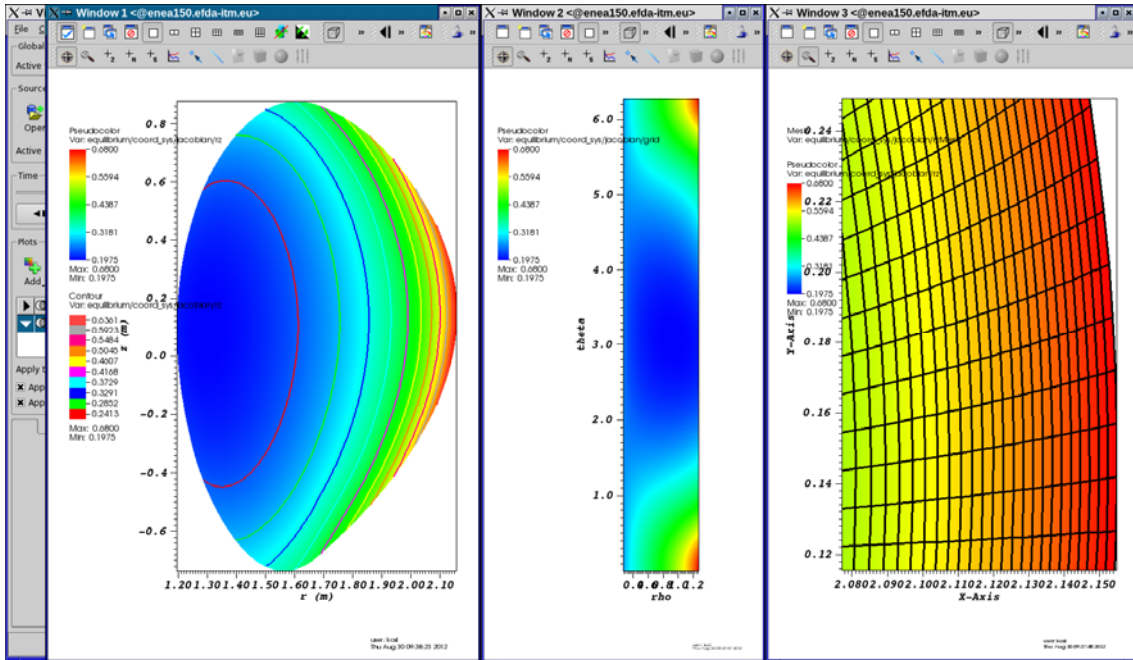

Figure 4: Equilibrium rectilinear mesh in Window 2 (center) is mapped onto curvilinear (r,z) grid shown in Window 1 (left) as pseudocolor plot overlayed with con tour plot. Detail of r,z-mesh with Jacobian is shown in Window 3 (right).

Representation tags describe "natural'' plots of data of interest and are related to conventions and a physicist way of thinking. For example, one needs to decide which field represents *x* and *y*-axis for *1D Curve*. XML representation tag consists of name, variable type, meshtype and corresponding axis links. The representation name is arbitrary and is shown as the last name in VisIt path when adding plots. The attribute describing the variable type can be scalar or vector and describes the kind of data mapped on mesh represented by one or more links. There are several meshtypes (curve0, axis1D0, rectlinear0, curvilinear0, ...), describing the type of variable mapping in space. Each meshtype can have a variable number of links (link1, link2 and/or link3) and thus different kinds of visualization that are constructed as VTK objects. Links provide axis mapping to corresponding vectors or matrices that constitute mesh. As the ITM project evolved, more representation tags were added together with deficiencies of a relatively simple approach that adds visualization with a single line.

Deficiencies were mostly solved by XSLT upgrades. Some representations like time dependence plots of scalar values and curve0 were templated without the need of representation tags. 3D timed data can be solved by slicing in VisIt. The power of XSLT code generation resulted in over 300000 lines of C++ generated code.

Missing representations were developed as shown in Fig.4 where additional representations and mesh relations (rectilinear, curvilinear) are used for the same data.

Standard representations were amended with ITMvis custom plots to round up missing links. However, there are still some open issues like representation completion, database correlation, multiple CPO handling and UAL database selection still needs to be properly addressed.

3   CONCLUSIONS AND OUTLOOK FOR 2013

Latest enhancements of ITM-ISIP VisIt-related tools targeted at UAL database reader plugin connects simplicity of plotting simple and complex data to end users as a set of predefined plots available with VisIt GUI. VisIt can be used as UAL data exploration tool as all meaningful plots are readily available and can be saved for reuse in Kepler workflows and for stand-alone use.

With current tags there are no possibilities for cross-CPO representations and such requests are now handled by ITMvis plots. ITMvis however misses "standard" plots available within UAL VisIt plugin. And users would like to have it in Python as well. The principle is known; XSLT translation for Python is needed. With standard representations in Python, C++ part of plugin might become obsolete. If there are no performance penalties that need to be further explored when more complex plots are created as the ITM project evolves.

3.1   Outlook for 2013

For 2013 under WP13-ITM-ISIP-ACT2-01 we foresee further integration of VisIt UAL plugin with VisIt Kepler Actor (VKA). As mentioned above, extension of standard plots to different backends (i.e. ITMvis) can be beneficial as then switching for 2D plots from one backend to another is simple.

A natural way to extend Kepler with VisIt is to build the VKA by calling the client engine Java interface (jVisIt) as it is provided. UAL access within VisIt is possible thanks to the ual_reader plugin. Currently, there are some limitations of the plugin that needs to be developed to complete VisIt usability beyond "standard" ones:
1. Multiple CPO handling is partially supported by "sessions" and database correlation is handled by VisIt. It is better to use UAL correlation and open multiple CPOs at once.
2. Currently CPOs are fetched as a whole. This can be limitation with large shots. It is better to use getSlice() and render slice by slice.
3. VisIt can be used as a browse of CPOs. Numerous visualizations can then be performed. Such huge metadata can take a long time to search for correct plot. ual_reader should be redesigned to use hashed map for getMesh() and getValue() procedures.
4. Further "representations" are needed by IMPs. Data structure needs to be updated after collecting requests for the "standard" visualizations.
5. From data structure one can extract Labels and Units.
6. Embedded Python needs to handle complex visualizations with unstructured meshes. Currently custom plots are prototypes only. Speed concerns will be tackled after getting workable visualizations.

Upgrading UAL plugin is thus needed to latest VisIt. Consolidation and extension of visualization capabilities of the ITM platform should provide to developers

tools for automated creation of specialized plots in workflows and as standalone tools for data analysis for users.

4   REFERENCES

1 F. Imbeaux, J. B. Lister, G. T. A. Huysmans,W. Zwingmann,M. Airaj, L. Appel, V. Basiuk, D. Coster, L.-G. Eriksson, B. Guillerminet, D. Kalupin, C. Konz, G. Manduchi, M. Ottaviani, G. Pereverzev, Y. Peysson, O. Sauter, J. Signoret, and P. Strand, Computer Physics Communications, 181 (2010), 987.
2 L. Kos, O. Hoenen, S. Kulovec, P. Huynh, J. Duhovnik, and F. Imbeaux, in 20th Int. Conf. Nuclear Energy for New Europe (Bovec, Slovenia, 2011), 1008.1–1008.8.

UPGRADE OF GAMMA-RAY CAMERAS – NEUTRON ATTENUATORS

I. Lengar, L. Snoj

Jožef Stefan Institute (IJS), Reactor Physics Department, Ljubljana, Slovenia
igor.lengar@ijs.si

1   INTRODUCTION

The main objective of the JET Enhancements (EP2) gamma-ray camera (GRC) diagnostics upgrade project is the design, construction and testing of neutron attenuators for the two sub-systems of the KN3 gamma-ray imaging diagnostics:

a) KN3 gamma-ray horizontal camera (KN3_HC) and

b) KN3 gamma-ray vertical camera (KN3_VC).

This diagnostics upgrade makes gamma-ray imaging measurements in high power deuterium JET pulses, and eventually in deuterium-tritium discharges possible [1].

The main purpose of the present neutron/photon calculations was the estimation of the influence of the KN3 neutron attenuators on the neutron and gamma field, especially on the influence of the reinforcement structures in the neutron attenuators on the flux of induced gamma rays. In order to satisfactory achieve this goal the neutronics performance of the neutron attenuators as a whole has to be studied, including the attenuator factors for neutrons and distributions of gamma rays. All of these studies are also presented in the report.

Most of the questions related to the short vertical camera attenuator, to be used in DD discharges together with the horizontal camera one, have been already previously solved and presented in reports [2, 3]. The emphasis in this report is given to the calculation of the main characteristics for the long neutron attenuator for the vertical camera (VC-NA-L), to be used during DT discharges. Similar calculations for the short neutron attenuator, used for the vertical camera during DD plasma discharges have been previously performed and reported [3]. The last design (2012) of the VC-NA-L neutron attenuator was used in order to perform the calculations.

The gamma or neutron flux in the KN3 detectors cannot be calculated with Monte Carlo techniques in a straightforward manner like for example the flux inside the torus. The reason is in the extreme degradation of the flux from the plasma to the KN3 detector position, which amounts to approximately nine orders of magnitude. MCNP has some built-in variance reduction techniques (e.g. the increased spatial importance in the direction of the detectors), which can, however, in the specific case of the KN3 not be used with success. In our case the very small fraction of neutrons, which pass un-collided through the flight tube of the KN3 camera collimators, is important.

Several methods were developed to tackle the described problems and adopted in the previous versions of our report. In the present version, basically the method of

directional biasing of the plasma neutron source towards the KN3 region was used. The attenuation was then calculated by examining the flux inside the flight tubes and detectors, as described below.

2   WORK PERFORMED IN 2012

2.1   Description of the initial model

Calculations for this report were performed with MCNP code version 5 1.60. Cross section data used were taken from ENDF/B-VII cross section library (no delayed photon data), or ENDF/B-VI and ENDF/B-V, where applicable. The original model used in the calculations is a well tested MCNP model of the 1st octant, first developed mainly by M.J. Loughlin. Some additional information about the model is available from [4]. An initial plasma neutron source was provided as well. The model was then modified in accordance with the needs of the calculation, i.e. the desired neutron attenuator – VC-NA-L – was inserted.
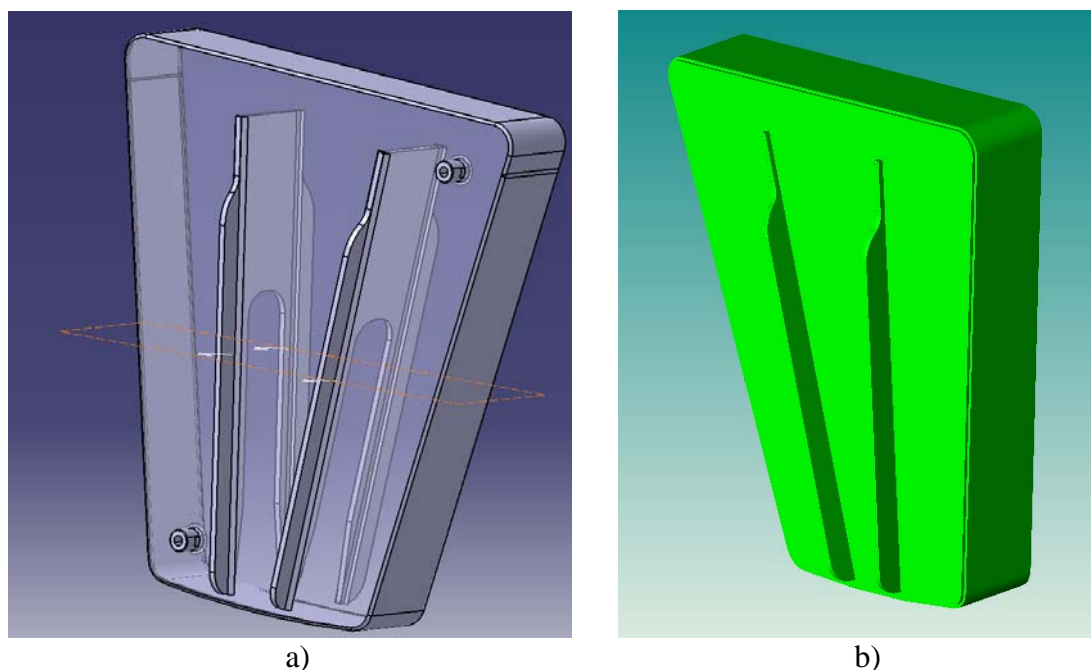

a)   b)

Figure 1: Long vertical neutron attenuator (for DT discharges); a) presented in CATIA format, b) the MCNP model (performed with MCAM [5])

The bases for the model of the neutron attenuator were original CATIA engineering drawings (Figure 1).

70

The CATIA files were transformed into the MCNP format with the help of the MCAM automatic conversion tool [5]. The resulting output file was then accordingly modified in order to be inserted into the MCNP model of octant 1. The level of detail of the neutron attenuator was somewhat higher than for the rest of the model what is reasonable, since it was the most important component to be studied. In order for the model not to grow too complex the inlet and outlet tubes on the front surface (in figure 1 in the lower left and upper right corner) were omitted from the MCNP model. The MCNP model of the neutron attenuator is also presented in Figure 1.

The sector of interest of the MCNP model with the inserted long vertical neutron attenuator is presented in Figure 2.

The calculations were performed for a DT plasma neutron source with the following major characteristics:
- plasma T: 20 KeV
- major radius: 290 cm
- minor radius: 80 cm

similar to the plasmas generally present in JET. On purpose a relatively small minor radius was used in order to easier study the effects in the edge channels.
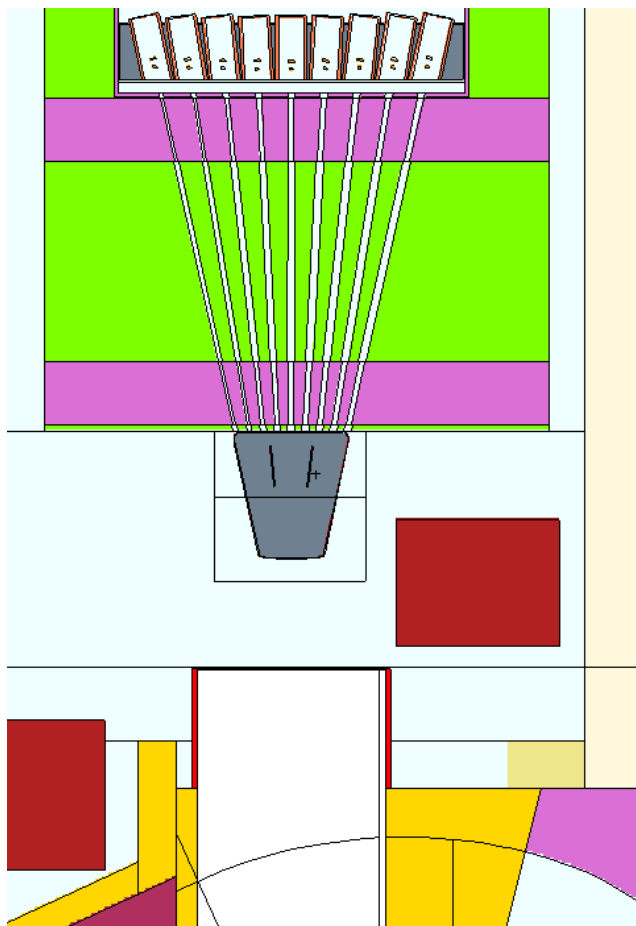
Figure 2: Section of the MCNP model with the region of interest; the neutron attenuators VC-NA-L is presented in grey colour (the lines around the attenuator are cells in MCNP and do not represent physical components).

2.2   Variance reduction – strong biasing of the plasma neutron source towards the detectors

As mentioned earlier the gamma or neutron flux in the KN3 detectors cannot be calculated with Monte Carlo techniques in a straightforward manner like the flux inside the torus since the statistical accuracy of results was much too low. The built-in variance reduction techniques of MCNP (e.g. weight windows) could in our case not be used since they relay on neutron scattering, but in our case the very small fraction of neutrons, which pass un-collided through the long flight tubes of the KN3 camera collimators, is important.

Calculation through a biased plasma neutron source

The Monte Carlo statistics of the neutron flux in the detector region can be improved by biasing the source in a way, in which much more neutrons are produced in the direction of the detectors and at plasma positions with line of sight of detectors. The advantage is an improved statistical accuracy the neutrons which are most likely to contribute to detector response. The drawback is, however, that the neutrons, scattered from the back side of the torus into the detectors, are not taken into the account.

A similar source biasing technique has been already introduced by Petrizzi et. al. [6] by solving a similar problem, namely the response of the profile monitor for ITER. Their proposed solution was modified to use a slightly less biased source. i.e. the results are a little bit closer to the non-biased case. The main features of our biased source are:

- the neutrons are not emitted from the entire plasma volume but the plasma source is modelled azimuthally only in an angle of 2°, directly below the vacuum port and the KN3 flight tubes.
- the angular emission of neutrons is biased in the forward direction towards the detectors in a cone of at least 1.3 degrees around the direction to the axis of any flight tube, i.e. cowering an around 3 times wider angle than needed to cower all neutron, hitting the detectors directly through the flight tubes.
- the probabilities of the biased events have been adequately normalized so that the final results give correct absolute values of the neutron fluxes and neutron energy spectra at the detectors, as if the source neutrons had been sampled all over the plasma volume (the case in reality)

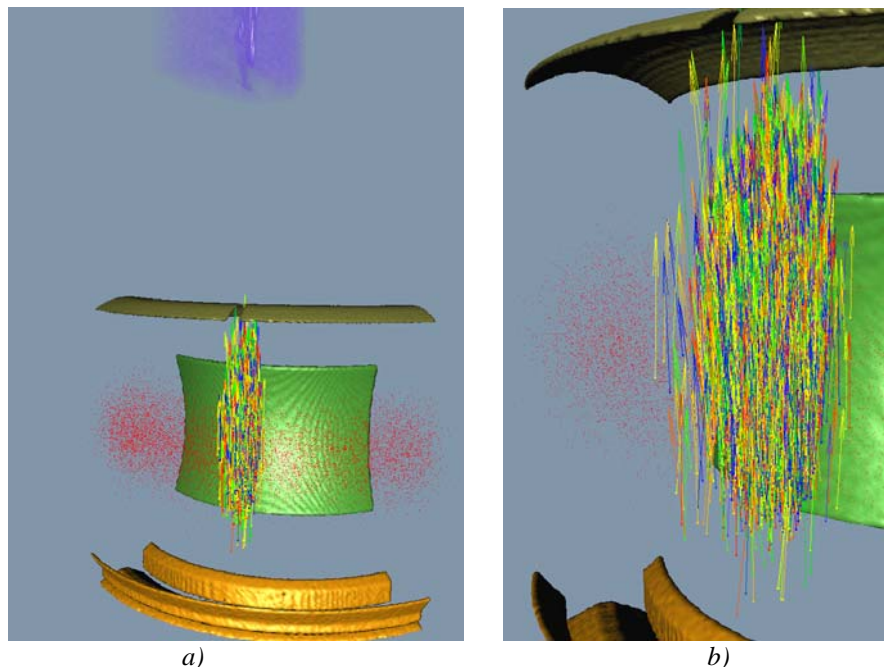*a)*   *b)*

Figure 3: Schematic presentation of source biasing; the red dots present the distribution of conventional (isotropic) plasma source. The lines present the spatial (narrow azimuth angle) and angular (in the direction of the flight tube) biasing of the source distribution. Presented are: a) some structures of the torus including the KN3 shield and b) the insert.

The cylindrical source biasing for the is schematically presented in Figure 3, the results have to be normalized.

2.3   Results

Attenuation factors for neutrons

      Due to the strong source biasing, the obtained results have good statistical accuracy. The ratio of neutrons, which would reach the detectors in the case without the neutron attenuators and with the attenuators in place, is represented as the attenuation factor. For the current calculations only the direct neutrons, i.e. not scattered within the attenuator into the flight tubes and detectors, were taken into account. These neutrons are dealt with in the following chapter (using a less biased sources). The results of the attenuation for direct neutrons are presented for individual channels in Figure 4.
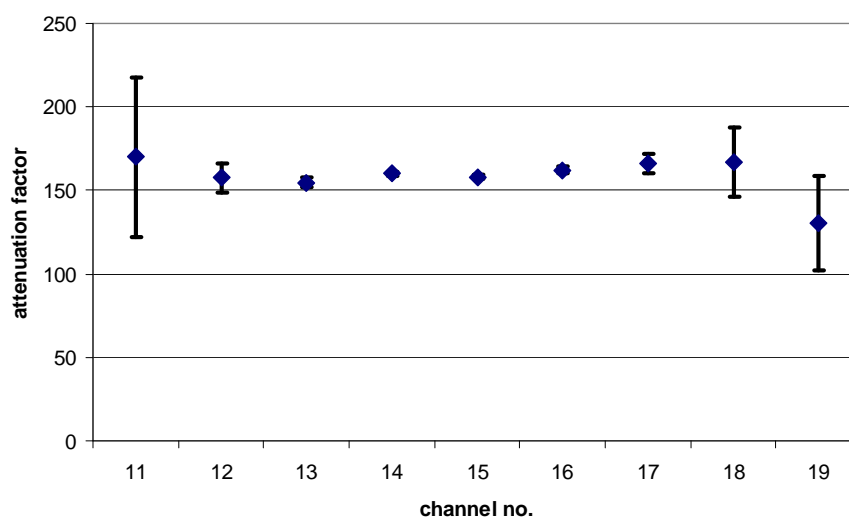

Figure 4: Attenuation factors for neutrons – ratio of neutrons reaching the detectors with and without the neutron attenuators – calculated with the biased source.

      The attenuation factors for all channels are similar, almost entirely within the error bars. The weighted average attenuation over all channels amounts to 152. The larger errors for the edge channels indicate the much lower neutron fluence for this channels with regards to the more centrally place channels.

      Presented are the neutron spectra of the transmitted neutrons; in case of strongly changing neutron cross-section within the energy range of the peak, the spectra could differ from that of the plasma source. They are presented in Figure 5.
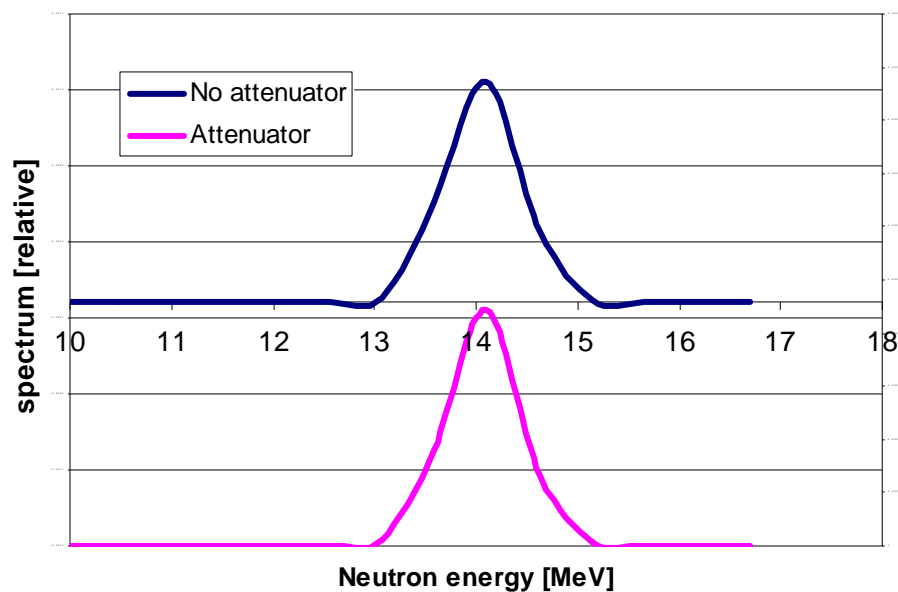
Figure 5: Neutron spectra below the KN3 shield; upper curve – without the neutron attenuator, lower curve - with the neutron attenuator in place.

It can be seen, that the spectrum of the direct neutrons does not changes a significantly by passing the neutron attenuator.

Neutrons scattered within the neutron attenuator

Estimation of the above results could also be obtained analytically. In addition to the transmitted neutrons, however, the neutrons scattered into the flight tubes from the neutron attenuator, have to be taken into account. In order to calculate the additional response of those neutrons, slightly different calculations have been performed. The plasma source was biased in a less stringent way in order to take into account all neutrons, possibly hitting the neutron attenuator which may subsequently scatter from the attenuator into detectors. For this reason the plasma source neutron were generated within a wider azimuth angle (12°) below the vacuum port and the neutron attenuator, and their the direction was chosen within broader angle, at least 4° with respect to any of the flight tubes. In this way all neutrons, possibly hitting the neutron attenuator directly (without scattering of the adjacent vacuum chamber wall) were taken into account.

The lower energy cut-off in the KN3 detectors is 0.5 MeV and the same neutron cut-off energy was used in the calculations. The results show, that in addition to a transmitted direct plasma neutron of the energy around 14 MeV, the detectors reach from 0.5 to 2.5 scattered neutrons with energy higher than 0.5 MeV per transmitted neutron, depending on the channel. The results for the channels 13 – 17 is presented in Figure 6, the statistical error for the other channels was too large for the result to be representative.
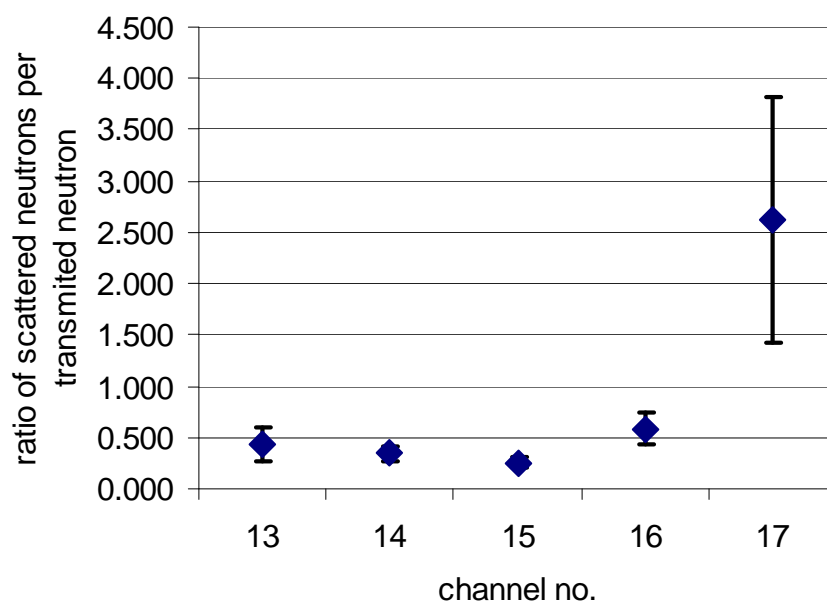
Figure 6. Number of the neutrons with energy higher than 0.5 MeV, scattered within the neutron attenuator and reaching the detectors. Presented is their ratio with respect to a transmitted neutron (shown for channels with reasonable statistical accuracy).

Presented is also the neutron spectrum at the position of the detectors, i.e. direct and scattered neutrons, for the central channel 15, Figure 7.
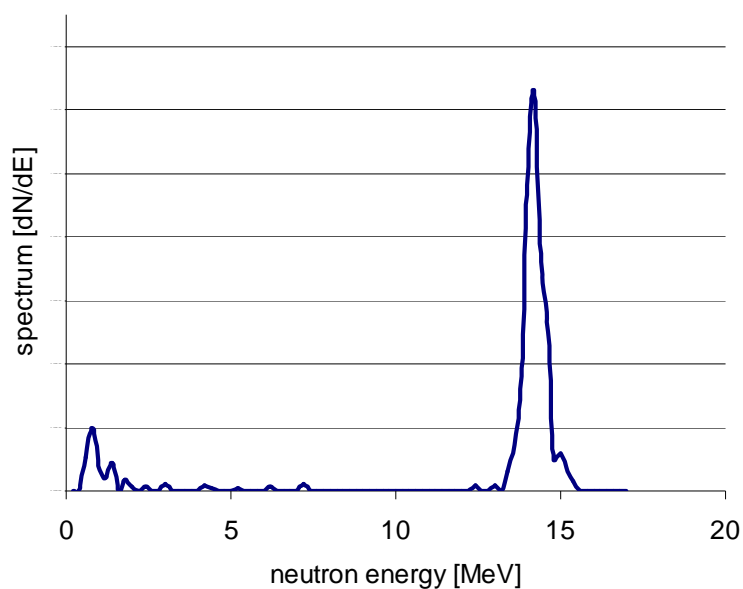

Figure 7: Neutron spectrum in the central channel 15.

It can be seen, that there are mainly two components, the neutrons with energies around 14 MeV, reaching the detectors directly from the plasma, and the neutrons, scattered from within the neutron attenuator.

The distribution of the thermal, epithermal and fast neutrons within the neutron attenuator is graphically presented in Figure 8.
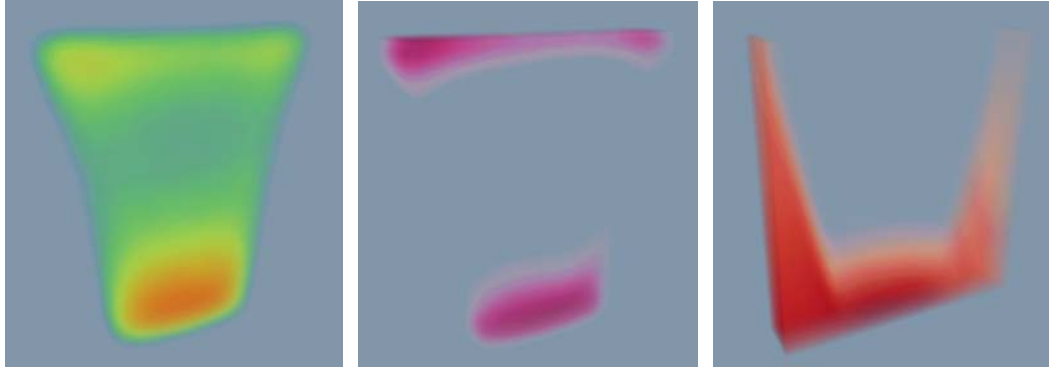

Figure 8: Distribution of the a) thermal, b) epithermal and c) fast neutrons within the neutron attenuator. The shape or the attenuator can be best be anticipated by the shape of the thermal neutron distribution.

Induced γ rays

A second requirement for the neutron attenuators (besides that of provide a high attenuation factor) is that of a minimum contribution to the gamma-ray background. It is thus also important, that there is not too much induced γ radiation from the attenuators, which could increase the gamma-ray background at the detector.

The intensity of gamma rays from the plasma, which should be measured, is varies with experiment. For this reason the neutron flux and the gamma flux are compared. The ratio of the flux of induced γ rays with respect to the neutron flux, if the attenuator was not present, is presented in Figure 9 and the spectrum in Figure 10. Presented are the total γ flux and only the γ flux, originating from the neutron attenuator.
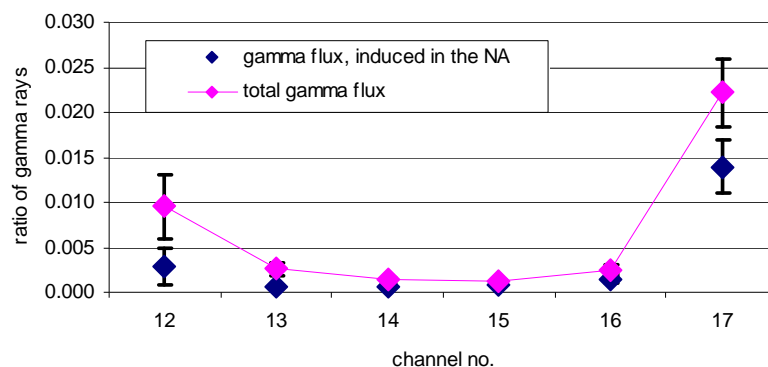

Figure 9: Flux of gamma rays at the detectors presented as the ratio with respect to the flux of plasma neutrons at detector position if the neutron attenuator was not present (shown for channels with reasonable statistical accuracy). Two cases are presented: the total γ flux and only the γ flux, induced in the NA.

The number of the induced γ rays hitting the detector per original forward-moving neutron, which would reach the detector is less than 3% in all cases. By combining the results with the number of transmitted neutrons, as presented in Figure 6, it can be observed, that the number of induced gammas reaching the detectors, per forward-moving transmitted neutron, is less than one for all cases.

It is observed from Figure 9 that for the majority of channels the component of the gamma rays, induced in the neutron attenuator is similar to the gammas, originating from elsewhere, i.e. approximately half of the gammas at detector position originate from the neutron attenuator and half from are induced in other structures. Probably they originate from fast neutrons, passing the attenuator and being absorbed in the flight tubes.

It is observed, that the total gamma flux at the detector position has a slight correlation to the flux of scattered neutrons at the detector position and further to the diameter of the flight tubes. This implies that a part of the gamma flux at the detector position is dependent on the flux of scattered neutrons producing gammas in the flight tubes and the vicinity of the detector and not only on the gamma rays, induced in the neutron attenuator.

The spectrum of the gammas in the middle portion of the central channel flight tube (30 cm above tube opening) is presented in Figure 10; this spectrum may differ form the spectrum at detector location, but the statistical accuracy of the flux in the flight tubes allows for spectrum presentation, whereas the accuracy at the detector position would be too low.
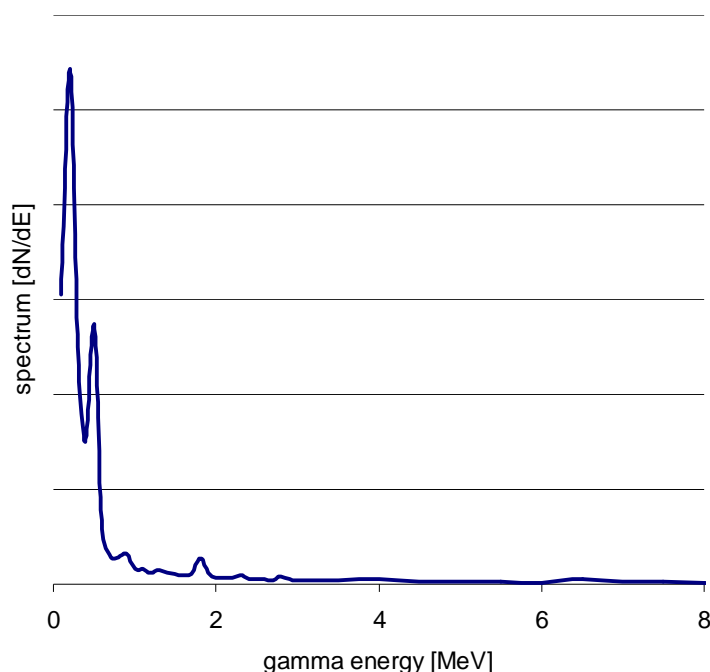

Figure 10: γ spectrum in the middle portion of the central channel flight tube

The origin of the portion of the gamma rays, induced within the attenuator, has been found to be mostly from the attenuator structures rather than from the water, filling the attenuator.

Influence of the reinforcement internal structures on the gamma field

The main reason for calculations was the estimation of the two reinforcement structures on the gamma field. The reinforcement structures 1 and 2 are visible in Figure 1 and repeated in Figure 11. In order to estimate their influence on the gamma flux at the detector position, it was divided on the flux, originating form the whole neutron attenuator and the flux, originating from each of the two reinforcement structures only.

The statistical accuracy of the gamma flux at the position of detectors was low, and the influence of the reinforcements was judged upon the gamma flux in the middle portion of the flight tubes, i.e. above 30 cm from tube opening. At this position in each flight tube, the gamma flux was divided on those, originating from neutrons, which passed either of the reinforcement structures with respect to the gamma flux, originating from the whole neutron attenuator. It is assumed, that the ratio of the gamma fluxes at the detector position has a similar value. It should be noted, that the results overestimate the true value of gammas, actually produced in the reinforcement structures, since neutrons passing the reinforcements can produce gamma rays also latter along their flight path. The result is presented in Figure 11.

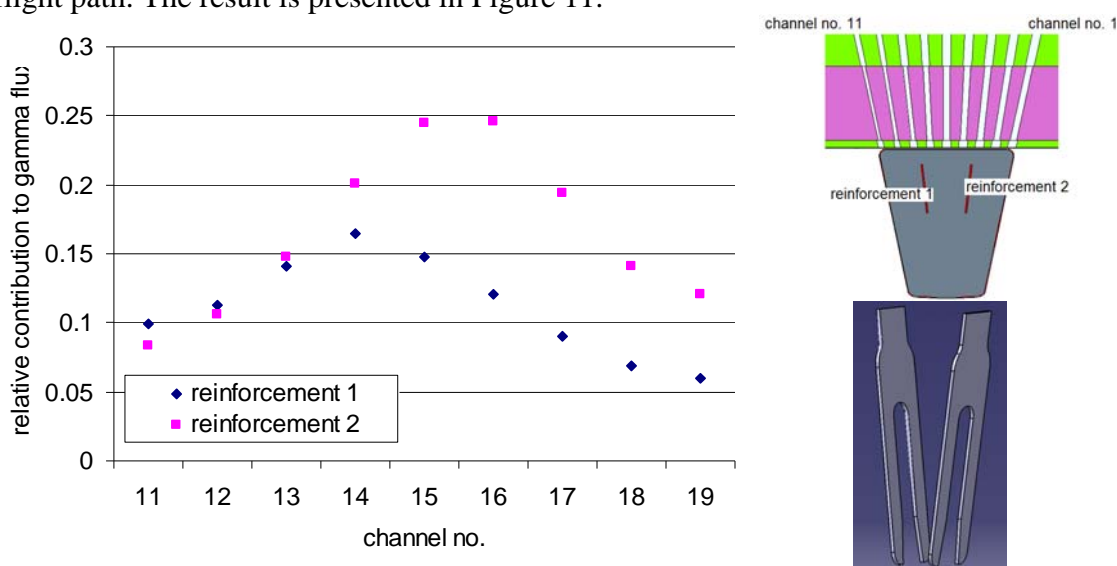*Figure 11: Ratio of the gamma fluxes in the middle portion of individual flight tubes (30 cm above tube opening) originating from neutrons, passing reinforcements 1 or 2 (right picture).*

It is observed from the picture, that the reinforcements represent a total of maximum 40 % of the induced gamma rays with respect to the rest of the attenuator structures. The ratio is dependent of channel number.

It should be repeated at this stage that the gamma flux at the detector position is represented not only form the gamma flux, originating from the neutron attenuator, but an equal component is the gamma flux, originating from neutrons, entering the flight tubes and induce gamma rays in the vicinity of detectors. It should also be repeated, that the results in Figure 11 represent the upper bound of gammas, produced in the reinforcements, since neutrons passing them can along their flight paths subsequently produce gammas in other structures.

In order to study the gamma rays, the positions of their origin in the neutron attenuator were established. A visualization of the positions, where the gamma rays are induced in the neutron attenuator are presented in Figure 12. Also presented are the lines-of-sight of the detectors (in red color) for the channel no. 15-17 and 19; none of the lines-of-sight directly intersects the reinforcements.
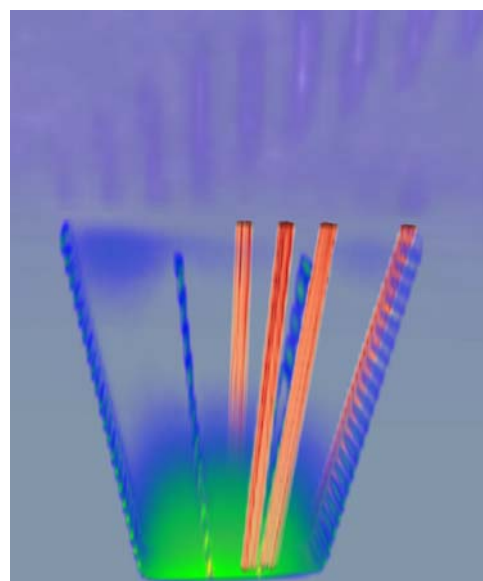

Figure 12: Visualisation of the positions, where the gamma rays are induced in the neutron attenuator. In red color the lines-of-sight for the channels no. 15-17 and 19are presented. The shape or the attenuator can be best be anticipated by the shape of the induced gamma positions.

3   CONCLUSIONS AND OUTLOOK FOR 2013

The attenuation factors for neutrons in the neutron attenuators for the KN3 vertical (long attenuator, only DT case) were estimated. The estimations were performed on the basis of Monte Carlo calculations using the MCNP5 code. Due to the extreme degradation of the flux from the plasma to the KN3 detector position a variance reduction techniques were use, developed for the specific case of the KN3 profile monitor.

The results can be summarized as:

- The attenuation ratio of long vertical camera neutron attenuator for 14.1 MeV neutrons is about 152 and is weakly dependent on the channel.
- The ratio of the neutrons scattered into the detectors from the neutron attenuators with respect to number of neutrons without the neutron attenuator in place is larger for the edge channels but less than 10% for all cases. The value is so low because the scattered neutrons have an isotropic angular distribution.
- The number of induced gammas reaching the detectors, per forward-moving transmitted neutron, is less than one for all cases.
- Approximately half of the induced gamma rays, hitting the detector, originate directly form the neutron attenuator and half of the gamma rays are induced from neutrons in the flight tubes or vicinity of the detectors.-

In 2013 additional calculations will be performed within the GRC project in order to determine the influence of the neutron Horizontal Attenuator, located in front of the Horizontal Camera. Preliminary calculations with the Horizontal Camera Neutron Attenuator have been performed by using an approximate shape of the HC-NA. The planned calculations will use the final version of the HC-NA.

4   REFERENCES

1   V. Zoita et all, Design of the JET Upgraded Gamma-Ray Cameras, Symposium on Fusion Technology, Rostock, (September 2008)

2   I Lengar; MCNP (Neutron Photon) Calculations for Gamma-Ray Cameras - Neutron Attenuators in Scheme Design Report Upgrade of Gamma-Ray Cameras – Neutron Attenuators (GRC-KN3), (2006).

3   I Lengar; Modelling of the neutron beam distribution for the KN3 attenuators; neutron-induced gamma-rays in the attenuator – (JET EP2 GRC) Upgrade of Gamma-Ray Cameras – Neutron Attenuators, (2008).

4   M. J. Loughlin et al; Neutron transport calculations in support of neutron diagnostics at JET, Rev. Sci. Instr., 70 (1999), 1126-1129.

5   Y. Wu, FDS Team; CAD-based interface programs for fusion neutron transport simulation Original Research Article, Fus. Eng. Des., 84 (2009), 1987-1992

6   L. Petrizzi, B. Esposito, E. Mainardi, L. Bertalot; Final Report on Design Analysis of ITER Neutron Camera diagnostic systems, ENEA-Frascati (EFDA/02-1002)

EXPANSION OF THE BE-WALL JET MCNP MODEL TO 360° AND TRANSPORT CALCULATIONS

I. Lengar, L. Snoj

Jožef Stefan Institute (IJS), Reactor Physics Department, Ljubljana, Slovenia
igor.lengar@ijs.si

1   INTRODUCTION

The aim of the project is the verification of the previously upgraded (FT task JW9-5.34) MCNP model of octant 3 of the JET torus, covering one quarter of the torus - the 3rd octant and halves of the octants 2 and 4. Another goal is the support of the experimental programs at JET with transport calculations of the relevant neutron and gamma fluxes. The calculations are focused also on the diagnostics needs.

The previously updated model does, however, comprised only one quarter of the torus – the 3rd octant with halves of octants 2 and 4. Practically all MCNP calculations are namely performed for a circularly symmetric plasma source, what can be performed by modelling only one (symmetrical) portion of the torus by a section model. The correct results are then obtained by impinging reflecting boundary conditions on the symmetry planes of the geometry, in our case on the planes bisecting the 2nd and the 4th octant. There exist, however, a limitation for this kind of simplification, namely in the rare case, where the neutron source is not circularly symmetric. One example of such a source is the Californium – 252Cf point neutrons source, to be used at JET for detector calibration.

In order to obtain correct results with point sources, the available section model, has to be adjusted. There exist different ways in order to adapt the verified models for this purpose. One way is to duplicate and rotate the existing sector of the model in order to fill the full torus. Another way is to modify the neutron transport code in order to mimic the whole torus. The probably longest way is to model the missing part of the torus anew. The first two options will be addressed in the project in order to provide the highly needed calculation support for the planned 252Cf source calibration.

The upgrade of the current MCNP model for JET was aimed in view of the support for the neutron calibration of JET diagnostic systems, which is to be carried out with a Californium point source. The current model is unsuitable for exact calculations with a point source.

In addition, since the maintenance of a MCNP model is a dynamic process, during the upgrade and calculations the model were checked on its appropriateness and possibly improved. Recently new data about the material composition of the JET torus components was found, which in some parts differs from that, used in the existing models. All models – the one sector model and the new whole JET model – were improved also by the usage of new data.

Another goal was the continuation of the up-to-date MCNP calculations. The availability of models and know-how for their usage was found important in the support of experiments, connected to the diagnostics of neutrons. Both are ensured by a continuous upgrade of the MCNP models.

The work was planned as an extension of the previous tasks JW9-FT 5.32 and JW10-FT 5.34. The previously upgraded model, suitable for the use with circularly symmetric neutron sources, was adjusted in order to be used also with point sources. The desired goal will was achieved in two different ways. On one hand, the current MCNP sector model, covering one quarter of JET, was expanded to the full 360° model. On the other hand, the MCNP code was modified in such a way, to enable the labelling of neutrons while transported inside the one quarter model, but effectively tracking them as if they were transported in the whole 360° model.

2   WORK PERFORMED IN 2012

2.1   Expansion of the model by replication to 360°

The existing MCNP model of one quarter or JET was used as the basis and replicated three times and accordingly rotated in order to fill the whole torus. This produced in the first place a model symmetrical 4-fold around the axis what is justifiable, since the JET torus is to a high degree axially symmetrical. First the original model was modified, replicated and then composed into the 360° model.

The use of the full 360° model is necessary for calculations, where some asymmetry exists between individual quarters of the geometry. An evident case is the mascot boom, used to hold the ^{252}Cf point neutron source, which brakes down the otherwise acceptable 4-fold torus symmetry.

The replication was done in several steps, which are described below.

The 1 sector 90° model was used as the origin and by replicating and rotating it 3 times by using the MCNP Universe feature a full 360° model was prepared.

Figure 1: Procedure tested on vacuum vessel only model.

First the procedure was tested on a simple one sector model; only the vacuum vessel was modeled and accordingly replicated and rotated as visible from Figure 1.

For this expansion, all structures of the 1 sector model have been put into a universe (a feature of MCNP. This has been accordingly replicated and rotated and put into a second level universe. The model was filled with this universe.

The next step was to copy replicate the full one sector model, as presented in Figure 2.

Figure 2: Schematic presentation of the replication of the one sector model

In the next step, the 4 fold symmetry was broken and 8 fold symmetry applied. In this way the more complicated ports could be modeled. Additionally a higher level of detail was introduced. The procedure is schematically presented in Figure 3.
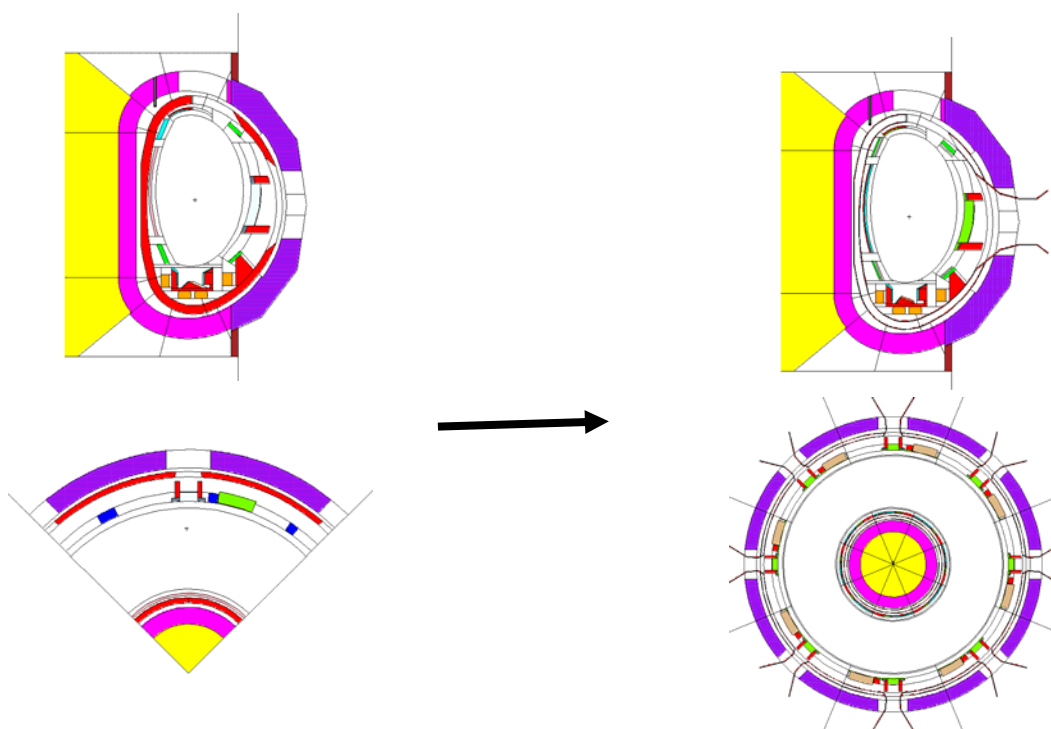
Figure 3: Schematic presentation of the higher level of detail, which was introduced and the 8 fold symmetry, needed for detailed port insertion.

The next modification was inserting the increased level of detail in the model. The 1 sector model was previously upgraded with to a higher level of detail, which was originally not introduced into the 360° model. The increased detail can be observed in Figure 4.
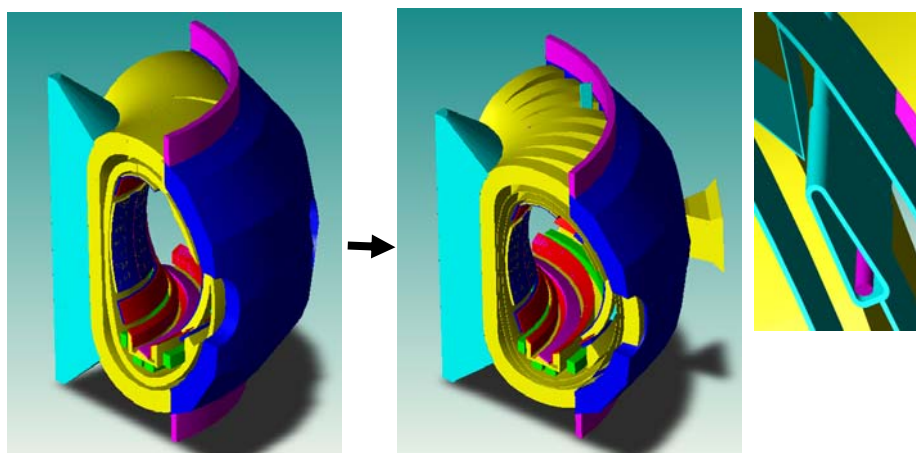
Figure 4: Previous upgrade of the 1 sector model, which was used as the basis of the last the 360° model. The individual modelling of toroidal coils and detailed structures around the small vertical port are visible in the figure.

The model has further been optimised for insertion of the mascot robot boom, which has to be inserted into the vacuum vessel region during neutron source calibration. A graphical presentation of the boom is presented in Figure 5.
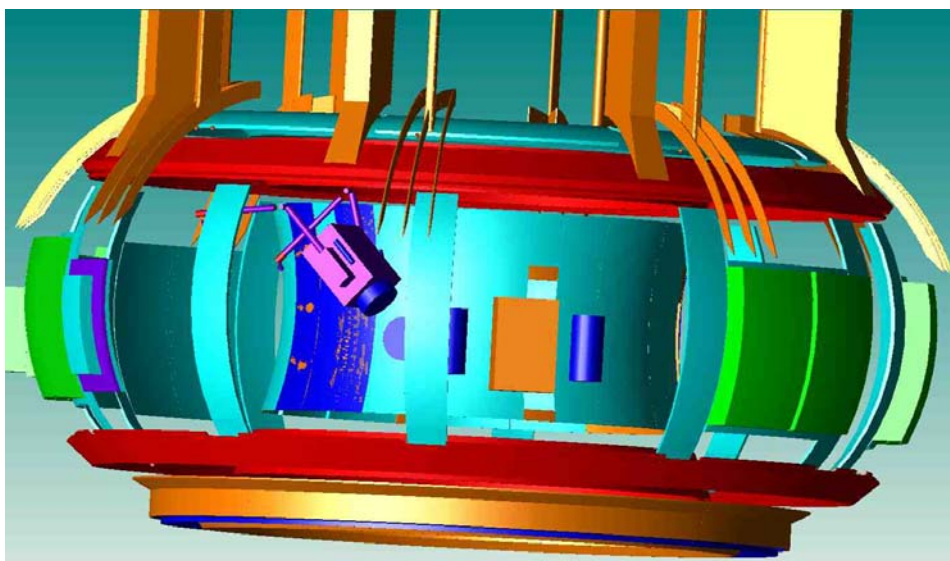
Figure 5: Presentation of the major in-vessel structures and the boom, inserted into the model. Graphics by MCAM [1].

2.2   360° model by MCNP code adjustment

In addition to the model expansion, the point source problem was treated by adjusting the MCNP code. The advantage of this approach is that the evaluated sector models can be used for quick calculation with point sources without any changes. This approach is possible due to the availability of the full MCNP source code for registered users.

The reflecting planes of the one quarter, sector model effectively expand the model symmetrically into 4 identical parts what is very effective if the source is symmetrical as well. But in the case of usage of point sources with such a model, the sources are also duplicated four times, giving a wrong answer. The problem can, however, be possibly overcome by labeling a neutron each time it bounces off a reflecting plane. In this way the track is kept, in which of the four replicated quarters the neutron was originally born, and in which quarter it has contributed to the calculated flux. There exist virtually no other way to solve the problem, but in changing the MCNP code. The neutrons are additionally labeled with respect to their quarter of origin.
The work was first focused on identifying the parts of the code in order to satisfactory label the neutrons. Then the correct transport of the secondary particles (e.g. photons produced by neutrons) was be determined. At the end the correctness of the modifications in the code were carefully studied, and the obtained tallies examined.

The final result is a set of all MCNP subroutines, which have to be modified in order to mimic of a full 360° model by MCNP but using only a one sector model.

Description of the MCNP code modification

Most of the models of tokamaks comprise only one sector of the torus (i.e. one octant at JET or 1/18 th of the torus for ITER). Practically all MCNP calculations are namely performed for a circularly symmetric plasma source, what can be performed by modeling only one (symmetrical) portion of the torus by a section model. The correct results are then obtained by impinging reflecting boundary conditions on the symmetry planes of the geometry. There exist, however, a limitation for this kind of simplification, namely in the rare case, where the neutron source is not circularly symmetric. One example of such a source is the Californium – ^{252}Cf point neutrons source, to be used at JET for detector calibration.

One way of obtaining correct results with point sources and sector models is modification of the MCNP code as described in the continuation.

Treating individual particles

The full 360° model can be simulated by tracking the individual neutrons and other particles. If a neutron is reflected from the edge surface (marked as 1 and 2 in Figure 6), it means that it should "in real life" be in another sector of the model. Figure 2 presents the history of a neutron (rainbow colored), which is by MCNP transported in the primary sector, bound by two reflecting planes. Also in the figure is shown the history of the neutron (blue and red), as it should scatter around the torus if the model would cover the full 360°.
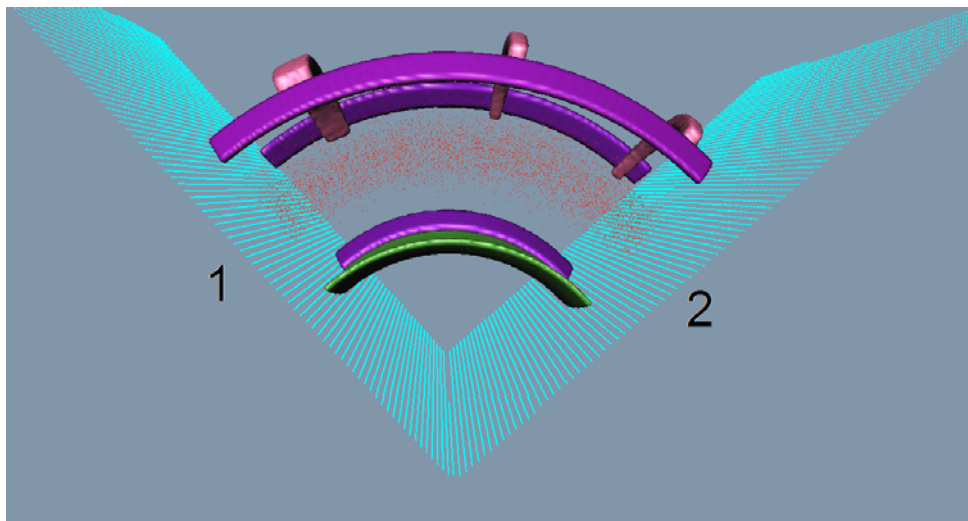
Figure 6: Sketch of a sector model with reflecting edge surfaces labeled as 1 and 2.
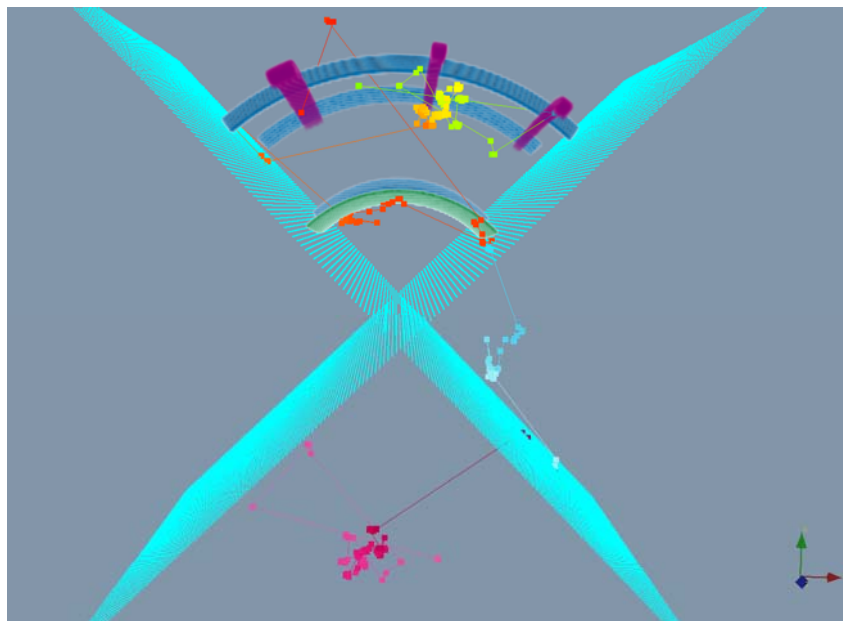
Figure 7: History of a neutron (rainbow colored), which is by MCNP transported in the primary sector. Also in the figure is shown also the history of the neutron (blue and red), as it should scatter around the torus if the model would cover the full 360°.

It can be followed from Figure 7, that each time a neutron hits a reflecting plane it should actually change the sector of the torus. In order to track the neutron, as it should scatter around the torus if the model would cover the full 360°, each time it hits a reflecting plane, a label is changed, in this way additional information is associated to each particle, namely in which sector it should be. In the code the sectors are numbered from 0 – the primary sector, the only one which is modeled, and then clockwise up to N-1, where N is the number of sectors (i.e. 4 for a 90° degree model of the torus). If the

particle circles around the torus and reaches the primary sector again, its flag is again set to zero.

The question is how to label particles in MCNP since no extra parameter, associated to particles, is available in the code. The solution is found by changing the time variable of the particle. During a particle history, at each moment the time is associated to the particle, which measure the time after its creation (the time after creation of the primary particle for induced particles, i.e. gammas from neutron capture). The time is measured in shakes, equal to 10 ns. The particles are labeled by increasing the time variable, TME, by $1s = 10^8$ shakes each time the particle should cross a reflecting plane in the clockwise direction, and by decreasing it by the same value each time the particle should cross a reflecting plane in the anti-clockwise direction. It should be noted, that the normal time tally can in this case be used with restrictions, since the TME constant is devoted also for particle tracking, with some effort, however, all the time information of a particle can also be extracted.

Testing of the code modifications

The modification has been tested on the following issues:

- primary neutrons: (variable TME ±1 sec by crossing a reflecting plane)
    o following neutrons by the PTRAC file
    o testing on tallies – comparing results
- "banked" particles
    o the secondary particles carry the correct value of TME
    o also in case of variance reduction
- induced gammas
    o gammas correctly change the value of TME
- source gammas treated correctly

and found to behave correctly.

3   CONCLUSIONS AND OUTLOOK FOR 2013

The 3D MCNP model of JET was further upgraded in order to be optimized for calculation of correction factors, needed for the neutron source calibration. The new boom was inserted into the upgraded 360° MCNP model, the correctness of the insertion was examined.

Individual components (limiter, RF, LHCD, …) have been modelled each in own universe. Identical components have only to be modelled once and are replicated on all occurrences. The model is optimized for the automatic insertion of the boom to the necessary 240 positions (automatic insertion of transformation cards).

The MCNP code was modified in order to track the real 3D location of particles while transported in only one sector. The MCNP6 code was found to perform in the same was as the previously used MCNP5. The code correctness of the corresponding transport has been examined in several ways. It was found that the modification correctly describes the primary neutrons, the induced gammas and "banked" particles and source gammas. A manual with instructions for MCNP code modification, needed to be done for the described calculations with point sources in sector models, was written for interested users.

3.1 Future work

The MCNP model will be, with regards to the diagnostics needs, further upgraded. It will subsequently be used for calculation of correction factors, needed for the evaluation of the neutron source calibration results. The model will also be used for calculation of the response of detector systems.

4 REFERENCES

1   Y. Wu, FDS Team, CAD-based interface programs for fusion neutron transport simulation, Fusion Engineering and Design, 84 (2009), 1987 – 1992.

CALCULATIONS TO SUPPORT JET NEUTRON YIELD CALIBRATION: EFFECT OF THE JET REMOTE HANDLING SYSTEM ON THE EXTERNAL NEUTRON MONITOR RESPONSES

Luka Snoj, Igor Lengar, Aljaž Čufar, Andrej Trkov

Jožef Stefan Institute
luka.snoj@ijs.si

1   INTRODUCTION

Neutron yield measurements are the basis for the determination of the absolute fusion reaction rate and the operational monitoring with respect to the neutron budget during any campaign for the Joint European Torus (JET).

After the Carbon wall to ITER-Like Wall (Beryllium/Tungsten/Carbon) transition in 2010-11, update of the neutron yield calibration will be ensured by direct measurements using a calibrated 'point' 252Cf neutron source (NS) deployed by the in-vessel remote handling (RH) boom and mascot manipulator inside the JET vacuum vessel [1].

This calibration will provide direct calibration of the external fission chambers (FC) system which was the original JET standard [2] and provide the first direct calibration of the JET activation system inside the torus. The objective of the calibration is to achieve at least 10 % accuracy in absolute calibration of the JET external neutron monitors.

As in all such calibrations, neutronic calculations are required to support the physics, safety and engineering efforts [3][4]. Many are based on Monte Carlo modelling using the advanced Monte Carlo transport codes, such as MCNP [5].

In total more than 200 locations of the NS inside the tokamak will be used for neutron monitor calibrations. The locations of all NS calibration points inside the torus are schematically presented in Figure 1. There are 40 locations in the toroidal direction round the torus, each location having 5 positions: one is centrally located (C) in the plasma centre 30 cm above the tokamak midplane and 4 positions are offset from this central one by 0.5 m in the upper (U), lower (L), inner (I) and outer (O) directions. These point source measurements simulate 5 rings round the torus; a central ring plus up, down, in and out rings.
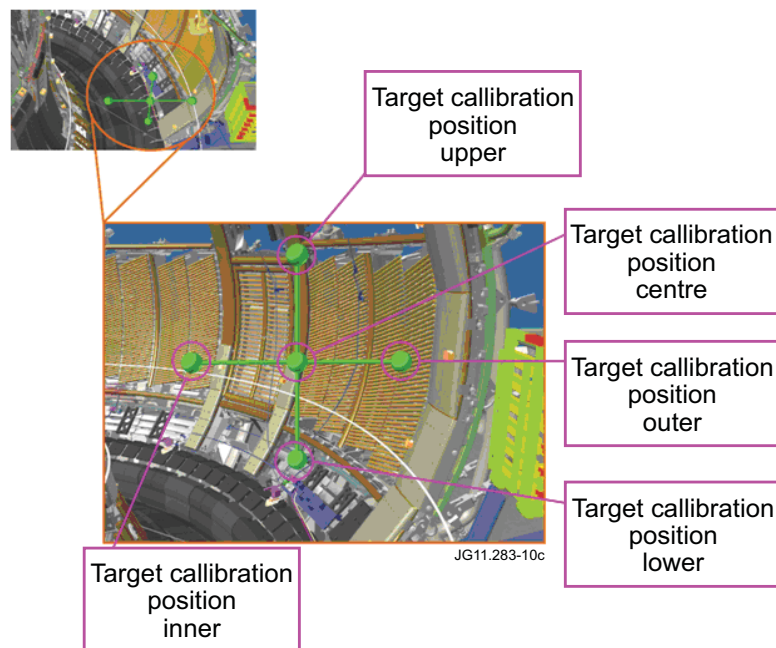
Figure 1: Draft of in-vessel scan pattern. There are 5 points at each toroidal location round the vessel, i.e. 5 rings of points, plus some subsidiary points at other particular locations. Only part of the JET structure is shown.

The JET RH system contains some massive components (the mascot manipulator and the boom), which will be inside the vacuum vessel during the calibration, hence it is expected that these objects will significantly affect the neutron transport from the NS to the neutron monitors. Hence neutronic calculations are required to calculate the effects of the JET remote handling system (RHS) on the neutron monitors. We developed a simplified but quick running 3D geometrical computational model of JET [3] in MCNP [5] (Figure 2), which has been validated against the only experimental values available, i.e. the measurements from the last calibration performed in 1989 by Laundy and Jarvis [2]. Modelling of the JET RHS has already been described in detail [6]. It is important to note that this simplified model will be used only for the purpose of investigating the nature of various effects but not for the final numerical calculations of the final correction factors, which will later be performed with a more detailed model of the JET tokamak [7].

The activity presented in this report is, in fact, the continuation of the work performed last year, when we investigated the modelling of the JET RHS in MCNP [6]. The objective of this work is to find out the geometric and material dependencies of the corrections due to the JET RHS and to estimate the size of these effects. This will help us minimize the effect of the JET RHS system on the final measurements.

Some predictions can be made *ab initio*: The presence of the boom entering the torus in Octant 5 will mostly affect the nearest detector (No D3); our purpose is to minimise this effect. Also, when the boom is on one side of the torus, it will not significantly affect the response of detectors at the far side. This can be seen from our earlier calculations and from the only existing previous data [2], which show that the response of the detector to the NS, versus the NS position is peaked at the nearest port to the detector and that 80 % of the total response comes from the nearest port and the two adjacent ports. Therefore the orientation of the mascot and the boom was chosen in

such way to ensure a clear line of sight between the NS and the 3 ports centred on the nearest port to the detector.

Of course, the scattering from the isolated neutron source casing and the baton, in which the source is present during the calibration, is a minimum distortion which is always present. The latter effect was thoroughly studied earlier [4] and it is found that its effect is negligible compared to the effect of the JET RHS.
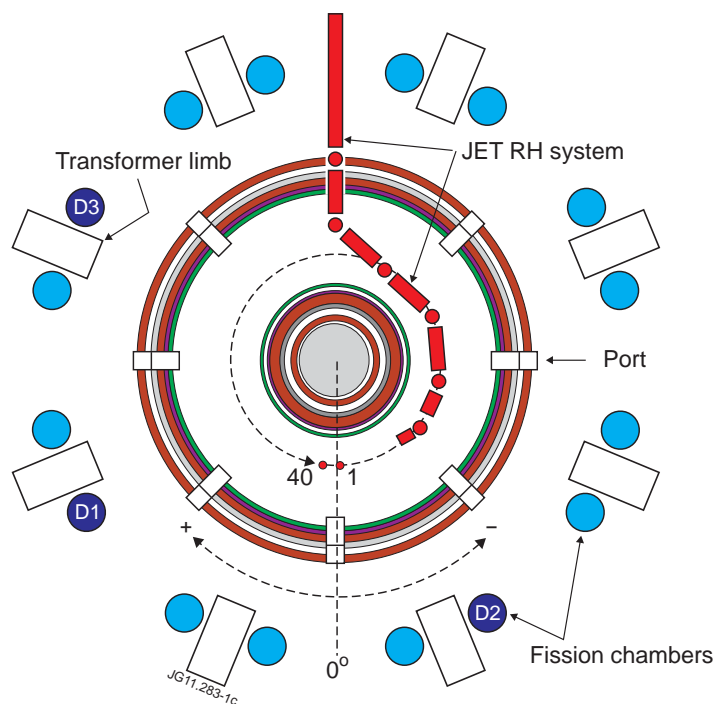
Figure 2: Top view of the MCNP JET geometrical model with the JET RHS deploying the source at location 1 C. The section is made at the tokamak midplane (z=0). As the mascot manipulator is tilted relative to the XY plane only the boom is visible. The positions of the JET external neutron monitors are denoted by D1, D2 and D3.

2   WORK PERFORMED IN 2012

2.1   Correction Factor

We studied the effect of the JET RHS. The effect of the JET RHS on the external neutron monitor response can be expressed in the term of the ratio between the undistorted and distorted neutron monitor response, which can be considered as correction factor.

Investigation of the effect of the major components of the JET RHS on the response of the external fission chambers on the transformer limbs and on the activation detectors located inside the vacuum vessel was performed in the following way. First we calculated the undistorted neutron monitor response versus the NS position for every calibration point, i.e. a response without the RHS in the vessel. Second we did the same calculation with the RHS included, i.e. the boom and the mascot manipulator holding the NS holder were modelled inside the tokamak in a specified configuration. Then we

91

calculated the RH correction factor (CF) for the i-th detector and the j-th toroidal NS position, at poloidal position k, $C_{RH}^{i,j,k}$, as the ratio between the distorted neutron monitor response, $\Phi_{RH}^{i,j,k}$ and the undistorted response, $\Phi_0^{i,j,k}$

$$C_{RH}^{i,j,k} = \frac{\Phi_{RH}^{i,j,k}}{\Phi_0^{i,j,k}}$$

$$\Phi_0^{i,j} = \text{undistorted neutron monitor response}$$
$$\Phi_{RH}^{i,j} = \text{distorted neutron monitor response} \qquad (1)$$
$$i = \text{detector index (i = 1,16)}$$
$$j = \text{NS toroidal position (j = 1,40)}$$
$$k = \text{NS poloidal position (k = 1,5); } k \in \{C,I,O,U,L\}$$

The calculations of the correction factors were performed for all 16 notional fission chambers in the model, and for all 200 NS positions, meaning that we calculated 3200 correction factor values. In order to present RH correction factors for all detectors and calibration points we used several modes of presentation: correction factor versus NS position, correction factor versus detector position, correction factor matrix, and correction factor distribution. The advantages and deficiencies of the above mentioned modes are presented in Table 1. Examples follow in the paper.

Calculation of final RH correction factors for all calibration points is out of scope of this paper. Hence the RH correction factors are presented only for some particular cases and for the central NS positions, which are the most representative as they correspond to the plasma centre. Special attention was paid to the three fission chambers, denoted by D1, D2 and D3 in Figure 2, which are located at the positions of the real fission chambers at the JET tokamak.

First we calculated the undistorted detector response for the central NS position (Figure 3 above). The FC response curve versus NS position represents the contribution to individual detector response from a certain NS position. It is found that the results are in agreement with [3], i.e. the neutron monitor response is the highest when the NS is closest to the detector, except for the position, which is approx. 30 ° from the detector. The peak at the latter position is due to a direct line of sight effect through the port, exaggerated because the size of the notional detectors is larger than their real size. Hence the location, shape and height of the peak strongly depend on the shape of the port and of the neutron detector in the computational model.

presentation mode	advantage	deficiency
CF vs. NS position	o presents the results of interest, which is directly applicable to the correction of the experiment	o only some of the detectors can be presented
CF vs. detector position	o study azimuthal dependence of CF for a certain NS position ➜ good for understanding the effect	o only some of the NS positions can be presented at once
CF matrix	o presenting CF values for all NS points and all detectors o good for observing the trends and understanding the effects	o difficult to read exact values of CF accurately
CF distribution	o observe changes in neutron flux distribution all over the torus hall and not just the detectors o good for understanding the effects	o difficult to read exact values of CF accurately o one picture valid for single NS position only ➜ need a movie or several pictures for all NS positions

Table 1: Comparison of modes for presenting effect of the JET RHS on the external neutron monitor response.
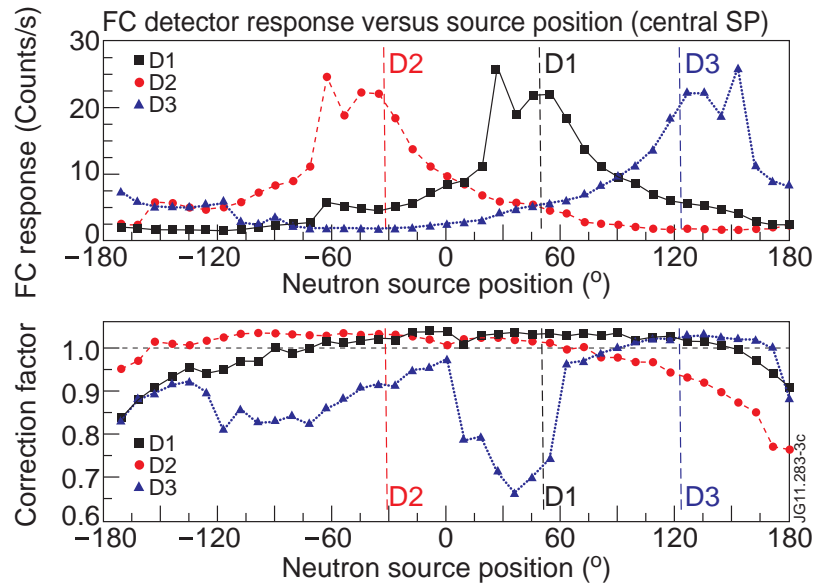
Figure 3: External FC response versus NS position for D1, D2 and D3 FCs (above). Remote handling correction factor versus NS position for D1, D2 and D3 FCs (below). NS is located on the central ring.

Secondly we calculated the RH correction factor (as defined in Equation (1)) for the NS at the central position and for the FCs at D1, D2 and D3 positions (Figure 3 below). It can be observed that FC response at location D3 is the most affected by the RHS as it is closest to the RH entrance port in Octant 5, which is blocked by the boom. Moreover the FC response for D1 and D2 positions is the most affected by the RHS when the NS is located in Octant 5. It is interesting to note that when the NS is located in the octant close to the FC position, the FC response is only slightly affected by the RHS, i.e. the RH correction factor is slightly larger than unity, mainly due to increased back-scattering from the mascot robot body. All these findings are in agreement with our previous studies showing that the highest contribution to a certain FC is via the

closest port and the second highest contribution is via the port closest to the neutron source [3]. The effects of the RHS depend on the RH configuration and on the neutron monitor location. The response can be decreased by the boom blocking a port or increased by favourable scattering.

Correction factor versus detector position for four representative NS positions are presented in Figure 4. It can be observed that correction is the highest for the detectors close to the RH entrance port. When the NS is at position 180°, which is just in front of the RH entrance port, the correction to all detectors is the highest, as the RHS is blocking the port next to the NS. In other cases the correction factor is the largest for detectors shadowed by the RH boom.
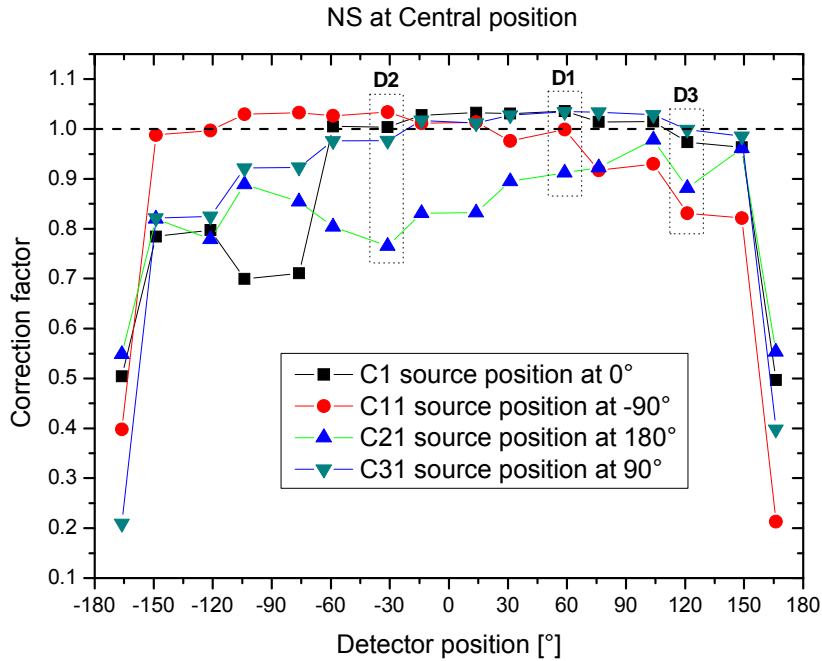
Figure 4: Correction factor versus detector position for 4 representative central NS positions.

2.2   Importance Weighted Correction factor

The RH correction factors are required for each of the 200 measurement positions. In order to obtain the plasma (volumetric neutron source) relevant response these should then be convoluted with the fission chambers position-dependent response (e.g. Figure 3 above) to generate the integrated ring responses for each detector. First we calculated the ring correction factors for each of 5 poloidal NS positions:

$$C_{RH-IW}^{i,k} = \frac{\sum_{j=1}^{40} \Phi_{RH}^{i,j,k}}{\sum_{j=1}^{40} \Phi_{0}^{i,j,k}} \qquad (2)$$

Secondly we calculated the total correction factor:

$$C_{RH-IW,tot}^{i} = \frac{\sum_{k=1}^{5}\left(w_k \cdot \sum_{j=1}^{40}\Phi_{RH}^{i,j,k}\right)}{\sum_{k=1}^{5}\left(w_k \cdot \sum_{j=1}^{40}\Phi_{0}^{i,j,k}\right)}, \qquad (3)$$

where w_k denotes the ring importance factor, which is proportional to the neutron emission from that part of the plasma and strongly depends on the poloidal plasma profile.

In calculations presented in Table 2, we assumed a flat plasma profile, meaning that all rings contribute equally to the detector response. This is not necessary true for all plasma shapes, especially the common ones which have highly peaked poloidal profiles. For such peaked plasma emission profiles, the data will be biased towards the central ring values.

All final importance-weighted correction factor results for D1, D2, and D3 detectors are presented in Table 2. For D3 detector the CF is by far the largest for the upper NS position, as its distance from the tokamak midplane is the largest (80 cm).

During the investigation of the effect of the JET RHS on the neutron monitor response, we closely interacted with the remote handling team trying to find the optimal configuration, i.e the one with the smallest correction factor. For example we changed the RHS deployment geometry for some of the most affected NS points in Octant 5. One such example is presented in Table 2, showing the total correction factors for two RH configurations.

The differences are relatively small meaning that already initial configurations were well optimised. However it can be seen that a reduction in the correction by~ 0.8 % was achieved for the most affected detector D3.

detector →	old Oct 5 positions			new Oct5 positions			new/old-1 [%]		
	D1	D2	D3	D1	D2	D3	D1	D2	D3
NS position ↓									
C	1.018	1.013	0.954	1.019	1.016	0.964	0.13 %	0.26 %	1.04 %
L	1.017	1.015	0.965	1.018	1.018	0.974	0.13 %	0.22 %	0.87 %
O	1.013	1.009	0.949	1.016	1.013	0.964	0.27 %	0.37 %	1.58 %
I	1.018	1.014	0.949	1.019	1.016	0.948	0.03 %	0.12 %	-0.09 %
U	1.014	1.009	0.918	1.015	1.011	0.923	0.09 %	0.18 %	0.49 %
total	1.016	1.012	0.948	1.017	1.015	0.956	**0.13 %**	**0.23 %**	**0.81 %**

Table 2: Importance weighted RH correction factors for all NS position for two RHs configurations, basic (old) and improved (new). C-centre, L-lower, O-outer, I-inner, U-upper

For D1 and D2 positions the integral correction factor is ~1.015, which is mainly due to neutrons back-scattered from the mascot body. In D3 position however the integral correction factor is approx. 0.95, mainly due to the boom blocking the port in Octant 5, which is relatively close to the D3 position in Octant 6.

3   CONCLUSIONS AND OUTLOOK FOR 2013

Performing an absolute calibration of the JET external neutron monitors with an inaccuracy lower than 10 % is a difficult task due to the complex geometry and due to numerous geometrical and material uncertainties. Hence it is essential to use an advanced neutron transport code, such as MCNP to computationally support the experiment by calculation of experimental corrections, uncertainties and, determination of biases. In this paper the effect of the remote handling system on neutron transport was investigated. Due to large number of results and relatively high complexity of the problem under investigation, several visualisation modes were used to present the results. The final results of the extensive analysis are summarised in the three preliminary RH correction factors presented in Table 2. However a detailed analysis of all results shows the following: D2 and D1 are the least affected FCs as they are furthest from the RH entrance port in Octant 5. D2 and D1 detector response is increased in presence of the RHS, mainly due to increased back –scattering of neutrons from the mascot robot body, meaning that the mascot robot body has to be modelled in detail to accurately simulate the effect.

 D3 is the most affected FC as it is closest to the RH entrance port in Oct 5 that is blocked by the boom. The D3 response is decreased in the presence of the JET RHS due to shadowing effect of the boom.

Although the RHS is a massive object its overall effect on the external neutron monitor response is not large, i.e. less than 5 % for the most affected detector, when taking into account the NS importance function.

It must be remembered that these calculations have used the simplified or the so called 'Quick Model' to allow production of results with reasonable computation times. To obtain more detailed and accurate estimates of the final corrections and their uncertainties, the calculations will be repeated with the more complete model of the JET [7].

The correction factors due to the presence of the JET RHS can potentially be significant in cases when the boom is blocking a port close to the detector under investigation; however we have chosen boom configurations so that this is avoided or minimised in the vast majority of the source locations. The results are of great interest for any RH application involving manipulation of strong neutron sources, e.g. neutron monitor calibration in ITER or DEMO.

We achieved all goals and milestones set for 2012 with exceptions of analysis of experimental calibration results. The latter was not possible to perform as the experimental calibration was rescheduled to 2013.

In 2013 calculations will be done to support the detailed model calculations with final configurations. The calculations will ensure understanding and enable the evaluation of the effects of differences between calibration conditions and later JET operational conditions.

In addition the work above we plan to perform another task, which is relevant to the development of neutron based plasma position monitoring system in DEMO. As DEMO will most probably lack neutron profile monitors, there is a possibility to monitor plasma vertical position with simpler neutron detectors. The purpose of the study proposed within this task is to perform preliminary computational analysis to support testing of such system at the JET tokamak.

4   REFERENCES

1   Syme D.B. et al., Fusion Yield Measurements on JET and their Calibration, Nuc. Eng. Des., 246 (2011), doi: 10.1016/j.nucengdes.2011.08.003, 185-190.

2   Laundy B.J., Jarvis O. N., Numerical study of the calibration factors for the neutron counters in use at the Joint European Torus, Fusion technology, 24 (1993), 150-160.

3   Snoj L. et al., Calculations to support JET neutron yield calibration: contributions to the external neutron monitor responses, Nuc. Eng. Des., 246 (2011), 191-197

4   Snoj L. et al., Calculations to support JET neutron yield calibration: neutron scattering in source holder, Fus. Eng. and Des., 87 (2012), 1846–1852.

5   X-5 Monte Carlo Team, MCNP - A general Monte Carlo N-particle Transport code, Version 5, LA-UR-03-1987, (April 24, 2003/revised June 30 2004).

6   Snoj L. et al., Calculations to support JET neutron yield calibration: modelling of the JET remote handling system, Nuc. Eng. and Des., in press

7   M. Gatu-Johnson et al., Modelling and TOFOR measurements of scattered neutrons at JET, Plasma Physics and Controlled Fusion, 52 (2010), 085002.

APPENDIX A: CORRECTION FACTOR MATRIX

In order to present CFs for all FCs and NS positions we developed the concept of the correction factor matrix visualised in orthoimage visualisation mode. The matrix elements for each poloidal position k are calculated according to the formula (1), meaning that all 3200 correction factor values can be presented by using 5 correction factor matrices. Such a presentation is very valuable for understanding the nature of the effects. However it should be noted that many of the effects seen in the matrix are then smeared-out when calculating the importance-weighted correction factor, which is much smaller than individual correction factors presented in the matrix. The correction factor matrix for the central NS position is presented in *Figure 5*. This figure clearly shows the area (black and purple) significantly affected by the JET RHS for all NS positions. This is the area close to the RH entrance port in Octant 5. In addition it can be seen that D1 and D2 detectors are the most effected when the NS is around position 20 in Octant 5.
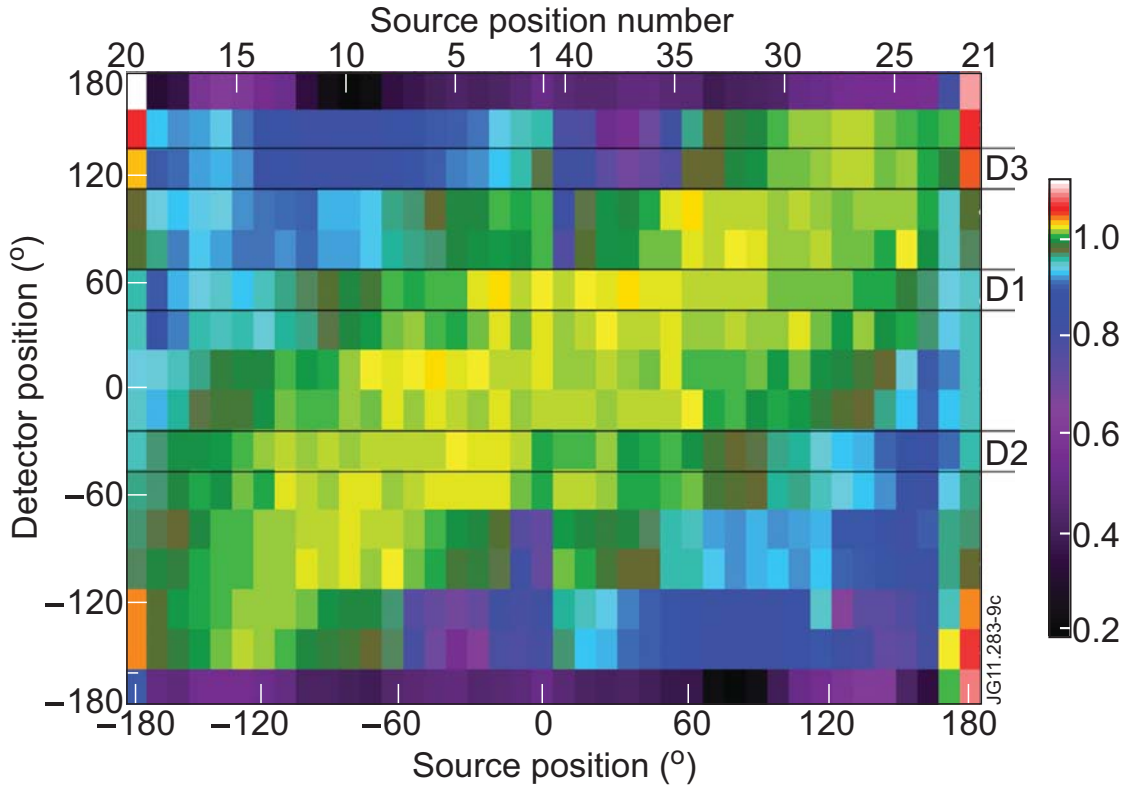

Figure 5: Correction factor matrix for the central NS position.

APPENDIX B: CORRECTION FACTOR DISTRIBUTION

In addition to the effect of the JET RHS on the external neutron monitor response we are interested in changes in the neutron flux distribution inside the torus hall due to the JET RH system. This was calculated by superimposing a mesh (500 × 500 × 10 ≈ length × width × height) over the model geometry and calculated the neutron flux in each of the mesh cells. For each NS position two calculations were performed with and without the JET RH system. The CF was then calculated by dividing the two meshes. The results for the central NS position are presented in *Figure 6*. In addition the JET RHS is visualised as well to enhance understanding. The NS is located at the end of the right arm of the JET RH system. Red and yellow areas in front of the mascot robot body indicate a 10-15 % increase in local neutron flux due to back-scattered neutrons. The green area covering more than half of the area denotes are where changes in neutron flux are lower than 5 %. The neutron flux in blue coloured areas is reduced mainly due to boom shadowing effects. Large depressions in neutron flux outside the RH entrance port in Octant 5 are also noticeable.

The results are as expected. When a port is shielded from the direct neutron flux by the RH Boom, the flux incident on the port is, of course reduced.
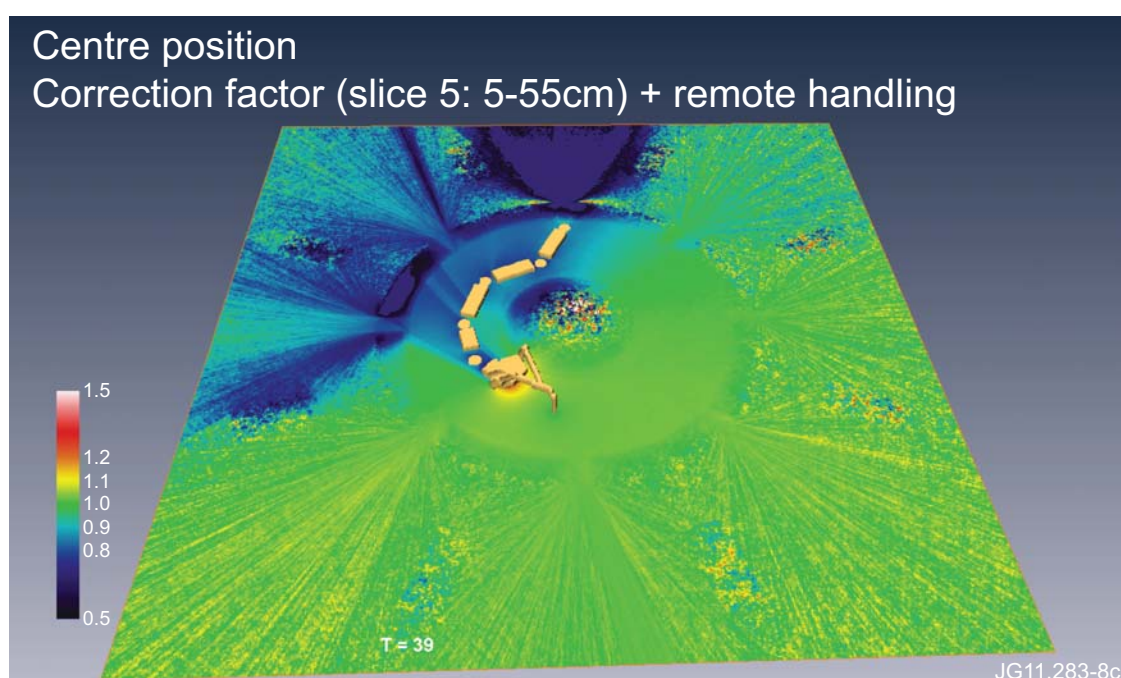

Figure 6: Correction factor distribution for the central NS position.

99

SHUTDOWN DOSE RATE AT JET WITH THE NEW ILW AND PREDICTION OF THE EXPECTED DOSE LEVEL AFTER FUTURE TRITIUM EXPERIMENT

I. Lengar, L. Snoj

Jožef Stefan Institute (IJS), Reactor Physics Department, Ljubljana, Slovenia
igor.lengar@ijs.si

1   INTRODUCTION

The activity was a joint work of the associations ENEA, KIT, CCFE and MESCS-SFA. The shutdown dose rate in the JET torus was determined experimentally, in parallel calculations have been done. The activity was a follow-up of past activities, performed over several years. Basically two different methodological approaches have been developed in the frame of the Fusion Technology Program for the three-dimensional calculation of the shutdown dose rate: the so-called Rigorous two-step method (R2S) developed by KIT and the Direct one-step method (D1S) developed by the ITER team and ENEA. Both methods, even if with different approaches, use the MCNP Monte Carlo Code for transport calculation and the FISPACT inventory code.

The aim of the present task is the measurement and corresponding calculation of the shutdown dose rate at short cooling times, more accurate with respect to the previous ones. Additional information on the main contributors to the doses is also obtained through gamma spectrometry. The goals are the validation of the shutdown dose rate calculation with the new ILW through dose measurements during 2012 off-operational period and estimation of shutdown dose rate following hypothetical DT irradiations in preparation of the future tritium experiment.

The task of the MESCS-SFA was the preparation/upgrade of the MCNP model for the calculations. The last version of MCNP model of Octant 1, used to estimate the preliminary effect of ILW in the frame of a previous task has been modified in order to include the description of relevant components (geometry and material).

2   WORK PERFORMED IN 2012

The task of JSI was the preparation of the MCNP model to be used by other associations, also collaborating on the project, for their calculations. Prior to the start of the project two MCNP models existed, which could be used, non of them was however satisfactory for calculations. The two models were:

- model of octant 1, including some ex-vessel structures like the KN3 and limbs. It was a model dating back to the year 2000, still containing the C-wall structures. Extent 45° with reflecting boundary conditions.

- model of octant 3, including mainly the in-vessel structures with emphasis on detail around the IE KN2-3U. It was a model updated to include the latest Be-wall in-vessel structures including Be limiters and the W divertor. Extent 90° with reflecting boundary conditions.

Both models are presented in Figure 1. During the task the new Be wall in-vessel structures from the octant 3 model were inserted into the octant 1 model where applicable.
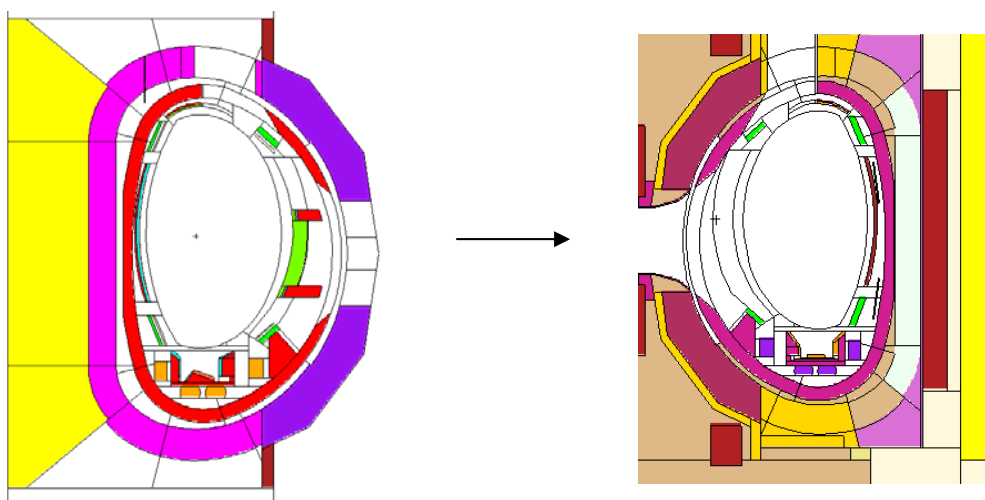
Figure 1: the models of Octant 3 (Be wall) and ocntant 1 (C wall).

The upgrade was done on hand of the data, obtained from CATIA files from the JET archive, which are the most complete set of information about torus components. The process is pictured in Figure 2.
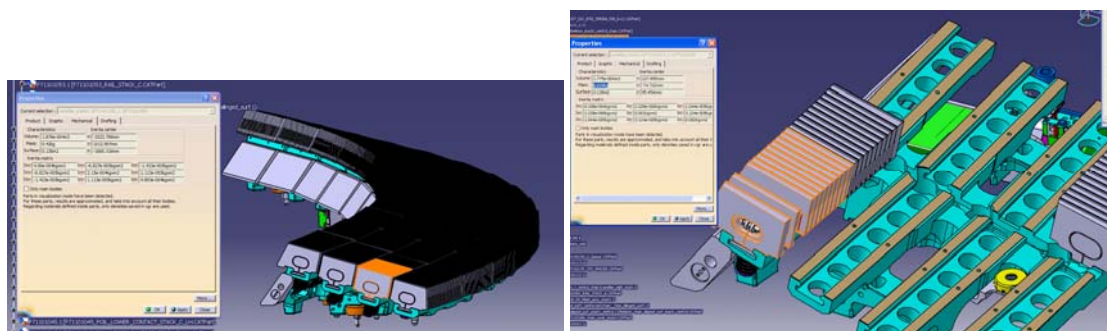
Figure 2: gathering data from CATIA; decomposition of larger components and analyzing individual parts.

It is visible from Figure 1, in which the MCNP models are pictured and from Figure 2 presenting the engineering drawing, that MCNP models are largely simplified with

respect to the latter ones. A lot of effort was thus invested into performing homogenization of geometry and materials starting from the study of CATIA files to the end product of the MCNP model.

The main changes, which have been introduced into the Octant 1 model, partly taken from the Octant 3 model, were:

- insertion of Be wall limiters
- insertion of the W divertor
- RF antenna
- detailed saddle coils
- detailed X guard, Z guard limiters

The following details had to bet taken into account during preparation of the model:

- the surfaces, if taken from the Octant 3 model, had to be properly rotated in order to fit into the Octant 1 geometry
- The cell and surface numbers of the newly inserted components start at a higher number in order to be compatible with previously changed models
- The model has been checked for lost particles

The final model is graphically presented in Figure 3.
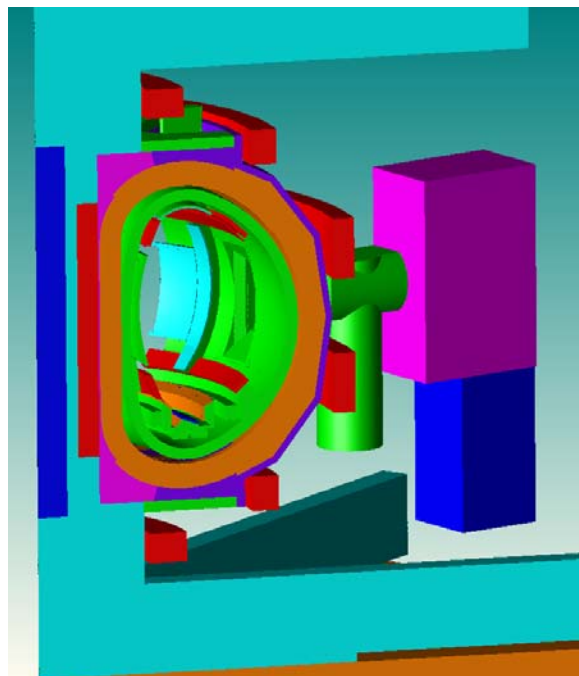
Figure 3: Graphical presentation of the final model (by MCAM graphical interface).

3   CONCLUSIONS AND OUTLOOK FOR 2013

The MCNP model of the Octant 1 of JET was further upgraded in order to be optimized for calculation of the shutdown doses, needed as support for the shut down dose measurements, carried out within the same project by ENEA and CCFE. The data needed for the upgrade was gathered from CATIA files and from already existing MCNP model of the Octant 3. Individual Be wall components (limiters, RF, LHCD,…) have replaced the components in the existing Octant 1 model, still featuring the C-wall.

3.1   Future work

The MCNP model will be, with regards to the experimental needs, further upgraded. The final calculations expected after the experimental data will be provided.

4   REFERENCES

1   Y. Wu, FDS Team, CAD-based interface programs for fusion neutron transport simulation, Fusion Engineering and Design, 84 (2009), pp. 1987 – 1992.

FABRICATION AND CHARACTERIZATION OF W-SIC COMPOSITES

Aljaž Iveković, Saša Novak

Jožef Stefan Institute, Jamova cesta 39, 1000 Ljubljana
sasa.novak@ijs.si

1   INTRODUCTION

Thermal conductivity is one of the critical properties limiting the use of SiC_f/SiC composites in future fusion power plants. By incorporation of high thermal conductivity (low activation) elements, thermal conductivity of the material could be improved, especially at high temperatures (600-1000 °C) proposed for operation. Tungsten (W), a material already utilised in the fusion reactor as the material of choice for the divertor applications might offer such improvement. Furthermore, W has been recognised as an active filler material and might contribute to faster densification of the material.

In addition, the knowledge on the interaction between W and SiC, that was identified as an issue in the case of W-cored SiC fibres produced by TISICS, is needed also to understand the stability of the proposed tungsten coating on SiC_f/SiC plates in the reactor, but it was also proposed that it could provide a possible way of joining.

2   WORK PERFORMED IN 2012

In order to establish the appropriate W-SiC ratio and evaluate the effect of W incorporation on mechanical and thermal properties, composite samples with various W-Si ratios were prepared by dry-pressing followed by polymer and pyrolysis or by slip-casting of W-powder in the pre-ceramic polymer. The samples were thermally treated at 1600°C and characterised for microstructure, phase composition (XRD), mechanical (bending strength, HV, elastic modulus) and thermal properties. With the aim to understand the interaction between both constituents, bulk samples were prepared by dry pressing of powder mixtures followed by impregnation by pre-ceramic polymer or by casting pre-ceramic polymer-powder mixtures into graphite dyes. The samples were pyrolysed at 1000 °C in Ar atmosphere and additionally heat treated up to 1600 °C. The bulk samples and the diffusion couples were cut and metallographically prepared for the analyses of cross-sections. In contrast to dry pressed W powder heat treated at 1600 °C (Figure 1a), which was not sintered, the polymer infiltrated sample of W powder was nearly completely densified after heat treatment (Figure 1b).
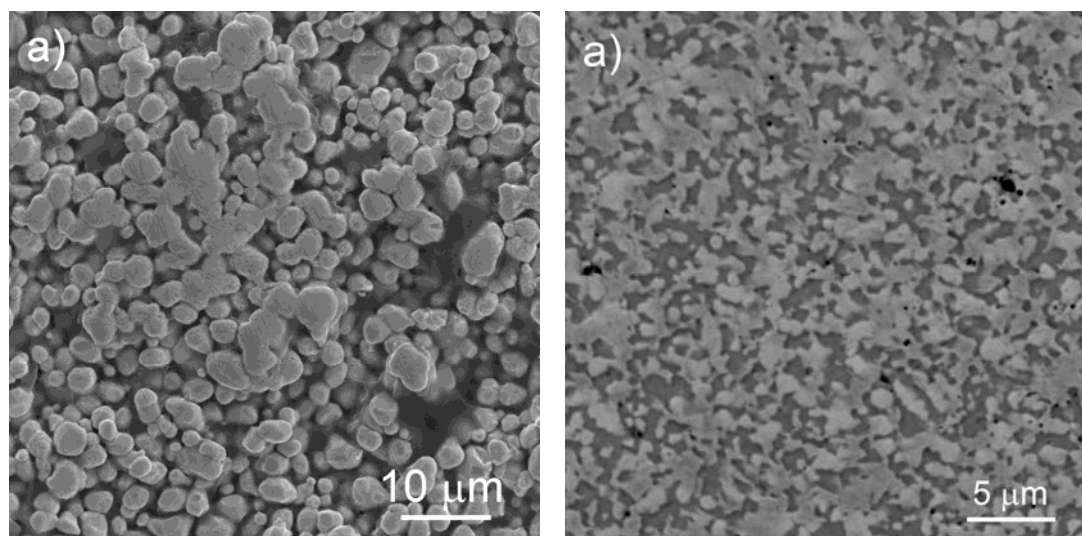
Figure 1: Polished cross sections of dry pressed matrix of a) W after heat treatment at 1600 °C and W and W-SiC mixture after polymer infiltration and pyrolysis process.

On the other hand samples with higher amount of SiC powder in the initial powder mixture exhibited poor densification and inhomogeneous microstructure with larger (~100 µm) W-rich or SiC-rich areas Figure 2.
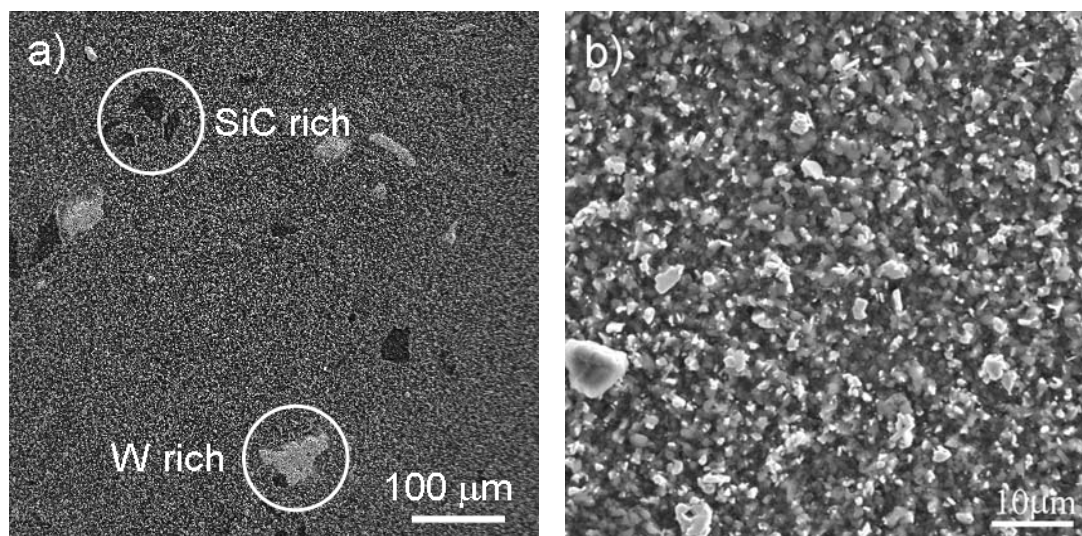
Figure 2: MIcrostructure of a W-SiC sample with 25 vol. % of W in the initial powder composition at different magnification.

The phase composition and the mechanical properties of the reaction zone in the contact of W and SiC were found to largely depend on the W-SiC ratio. XRD analysis revealed that high W content (>50 vol. %) results in a hard, dense material composed of W, W_2C and W_5Si_3. Samples with lower amount of W in the initial composition were composed also from WC and WSi_2. In the case of samples with low W content (< 25 vol. %) the tungsten metal was fully reacted to form WC and WSi_2. Tungsten metal was observed only in the samples with high tungsten content in the starting composition.

106
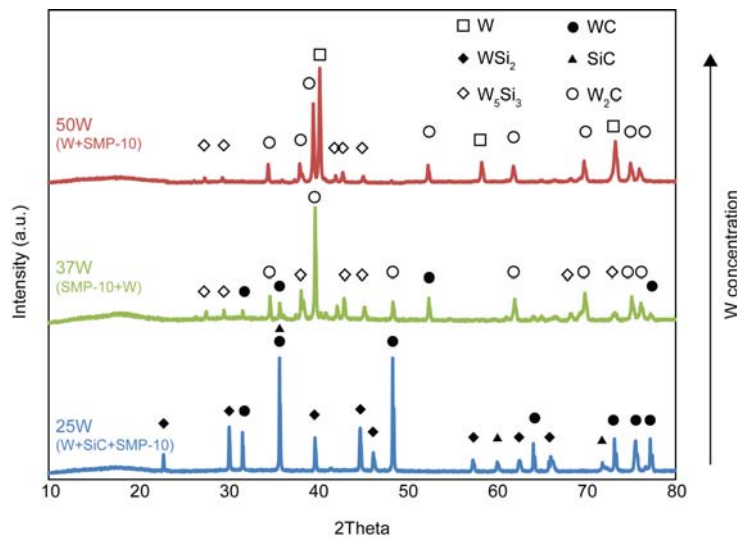
Figure 3: XRD spectrum of samples with different W-SiC ratio.

Flexural strength of samples with various W-SiC ratio was measured using biaxial piston-on-three balls test. As expected the samples with low amount of W exhibited very low values of flexural strength, due to poor densification. On the other hand, the samples with high W concentration (> 35 vol. %) exhibited higher strength up to ~350 MPa for sample with 50 vol. % of W in the initial sample composition.
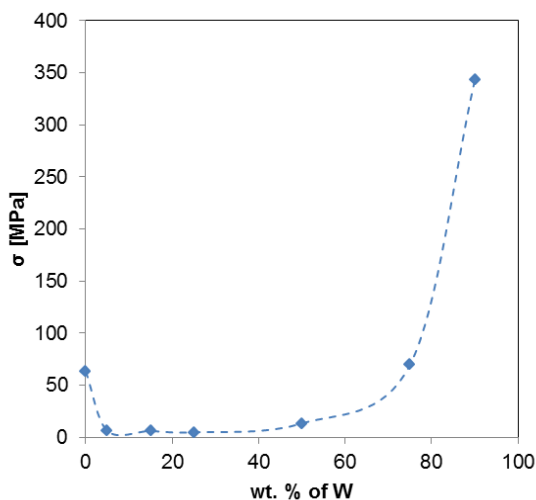
Figure 4: Flexural strength of samples as a function of W content in the starting composition.

Due to insufficient density of samples with low W content, only samples with high (50 vol %) W content were used for hardness testing using Vickers indentation. Nano-indentation was also used to evaluate harness and elastic modulus of the material. Both micro and nano-indntation gave comparable results in the range of 970-1090 HV. Elastic modulus was determined to be ~270 GPa.

Thermal diffusivity (α) of the material was measured at the National Institute of Materials Physics in Bucharest, in the range from room temperature to 1000 °C, using laser flash analysis (LFA 457, Netzsch, Germany). Thermal conductivity (λ) can be calculated from diffusivity measurements using a simple equation:

$$\lambda = \alpha \cdot \rho \cdot C_p$$

where ρ is the density of the material and C_p specific heat of the material. Density of the samples was measured using Archimedes method and heat capacity is measured simultaneously during thermal diffusivity measurements. Room temperature of all samples was lower than thermal conductivity of pure SiC densified at the same conditions. Interestingly, by increasing the amount of W the trend of thermal conductivity reduction at higher temperatures was reduced or even reversed for samples with 50 vol. % of W. This indicates that additional densification of samples with low W content by polymer infiltration and pyrolysis steps, might lead to a material with improved high temperature thermal conductivity. Furthermore additional heat treatment at 1700 °C further increased the diffusivity of the material due to densification and grain growth.
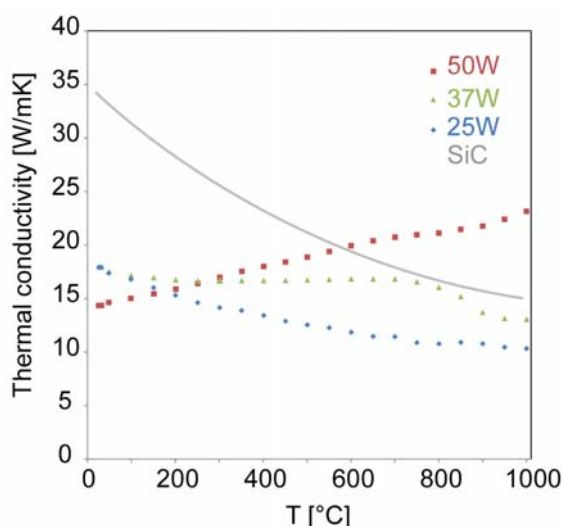
Figure 5: Thermal conductivity of samples with different W-SiC ratio as a function temperature.

2.1 Joining

Part of the experiments was performed in parallel at Politecnico di Torino in the frame of the 2.5 months scientific mission of S. Novak. The main objective of the work in collaboration with the group of prof. Monica Ferarris at Politecnico di Torino was to perform a feasibility study of the joining of fusion relevant SiC_f/SiC composites by employing a colloidal suspension of pre-ceramic polymer containing tungsten powder as an active and SiC powder as a passive fillers. The research work comprised a study of joints prepared by various procedures and using suspensions with different W and SiC loading as well as different W-SiC ratio.

The first results reveal that the W-polymer suspension well wets SiC-based ceramics and the wetting is also very good during the thermal treatment. This yields in a relatively good contact between the SiC_f/SiC and the joining material (Figure 6). However, in the first samples, large ellipsoidal shaped voids were observed within the joining material, presumably as a consequence of entrapped gas bubbles. Based on the observation of the bulk samples it was proposed that the viscoelastic properties of the W-polymer system is most probably the key parameter in formation of the voids: in the case of low viscous suspension, the gas produced during heating forms large voids, while in the case of high viscosity/viscoelasticity (e.g. polymer infiltrated W preform) it diffuses out without producing large voids.
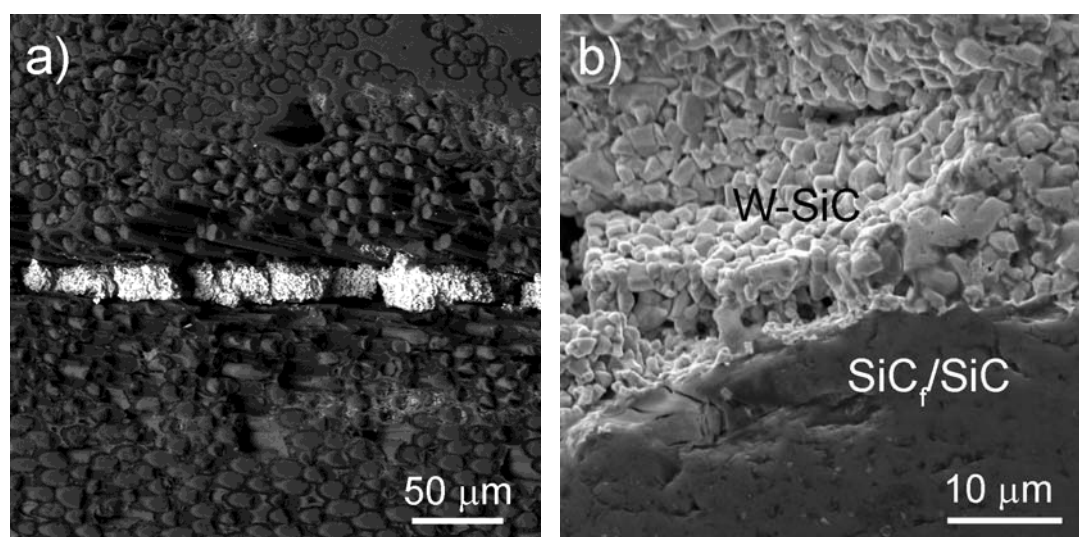
Figure 6: W-polymer joint between two SiCf/SiC bars.

2.2   Coating

The same W-SiC system was also proposed for the formation of a dense coating on SiC_f/SiC composite to prevent permeation of helium. W was deposited on a SiC substrate by electrophoretic deposition from ethanol suspension. Coatings up to 2 mm could be formed, however thicker coatings exhibited irregular surface morphology, most likely due to high density of W, which was detached from the surface due to gravity. Coatings were infiltrated by pre-ceramic polymer and heat treated to 1600 °C. After heat treatment most of the coatings was delaminated from the surface and only few areas could be found where there was contact of the coating and the substrate (Figure 7).
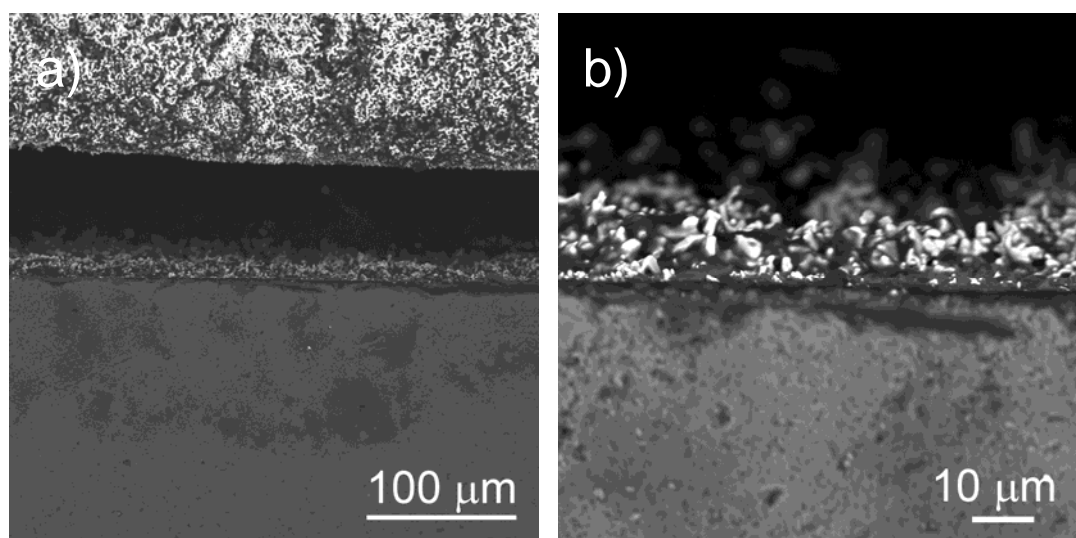
Figure 7: Delaminated W-SiC coating on SiC substrate a) and coating-substrate contact b).

3   CONCLUSIONS AND OUTLOOK FOR 2013

Initial investigation of the W-SiC composite densified by polymer infiltration and pyrolysis revealed that samples with high tungsten content (>50 vol. %) in the initial powder mixture can be densified in a single densification step at 1600 °C, which is a great advantage in comparison to densification of pure SiC material, which requires multiple PIP cycles in order to significantly densify the material. The material with 50 vol. % of W exhibited good mechanical properties (flexural strength of 350 MPa, harness of 970-1090 HV and elastic modulus of ~270 GPa). Room temperature thermal conductivity of such material was relatively low (~ 15 W/mK), however it exhibited an unusual increase of conductivity with temperature achieving ~ 25 W/mK at 1000 °C.

Joining of SiCf/SiC composites by W-SiC composite material remains a viable option, however further optimisation of the process is needed in order to prevent the formation of ellipsoidal voids.

In our further investigation we plan to investigate the effect of final temperature on mechanical and thermal properties of high tungsten content material (> 50 vol. % of W) and further densification of samples with low tungsten content (<35 vol % of W) followed by mechanical and thermal characterisation of the material.

3-D SIC/SIC COMPOSITES
PREPARED BY SITE-P PROCESS

Aljaž Iveković, Saša Novak

Jožef Stefan Institute, Jamova cesta 39, 1000 Ljubljana
sasa.novak@ijs.si

1 INTRODUCTION

In order to achieve sufficient shear strength and increase the through thickness thermal conductivity, 3D continuous fibre reinforcement is proposed for fabrication of SiC_f/SiC composites. In contrast to frequently used techniques of stacking 2D fabric, the fabrication of such composites is much more challenging. SITE process, a combination of electrophoretic infiltration (EPI) and polymer infiltration and pyrolysis (PIP) process, was introduced as an alternative to the existing state-of-art techniques (CVI, PIP, NITE). The SITE-SiC_f/SiC was characterised by high thermal conductivity in comparison to other techniques[1], due to high crystallinity and favourable microstructure (no oxide phase, small pore size, large grain size). However, further research and development is needed in order to properly characterise the material.

2 WORK PERFORMED IN 2012

2.1 Upscaling

In 2012 the main focus was on fabrication of larger samples which would enable fabrication of samples for mechanical testing and evaluation of flexural strength and toughness of the material Since both processing steps used in SITE process (electrophoretic infiltration-EPI and polymer infiltration and pyrolyis – PIP) are basically independent of sample size, only minor adjustments to the experimental setup and processing conditions had to be made. Higher constant current was applied during electrophoretic deposition in order to maintain the same current density during infiltration. Likewise, the experimental system for polymer infiltration was modified to enable infiltration of larger samples.
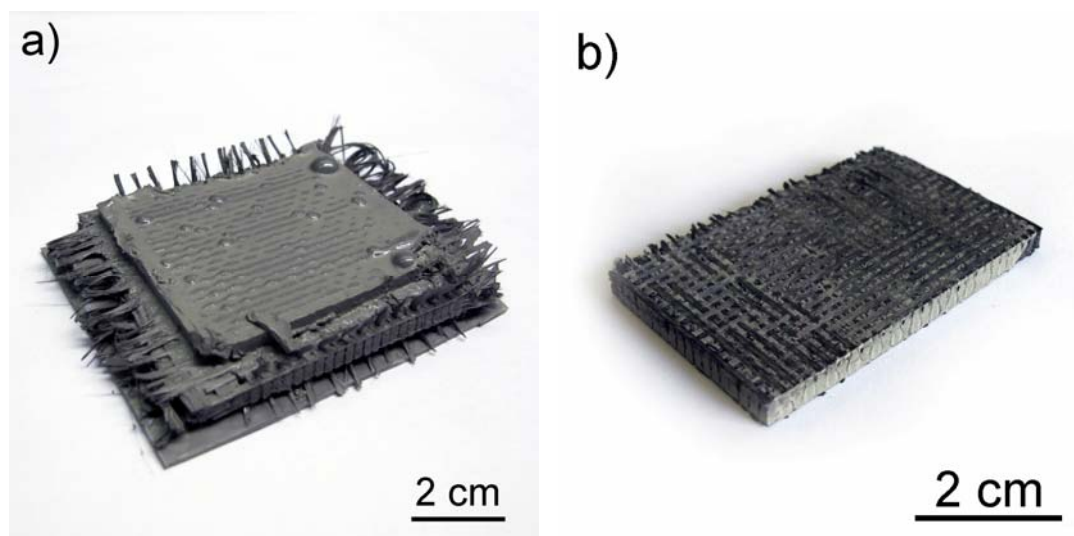
Figure 1: As deposited SiCf/SiC composite and SITE-SiC/SiC composite after one densification step (EP1).

2.2   Evaluation of porosity

Densities of green deposits and samples after densification were measured using Bulk Density Measurement System (Densitec, Exelia AG, Switzerland) based on the Archimedes principle in silicone oil (M350, Carl Röth Gmbh, Germany). Porosimetry measurements were performed using a Hg-intrusion porosimeter (Pascal 140 / 440, Thermo Scientific, USA) in the range of 100 kPa-400 MPa. Pore size and distribution of the material was also characterised by 3D X-ray computed tomography (CT) at Henry Moseley X-ray Imaging Facility at University of Manchester. Imaging was performed on disk shaped sample with diameter of 10 mm and 4 mm thickness, using the Nikon Metris 320 kV custom bay.
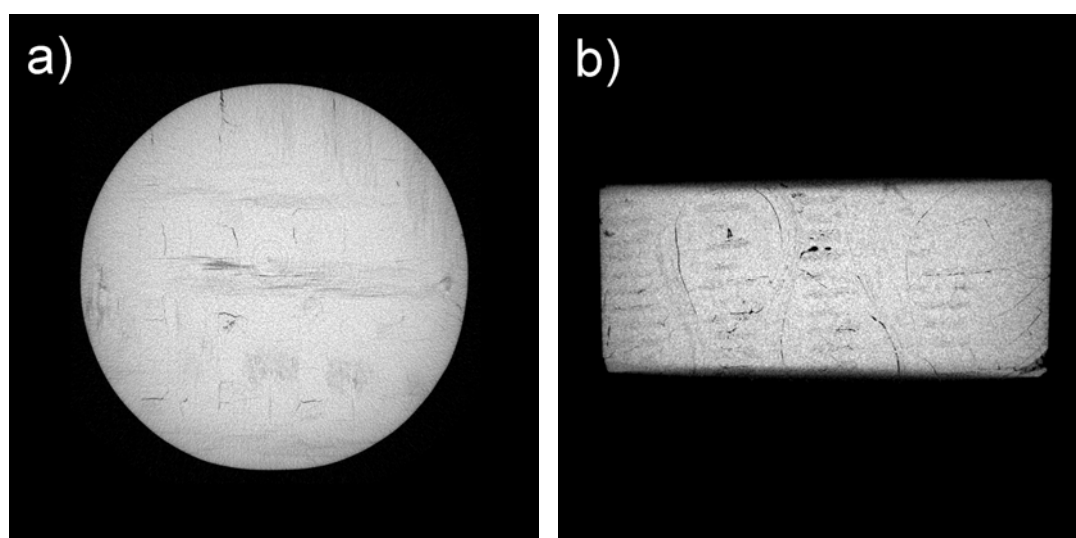
Figure 2: CT single slices of SITE-SiCf/SiC composite in a) x-y direction and b) x-z direction.

2.3   Mechanical properties

Research conducted on bulk SiC matrix fabricated by SITE process revealed that by using higher heat treatment temperature also the strength of the material is improved. Samples densified at higher temperature (1700 °C) exhibited more uniform failure behaviour. After six PIP cycles (EP6) the average strength of the samples densified at 1600 °C was 230±160 MPa and for samples densified at 1700 °C, 336.6±74.6 MPa, with highest measured value of 411.2 MPa. The effect of higher heat treatment was less pronounced in the measurements of Vickers hardness and elastic modulus. Samples densified at 1600 °C or 1700 °C exhibited nearly the same values of elastic modulus. From initial value of 70 GPa after one PIP cycle, elastic modulus was increased up to 260 GPa after six PIP cycles. Microhardnes measurements of samples heat treated at 1600 °C also show an increase with density. From initial value of ~390 HV after one PIP cycle the value was increased to 2300 HV after six PIP cycles respectively. In the case of samples densified at 1700 °C, hardness values after one PIP cycle were comparable to the ones densified at 1600 °C. After additional densification, values of microhardness were slightly lower than for the samples densified at 1600 °C achieving 1740 HV after three and six PIP cycles respectively.
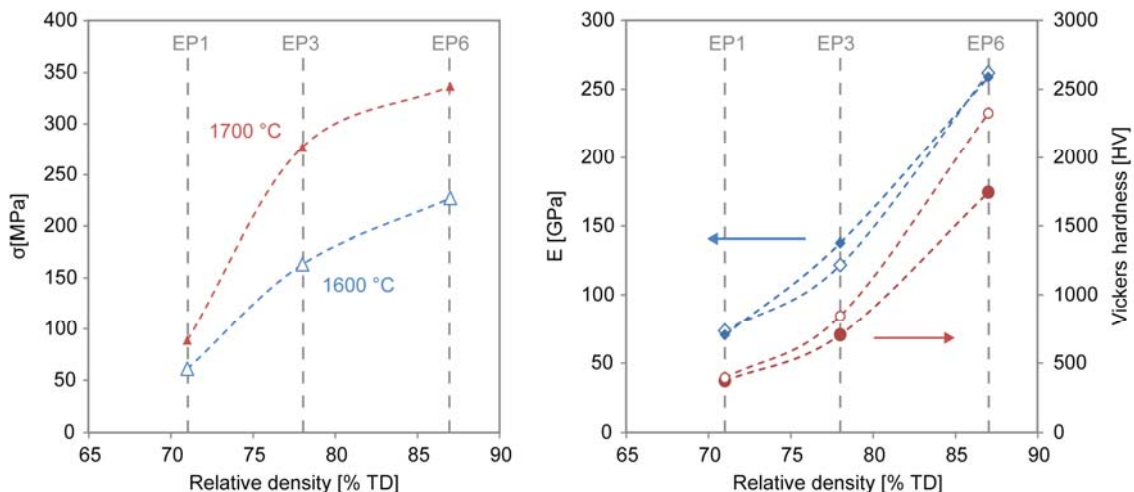
Figure 3: Evolution of flexural strength, Young's modulus and Vickers hardness measured at room temperature. Open symbols represent samples densified at 1600 °C and full symbols represent samples densified at 1700 °C.

Initially the composite mechanical testing was planned to be conducted at NRG in Petten (Nederlands), however due to relocation of their reference laboratory, an alternative measuring facility had to be identified. Within EFDA collaboration with Universidad Politechnica de Madrid was established and in November samples were sent for mechanical characterisation. Flexural strength measurements were performed in vacuum and in air up to 1400 °C. The initial results were between 60 and 90 MPa regardless of the measured atmosphere and the properties were retained up to 1400 °C.
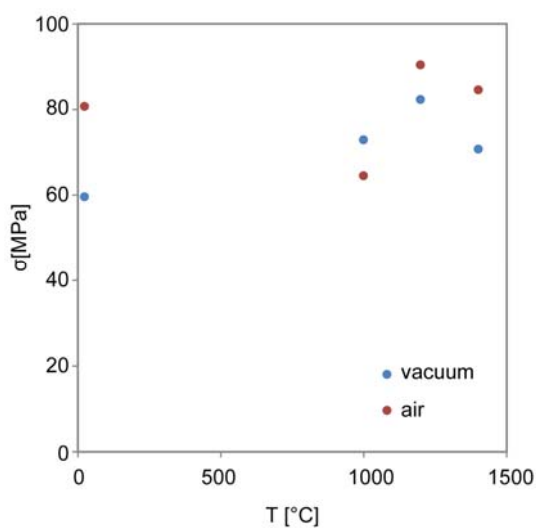
Figure 4: Flexural strength of SITE-SiCf/SiC composite densified at 1700 °C as a function of temperature in vacuum and in air.

Low values of flexural strength in comparison to other reported values [1] were attributed to the lack of interphase layer, which appears to react with polymer decomposition products and forms carbon-rich SiC layer. Furthermore, due to inexistance of the interphase layer, after annealing at 1700 °C the reinforcing fibres were sintered together, most likely in the consecutive polymer infiltration and pyrolysis cycles. Sintered fibres no longer acted as a reinforcing phase and the material behaved as a porous bulk ceramic. Therefore, a more stable interphase layer is essential in order to protect the fibres and to obtain a material with desired mechanical properties.
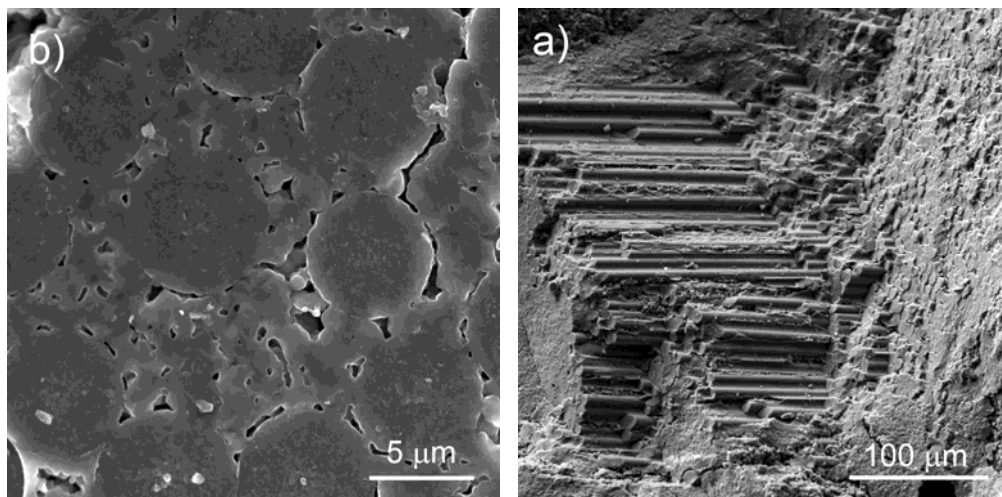
Figure 5: Fracture surface of SITE-SiCf/SiC at different magnification.

2.4   Thermal conductivity

SiC$_f$/SiC composite prepared by SITE-P process is among the materials with the highest reported thermal conductivity [1] and is well above the design assumed value set

114

for this material for use in structural applications in fusion reactor chamber [2]. However, since thermal conductivity of SiC based composites will inevitably be reduced after neutron irradiation [3] and might even limit the use of such materials, a need for even higher thermal conductivity remains. Higher processing temperature should result in a larger grain size and consequently higher (room temperature) thermal conductivity. Surprisingly, the SITE-SiCf/SiC densified at higher temperature of 1700 °C, exhibited slightly lower values than material densified at 1600 °C.
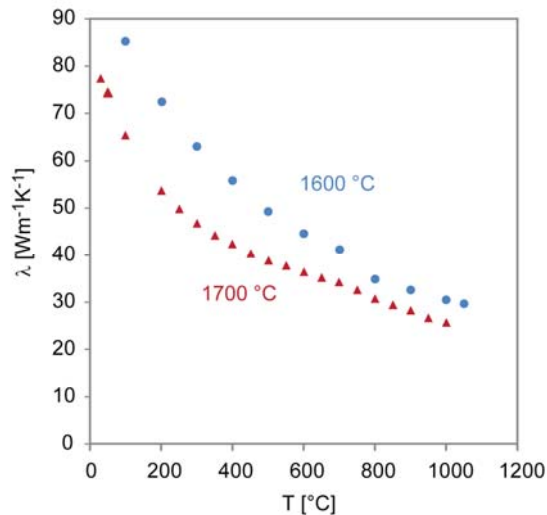
Figure 6: Thermal conductivity of SITE-SiCf/SiC densified at maximal temperature of 1600 °C and 1700 °C

2.5   Investigation of permeability

In collaboration with Department of Surface Engineering and Optoelectronics (F-4) of Jožef Stefan Institute we conducted preliminary tests of He permeability. Bulk SiC samples densified by solid state sintering at 2100° C in vacuum, with addition of B and C, were used as a model system.Tests revealed that measuring techniques previously developed and well established at the F-4 department are not suitable for testing of the SiCf/SiC composite samples. Therefore efforts were made to construct a new measuring system (Figure 2) based on the bubble point test which enables also determination of larger pores and permeability of the material. After resolving the initial problems of sealing (standard sealing procedure resulted in cracking of samples), the permeability of the samples was determined to be $1.7–2.1\times10^{-3}$ cm^2/s. The goal of the experiment was to fabricate and properly evaluate a closing layer, to prevent He permeation, which is one of the requirements of the material [2]
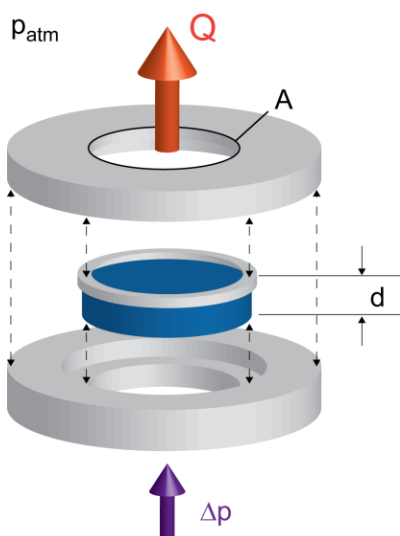
Figure 7: Schematic representation of the measuring system.

3   CONCLUSIONS AND OUTLOOK FOR 2013

Upscaling of the process was successfully demonstrated by fabrication of larger specimens (5×5 cm). The maximal dimensions of the specimens was determined by the size of available fibre preform, however, providing a larger preform, also larger pieces could be produced. The effect of increasing maximum processing temperature from 1600 °C to 1700 °C on the properties of SITE-SiC$_f$/SiC was investigated. In bulk SiC matrix samples the increase in processing temperature had a positive effect on the mechanical performance of the matrix material, increasing the flexural strength after six PIP cycles from 230±160 MPa to 336.6±74.6 MPa. Interestingly the effect of higher heat treatment temperature had a negative effect on the measured thermal conductivity of the SiTE-SiC$_f$/SiC, nevertheless, the measured values were still high in comparison to other fabrication techniques.

4   REFERENCES

1   A. Iveković, S. Novak, G. Dražić, D. Blagoeva, S.G. de Vicente, Current status and prospects of SiCf/SiC for fusion structural applications, Journal of the European Ceramic Society, 33 (2013), 1577-1589.

2.   D. Maisonnier, I. Cook, P. Sardain, P. R. Andreani, L. D. Pace, R. Forrest, L. Giancarli, S. Hermsmeyer, P. Norajitra, N. Taylor, D. A. Ward, A Conceptual Study of Commercial Fusion Power Plants: Final Report of the European Power Plant Conceptual Study (European Fusion Development Agreement, Garching, 2005).

2.   Y. Katoh, T. Nozawa, L. L. Snead, K. Ozawa, H. Tanigawa, Stability of SiC and its composites at high neutron fluence, Journal of Nuclear Materials, 417 (2011), 400-405.

THERMAL-HYDRAULIC ANALYSES OF ALTERNATIVE HE-COOLED DIVERTOR CONCEPTS

Boštjan Končar

Jožef Stefan Institute, Jamova cesta 39, 1000 Ljubljana, Slovenia
Bostjan.koncar@ijs.si@ijs.si

1   INTRODUCTION

Helium has a number of advantages that makes it attractive as IVC-coolant apart from a possible high outlet temperature, namely its chemical compatibility with all the fusion materials and the possibility to accommodate the coolant temperatures to the various operational windows of the materials. However, compared to ITER-like water-cooled divertor targets helium-cooled divertor targets seem to have lower heat flux removal capability.

Therefore the main objective of our research was to investigate alternative He-cooled divertor target concepts for updated design requirements in an early DEMO. The requirements assumed in the past for the He-cooled multi-finger divertor target concept include [1]:

- High helium outlet temperature (~700°C).
- Heat flux capability: 10 MW/m² - 1000 heat cycles.

For an "early DEMO" it would be preferable to operate at lower temperature, simplifying the technology of the reactor systems and balance of plant. Similar temperatures as in the He cooled blanket systems would be in this context an advantage. The high helium outlet temperature defined previously in the frame of the PPCS is not only due to the high thermal efficiency but also due to the relatively narrow operating temperature window of the current thimble material (WL10), which is limited downward by the Ductile to Brittle Transition Temperature (DBTT). With reference to the existing multi-finger concept all design features (with the exception of coolant and armour material) may be changed, including materials for the thimble, brazing and cooling channel.

2   WORK PERFORMED IN 2012

The research activities in 2012 were carried out in the framework of the PPP&T programme, workpackage Design Assessment Studies (DAS), Task DAS02-T06. The main objective of the task was to perform thermal-hydraulic analyses of alternative cooling finger designs in terms of material choice and geometry of the tile.

In the frame of this study, two assumptions of the peak heat flux were examined, 10 MW/m2 and 8.7 MW/m2, where the lower assumption is based on the relaxed

parameters of the "early-DEMO" study [11]. The scoping analyses were carried out in two directions. In the first case the alternative material (T-111) for the thimble with a much lower DBTT was investigated that allow a reduction of the coolant temperature and a better operational temperature window of the materials (e.g. steel). Thermal loading of the finger structures and pressure drop in the cooling channel are compared with the existing design [2] at high helium temperature. In the second case, the alternative finger geometries (the hexagonal finger being the reference) at high helium outlet temperature were investigated. These analyses are performed as a cross-border activity with DAS-02-T05 from the perspective of shadowing of the target plate edges against damage caused by the incident particles.

The work was carried out in cooperation with the Karlsruhe Institute of Technology (KIT) - Institute for Applied Materials-Materials Processing Technology.

3 LOW TEMPERATURE HELIUM COOLING USING T-111 AS A THIMBLE MATERIAL

In order to cool the divertor with lower helium inlet temperatures, the minimum temperature limit of the thimble material facing the coolant has to be reduced. The minimum allowable temperature of the material is dictated by the Ductile to Brittle Temperature (DBTT). The thimble in the reference design is made of tungsten alloy WL10, where DBTT under irradiated conditions is limited to 700 $^\circ$C [3]. The temperature windows of divertor structure materials are shown in Figure 1. The full coloured bars represent the temperature windows of the reference HEMJ materials and coolant. Due to the high DBTT of the WL10, the thimble has to be cooled with the high temperature helium flow, where and the inlet temperature should not be below 600°C. Alternatively, a material T-111 is proposed for the thimble structure. The DBTT of the Tantalum based alloy doped with 8% of tungsten and 2% of hafnium is however much lower: 420 $^\circ$C under irradiation [4]. Its temperature widow is represented with a hatched red bar in Figure 1. As a consequence, the He inlet temperature can be reduced to 400 $^\circ$C (blue hatched bar in Figure 1).

The tantalum-based alloy T-111 [5] was developed in early sixties for space power applications and was commercially produced until early seventies. The development work on refractory metals was then stopped due to suspension of funding and the decision to use surface ceramic tiles instead of refractory metals for the space power systems. The T-111 is presently not being produced due to lack of demand, which could pose some serious problems in order to establish reliable production. The alternative could be also the alloy T-222 with 10% of W, 2.5% of Hf and 0.01% of C, but T-222 is not investigated in this task. The alloy T-222 is commercially available, but there is much less information on its material properties as for the alloy T-111.
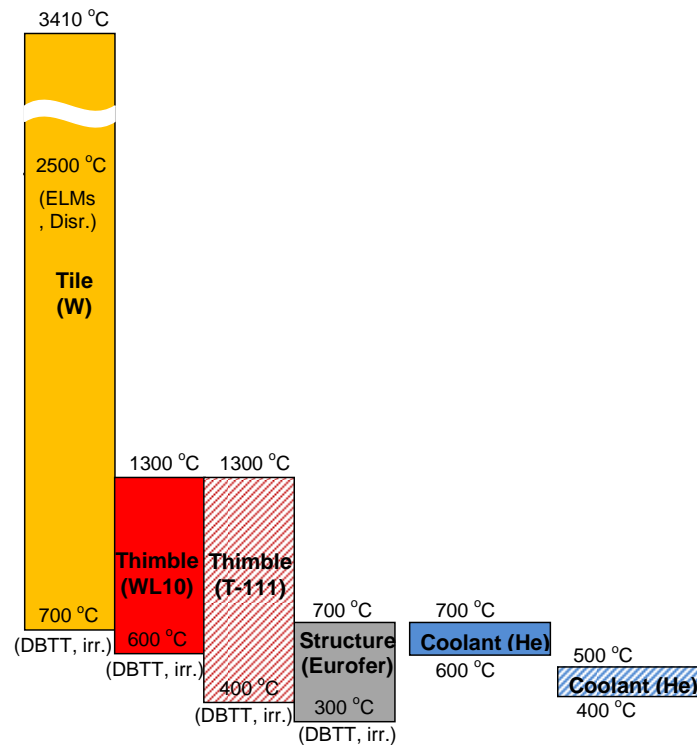
Figure 1: Design temperature windows.

Thermal conductivity and heat capacity of different materials (all considered as possible candidates for the divertor structures) are compared in Figure 2. As shown, the thermal conductivity of T-111 [5],[6] is much lower than in the case of pure tungsten (W) and tungsten alloy (WL10).
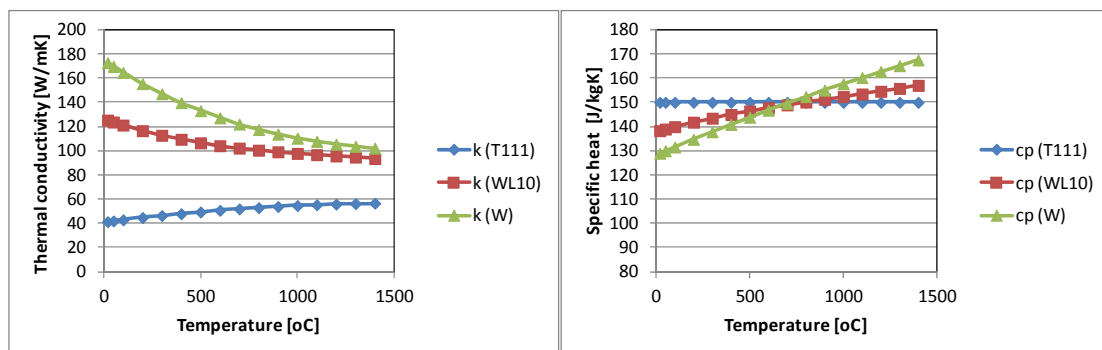
Figure 2: Comparison of thermal conductivity and specific heat for different materials.

3.1   CFD model and boundary conditions

A steady-state CFD analysis using ANSYS-CFX [7] was performed to compute the flow fields in the helium coolant and temperature distributions in finger structures. Numerical domain consisted of 3 solid domains (tile, thimble and cartridge) and of one fluid domain. Heat transfer equations in fluid and solid domains were solved simultaneously. In the fluid domain, the helium was modelled as an ideal gas. Shear stress transport (SST) two-equation turbulence model [8] was used to resolve turbulence

and heat transfer scales in the helium flow. In the solid domain the heat conduction equation was solved. Details of the modelling approach are extensively described in [9].

Uniform heat flux was applied at the upper surface of the tile and adiabatic boundary conditions are assumed at the outer walls. Helium flow enters the cartridge at the constant mass flow rate. The reference boundary conditions (see Table 1) are such as anticipated in the EU PPCS Model C study [1].

The HEMJ finger [2] with a hexagonal shape of the tile was used to confront the results of the reference case with the WL10 thimble material against the Ta-based thimble material and low helium cooling. Comparison of implemented boundary conditions for the two cases is shown in Table 1. Helium inlet velocity is dictated by its inlet temperature. Although the inlet mass flow rate is the same for both cases, the average inlet velocity decreases with a lower inlet temperature as a consequence of higher density (7 kg/m3 at 400 oC) [10].

Reference case (Thimble WL10)	*Thimble T-111*
Mass flow rate = 6.8 g/s (per finger)	6.8 g/s (per finger)
<U inlet> = 17.95 m/s	13.36 m/s
Pressure = 10 MPa	10 MPa
Heat flux = 10 MW/m^2	10 MW/m^2
Internal heat generation = 17 MW/m^3	17 MW/m^3
He inlet temperature = 634 ^{o}C	400 ^{o}C
He density = 5.23 kg/m^3	7.02 kg/m^3

Table 1: Boundary conditions

3.2   Results

Simulations were performed in the steady-state mode using at least 500 iterations to reach the converged solution. All computational domains (1 fluid and 3 solid domains) were meshed with hexahedral elements which amounts to the mesh with 13.5 million elements for the full-scale finger model.

Comparison of main simulation results for both cases is presented in Table 2. Due to the lower helium temperature, the maximum thimble temperature for the Ta alloy is about 100 ^{o}C lower and does not exceed 1100 ^{o}C. As a consequence of lower helium temperature, the jet velocities are much lower and contribute to significant reduction of the pressure drop (for more than 25%) comparing to the reference case.

Reference case (Thimble WL10)	*Thimble T-111*
Max Tile temp= 1783 ^{o}C	1653 ^{o}C
Max Thimble temp= 1201 ^{o}C	1096 ^{o}C
He outlet temp= 712 ^{o}C	480 ^{o}C
Pressure loss= 122.5 kPa	92.3 kPa
Max He jet velocity= 245 m/s	182 m/s

Table 2: Results summary

120

To analyse the wider range of T-111 material response, the temperature loading for the finger structures was investigated also for higher inlet temperatures (450 ^{o}C, 500 ^{o}C) and two other tile geometries (small and large square described in the following section 4). The results are shown in Figure 3. As may be observed, the maximum temperatures of the thimble and tile for the small-square finger (16.5 mm edge) are almost the same as for the hexagonal tile. However, the structure temperatures significantly increase in the case of larger square-edged tile (17.8 mm). The maximum tile temperature is about 130 ^{o}C higher than for the hexagonal tile, whereas the thimble temperature maximum is higher for about 60 ^{o}C. As shown, tile and thimble temperature peaks increase linearly with the increased inlet helium temperature. The thimble temperature exceeds the allowable temperature (1200 ^{o}C) for the large square finger at 500 ^{o}C of inlet temperature.

Recent data for DEMO-1 [11] indicate that the maximum surface heat flux can be reduced to 8.7 MW/m^2. Referring to the related design description report of Norajitra et al. [12], 4 sensitivity cases with the reduced heat flux (8.7 MW/m^2) were additionally calculated for hexagonal finger only. Namely, as there is no reliable data for the material T-111 under irradiated conditions, a parametric study varying the inlet temperature from 450 ^{o}C to 650 oC was made to cover the estimated uncertainty range of DBTT irradiation values. Boundary conditions and results for the calculated "low heat flux" cases are listed in Table 3. According to [12], the case A with 450 ^{o}C of inlet helium temperature denotes optimistic assumption, case B (550 ^{o}C) moderate-optimistic and case C (650 ^{o}C) pessimistic assumption. The fourth case refers to the reference design with WL10 thimble but with heat flux 8.7 MW/m^2.

	mfr [g/s]	$T_{He,inlet}$ [°C]	T_{max} tile [°C]	T_{max} thimble [°C]	$T_{He,outlet}$ [°C]	Pressure loss [kPa]
A (T-111 hexa)	6.8	450	1527	1048	519	96.8
B (T-111 hexa)	6.8	550	1624	1135	619	110.5
C (T-111 hexa)	6.8	650	1721	1225	719	123.9
WL10 hexa87	6.8	634	1627	1127	704	121.7

Table 3: Examined cases at the heat flux 8.7 MW/m^2.

As can be observed in Figure 3, the temperature curves for lower heat flux are shifted downwards comparing to the cases with a higher heat flux (10 MW/m^2).
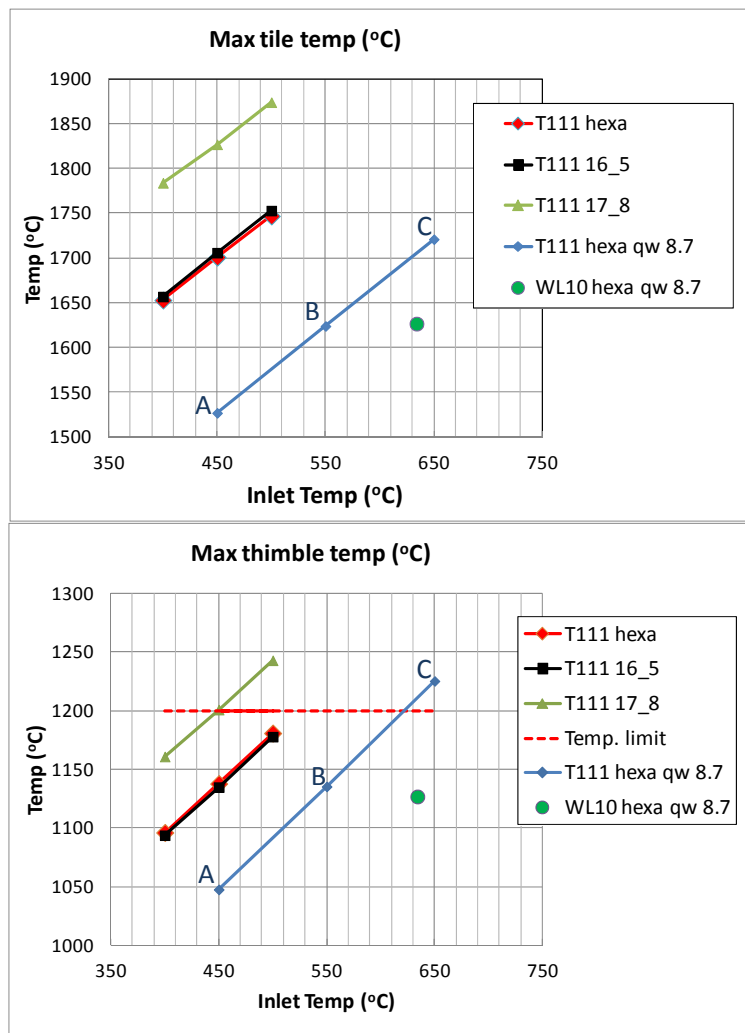
Figure 3: Maximum tile and thimble temperatures

4 ALTERNATIVE FINGER DESIGNS FOR THE TOROIDAL EDGE OF THE TARGET PLATE

Reference shape of plasma-facing tiles on the plasma-facing side of the target plate is hexagonal [2], which ensures relatively uniform cooling and can be compactly assembled together. However, to keep the necessary tilt angle of the target plate in toroidal direction as small as possible, the edge fingers at the plate boundary should ideally form a flat surface. This should help to prevent damaging of the plate edge due to incident particles. As the target plate is assembled of hexagonal tiles, it cannot form a flat closing boundary. Therefore, different design of boundary elements is of great importance. One possibility is to attach pentagonal elements to the hexagonal tiles (see Fig. 7 left). Another option is to completely replace hexagonal elements with square fingers (Fig. 7 right).

Three possible cooling finger geometries were investigated: pentagonal fingers and two square fingers with different edge lengths, all cooled by the same type of concentric cartridge. Their heat transfer performance is analyzed in a view of maximum temperature of the thimble material and compared to the results of the reference

hexagonal finger. The computational fluid dynamics (CFD) analyses of these different edge elements were performed in order to obtain the minimum mass flow rate of the coolant which is necessary to keep the structure's temperature below the allowable limit.
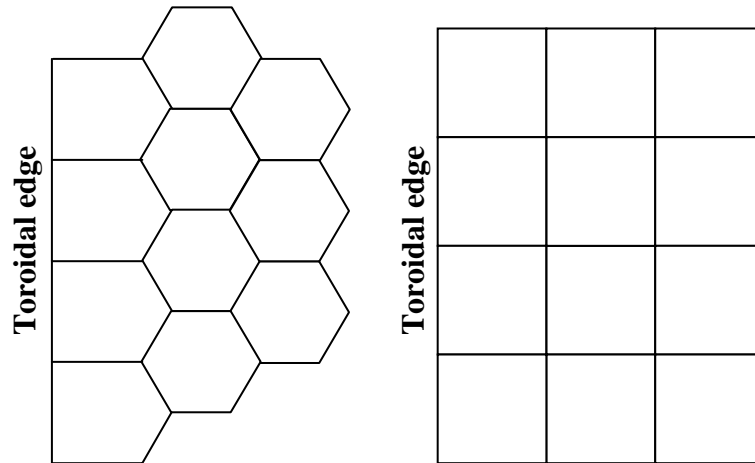
Figure 4: Possible finger assemblies for the target plate with the formation of a flat toroidal edge.

4.1 Analyzed designs

Different geometries of tested cooling fingers are shown in Figure 5. Having in mind the toroidal edge of the target plate, the following geometries were investigated: hexagonal finger (reference design), pentagonal finger square finger with 16.5 mm edge and square finger with 17.8 mm edge. Thimble and cartridge are the same for all cases only the tile shapes are different. To see all parts of the cooling finger (cartridge, thimble and tile), the schematic finger cross sections are shown.
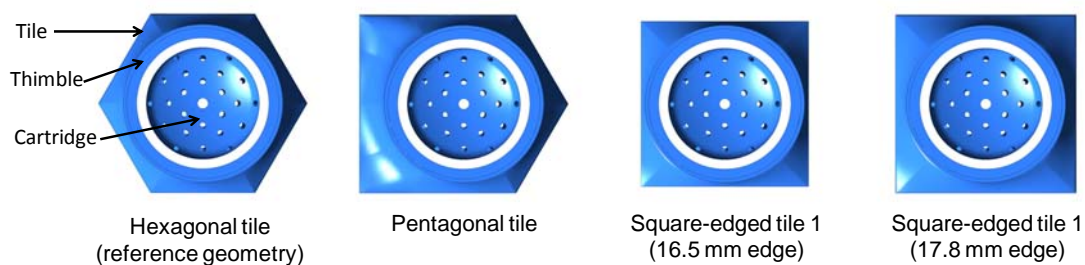
Figure 5:assessed cooling finger geometries.

Here, the main objective is to calculate the limiting mass flow rate for each of the tested finger geometries. At the limiting mass flow rate the cooling finger has to withstand the heat flux of 10 MW/m^2 under the condition that the maximum thimble temperature remains below an engineering limit of 1200 $^{\circ}$C. This value is set on the basis of re-crystallization temperature (RCT) of the thimble material WL10, which is estimated to be 1300 $^{\circ}$C under the neutron irradiation and reduced for additional 100 $^{\circ}$C to consider the necessary safety margin.

4.2   Results and discussion

Simulated temperature distributions of different finger geometries at the nominal mass flow rate of 6.8 g/s are presented in Figure 6. Temperatures of the tile's top surface are shown on the left side of Figure 6. For all tested fingers the highest temperatures appear at the corners of the tile, where the structure thickness or the heat flow path (i.e. the thickness in the direction perpendicular to the inner surface of the thimble) is the largest. The lowest temperature maximum is obtained for the reference hexagonal finger (1783 ^{o}C). A very good result is obtained also for the smaller square-shaped finger, which has only 12 ^{o}C higher temperature maximum than the hexagonal one. As expected the most unfavourable results were obtained for the unsymmetrical pentagonal finger, where the temperature maximum reached almost 2000 ^{o}C. Very likely, such high temperature peak is induced by the eccentric position of the thimble. It can be assumed that positioning of the thimble and cartridge towards the gravity center of the pentagon would reduce the maximum thimble temperature.

Temperatures for the thimble top surface are shown on the right side of Figure 6. Except for the pentagonal finger, in all other cases, the maximum temperatures occur at the center of the thimble. The lowest temperatures, just at the temperature limit for the thimble material (1200 ^{o}C) are calculated for two geometries – hexagonal and smaller square-shaped finger. This means that both fingers could be cooled efficiently at the reference mass flow rate of 6.8 g/s, which amounts to a relatively low pressure drop of around 120 kPa. The thimble temperature peaks are too high for the other two geometries at the same mass flow rate; 1256 ^{o}C for the larger square (17.8 mm) and even 1306 ^{o}C for the pentagonal geometry.

To determine the so-called limiting mass flow rate, the simulations for each of the test geometries were performed at 3 different mass flow rates (6.8 g/s, 9 g/s and 13.5 g/s). The limiting mass flow rate for the specific design is defined as the mass flow rate at which the maximum temperature of the thimble reaches 1200 ^{o}C. From top to the bottom of the Figure 7, the variations of maximum thimble temperature, tile temperature and pressure drop with respect to the mass flow rate are presented.
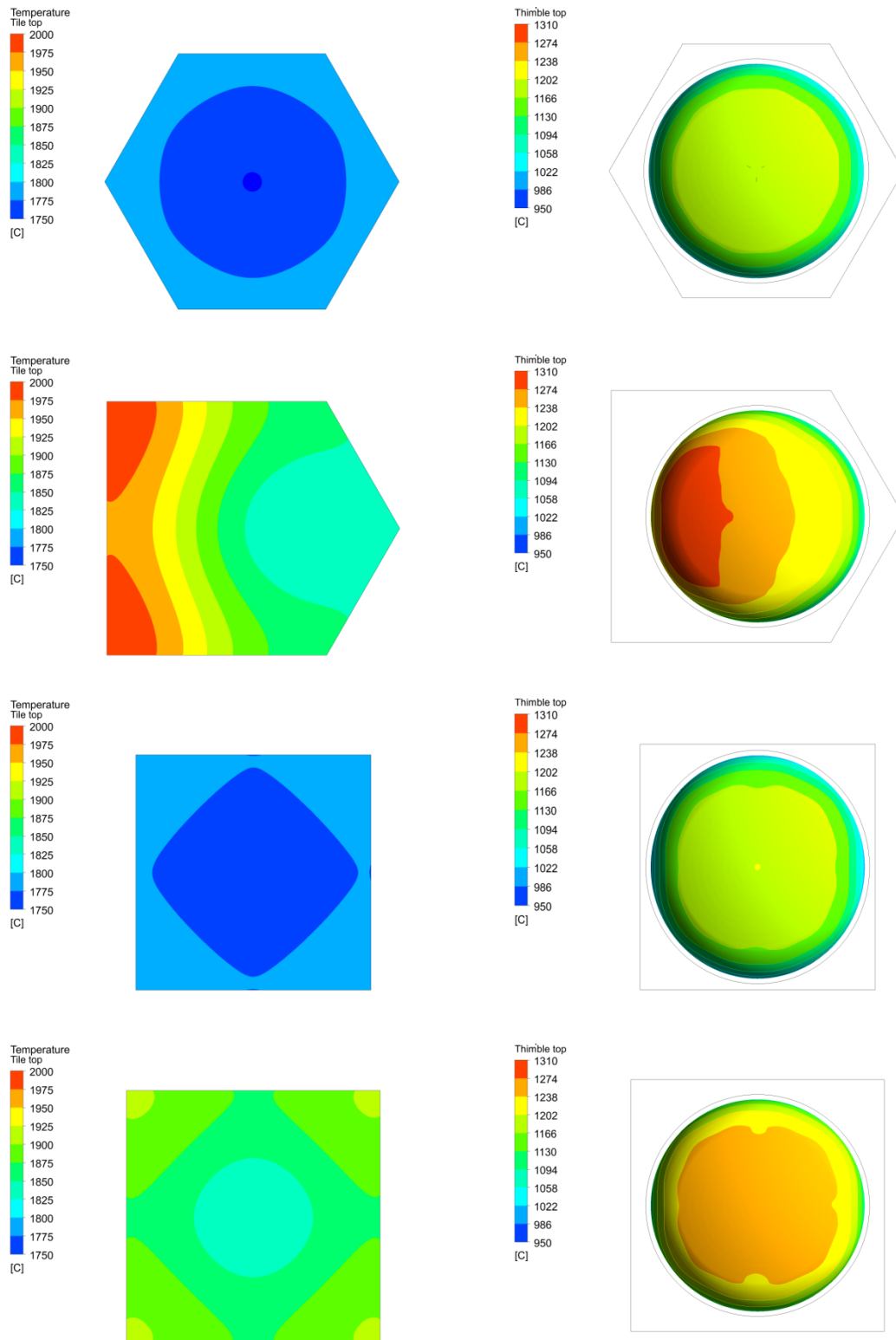
Figure 6: Temperature distributions of the tile's top surface (up) and of the thimble's top surface (down) for the different cooling fingers at a mass flow rate of 6.8 g/s.

125
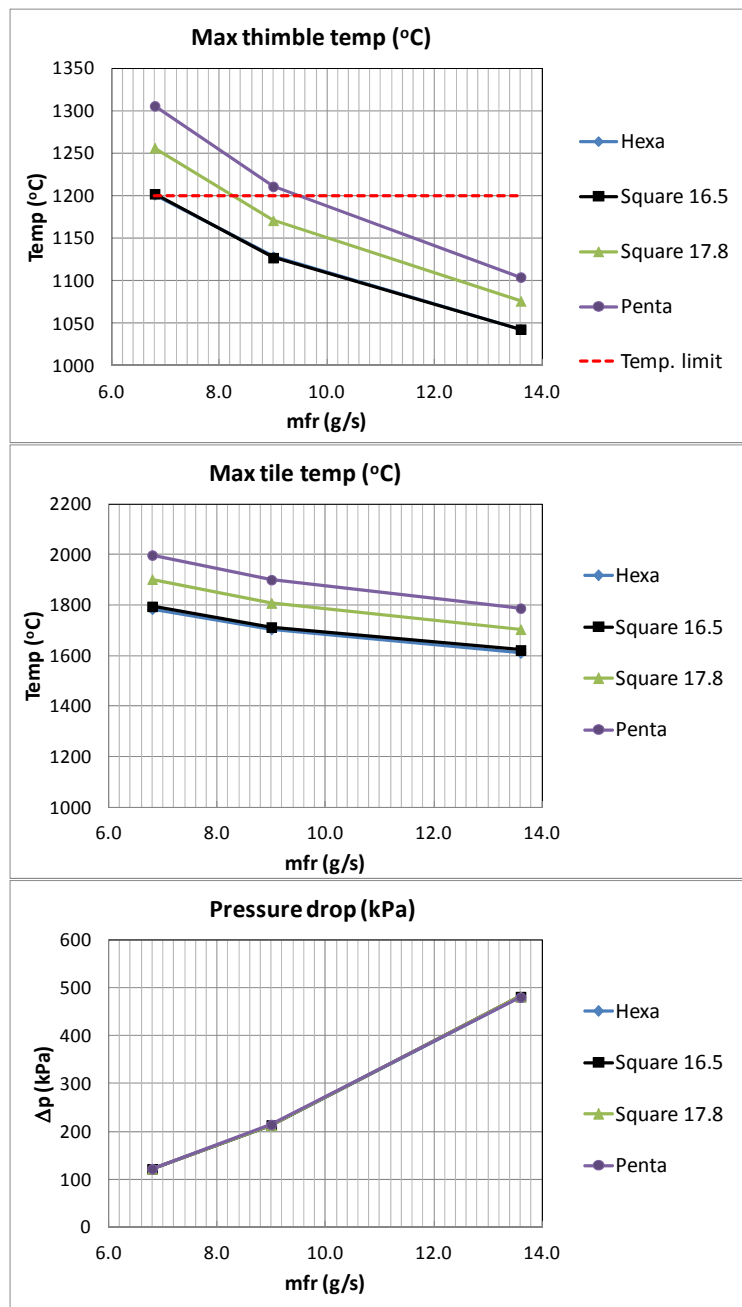
Figure 7: Maximum thimble and tile temperatures and pressure drop for different geometries and different mass flow rates.

The maximum tile and thimble temperatures decrease with increasing mass flow rate, while the pressure drop increases quadratically. At a constant mass flow rate and flow cross-section, the pressure drop depends only on the coolant flow path and the flow resistances. Since the same cooling cartridge and thimble structure are used for all geometries, the pressure drop tendency is the same for all fingers and depends only on the mass flow rate. The temperature trends are similar for all finger geometries, only the curves are shifted almost equidistantly. The most important are tendencies of the thimble temperature, which define the limiting mass flow rate. The lowest temperatures

are obtained for the hexagonal and square finger with the 16.5 mm edge. The values are almost the same in both cases.

The limiting mass flow rate (see Table 4) is obtained by linear interpolation of results at different mass flow rates and taking into account the thimble engineering temperature limit of 1200 $^{\circ}$C. The lowest mass flow rate of 6.8 g/s is obtained for the hexagonal and for the smaller square-shaped finger. The limiting mass flow rate for the square finger with longer edge (17.8 mm) is 8.2 g/s. Pentagonal finger requires the highest limiting mass flow rate of 9.5 g/s, which leads to the highest pressure drop of 240 kPa.

	Limiting mass flow rate [g/s]	T_max tile [$^{\bullet}$C]	T_{max} thimble [$^{\circ}$C]	Pressure loss [kPa]
Hexa	6.8	1782	1200	124
Square 16.5	6.8	1792	1200	124
Square 17.8	8.2	1840	1200	182
Penta	9.5	1889	1200	240

Table 4: Limiting mass flow rates for different cooling finger shapes.

5   CONCLUSIONS AND OUTLOOK FOR 2013

The alternative designs for the 1-finger target module are proposed and thermo-hydraulic analyses were performed to demonstrate the heat removal capability of the designs. The scoping analyses were carried out in two directions.

In the first case the Ta-based alloy (T-111) for the thimble was analysed at lower helium temperatures ranging from 400 to 500 $^{\circ}$C. The alloy T-111 has a lower DBTT value (rough estimation ~ 400 $^{\circ}$C) at irradiation conditions than the reference thimble material WL10 (600 $^{\circ}$C). Thermal loading of the finger structures and pressure drop in the cooling channel are compared with the reference design at high helium temperature. At 400 $^{\circ}$C of the helium inlet temperature, the maximum thimble temperature for T-111 is about 100 $^{\circ}$C lower and does not exceed 1100 $^{\circ}$C. The pressure drop in the cooling channel is also reduced by more than 25% compared to the reference case. It is shown that the maximum thermal loading increases linearly with the increased helium inlet temperature. To reflect the recent data for the early DEMO design (the so-called DEMO1), additional sensitivity cases were calculated with the lower peak heat flux 8.7 MW/m2. The inlet helium temperature was varied between 450 $^{\circ}$C and 650 $^{\circ}$C to cover the estimated uncertainty range of irradiated DBTT of T-111.

In the second case, the alternative finger geometries were investigated from the perspective of shadowing of the target plate edges against damage caused by the incident particles. In order to form a flat toroidal edge of the target plate, alternative tile geometries (non-symmetric pentagon, square) were analysed with respect to the reference hexagonal design. CFD analyses were performed from the point of view of maximum allowable thimble temperature and minimum required helium flow through the finger module. The results have shown, that apart from the reference hexagonal finger, the square-shaped finger with a 16.5 mm edge shows the best performance (6.8 g/s at 124 kPa pressure loss). This indicates that a helium cooled divertor could be composed entirely of the square-edged fingers, which would simplify the manufacturing process and assembling of the target plate. Thermo-hydraulic analyses show that square

127

fingers need to be slightly smaller (only 1%) than hexagonal fingers to reach equivalent performance.

The research activities in 2013 will be continued in the framework of PPP&T Design Assessment Studies (DAS). The continuation of the research related to CFD assessment of alternative diverter materials and finger geometries is envisaged as well as thermal-hydraulic assessment of multi-finger module.

6   REFERENCES

1   D. Maisonnier, I. Cook, P. Sardain, L.V. Boccaccini, L. Di Pace, L. Giancarli, P. Norajitra, A. Pizzuto, DEMO and fusion power plant conceptual studies in Europe, Fusion Eng. and Des., 81 (2006), 1123–1130.

2   P. Norajitra, R. Giniyatulin, T. Ihli, G. Janeschitz, W. Krauss, R. Kruessmann, et al., He-cooled divertor development for DEMO, Fusion Eng. Des., 82 (2007), 2740–2744.

3   M. Rieth, et al, Tungsten as a Structural Divertor Material, Adv. Sci. Tech., 73 (2010), 11-21.

4   P. Norajitra, T-111 alloy for the thimble material, personal e-mail communication, (2012).

5   Moorhead P.E., Stone P. L., Survey of properties of T-111 (Tantalum-8 Tungsten-2 Hafnium), NASA Techical note D-5873, (June 1970).

6   Zinkle S.J., Thermophysical and mechanical properties for Ta-8%W-2%Hf , ORNL, (June 1998).

7   ANSYS CFX, Release13.0, ANSYS CFX-Solver Theory Guide, ANSYS, (2010).

8   F.R Menter., Multiscale model for turbulent flows, 24th Fluid Dynamics Conference, American institute of aeronautics and astronautics, (1986).

9   B. Končar, I. Simonovski, M. Draksler, Influence of multiple jet cooling on the heat transfer and thermal stresses in DEMO divertor cooling finger, Fusion Eng. Des., 86 (2011), 167-173.

10 Thermophysical Properties of Fluid Systems, NIST, http://webbook.nist.gov/chemistry/fluid/

11 C. Bachmann, DEMOparametersMarch2012.pdf, personal email communication, (2012).

12 P. Norajitra, W. Basuki, L. Spatafora, Design description report of alternative He   cooled divertor concepts, Report for TA WP12   DAS02   T06-D1, EFDA_D_2L78SD, (2012).

13 Link to input models of this study: https://user.efda.org/?uid=2LAPN4.

INTERFACE ASSESMENT BETWEEN MCNP AND ANSYS CFX FOR THE BLANKET TEST CASE

Matjaž Leskovar, Boštjan Končar, Igor Lengar, Samo Košmrlj

Jožef Stefan Institute, Jamova cesta 39, 1000 Ljubljana, Slovenia
matjaz.leskovar@ijs.si

1 INTRODUCTION

The development of the DEMO fusion power plant blanket is a complex task, because it is necessary to take into account several branches of physics, including fluid dynamics, volumetric heat generation due to neutrons, heat transfer etc. Therefore, in order to support the development of the DEMO breeding blanket it is important to develop a computational model, which will take into account all the relevant data and physical processes. The volumetric heat generation in a Helium Cooled Pebble Bed Test Blanket Module due to neutrons, together with the surface heating from the plasma and the removal of heat by the helium coolant was investigated.

The breeding blanket in a fusion reactor has the function of removing the heat, generated by fusion reactions in the plasma. Additionally, it produces tritium, required for fusion reactions, from Lithium Orthosilicate (OSI). The surface heat load from plasma heating amounts up to 500 kW/m^2 and the volumetric heat generation from neutrons ranges up to 8 MW/m^3 in the region of OSI, closest to the first wall. The absorbed heat is removed by a helium coolant loop, which is divided into five components:

- First wall cooling loop, which runs near the outer first wall and removes the heat, which comes from the plasma surface heating.
- Breeder unit cooling loops, which remove the heat, generated in the OSI and in the beryllium neutron multiplier in the breeder units.
- Cooling loops in horizontal and vertical grids and in the side caps, which run between the separate breeder units.

2 WORK PERFORMED IN 2012

The research activities in 2012 were carried out in the framework of the PPP&T programme, workpackage Design Tools and Methodologies (DTM), Task DTM01-T03 Assessment of ANSYS Workbench hybrid platform. The main objective of the task was to test the possibilities for data transfer from the MCNP neutronic analysis to the ANSYS CFX thermo-hydraulic analysis. The assessment of the data transfer was performed for the Blanket Test Case [1], defined by the Karlsruhe Institute of Technology, which provided also the nuclear heating data [2], calculated with MCNP. For testing purposes a simplified blanket model was used, where only a slice of the

actual blanket unit was simulated. Furthermore, the helium region of the manifold was neglected, since it was estimated, that the manifold itself does not play a significant role in the heat balance of the blanket unit.

3   ANSYS CFX MODELLING AND SIMULATION RESULTS

3.1   Geometry of simulated region

A blanket module consists of six breeder units. The constituent materials absorb a lot of energy from the neutrons produced in the fusion reactions and have to be cooled effectively to prevent damage. Additionally, OSI has a relatively low thermal conductivity, which requires it to be cooled by an additional coolant loop running around it. The layout of the breeder units, consisting of beryllium, Eurofer, helium and OSI domains, is shown in Figure 1 (note: breeder units are held in place by an Eurofer structure, which also contains vertical and horizontal helium loops, but these are not shown).

(a) Breeder units in a single module   (b) Detailed view
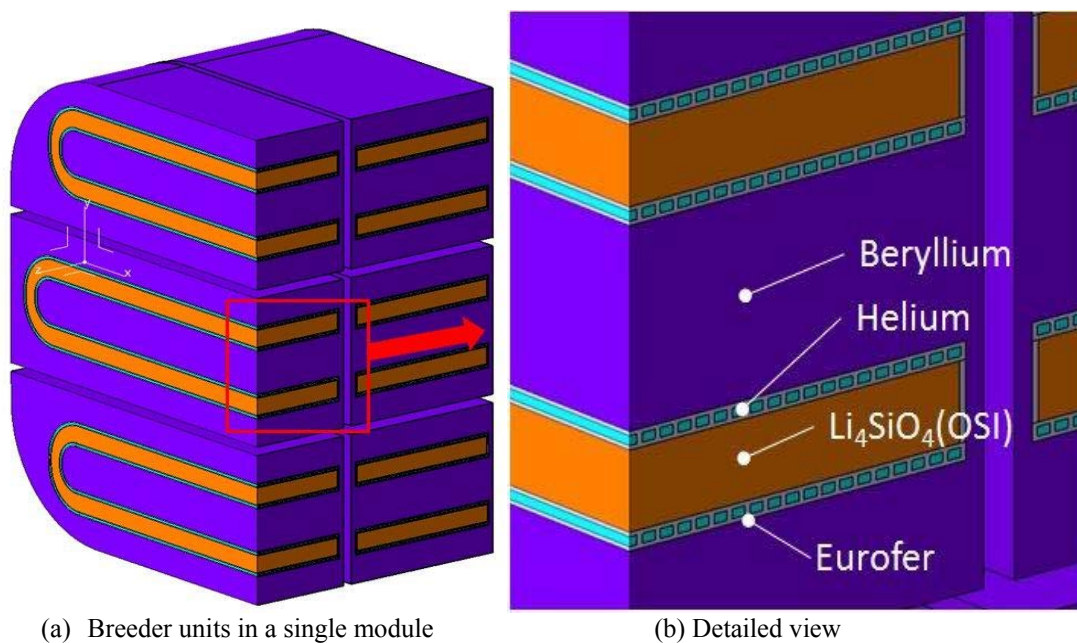
Figure 1: Breeder unit layout.

Only part of the actual blanket module was simulated, as proposed in the Blanket Test Case Definition by Karlsruhe Institute of Technology [1] that should serve as a benchmark case for data transfer between CFD and neutronic codes on the two tested platforms (ANSYS CFX and Salome). The so called "slice" model takes into account a vertical slice of the blanket module, as shown in Figure 2.
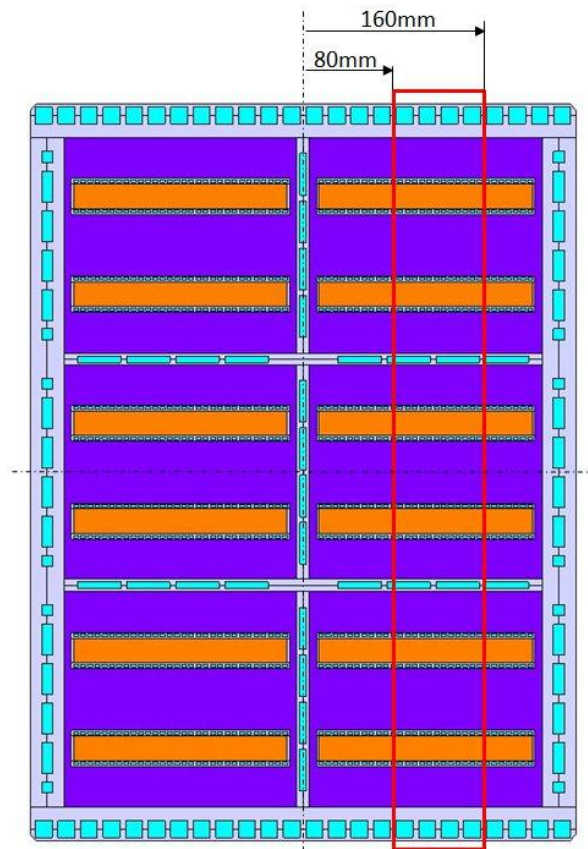
Figure 2: Location of slice model. Colours used correspond to materials, as shown in Figure 1.

Slicing the blanket unit at the proposed coordinates leaves the helium loop at the first wall intact, but cuts some of helium channels in the breeder unit in half, which can be compensated by applying symmetry boundary conditions there. Channels in the horizontal grid are however cut on the more unfavourable location, near the wall of the channel. Therefore an additional modification of the geometry was required: the sliced tubes were reduced in width, so that the wall of the pipe that was originally located just outside of the slicing plane was moved toward the inside of the slice model. This is considered to be a better solution than using a symmetry boundary condition. Using the symmetry boundary condition is not justified, as the nearest wall lies just outside the slice and therefore the fluid flow is not symmetric with respect to the slicing plane.

For simplicity, the helium domain in the manifold was ignored. Even though this would mean a violation of physics in reality, the simulation has no problems with that, as we can define inlets and outlets anywhere in the domain without needing to actually connect it with the helium source. Figure 3 shows the complete helium domain in a blanket module and the simplified helium domain in the slice. To overcome the absence of heat removal, the neutron heat generation was set to zero in the manifold region.

(a) Entire helium domain   (b) Simplified helium domain in slice
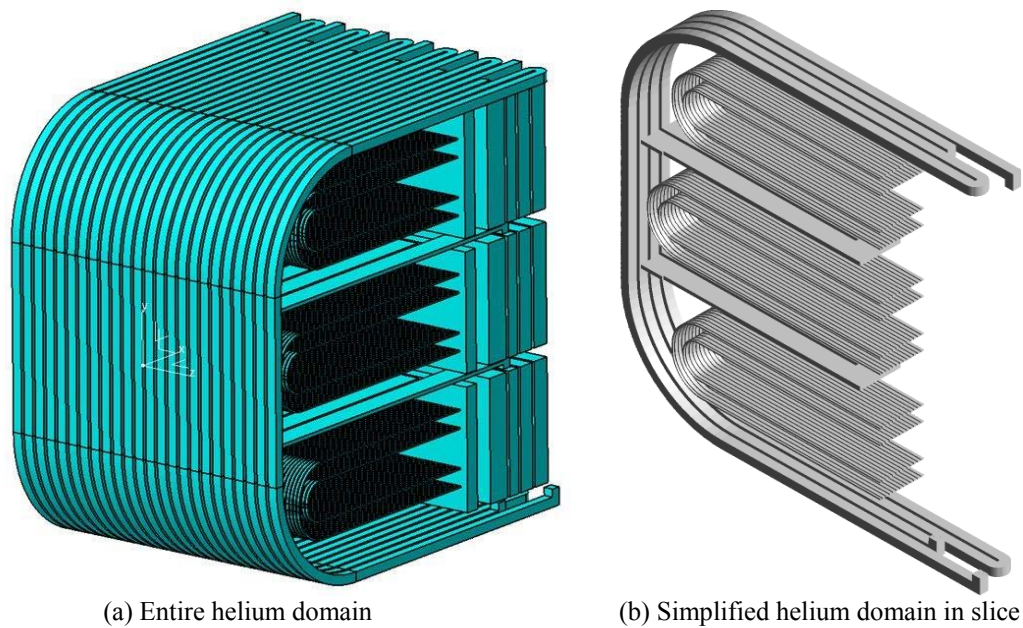
Figure 3: Helium loops.

3.2   Numerical mesh

The blanket module was meshed using a fully hexahedral mesh. The mesh consists of 1.49 million elements. The standard mesh quality criteria were taken into consideration when constructing the mesh:

The minimum mesh angle was mostly kept above the safe angle 20 degrees, 250 elements were between the (still acceptable) angle of 10 degrees and 20 degrees.

The 2x2x2 determinant of all elements was above 0.1, which is considered to be the limit for fast convergence.

The close-up of the mesh of the breeder unit closest to the first wall is shown in Figure 4.
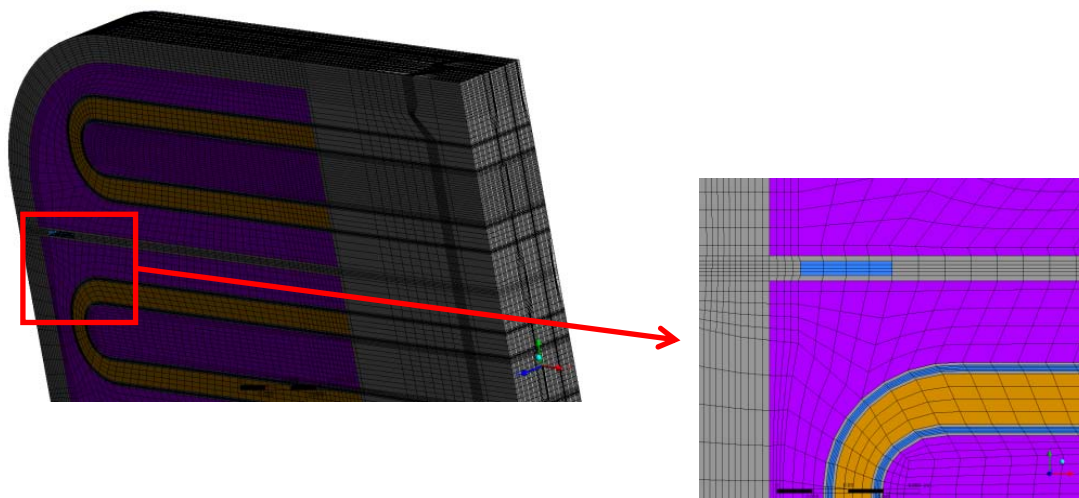
Figure 4: Detail of the mesh near the first wall.

132

3.3 Model setup and boundary conditions

The simulations were performed with the ANSYS CFX 13.0 code. Three solid domains (Beryllium, OSI and Eurofer) and one fluid domain (helium) were modelled. The heat transfer was solved simultaneously in the solid and fluid domains using the conjugate heat transfer approach. In the fluid domain the momentum and thermal energy equations were solved. Due to the low velocities (well below the sound of speed) the helium was treated as incompressible. The fluid turbulence was solved using the two-equation Shear-Stress-Turbulence model (SST). The boundary conditions for the simulated case are listed in Table 1.

Parameter	*Value*
He inlet mass flow rate	as defined in [1]
He inlet temperature	300 $^{\circ}$C
H inlet pressure	8 MPa
FW surface heat flux (front)	500 kW/m^2
FW surface heat flux (bending)	0 to 500 kW/m^2

Table 1: Boundary conditions for the slice blanket module model

3.4 Setting up the volumetric heating in CFX-PRE

The data for the volumetric absorbed power density was obtained from neutronic calculations using the Monte Carlo Neutron Program (MCNP) [2]. The 3D volumetric absorbed power density was provided in the form of txt files, where the coordinates and heating power density columns were separated by a comma - the so-called comma separated values format (csv), which is the default format for CFX, i.e. import and export of numeric values is primarily done in csv format.

To add volumetric heating to a CFX model, it is required to define an additional subdomain inside a domain (in Beryllium, Eurofer and OSI), which serves as a heat source. The source can be defined by a constant value, equation or by a user function, which is in our case represented by a 3D table of values. The table of values is imported into CFX-PRE via a user function. The user function requires the users to define the argument units, which are measurement units in the first column (in case of 1D data) or in the first three columns (in case of 3D data), and result units, which are measurement units in the last column. The data can be imported from the file by right clicking into the coordinate/value field. When importing the data, it is not possible to import several files, because every import overwrites the previous one. This is overcome simply by merging input files (by copy+paste). When the user function is defined, it can be applied (after specifying which quantities should be used for the arguments, usually the x, y and z coordinates) into the source subdomain.

The volumetric heating data was provided in several separate files, where files for the beryllium and lithium orthosilicate regions were some 100 kb in size, but files for the steel support structure were about 6 Mb in size. Considering the fact, that the steel structure is about the same volume as beryllium, this means that the data points are much more close together, which is probably the main reason why the loading time in both the CFX-PRE and the CFX-Solver was unreasonably increased (from 3-4 minutes to several hours). The significant increase of the volumetric heating data processing time was not a consequence of insufficient RAM, which would result in the much

slower data operation on the disk. The data processing time can also not be speed up by parallel computing, as parallelized data processing is not available in CFX-PRE and CFX-Solver. This shows that special care should be taken in the nuclear heating data preparation to not impose unnecessary computational demands.

It seems that it is currently impossible to import external data to CFX directly through the ANSYS Workbench, i.e. to import the data through the module called "External Data", as the "External Data" module does not support transferring data to CFX. Also if it would be possible to import the data through the "External Data" module, this would not simplify the setup of the simulation, because similar steps would be required as when importing data with the user function.

3.5   Simulation results

The simulation converges to the final stable state in less than 500 steps. The temperature distribution in the middle of the slice model is shown in Figure 5.
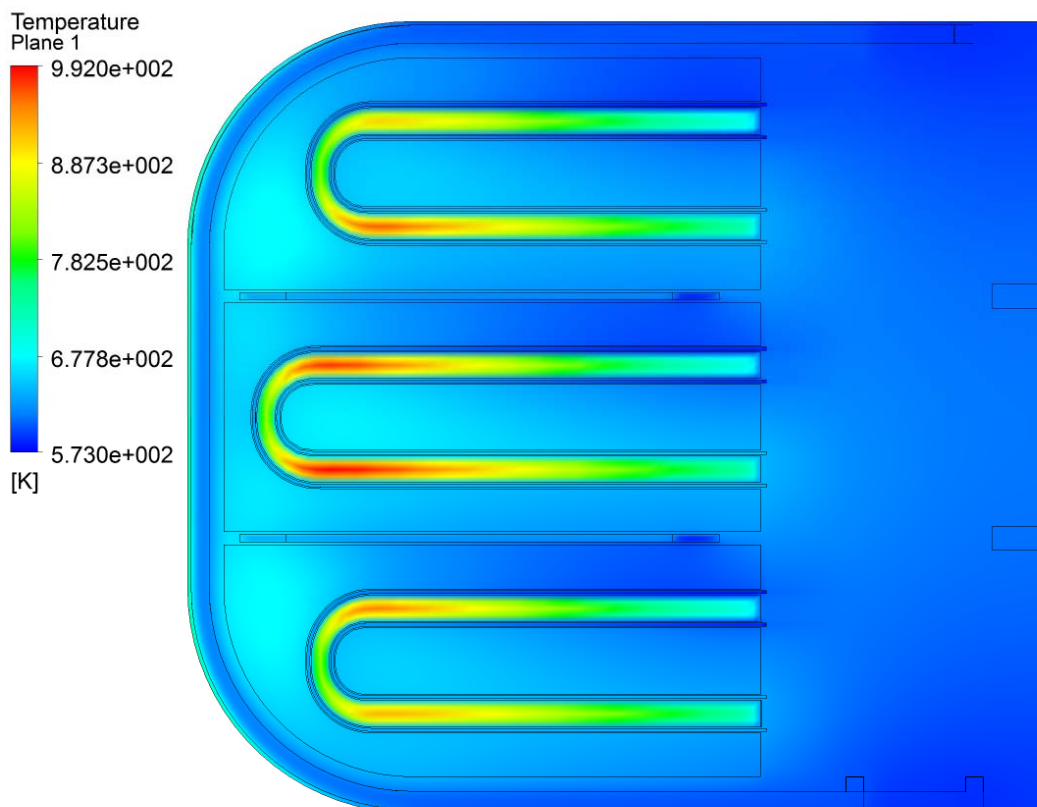
Figure 5: Temperature distribution in the middle of the slice model.

The highest temperatures occur in the OSI region due to its high volumetric heating and the low thermal conductivity. The maximum temperatures in the slice in various material regions are the following – OSI: 996 K, Eurofer: 751 K and Beryllium: 679 K. The temperature in the lower parts of the breeder units is a bit higher than in the upper parts, because the helium coolant, which comes from the inlet and passes through the upper parts of the tubes has a lower temperature than in the lower parts, where it has

already taken the heat from the upper parts. The manifold region receives some heat flux due to conduction through the solid, but that region is far away from the regions of interest and the temperature gradients are low. Therefore it is expected, that replacing the helium region of the manifold with Eurofer should not significantly affect the area of interest near the first wall.

In Table 2 the main characteristics of the helium cooling circuits are presented. Most of the heat is removed by the helium cooling circuit in the first wall (~38 kW). The heat removal in the breeder units is also significant (~22 kW), whereas the cooling power of the horizontal grids is much lower (only ~3 kW each).

Location	Mass flow rate [kg/s]	Outlet average temperature [K]	Cooling power [kW]
First wall	0.223	605.7	37.9
Horizontal grid 1	0.021	599.9	2.9
Horizontal grid 2	0.021	601.4	3.1
Breeder units	0.066	638.2	22.4
Total			66.3

Table 2: Main characteristics of helium cooling circuit.

If one considers that the plasma heating of the first wall is 23.0 kW (2x 5.83 kW curved part + 11.32 kW flat part), one obtains from the heat balance for the volumetric nuclear heating 43.3 kW. Thus the volumetric nuclear heating is about two times larger than the plasma heating.

4 POSSIBILITIES OF IMPORTING MCNP OUTPUT AS INPUT TO ANSYS

MCNP (version 5) has the ability to define a mesh, superimposed over the problem geometry for tallying purposes. These mesh tallies can have rectangular or cylindrical geometry. Within each cell of this three-dimensional mesh a value for the tallied quantity is calculated by MCNP. MCNP can, among other possibilities, tally gamma and neutron fluxes and neutron and gamma heating. In versions 5 and 6 it is possible to tally also the hating due to neutrons and gammas with a mesh tally. The use of the mesh tally makes it much easier to transform the heating data into ANSYS since the model geometry, which is most likely not rectangular, does not have to be modified.

Neutron and gamma heating are calculated by MCNP during the same run, but are output in two separate sets of data. They have later to be combined in order to obtain the needed input for ANSYS. It should be noted that MCNP, by default, covers only the transport of prompt gamma rays, but not delayed gammas. If it is, due to the choice of construction materials expected, that delayed gammas may have significant impact on material heating, special techniques have to be involved which make MCNP source code modification and recompilation necessary [3], [4]. These approaches are usually employed for shut down dose rate calculations. For most applications, using only neutron and prompt gamma heating would be sufficient.

It turns out, that photon heating can be for several factors higher than neutron heating, which means the photon heating can dominate in nuclear heating. During

calculations for the ITER tokamak it turned out that for some components photon heating may significantly contribute to the total nuclear heating [5].

As an example of the capabilities of the transformation of heating data, obtained with MCNP into ANSYS, the nuclear heating calculations were performed for the MCNP model of the DEMO tokamak. The model was released by KIT in July 2012 in the frame of the WP12-DTM-03-T02 task – Provisional DEMO MCNP Model. The calculations were performed by JSI, imposing a cartesian mesh tally over the whole geometry; the resolution of the mesh was 117x28x174 points, corresponding to dimensions of the model. The obtained distribution of the neutron and gamma heating are presented in Figure 6; included is also the mesh tally resolution, presented by yellow dots.

| Gamma heating | Neutron heating |
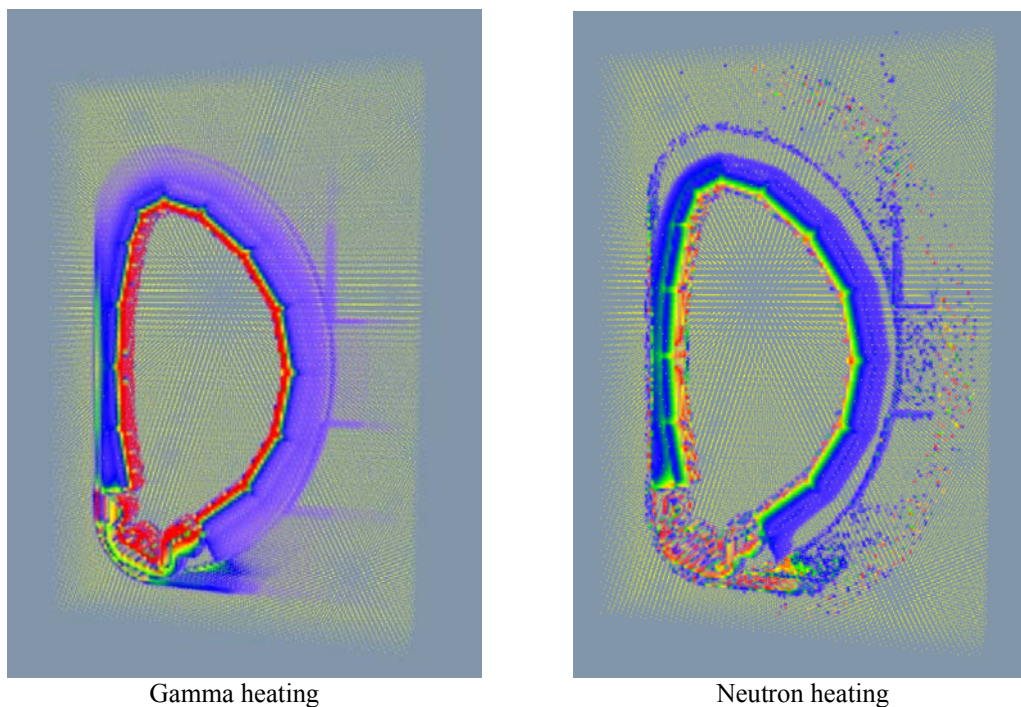
Figure 6: Presentation of the heating distribution, obtained by using a mesh tally. Calculations were done for the provisional MCNP model for DEMO (supplied by KIT). The yellow dots represent the distribution of the mesh tally cells.

For the calculations the MCNP5 mesh tally technique was applied for heating calculations by using the FMESH card with its FM tally multiplier card in which the material number "m" was set to zero, implying that the heating cross sections for the material in which the particle is traveling are used.

The largest difficulty in calculating the heating is to make the MCNP model and then to run it accordingly for the statistical errors in the regions of interest to be low enough. Several variance reduction techniques can be applied for this purpose, the most widely used being the application of weight windows.

Most likely the heating will not be calculated for the whole geometry, as was done in our example, but only for specific components. In this case the mesh is applied

only over those components and the MCNP run optimized to give the lowest statistical error in the region of interest.

It should be also mentioned that the regular x-y-z rectangular cells of mesh-tally used for heating calculations does not necessarily coincide with the arbitrary oriented MCNP cells. Since the heating is averaged inside the mesh cells, along the border regions between two materials and especially between material and void, the material-to-void ratio inside the mesh-tally elements is changing substantially, causing quite visible difference in averaged mesh-tally heating for that mesh cell. This difference can be diminished by reducing the size of mesh-tally cells.

MCNP gives statistical errors for each mesh tally cell. They have to be kept within reasonable limits, which should in normal runs not exceed 0.10. Prior to export the mesh tallies into ANSYS, a check of the fulfilment of this restriction should be made. MCNP normalizes each run with respect to 1 source neutron. Care should be devoted to normalize the results to the determined fusion power.

5   CONCLUSIONS AND OUTLOOK FOR 2013

The main objective of the performed task was to test the possibilities for data transfer from the MCNP neutronic analysis to the ANSYS CFX thermo-hydraulic analysis. The assessment was performed for the Blanket Test Case. The objectives of the task were fully achieved and the continuation of these activities in 2013 is not foreseen.

Based on the provided Test Blanket Module CAD model and the test specifications, the ANSYS CFX model was developed for the so called "slice" model, which considers a vertical slice of the blanket module. The modelled slice part of the blanket module was meshed using a fully hexahedral mesh, consisting of 1.49 million elements.

The inclusion of nuclear heating in the CFX model is straightforward. Inside each domain (Beryllium, Eurofer, OSI) one has to define an additional subdomain, which serves as a heat source. The heat source can be defined by a user function, which can be a table of nuclear heating data provided for different locations in 3D. The table can be imported from a text file. In ANSYS Workbench it is possible to import data through the module called "External Data", but it seems that this option is not available for CFX. Also if it would be possible to import the data through the "External Data" module, this would not simplify the setup of the simulation, because similar steps would be required as when importing data with the user function.

MCNP has the ability to define a mesh, superimposed over the problem geometry for tallying purposes. The mesh does not need to cover the whole geometry; it may be defined only in specific regions and it may be adequately refined where needed. Within each cell of this 3D mesh the nuclear heating may be calculated. The calculated nuclear heating data is given in form of a table in a text file, which may be directly imported into CFX after some basic editing.

The Blanket Test Case was simulated with ANSYS CFX, considering the provided 3D nuclear heating data. The loading time of the nuclear heating data in both, the CFX-PRE and the CFX-Solver, significantly depends on the size of the data files, thus the density of the nuclear heating data points should be optimized.

The simulation showed that the highest temperatures occur in the OSI region (996 K) due to its high volumetric heating and the low thermal conductivity. The volumetric nuclear heating (43 kW) is about two times larger than the plasma heating (23 kW). Most of the heat is removed by the helium cooling circuit in the first wall (38 kW). The heat removal in the breeder units is also significant (22 kW), whereas the cooling power of the horizontal grids is much lower (3 kW each).

6   REFERENCES

1   Blanket Test Case Definition, Karlsruhe Institute of Technology, (2012).

2   S. Keckes, L. Boccaccini, "Volumetric Heating Data for the Blanket Test Module Calculated by MCNP", personal communication, (October 2012).

3   R. Villari at al., "Shutdown dose rate benchmark experiment at JET to validate the three-dimensional Advanced-D1S method", Fus. Eng. Des, 87 (2012), 1095-1100.

4   Y. Chen, U. Fischer, "Rigorous mcnp based shutdown dose rate calculations: computational scheme, verification calculations and application to ITER", Fus. Eng. Des, 63–64 (2002), 107-114

5   A. Serikov, U. Fischer, D. Grosse, High Performance Parallel Monte Carlo Transport Computations for ITER Fusion Neutronics Applications, Progress Nucl. Sci. Tech., 2 (2011), 294-300.

NEUTRONIC STUDIES FOR DEMO – HELIUM PRODUCTION IN THE UPPER VERTICAL PORT

I. Lengar, L. Snoj

Jožef Stefan Institute (IJS), Reactor Physics Department, Ljubljana, Slovenia
igor.lengar@ijs.si

1   INTRODUCTION

The helium production in components of fusion reactors is dependent on the component material and the neutron spectrum. In stainless-steel the helium production occurs principally from fast neutron reactions with Ni, Fe and Cr component in the steel. In the thermal part of the neutron spectrum the reactions with trace elements, exhibiting large (n, α) cross-sections can be important, in particular with boron due to the large 10B(n, α) reaction cross-section.

In the frame of the project, the helium production was calculated in the upper vertical port and in the blanket cooling pipes. MCNP5 Monte Carlo transport code was used for the calculations using JEFF 3.1 data libraries, a few runs were done with the MCNPX code. The MCNP model of DEMO, earlier developed by KIT and provided for usage, is very complex – it comprises more than 14000 cells. For this reason a simpler model was made by excluding the blanket modules, which numbered more than 90% of the whole model in terms of the number of cells. In this way the familiarization with the model was much simpler.

The blanket cooling pipes in the vertical port were not present in the provided MCNP model. They were inserted into the model after studying their geometry first on the simple model.

The calculations of the neutron flux were subsequently performed. The main target was the region around the upper vertical port where the knowledge of the neutron flux was needed. In parallel with the flux calculations the reaction rate for the helium production was determined.

2   WORK PERFORMED IN 2012

2.1   Studying the model

The MCNP model was provided by KIT. It was quickly found that the model is very complex; it numbered more than 14.000 cells. For this reason it was difficult to handle, particular it's presentation with MCNP visualization tools. A simpler model was thus made from the original model.

Simplified model

The most complexity in the MCNP model was found to be concentrated in the blanket modules. Although they cover less than 10% of the model's volume, they comprise more than 90% of the whole model in terms of the number of cells and the size of the input file.

A simpler model was developed, in which all interior cells of the complicated blanket were excluded and filled with void. The procedure is graphically presented in Figure 1.
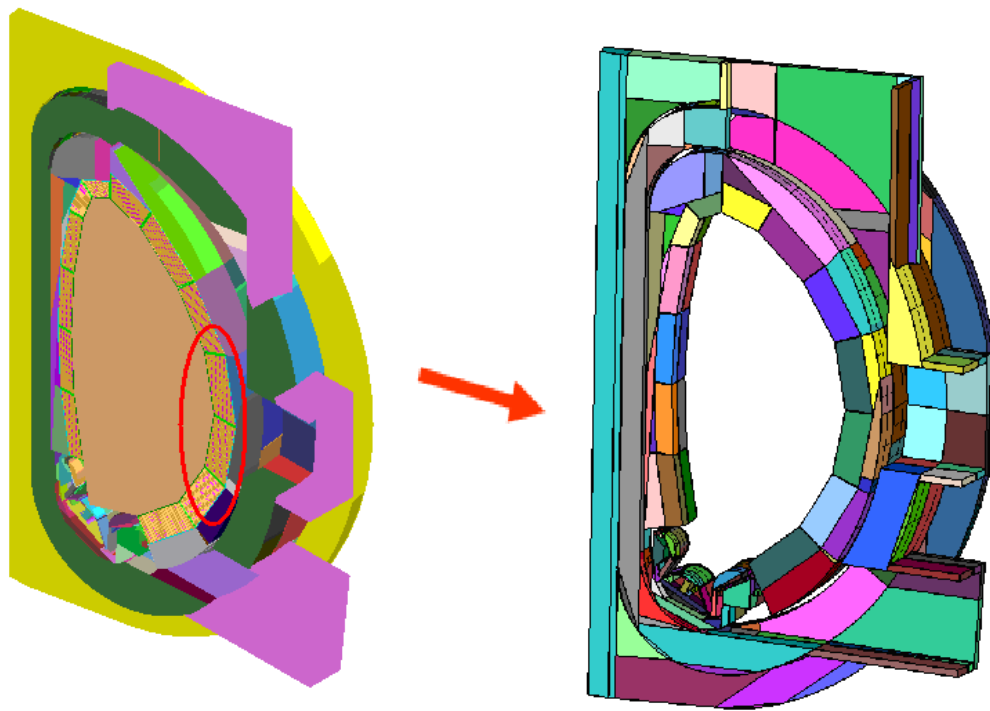
Figure 1: Simplification of the DEMO model with removal of cells from the blanket (presentation with the McCad GUI).

In this way the results of calculations were not fully representative, but the handling of the model and its visual representation become much easier. It was used for familiarization and for testing of modifications on the complex model.

Insertion of cooling pipes

Using the simplified model, cooling pipes were inserted first into the simplified model, and the same cells and surfaces inserted subsequently into the full model. The pipe material was chosen to be Stainless Steel 316.
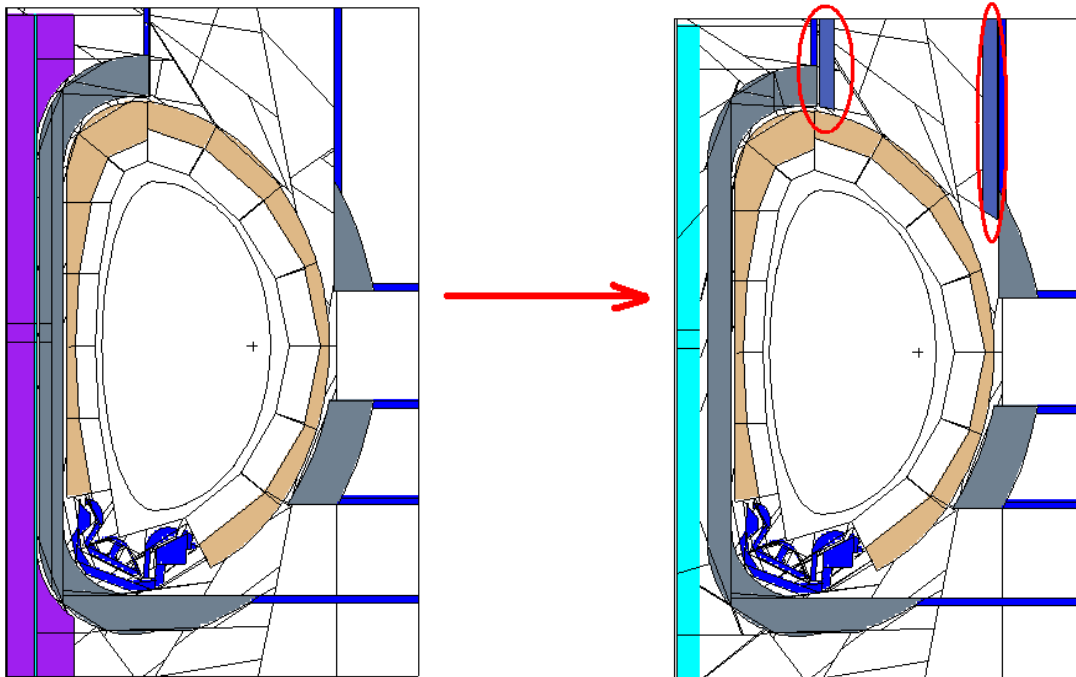
Figure 2: Insertion of the cooling pipes into the MCNP model.

Lost particles

Since the pipes were copied from the simple model the full model had first to be tested. It was found during previous experience with a different MCNP model for DEMO, that due to the lack of possibility for visualization of the model with MCNP visualization tools, a good way to study the model is by examining particles, which are lost during calculations. An analysis was thus performed by accessing the locations where particles were lost, if any. A longer MCNP run with the full model was performed and the locations where the particles are being lost were determined. A script was written for this purpose in order to extract the locations of the lost particles. With another application the surfaces in the model were visualized. The combined picture, inducing the geometry and location of the lost particles, is presented in Figure 3.
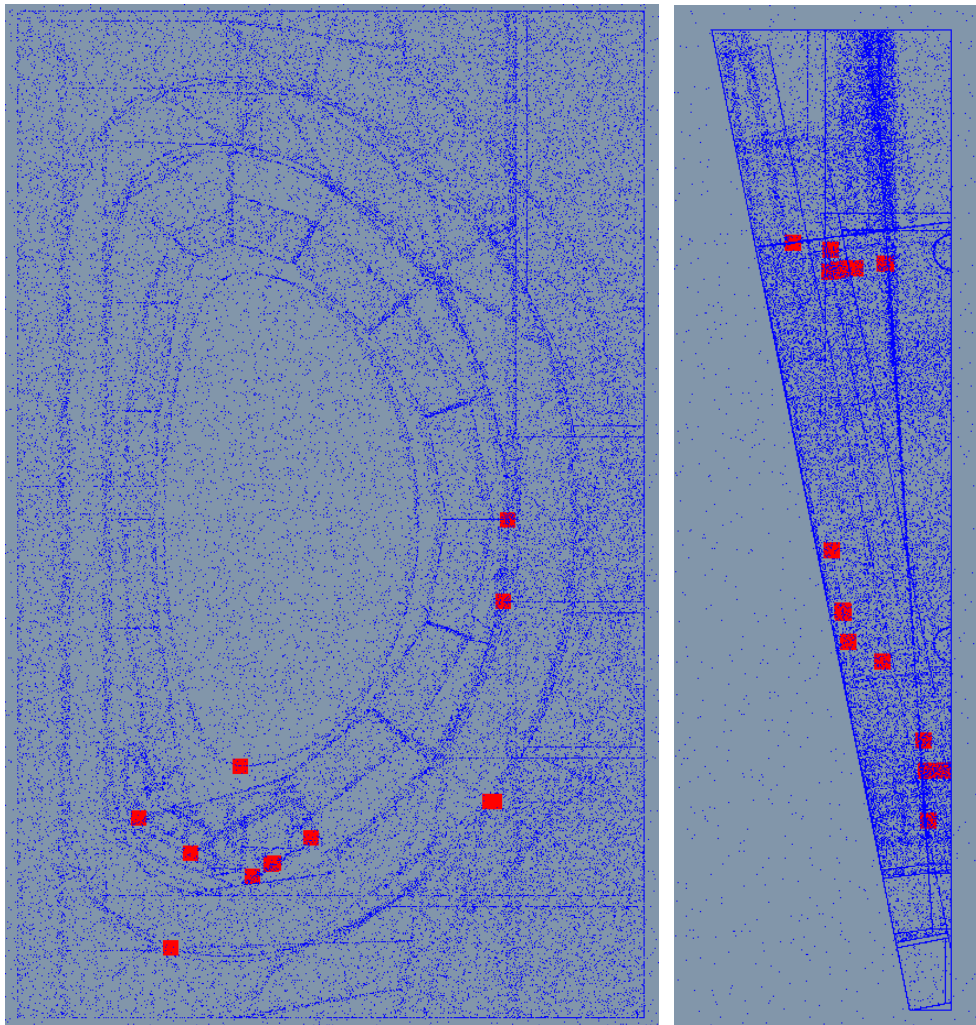
Figure 3: Side and top view of the full MCNP model including the rough location of the spots, where the particles are being lost (red spots).

It was found that less than 10^{-7} particles are lost, and that their positions are far from the region modified due to the insertion of the pipes. The very few lost particles can be attributed to MCNP, which in rare cases makes mistakes in determining the intersection of particle tracks with surfaces due to finite numerical accuracy of calculations. The model was thus found satisfactory in order to perform the needed calculations.

Variance reduction

Sample runs with the model were performed in order to estimate the neutron flux in the DEMO geometry. It was soon found, as expected, that the attenuation of neutrons on the blanket is large and few neutrons penetrate it in an analog Monte Carlo run (i.e. without using variance reduction techniques). An example of the flux field is presented in Figure 5 for two cases - the total neutron flux and only the scattered neutrons.

a)   b)
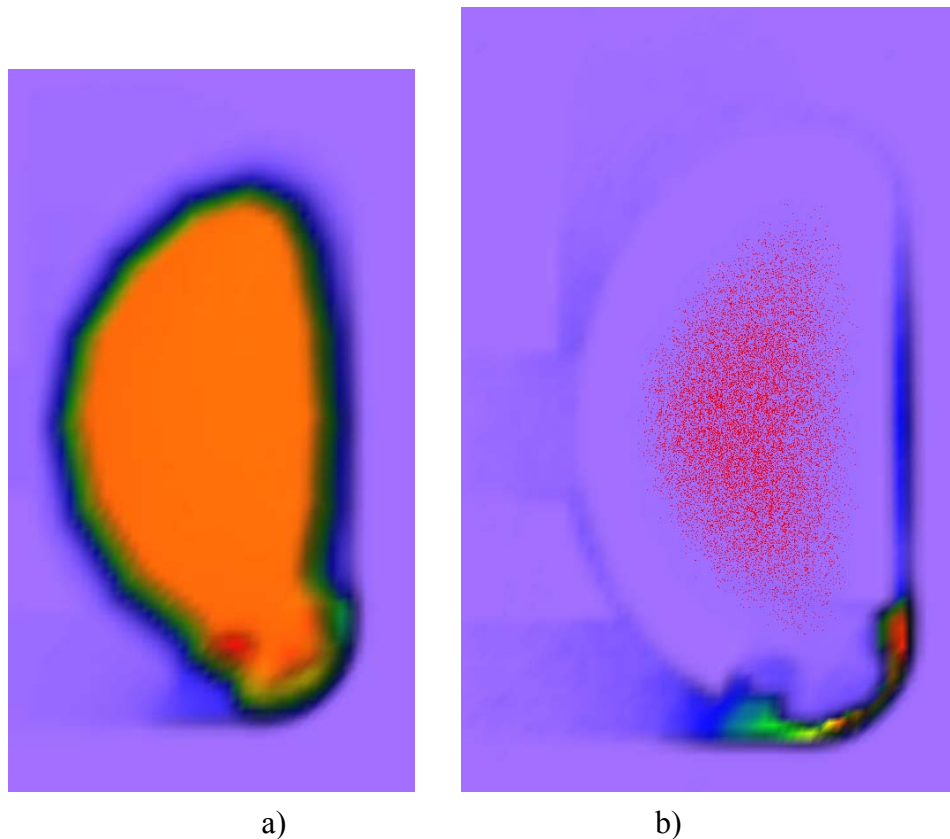
Figure 5: Example of the flux field from the: a) total neutrons flux and b) only for the scattered neutrons. In figure b) the plasma source is also presented. The DEMO geometry can be well anticipated from the flux shape in figure b).

It can be seen from Figure 5 that the flux is strongly attenuated and reduced for several orders of magnitude before reaching the region of interest, i.e. the upper vertical port. In order to obtain any statistically meaningful results for helium production in that region, variance reduction techniques had to be applied.

Since successful use of MCNP variance reduction techniques is often difficult and tending to be more art than science [1], a careful study of the phase space involving the variance reduction parameters has been performed. The exponential transform in the vertical direction has been employed in connection with the usage of weight windows. The parameters of both techniques have to be carefully adjusted in order for the non-analog Monte Carlo to give reliable results. In this process the weight window adjustment was done by recursion – the generated weight windows were used as an input for the next approximation. A graphical example of adjusting the parameters is presented in Figure 6; in figure a) the neutron flux in DEMO without variance reduction techniques is represented. It is observed, that in the region of interest – the upper vertical port – the flux is very low. In figure b) the scattering positions of neutrons transported in MCNP are presented regardless of their weight – the variance reduction parameters impose an under-sampling of the important region.   In figure c) oversampling of the region is observed – all represented tracks have very low weight and are progeny of a single source neutron. In figure d) tracks in the case of satisfactory variance reduction parameters are presented.

143

a)   b)   c)   d)
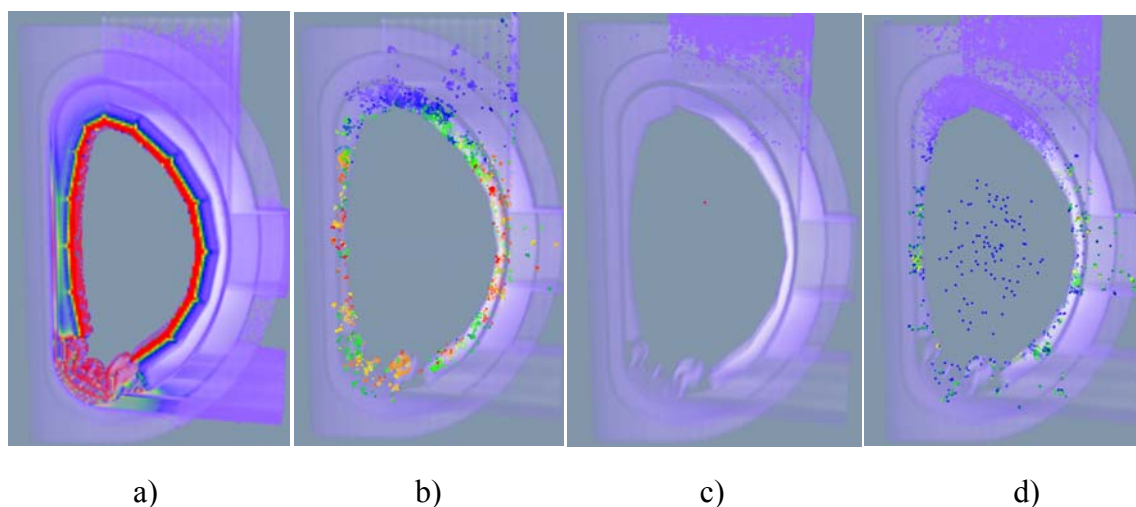
Figure 6: Variance reduction parameter adjustment: a) neutron flux filed in DEMO without variance reduction, b) scattering positions of neutrons – under-sampling of the important region, c) over-sampling of the region, d) satisfactory sampling.

Results

The DEMO plasma source, needed for these calculations, was also provided by KIT and MCNP was re-compiled by usage of this source. A plasma source strength of $6.106 \cdot 10^{20}$ n/s was used and 5 years of full power operation were assumed for the calculations.

The helium production has been estimated using the track length estimate of cell flux (F4) and a tally multiplier with the ENDF reaction numbers for ^{3}He - MT = 206 and ^{4}He - MT = 207.
It has been calculated in all MCNP cells of the upper vertical port (12 cells) and in the cooling pipes (2 cells). In this way an average of the helium production was determined.

The values were lower than expected and ranged for individual cells of the port from 0.4 appm to 2.5 appm for 5 years of operation. The average helium production through the whole upper vertical port material is 0.6 appm.

The helium production in the outboard pipe is 0.9 appm and in the inboard pipe 0.5

It has been found, that the helium production is crucially dependent on the boron concentration in materials. A value of 10 ppm of natural boron has been used for the calculations, and it has been found to be the main contributor of helium production. For more accurate estimations a more accurate knowledge about trace elements should be known, especially about the boron concentration.

The ^{3}He production was also calculated, but found to be much less than the alpha production. It was estimated to be for a factor of 10^5 smaller. It was also not affected by the boron presence in materials, as was anticipated.

144

The graphical presentation of the helium production in the upper vertical port and pipes is presented in Figure 7.
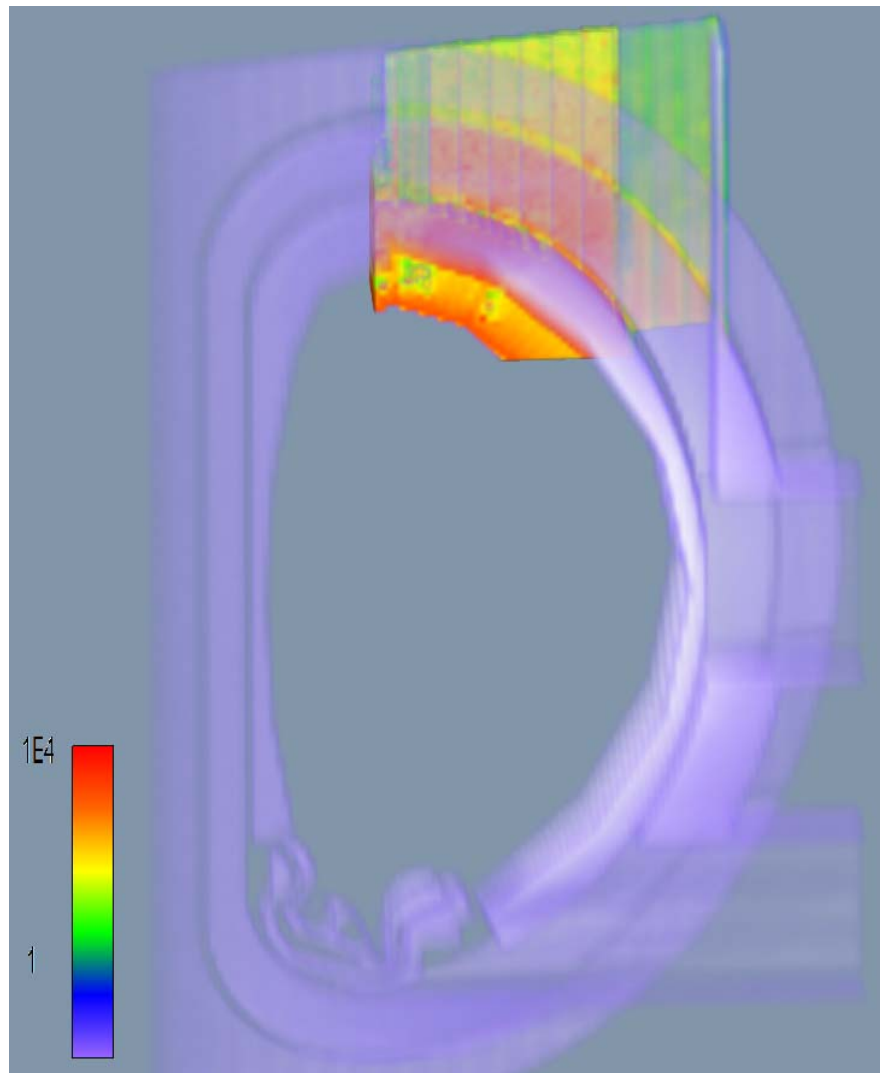
Figure 7: Graphical presentation of the helium production in the upper vertical port and pipes (appm). The whole DEMO structure is presented, He production is shown only for the region around the vertical port.

3   CONCLUSIONS AND OUTLOOK FOR 2013

The Helium production in the upper vertical port was calculated by using MCNP. The model for DEMO was provided by KIT and was slightly modified by the insertion of the blanket cooling pipes. A plasma neutron source was also provided.

The neutron flux was calculated with the MCNP5 Monte Carlo transport code, a few runs were done with the MCNPX code. Firstly the modified model was studied by examining the lost particles in MCNP. The main part of the task was devoted to

variance reduction since the flux is strongly attenuated before reaching the vertical port and it is the only way for obtaining any statistically meaningful results.

It was found that the helium production amounted between 0.4 appm and 2.5 appm for 5 years of operation for the vertical port and pipes. It was strongly dependent on boron concentration in the material.

In 2013 the influence of different first wall materials on the tritium breeding ratio (TBR) will be examined. Either helium or water will be assumed as coolants and the impact of various first wall design options on the TBR will be studied.

REFERENCES

1   X-5 Monte Carlo Team, MCNP — A General Monte Carlo N-Particle Transport Code, Version 5, Los Alamos National Laboratory, Los Alamos, New Mexico, (April 2003).

NEUTRONIC STUDIES FOR DEMO – CAD IMPORT INTO MCNP USING McCAD

I. Lengar, L. Snoj

Jožef Stefan Institute (IJS), Reactor Physics Department, Ljubljana, Slovenia
igor.lengar@ijs.si

1   INTRODUCTION

The activity was a joint work of the associations KIT, CCFE, ENEA and MESCS-SFA. Different tools for conversion of the CAD (Computer Aided Design) geometry into the MCNP (Monte Carlo N-Particle) [1] geometry have been tested. The tool used by the SFA was the McCad conversion tool developed by KIT.

The installation files were provided by KIT together with a model of DEMO in the step format (*.stp), a program independent format to be used with CAD graphic programs.

The installation of McCad and the conversion of the model were performed with some support of KIT. The provided CAD model of DEMO was rather complex, comprising more than 13000 cells. The correctness of the resulting converted MCNP model was evaluated by it's visual representation and examination and by comparing the volumes of the cells in the CAD model and those, obtained stochastically with MCNP.

The comparison of the volumes showed satisfactory results.

The power due to the flux of direct neutrons on the first wall was also calculated for a void model (no materials were inserted). These calculations resembled the wall loading and were performed by using the DEMO plasma source, also provided by KIT.

2   WORK PERFORMED IN 2012

2.1   Installation of McCad

The McCAD software is still under development and the installation and the conversion of the model were performed with some support of KIT. The first version of McCad provided was McCad 0.3.0, it consisted of the debian package mccad-0.3.0_i386.deb, additionally the source was provided. It turned out, that the right choice of the platform and the libraries is crucial for operation of the software. It was tested on the Linux Ubuntu 12.04 LTS system. The source was compiled, but several problems were encountered. It turned out that the reason was an OpenCascade library version compatibility problem. In interaction with KIT the problem was solved with the usage of the corrected OpenCascade library.

After the experience gained with the version McCad 0.3.0, the installation of the next versions was easier to master. It was, however, found, that the debian binary package was in no case enough for successful installation on our computer. Only after obtaining the source code and being able to compile our own code the McCad installation could be successfully mastered. In interaction with the developers the specification of the exact version of the Linux platform including the libraries was suggested. Even better, was to provide the libraries with the installation files to avoid compatibility problems.

2.2 CAD model of DEMO

The provided CAD model in the *.stp format contained seven parts:
- coils
- manifold blanket
- port
- divertor
- vacuum vessel
- plasma
- detailed blanket

A graphical presentation of the model is done in Figure 1, using the McCad Graphical User Interface.
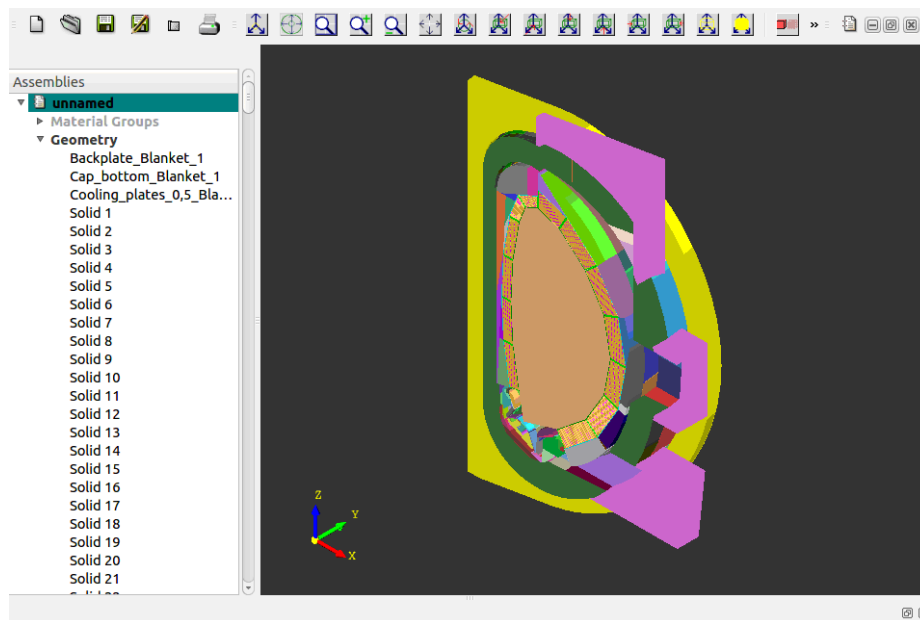

*Figure 1: Graphical presentation of the DEMO model, provided in the *.stp format, using the McCad GUI.*

The first six of the listed components were of moderate geometrical complexity. The seventh component, the detailed blanket, was however very complex. The size of the

file for the detailed blanket alone was cca. 30 times larger than the sizes of all other components combined. It was a really complex structure, composed of more than 13000 cells.

Conversion of CAD model of DEMO with McCad

The final conversion of the DEMO CAD model was done with the McCad code, version 0.3.2. Since it was available only in December 2012, the familiarization with the software was done by using the versions 0.3.0 and 0.3.1.

During the first conversion, individual components, listed in Section 2.2 were converted and found, that five components were straight forward to convert and two were posing difficulties. Successful conversion could be performed for:

- coils
- manifold blanket
- port
- part of the divertor
- vacuum vessel

while at first we encountered problems with converting the full blanket:

- if the interior structures of the blanket were
  excluded, the conversion was successful,
- the divertor parts could be converted individually,
  but not the whole divertor.

We studied the conversion process by using different values for the McCad input parameters like the Minimum Input of Solid Volumes, the Minimum Void Volume or the Minimum Size Of Decomposition Face Area. We found that the success of conversion is dependent on the right choice of these parameters. The complicated blanket could, however, also due to it's complexity (more than 13000 cells), not be converted.

Usage of McCad 0.3.2

In December 2012 the McCad version 0.3.2 was released, which improved the possibility of converting complicated structures. In the previous versions the material cells were produced and subsequently the remaining void space was filled with void cells. In case of the complicated blanket the preparation of the void cells was very time consuming due to the large number of surfaces of the material cells, which had to be checked.

In McCad 0.3.2 a function was added, which enabled the void generation to be switched off and only the material cells are produced. The void can be produced by the user in simpler geometry separately.

In our case it was done, by the advice of the developers, by generating the void space with the simple blanket model, comprising a far smaller number of cells. Consequently the void cells were also simpler.

In the next step the complicated blanket was successfully converted with McCad but the surrounding void space was not produced.
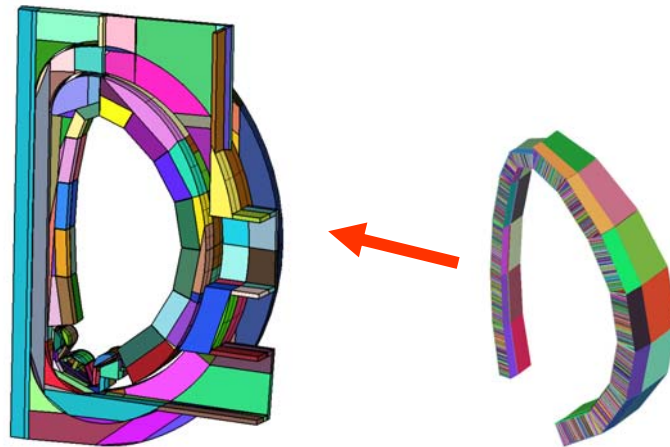
Figure 2: Procedure of the separate conversion of the simple model without the complicated blanket and filling of the complicated blanket into the simple model.

In the following step the cells of the complicated blanket were filled into the cells of the simple blanket. The simplest way was found to assign all the cells of the complicated blanket the attribute of the universe (1st level of universe), a feature of MCNP. The simple blanket in the ground level of the geometry was then filled with this universe. The procedure is graphically presented in Figure 2.

2.3 Checking the MCNP model

As described earlier, the success of conversion was dependent on the right choice of some parameters in the input file for McCad. The output file has been checked with the Visual editor and a run for lost particles was performed. The number of problematic zones, in which the geometry was ill defined, was found to be dependent on the choice of the parameters. These were adjusted in order to lower the problematic zones to a minimum; when only one or two zones were found in the model, they were manually corrected. An example of an incorrectly defined geometry is graphically presented in Figure 3.

It was found, that different cells were defined by almost identical surfaces, differing only by one parameter on the sixth digit. The problem has been fixed by setting the surfaces to being equal and MCNP then automatically rejects one of the surfaces.

The described procedure was possible for the simple blanket model, i.e. the full DEMO model but without the complicated blanket inserted, since the model is simple enough to be visualized with the MCNP visualization tools. The method could in this form, however not be used for the full model or even for the complicated blanket alone, since they were too complex to be opened by the visualization tools.
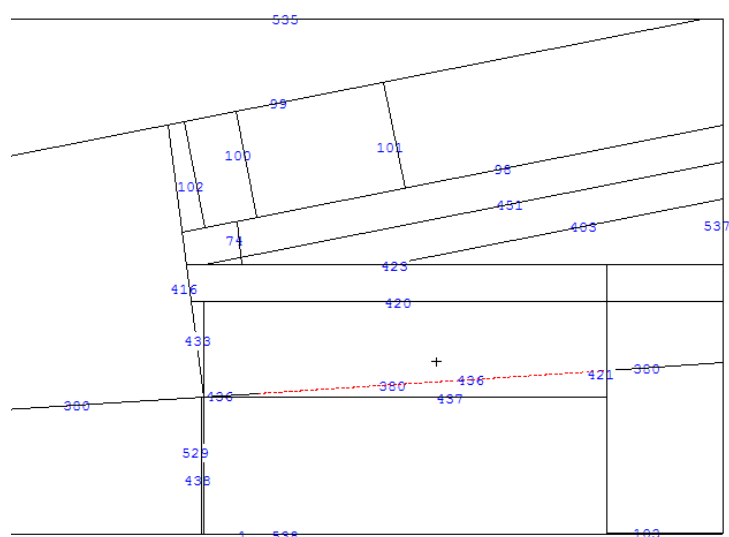
Figure 3: Example of a part of the geometry, incorrectly defined after the automatic conversion.

An analysis was though performed by accessing the locations where particles were lost. A longer MCNP run with the full model (including the complicated blanket) was performed and the locations where the particles are being lost were determined. A script was written for this purpose in order to extract the locations of the lost particles. With another application the surfaces in the model were visualized. The combined picture, inducing the geometry and location of the lost particles, is presented in Figure 4.
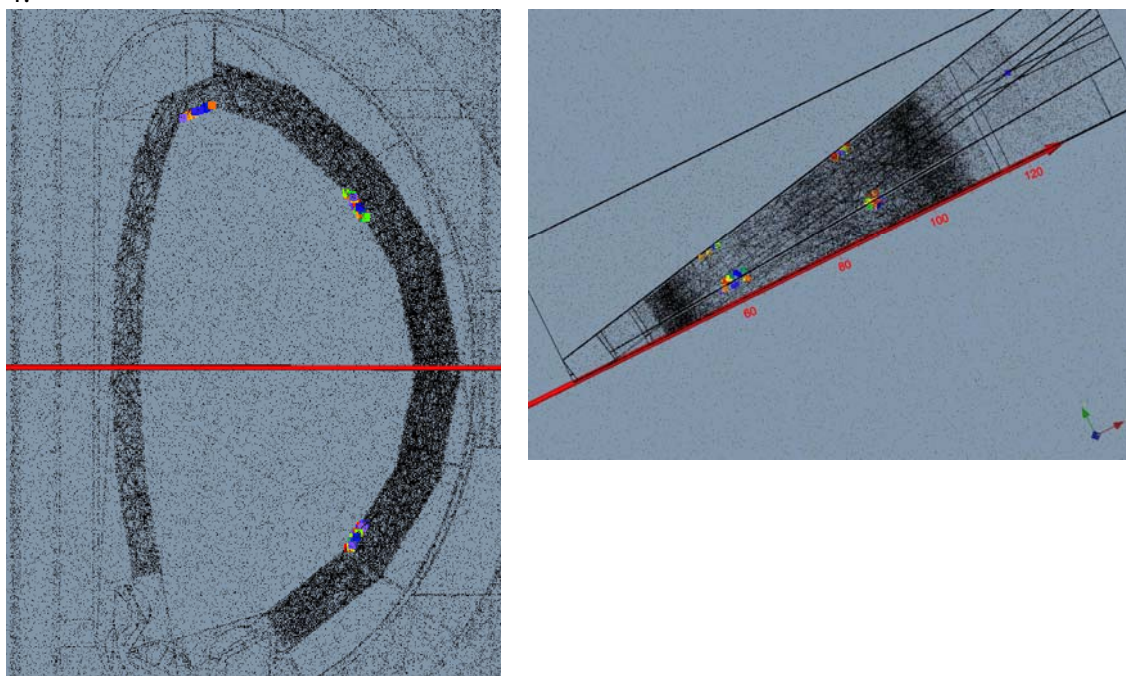
Figure 4: Side and top view of the DEMO geometry including the rough location of the lost particles (colored spots).
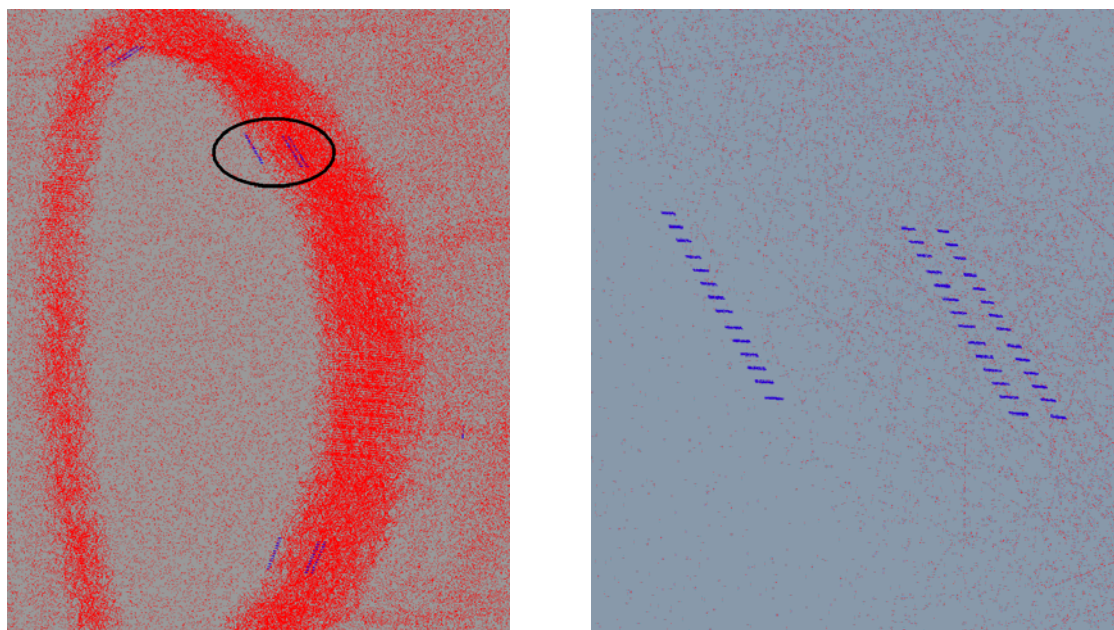
Figure 5: Closer studies of the locations were the particles are lost. The DEMO geometry is clearly visible in the left picture. One of the areas including lst particles is magnified in the right picture.

Three areas in which particles were lost were identified (seen in Figure 4) and studied in more detail. It was found, that the lost particles in this areas have a definite pattern; this pattern is obviously linked to the shape of the cells in the complicated blanket (pictured in Figures 1 and 2).

The surfaces near which the geometry is incorrectly defined have been identified. It was shown on an example that this problem can be solved in such a way, that these areas are excluded from the volume, which is filled with the universe of the complicated blanket. These volumes are filled with void. In this way the particles do not enter the problematic portion of the geometry. Since the problematic areas were identified to lie on a surface, the portions of the geometry, which are left void rather than being filled with the complicated blanket universe, are very thin. In this way the volume, which is not modeled correctly is left small and should thus not affect the results significantly.

It should be noted that with the right adjustment of the parameters in the McCad input file the geometry errors in the MCNP model of the complicated blanket could possibly be avoided. The McCad version 0.3.2 has, however, been released shortly before the end of the project and due to the lack of time the possibility of studying the complicated blanket, converted with a variety of input parameters, was performed only in a limited way. The other option, removal of the troublesome portions of geometry, has been found to be straighter forward.

With the last version of McCad the conversion time dropped dramatically. The longest single step, the generation of the material cells for the complicated blanket took 11min 5s.

152

2.4   Comparison of volumes

In order to judge the correctness of the conversion process, the volumes of the CAD model were compared with the volumes, stochastically calculated with the resulting MCNP input. The CAD volumes were extracted in two ways:
1. from the provided step file using CATIA
2. from the McCad file, generated during the conversion process.

1.

With CATIA the volumes were determined only for the major six structures, listed at the beginning of Section 2.2, which were partly divided into substructures (the complicated blanket was excluded). They were compared with the MCNP stochastically calculated volumes and the McCad provided values for the CAD model. A brief result of the comparison of volumes is presented in Figure 6.

It was found, that within the MCNP statistical error margin, the volumes match each-other.

2.

A more detailed comparison has been done by comparing the values for individual cells, provided by McCad from the step files with the values, obtained with stochastic volume calculations with MCNP. The comparison was made separately for the model of the simple blanket (less than 300 cells), presented in Figure 7 and for the model of the complicated blanket (more than 13000 cells). The results of the latter are presented in Figure 8.
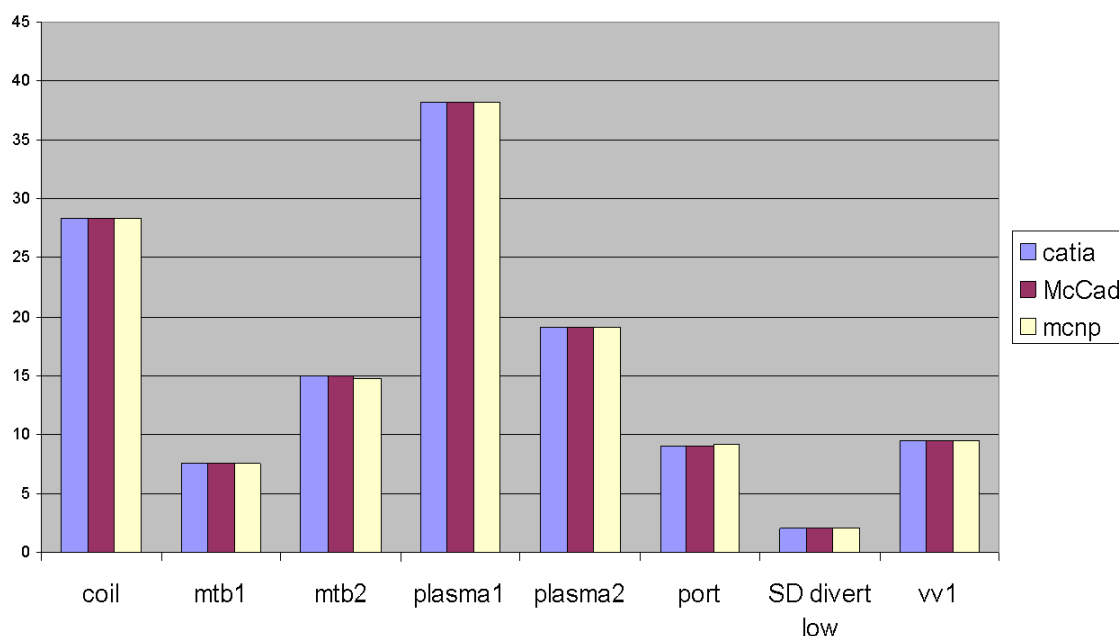
Figure 6: Comparison of volumes for the major six structures: accessed with CATIA from the step files, calculated stochastically with MCNP and provided by McCad for the CAD model.
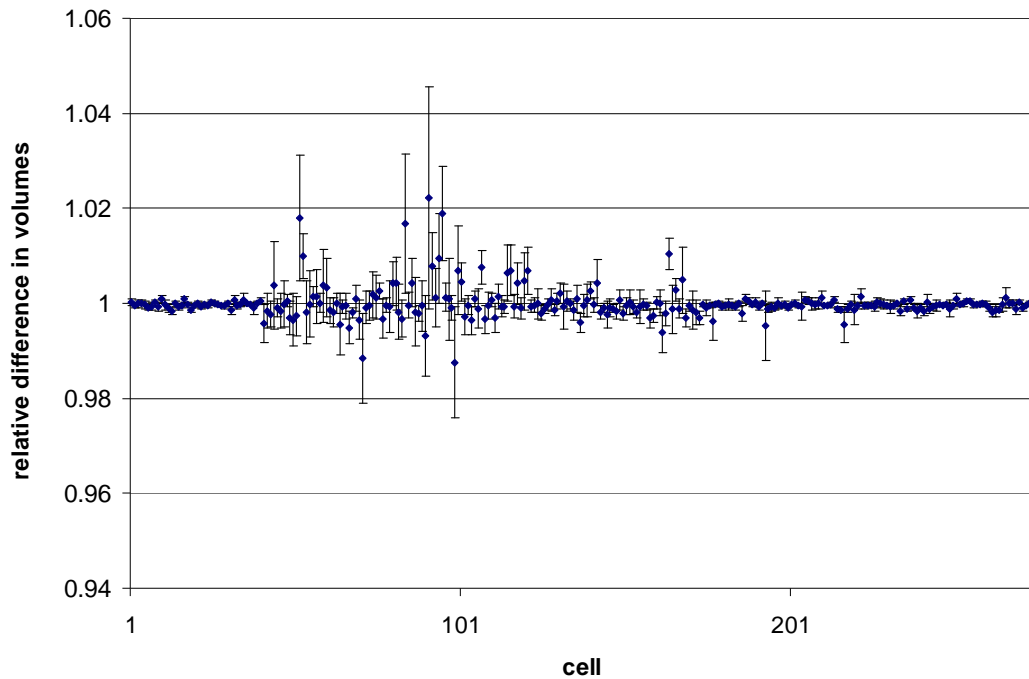
Figure 7: Comparison of volumes for the cells in the simple blanket model Presented is the ratio of the volumes provided by McCad from the CAD model and calculated stochastically with MCNP (the MCNP statistical error is also presented in the picture).

It was found, that the volumes for individual cells perfectly match within the statistical error; 69.7% are within 1σ, 95.3 within 2σ and 99.3 within 3σ and all within 4σ.

The same calculation has been performed also for the whole model, i.e. filled also with the complicated blanket, although not all of the geometry errors have been fixed. The results are thus weighted with errors due to the uncertainty of the lost particles and are presented in Figure 8.

154
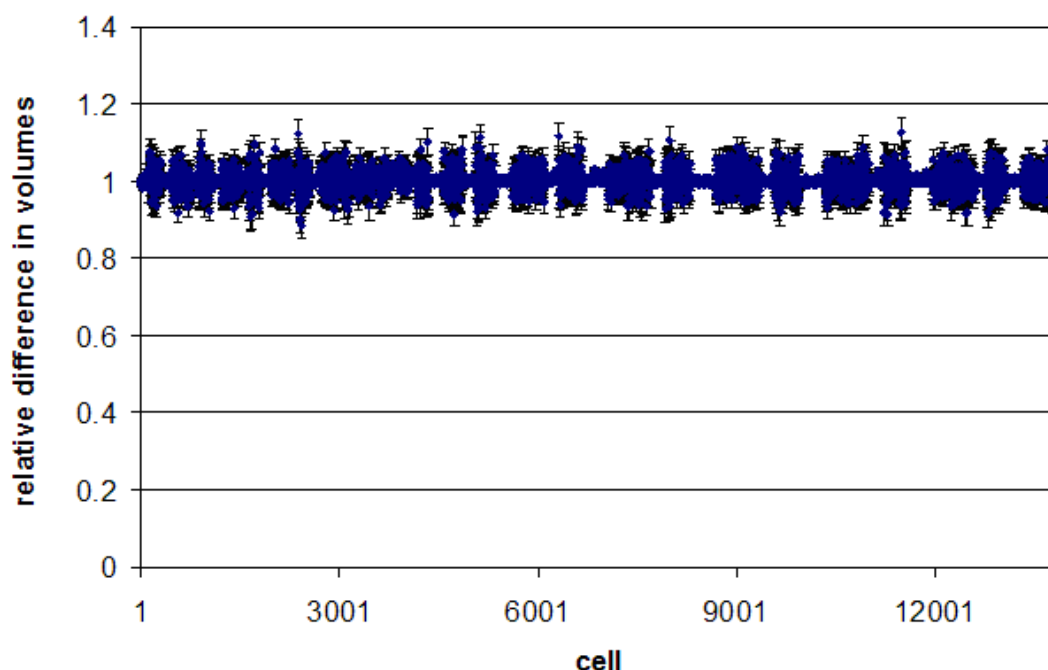
Figure 8: Comparison of volumes for the cells in the complicated blanket model, Presented is the ratio of the volumes provided by McCad from the CAD model and calculated stochastically with MCNP.

As seen form Figure 8 the match between both values for the cell volumes is in case of the complicated model less accurate. This is probably the consequence of the described problem with the lost particles. The volumes for individual cells with respect to the MC statistical error were distributed as follows; 61.5% are within 1σ, 89.0 within 2σ and 96.3 within 3σ, 98.1 within 4σ and 98.9 within 5σ and 99.5 within 6σ.

As noted the results for the simple blanket are more relevant due to the errorless geometry. The unknown error, related to the lost particles, makes the results, presented in Figure 8, to be treated with caution.

2.5   Flux on the first wall

The flux due to direct neutrons on the first wall was calculated. The DEMO plasma source, needed for these calculations was also provided by KIT and MCNP was re-compiled by usage of this source. It should be noted, that due to the complicated procedure of filling the materials correctly into the more than 14000 cells of the MCNP model no materials were filled into the model, i.e. the model was left void. A hypothetical calculation of the wall loading was performed taking into account only direct neutrons and assuming that they deposit all their energy at the first wall. The results are normalized to 2358 MW of fusion power ($8,468 \cdot 10^{20}$ n/s).

The positions on the first wall, where the flux (wall loading) was calculated are presented in Figure 9.
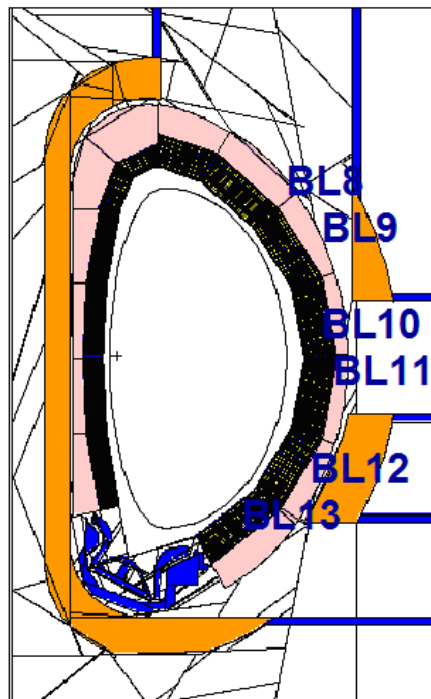
Figure 9: Positions on the first wall, where the flux (wall loading) was calculated.

Scaling the MCNP model

The provided model in step format had, when read by the CAD visualization software (i.e. CATIA) a total vertical dimension of less than 2m, i.e. it was, when directly read by CATIA, for a factor of 10 to small in all dimensions. This did not affect the conversion, the analyses of the model and comparison of volumes. When calculating the wall loading, the absolute dimensions are, however, important. One way would be to differently process the original model in order to obtain a model, which is larger. Since the model was assembled already, it was chosen to change the dimension in the MCNP input file.

Only the definitions of the surfaces and transformations needed to be changed. Since McCad presents the surfaces, produced in the conversion process in a well defined way, the task was not too difficult. The MCNP model also contained only surfaces of the types P, PX, PY, PZ, C/Y, CZ and S. The absence of toroidal or other types of surfaces made the scaling for a factor of 10 easier. The transformations were also accordingly scaled for the same factor. The model was subsequently tested.

Flux on the first wall – wall loading approximation

The wall loading on the first wall was approximated by the current of direct neutrons on the surfaces, marked in Figure 9. The results resemble the situation, when only direct plasma neutrons would contribute to the wall loading and all of them would be absorbed on the first wall. The results of the approximation are presented in Table 1.

Blanket module	direct flux power through module [MW/m^2]
BL8	2.5
BL9	2.7
BL10	2.8
BL11	2.8
BL12	2.7
BL13	2.3

Table 1: Wall loading approximation: direct flux power through individual blanket modules, numbered in Figure 9.

3   CONCLUSIONS AND OUTLOOK FOR 2013

The activity was a joint work of the associations KIT, CCFE, ENEA and MESCS-SFA in which different tools for conversion of the CAD geometry into MCNP geometry were tested. The tool tested by the SFA and described in this work was the McCad program developed by KIT.

The first major step was the installation of the software on the home machine. The installation files were provided by KIT, which was also of support during the procedure. Altogether three versions (McCad 0.3.0 – 0.3.2) were tested, the last one used for the majority of results, presented in the report. The main difficulty encountered during installation was a compatibility problem due to different distributions of the libraries for the Linux platform. The recommendation is to provide the source code of McCad to be compiled on ones machines and to additionally distribute the correct libraries.

A model of DEMO in the step format (*.stp), a program independent format to be used with the CAD graphic programs, was also provided by KIT. The provided CAD model of DEMO was rather complex, comprising more than 13000 cells. The conversion was carried out in two steps; first all of the components were converted using McCad except the complicated blanket model, which however covers 95% of the data. In the next step the complicated blanket was successfully converted with McCad but the surrounding void space was not produced. In the following step the cells of the complicated blanket were filled into the cells of the simple blanket.

The correctness of the resulting converted MCNP model was subsequently evaluated on errors by visual representation and examination of the resulting MCNP input files. A script was written for visualization of the positions were lost particles appear. This was necessary since the usual MCNP visual editor could not open the complex DEMO model.

Subsequently the volumes of the cells in the CAD model were compared with those, obtained stochastically with MCNP. Comparison of the volumes showed satisfactory results.

The flux due to the direct neutrons on the first wall was calculated for a model without materials. These calculations resembled the wall loading and were performed by using the DEMO plasma source, also provided by KIT.

In 2013 the influence of different first wall materials on the tritium breeding ratio (TBR) will be examined. Either helium or water will be assumed as coolants and the impact of various first wall design options on the TBR will be studied.

4   REFERENCES

1   X-5 Monte Carlo Team, MCNP — A General Monte Carlo N-Particle Transport Code, Version 5, Los Alamos National Laboratory, Los Alamos, New Mexico, April 2003.

PUBLIC INFORMATION ACTIVITIES

Saša Novak, Luka Snoj, Tomaž Skobe

Jožef Stefan Institute, Jamova cesta 39, SI-1000 Ljubljana
sasa.novak@ijs.si

1   INTRODUCTION

The report summarizes various public information activities in 2012. It involves basic information on the permanent exposition run by the Nuclear Training Centre and on other regular activities.

2   WORK PERFORMED IN 2012

Permanent fusion exhibition at the Nuclear training centre (http://www.icjt.org/an/index.htm) of the Jožef Stefan Institute was visited in 2012 by 164 organized groups of 7264 visitors altogether, mainly youngsters from primary, secondary and high schools. We were often visited also by graduate and postgraduate students and organized groups of adults.

We gave 21 lectures on Fusion technology and ITER project and 24 on Radioactivity and radioactive waste. We also gave 118 lectures on electricity from nuclear energy, where we talk also about fusion as safe, sustainable and environmentally responsible source of energy in the future. We performed experiments on radioactivity and ionizing radiation and provided guided tours of the permanent exhibition on fusion.

In March, within the annual Open day at the Jožef Stefan Institute, we organized an exhibition of the activities performed within the project Fusion Expo and so we used this opportunity to increase the awareness of the fusion research.

The exhibition was at both sites of the JSI, in Ljubljana and at the Reactor Centre in Podgorica. The visitors could learn about the travelling exhibition and the guides were giving the explanation on the fusion-related questions.

Figure 1: Open day at the Reactor Centre in Podgorica

Figure 2: Open day at the Jožef Stefan Institute in Ljubljana

In parallel, the Fusion Expo was presented in an article published in IJS Novice, the official quarterly J. Stefan Institute publication, which is distributed also to some public bodies, such as Ministries and Slovenian Agency for Science.

In the 239th edition of ITER Newsline an interview with dr. David Jezeršek was published (http://www.iter.org/newsline/239/1299). David is known to some of the PIs as the creator of the Unofficial ITER Fan Club website, which has been collected ITER-related news since even before ITER organisation itself created its own webpage.

In newspaper DELO an article »Step by step to fusion reactor« was published in October.

SFA MESCS video clip was subtitled in English and published at EFDA web page http://www.efda.org/2013/01/association-euratom-mescs-slovenia/.

SFA MESCS members were present at presentation of new book (Patent chasing, Lov na patent, http://www.bukla.si/?action=books&book_id=14699.

3 CONCLUSIONS AND OUTLOOK FOR 2013

The tasks proposed for the 2012 have been done. In 2013 attention will be paid to spread information about new fusion achievements, especially on current activities in ITER (Cadarache). One of important goals is going to be different presentations of Slovenian fusion research for general public (like lectures and workshops for schools, articles for media, announcements on SFA web site). In 2013 during Jožef Stefan days SFA plans to be present with fusion lecture, live coverage from JET and ITER and some parts of Fusion Expo.

4 REFERENCES

1   http://www.iter.org/newsline/239/1299

FUSION EXPO SUPPORT ACTION

Tomaž Skobe, Saša Bobič, Saša Novak, Mateja Južnik, Igor Jenčič, Borut Mavec,
Damjan Klep, Dušan Rudman, Nina Udir, Aljaž Iveković and others

Jožef Stefan Institute, Jamova cesta 39, SI-1000 Ljubljana
tomaz.skobe@ijs.si

1   INTRODUCTION

Slovenian Fusion Association (SFA) EURATOM – MESCS has taken over responsibility to run the Fusion Expo from 6th October 2008. The first Fusion Expo Support Action (WP08-PIN-FUSEX) has finished on 31st July 2010. The new support action under WP10-PIN-FUSEX started on 1st August 2010 and was extended until the end of year 2013. The main goal and intention of this project remain the same since beginning of our task agreement: to run the Fusion Expo in the most efficient way possible and to follow our tasks, which needs to be fulfilled:

1. Scheduling the exhibition
2. Supervising the local organisation
3. Graphical work and printing Fusion Expo panels
4. Moving the exhibits
5. Assembling/Disassembling Fusion Expo
6. Maintenance
7. Continuous report to EFDA
8. Organisation of a supporting participation in international events for young generations
9. Providing the Fusion Expo with Fusion Show for larger events

2   WORK PERFORMED IN 2012

Fusion Expo is an itinerant exhibition presenting various aspects of fusion research such as: fusion as a natural phenomenon and energy source science, fusion as a European research project, history of fusion research, European research facilities, ITER, future plans toward a power plant, technological, environmental and sociological aspects of this energy source etc.

The main target group of Fusion Expo is the general public. It is specifically designed to address young students and it is also appropriate to addressing other audiences, such as decision makers or journalists. Being modular, it can easily be adapted to different kind of events.

Activities described in this report were carried out in 2012. During this period eleven events were organized: five Maxi Fusion Expos, one Mini Fusion Expo, four

events with some parts of expo and additionally one internal event (during PIN meeting in Culham). In 2012 all exhibitions were succesfully finished.

In 2012 Fusion Expo team prepared guidelines for exhibitions (allowing the best possible choice for exhibitions, providing best possible feedbacks), mission statement (for a clear definition of Fusion Expo mission), specifications for new Fusion Expo (specifications will be delivered to different companies – call for tender and after that, examination of proposals are going to be on the schedule).

Host / Event	Type of participation	Place	Date
Plasmas chauds	Maxi Expo	Nancy, France	26th January – 6th February, 2012
Science festival "Printemps des Sciences"	Maxi Expo	Charleroi, Belgium	16th March – 20th April, 2012
Jozef Stefan Institute open day	Hands on experiments	Ljubljana (two locations)	24th March 2012
2nd European Energy Conference	Part of expo, Remote handling	Maastricht, The Nederlands	17th – 20th April, 2012
Visiatome	Maxi Expo	Marcoule, France	12th May – 8th July, 2012
Internal Event, PIN meeting	Hands on experiments	Culham, UK	14th – 15th June, 2012
Karlsruhe Institute of Technology (KIT), Fusion Programme	Some parts of Fusion Expo	Karlsruhe, Germany	3rd September - 14th September, 2012
European Commission - SOFT 2012	Maxi Expo	Liege, Belgium	19th September – 7th October, 2012
Light12 event - European Night of Research	Some parts of Fusion Expo	Rome, Italy	28th September, 2012
Genoa Science Festival	Maxi Expo	Genova, Italy	25th October – 4th November, 2012
ITER Organization	Mini Expo	Aix-en-Provence, France	13th November – 28th November, 2012

Table 1: List of realised exhibitions in 2012

2.1. Nancy

Year 2012 started with Maxi Fusion Expo in Nancy (Faculty of Sciences & Technologies Vandoeuvre). According to host report the action was a success regarding main objectives which were above all to disseminate knowledge among students and persons interested in energy topics and to try to encourage high school students for physics. The mobilization of researcher teams but also of high school professors and local educational authority shows a major interest for this topic.

2.2. Charleoi

Second exhibition in 2012 (Maxi Fusion Expo) was hosted by Centre de Culture Scientifique (CCS) de l'Université libre de Bruxelles" in Charleroi from March 16 to April 20. Science festival "Printemps des Sciences" was also very interesting for youngsters – especially 3D movie - Fusia.

2.3. Ljubljana

On March 24 all departments of Jozef Stefan Institute were opened for general public. This year also Fusion Expo was present on two locations of the Institute - on the location in Ljubljana there was a Fusion Expo truck, panel with all Fusion Expo venues and human powered plant. On the TRIGA reactor location was a presentation of hands on experiments - roller coaster, smoking gun, turntable and Remote handling demo.

Figure 1: Fusion Expo in Nancy

Figure 2: Fusion Expo in Charleoi

Figure 3: Jozef Stefan Institute Open Day in Ljubljana

2.4. Maastricht

In April 2012 the new Remote Handling Experience exhibit, which simulates the maintenance operation at JET, was a central attraction at the European Energy Conference in Maastricht. Visitors were challenged to manipulate "tiles" – wooden blocks – into their allotted spaces using only the on-screen camera view. However, the two minute time limit for the four tiles proved too testing for all but one contestant, giving visitors an appreciation of the skill that the JET technicians showed. During the 2009 – 2011 shutdown, they replaced 86,000 components inside the JET vessel using remote handling techniques. The conference brought together policy makers and specialists from many different fields, who shared the progress in their areas, with the aim to "optimise the necessary interdisciplinary cooperation and communication in energy research, development and the support to industrial innovation" to the solution.

2.5. Marcoule

Third Maxi Fusion Expo was organized in exhibition centre Visiatome - CEA Marcoule UCCAP from 12th May – 8th July, 2012. Fusion Expo exhibition was placed in Visiatome - a centre for discovery and learning proposed by the Atomic Energy and Alternative Energies Commission (CEA), a French public research organization. Intended for the general public, it is entirely devoted to energy challenges, radioactivity, and the issues of nuclear

Figure 4: Fusion Expo in Marcoule.

energy and radioactive waste. Its science museum with 600 m2 of colourful mock-ups, interactive educational tools and discovery modules is well known in the area and abroad and it is visited by approximately 8000 visitors per year.

Fusion Expo exhibition fitted very well to the present layout since the content about the fusion research and appliances are not covered in the permanent exhibition in the science museum.

2.6. Culham

In June 2012 was an internal event – Public Information Network yearly meeting, which was organized in Culham from 14 to 15 June. Fusion Expo team sent hands on experiments, which were presented to PIN members and other visitors of Culham centre.

2.7. Karlsruhe

The 6th "Karlsruhe International School on Fusion Technology" took place in Karlsruhe at the beginning of September 2012. This summer school, annually organized by the Karlsruhe Institute of Technology (KIT) was focused on the development of the fusion components as well as the associated processes like cooling and fuel cycle. Over 50 participants from 7 Nations listened to 42 lecturers who presented topics in their specific field of competence. Fusion Expo was present with two hands-on experiments (Remote handling and Turning table).

Figure 5: Fusion Expo in Karlsruhe

2.8. Liege

Liege in Belgium hosted 27th Symposium on Fusion Technology (SOFT) and within the framework of the SOFT, EFDA and Fusion Expo presented exhibition on Nuclear Fusion.

2.9. Rome

Turn on the light on science was European project in Rome (already since 2008) as the "European Researchers Night." An event was held on September 28, 2012 at

Figure 6: Fusion Expo in Liege

the Planetarium of Rome. As every year, the scientific and artistic programming revolved around a central theme, which this year was "Science on Breaking News." LIGHT'12 took inspiration from major scientific news conveyed by the mass media to provide the general public proposals that are able to intrigue, inform, entertain and above all turn attention to the importance of scientific research and its products, even those that not been the subject of media attention. Fusion Expo contributed to this event with some parts of Fusion Expo − plasma ball, bicycle (human powered plant) and ITER/JET model.

2.10. Genoa

From 24 October to 4 November 2012 Fusion Expo has been hosted in the prestigious new University Library, in Genoa City Center. It has been part of the official program of the tenth edition of the Genoa Science Festival and has been included in the web-site, as one of the "high-lights" of the 2012. The venue hosting Fusion Expo (Nuova Biblioteca Universitaria) has been visited by 3.200 people in 11 days. The

Figure 7: Fusion Expo in Genoa

public answered enthusiastically, despite weather alerts and the closures of some schools during the first days of the event.

2.11. Aix en Provence

In November Fusion Expo has been hosted in the prestigious location of the Aix en Provence Tourist Office in a very centre of the city. Host of the event was ITER organization. ITER is designed to demonstrate the scientific and technological feasibility of fusion power and will be the world's largest experimental fusion facility. The speeches at the opening ceremony were given by the Mr. Joissains-Masini, Mayor of Aix-en-Provence and Mr. Osamu Motojima, director-general of the ITER organization.

Figure 8: Fusion Expo in Aix en Provence

3   CONCLUSIONS AND OUTLOOK FOR 2013

In 2011 the Fusion Expo Support team experienced difficulties to find hosts for exhibitions and after discussions between Slovenian Fusion Association and EFDA a decision was taken to work also on a new exhibition. In 2012 Fusion Expo team prepared guidelines for exhibitions (allowing the best possible choice for exhibitions, providing best possible feedbacks) and mission statement (for a clear definition of Fusion Expo mission). One of the most important target places for Fusion Expo in 2013 are science centers and science festivals. Fusion Expo team started already in 2011 to investigate different science events and centers – the result was very positive and the majority of Fusion Expo events in 2013 are going to be organized in science centers (Estonia) and during science festivals (Germany, Czech Republic, Latvia).

166

PUBLICATIONS

1 Journal articles

[1] T. Gyergyek, J. Kovačič, Floating potential of an electron emitting collector that teminates a bounded plasma system, Contrib. Plasma Phys, Contrib. Plasma Phys., **52,** 2012, pp. 699-721.

[2] J. Adamek, M. Peterka, T. Gyergyek, P. Kudrna, M. Tichy, Diagnostics of magnetized low temperature plasma by ball-pen probe, Nukleonika, **57**, 2012, pp. 297-300.

[3] T. Gyergyek, J. Kovačič, Saturation of a floating potential of an electron emitting electrode with increased electron emission: a one-dimensional kinetic model and particle-in-cell simulation., Phys. Plasmas, **19**, 2012, 013506.

[4] Tsv. K. Popov, P. Ivanova, M. Dimitrova, J. Kovačič, T. Gyergyek, M. Čerček, Langmuir probe measurements of the electron energy distribution function in magnetized gas discharge plasmas, Plasma Sources Sci. Technol., **21**, 2012, 025004.

[5] I. Čadež, S. Markelj, Z. Rupnik. Low energy H⁻ production by electron collision with small hydrocarbons, Eur. Phys. J. D, **66**, 2012, 73

[6] S. Markelj, P. Pelicon, I. Čadež. Th. Schwarz-Selinger and W. Jacob. In situ study of erosion and deposition of amorphous hydrogenated carbon films by exposure to a hydrogen atom beam, J. Vac. Sci. Technol., **A 30,** 2012, 041601-1-8.

[7] M. Mozetič, Removal of hydrogenated carbon deposits formed in fusion reactors with carbon walls by reactive oxygen particles, Nukleonika (Wyd. pol.) **57**, 2012, 269-275.

[8] F. L. Tabarés, D. Alegre, M. Mozetič, A. Vesel, Methane cracking and secondary hydrocarbon generation in

inductively coupled RF plasmas, Nukleonika (Wyd. pol.) **57**, 2012, 287-290.

[9] R. Zaplotnik, A. Vesel, M. Mozetič, A fiber optic catalytic sensor for neutral atom measurements in oxygen plasma, Sensors, **12**, 2012, 3857-3867.

[10] A. Vesel, M. Mozetič, M. Balat-Pichelin, Interaction of highly dissociated low pressure hydrogen plasma with W-C thin film deposits, Thin solid films, **520**, 2012, 2916-2921.

[11] R. Zaplotnik, A. Vesel, M. Mozetič, Merjenje gostote nevtralnih atomov v porazelektritvenem območju plazme (= Neutral atom density measurements in the plasma postglow region), Vakuumist, **32**, 2012, 8-12.

[12] V. Nemanič, P. J. McGuiness, N. Daneu, B. Zajec, Z. Siketić, W. E. Waldhauser, Hydrogen permeation through silicon nitride films, J. alloys compd., **539,** 2012, pp. 184-189.

[13] V. Nemanič, B. Zajec, D. Dellasega, M. Passoni, Hydrogen permeation through disordered nanostructured tungsten films, J. nucl. mater., **429,** 2012, pp. 92-98.

[14] C. P. Lungu, J. Kovač, V. Nemanič, Terawatt laser system irradiation of carbon/tungsten bilayers, Phys. status solidi A, Appl. res., **209,** 2012, pp. 1732-1737.

[15] M. Čekada, M. Kahn, P. Pelicon, Z. Siketić,I. Bogdanović-Radović, W. E. Waldhauser, S. Paskvale, Analysis of nitrogen-doped ion-beam-deposited hydrogenated diamond-like carbon films using ERDA/RBS, TOF-ERDA and Raman spectroscopy, Surf. coat. technol, **211**, 2012, pp. 72-75.

[16] M. Novotny, J. Bulir, P. Pokorny, J. Lančok, L. Fekete, M. Jindrich, M. Čekada, RF magnetron sputtering of silver thin film in Ne, Ar and Kr dischargesplasma characterisation and surface morphology. Surf. coat. technol., 2012 (in press).

[17] A. Barna, S. Gurban, L. Kotis, J. L. Labar, A. Sulyok, A. L. Toth, M. Menyhard, J. Kovač, P. Panjan, Growth of amorphous SiC film on Si by means of ion beam induced mixing, Appl. surf. sci., **263**, 2012, pp. 367-372.

[18] P. A. Ni, C. Hornschuch, M. Panjan, A. Anders, Plasma flares in high power impulse magnetron sputtering, Appl. phys. lett., **101**, 2012, pp. 224102.

[19] L. Snoj, A. Trkov, I. Lengar, S. Popovichev, S. Conroy, B. Syme and JET EFDA Contributors, Calculations to support JET neutron yield calibration: Neutron scattering in source holder, Fusion eng. des, **87**, 2012, pp. 1846-1852.

[20] L. Snoj, B. Syme, S. Popovichev, I. Lengar, S. Conroy, A. Trkov and JET EFDA Contributors, Calculations to support JET neutron yield calibration: Contributions to the external neutron monitor responses, Nucl. Eng. Des., **246**, 2012, pp. 191-197.

[21] B. Syme, S. Popovichev, S. Conroy, I. Lengar, L. Snoj, A. Trkov and JET EFDA Contributors, Fusion yield measurements on JET and their calibration, Nucl. Eng. Des., **246**, 2012, pp. 185-190.

[22] S. Novak, A. Iveković, Fabrication of SiCf/SiC composites by SITE-P process, Journal of Nuclear Materials, **427**, 2012, pp. 110-115.

[23] B. Končar, S. Košmrlj, P. Norajitra, On the accuracy of CFD modeling of cyclic high heat flux divertor experiment, Fusion eng. des., **87**, 2012, pp. 1621-1627.

2 Conference papers

[24] S. Rupnik, J. Kovačič, M. Čerček, T. Gyergyek, V. Pohoata, G. Popa, C. Ionita, R. Schrittwieser, Measurements of the ion energy distribution function during the creation of a fire-rod in a weakly magnetized discharge plasma column, 39th EPS Conference and 16th Int. Congress on Plasma Physics, Stockholm, Sweden, 2 - 6 July 2012 – CD Abstracts P5.157.

[25] J. Kovačič, T. Gyergyek, M. Čerček, Validity of Boltzmann factor in magnetized plasmas, 21st International Conference Nuclear Energy for New Europe, Ljubljana, Slovenia, 5 - 7 September 2012, Proceedings, Nuclear Society of Slovenia, pp. 8.

[26] T. Gyergyek, J. Kovačič, Dependence of the floating potential of an electron emitting collector that terminates a bounded plasma system on electron emission studied by a

particle-in-cell computer simulation. 48th International Conference on Microelectronics, Devices and Materials & the Workshop on Ceramic Microsystems, 19 – 21 September 2012, Otočec, Slovenia, Proceedings, MIDEM - Society for Microelectronics, Electronic Components and Materials, pp. 115-120.

[27] Tsv. K. Popov, M. Mitov, A. Bankova, P. Ivanova, M. Dimitrova, S. Rupnik, J. Kovačič, T. Gyergyek, M. Čerček, F. M. Dias, Langmuir probe evaluation of the negative ion density in oxygen gas discharge magnetized plasma, ESCAMPIG 2012, XXI. Europhysics Conference on the Atomic and Molecular Physics of Ionized Gases, 10-14 July 2012, Viana do Castelo, Portugal. Proceedings, European Physical Society, pp. 2.

[28] T. Gyergyek, J. Kovačič, M. Čerček, Formation of a virtual cathode in front of an electron emitting collector that terminates a bounded plasma system, Proceedings of the 21st International Electrotechnical and Computer Science Conference ERK 2012, 17 – 19 September 2012, Portorož, Slovenia, Ljubljana, IEEE Region 8, Slovenian section IEEE, pp. A 199-202.

[29] I. Čadež and S. Markelj, Hydrogen Desorption from Hydrogenated Carbon on Tungsten, 21st International Conference Nuclear Energy for New Europe, Ljubljana, Slovenia, 5 – 7 September 2012, Proceedings, Nuclear Society of Slovenia, P1113.1-1113.7.

[30] S. Markelj, O. V. Ogorodnikova, P. Pelicon, T. Schwarz-Selinger, K. Sugiyama and I. Čadež. Study of Thermal Hydrogen Atom Interaction with Undamaged and Self-Damaged Tungsten, 20th PSI, Aachen, Germany 21-25 May, 2012, P3-28.

[31] A. Drenik, L. Šalamon, R. Zaplotnik, G. Primc, M. Mozetič, D. Alegre, F. L. Tabarés Interaction of a-C:H thin films with ICP plasma of ammonia, 21st International Conference Nuclear Energy for New Europe, Ljubljana 2012, 5-7 September, Proceedings, Ljubljana: Nuclear Society of Slovenia, 2012, pp. 9.

[32] R. Zaplotnik, L. Šalamon, A. Drenik, A. Vesel, M. Mozetič. Laboratory plasma reactors as sources of low temperature atomic oxygen for fuel removal, 21st International Conference Nuclear Energy for New Europe, Ljubljana

2012, 5-7 September Proceedings. Ljubljana: Nuclear Society of Slovenia, 2012, pp. 9.

[33] A. Drenik, A. Vesel, M. Mozetič. Probability of heterogeneous recombination of atomic hydrogen on fine-grain graphite surface, Europhysics Conference on the Atomic and Molecular Physics of Ionized Gases, 10 - 14 July 2012, Viana do Castelo, Portugal. Proceedings, European Physical Society, 2012, pp. 2.

[34] B. Pégourié, S. Panayotis, P. Languille, C. Martin, T. Dittmar, l, E. Gauthier, J.-C. Hatchressian, J.-Y. Pascal, P. Roubin, R. Ruffe, E. Tsitrone, S. Vartanian, H. Wang, m, A. Beauté, J. Bouvet, C. Brosset, J. Bucalossi, M. Cabié, E. Caprin, X. Courtois, R. Dachicourt, E. Delchambre, C. Dominici, D. Douai, A. Ekedahl, J.P. Gunn, A. Hakola, W. Jacob, H. Khodja, J. Likonen, F. Linez, A. Litnovsky, Y. Marandet, S. Markelj, A. Martinez, M. Mayer, O. Meyer, P. Monier-Garbet, P. Moreau, V. Negrier, P. Oddon, C. Pardanaud, B. Pasquet, P. Pelicon, P. Petersson, V. Philipps, G. Possnert, D. Reiter, J. Roth, I. Roure, M. Rubel, F. Saint-Laurent, F. Samaille, P. Vavpetič, Deuterium inventory in Tore Supra: Coupled carbon–deuterium balance, 20th PSI, Aachen, Germany 21 -25 May 2012, Paper in press in J.Nucl.Mater. 2013.

[35] V. Nemanič, D. Dellasega, G. Merlo, B. Zajec, M. Passoni, Hydrogen permeation through nano-structured tungsten films, 20th International Conference on Plasma Surface Interactions 2012, Eurogress, Aachen, Germany, 21 – 25 May 2012.

[36] D. Dellasega, G. Merlo, E. Vassallo, C. Conti, V. Nemanic, B. Zajec, M. Passoni, Permeation and Erosion Properties of Nanostructured W and W-Ta Coatings, 20th International Conference on Plasma Surface Interactions 2012, Eurogress, Aachen, Germany, 21 – 25 May 2012.

[37] L. Kos, D. D. Tskhakaya, N. Jelić, J. Duhovnik, Analytic properties of the sheath solution with warm ions, 39th EPS Conference on Plasma Physics and 16th International Congress on Plasma Physics, 2 -6 July 2012, Stockholm, Sweden, European Physical Society EPS, PD6.006.

[38] N. Jelić, L. Kos, D. D. Tskhakaya, S. Kuhn, Analytic solution to the plasma equation with warm ions, 39th EPS Conference on Plasma Physics and 16th International

171

Congress on Plasma Physics, 2 – 6 July 2012, Stockholm, Sweden, European Physical Society EPS, PD4.007.

[39] L. Kos, H.-J. Klingshirn, P. L. García Müller, F. Imbeaux, Extension of the visualization capabilities within the European Integrated Tokamak Modelling platform, 21st International Conference Nuclear Energy for New Europe, Ljubljana, Slovenia, 5 – 7 September 2012, pp. 1117.1-1117.8.

[40] N. Jelić, L. Kos, J. Krek, Warm plasma-boundary properties, 21st International Conference Nuclear Energy for New Europe, Ljubljana, Slovenia, 5 – 7 September 2012, pp. 1118.1-1118.9.

[41] S. Kuhn, D. D. Tskhakaya, N. Jelić, L. Kos, J. Duhovnik, Polytropic-Coefficient Function (PCF) vs. polytropic-exponent function (PEF), 39th IEEE International Congress on Plasma Science, ICOPS 2012, 8 – 12 July 2012, Edinburgh, Scotland, Edinburgh, IEEE Nuclear and Plasma Science Society.

[42] N. Jelić, L. Kos, J. Duhovnik, A semi-analytic solution of the plane discharge with warm ions, 39th IEEE International Congress on Plasma Science, ICOPS 2012, 8.-12.7.2012, Edinburgh, Scotland, Edinburgh, IEEE Nuclear and Plasma Science Society, 2012.

[43] L. Snoj, I. Lengar, A, Čufar, B. Syme, S. Popovichev, S. Conroy, Calculations to support JET neutron yield calibration : Effect of the JET Remote handling system on the external neutron monitor responses, 21st International Conference Nuclear Energy for New Europe, Ljubljana, 5 – 7 July 2012, Proceedings, Nuclear Society of Slovenia.

[44] B. Končar, M. Draksler, P. Norajitra, Comparison of divertor concepts from the perspective of heat removal from target plate edges, 21st International Conference Nuclear Energy for New Europe, Ljubljana, 5 – 7 September 2012, Proceedings: Nuclear Society of Slovenia, pp. 7.

172

3   Chapter in a book

[45] M. Cannio, S. Novak, L. Besra, A.R. Boccaccini, Ceramics and composites processing methods. Hoboken: Wiley, cop. 2012, pp. 517-549.

4   Invited talks, reports and presentations

[46] I. Čadež, Dissociative electron attachment in molecules - needs and current status of available data, VAMDC Regional workshop on atomic and molecular data, Belgrade, Serbia, June 14-16, 2012.

[47] I. Čadež and S. Markelj. Interaction of atomic hydrogen with amorphous hydrogenated carbon, Annual meeting of COST action CM0805 – The chemical cosmos, Catania, Italy, 2 – 5 October 2012.

[48] O. Ogorodnikova, S. Markelj, K. Sugiyama, I. Čadež, Yu. Gasparzan, V.V. Efimov, Atomic and low energy deuterium interaction with self-damage tungsten, 11th International Workshop on Hydrogen Isotopes in Fusion Reactor Materials, Garching, Germany, 29 – 31 May 2012.

[49] S. Markelj, P. Pelicon and I. Čadež, NRA and ERDA measurements for fusion at JSI, Research about tungsten for WEST, the French meeting, Paris, France, 2nd October 2012.

[50] V. Nemanič, Insight in hydrogen diffusion, absorption and vacancy trapping in nano-structured films by means of outgassing and permeation measurements on duplex membranes, 8th International Conference on Diffusion in solids and liquids, Istanbul, 25. - 29.6.2012.

[51] V. Nemanič, Hydrogen permeation and outgassing: investigation tools of materials for nuclear fusion and the extreme high vacuum, The 6th Vacuum and Surface Sciences Conference of Asia and Australia, Islamabad, Pakistan Vacuum Society, 2012, Conference guide, technical program & abstracts. pp. 160.

[52] M. Čekada, M. Kahn, W. E. Waldhauser, S. Paskvale, Structural and mechanical properties of ion beam deposited DLC coatings, 9. Werkstoffkongress Leoben (Austria), 28 - 29 March 2012.

[53] J. Krek, N. Jelić, L. Kos, J. Duhovnik, PEG-PIC and PEG-TC simulation codes, A suite of plasma engineering R&D software, Ljubljana, Faculty of Mechanical Engineering, LECAD Laboratory, 2012.

[54] A. Iveković, S. Novak, Fabrication of SiC based composite for fusion application by SITE-P process, 21st International Conference Nuclear Energy for New Europe, 5 – 7 September 2012.

[55] A. Iveković, S. Novak, Fabrication of SiC[sub]f/SIC composite by SITE-P process, 6th Young Researchers' Day 2012, Ljubljana, 27 – 28 February 2012.

[56] A. Iveković, S. Novak, 20th Conference on Materials and Technology, Portorož, 17 – 19 October 2012.

[57] S. Novak , A. Iveković, S. Rizzo, V. Casalegno, W/SiC based joining of SiC/SiC composites, 27th Symposium on Fusion Technology, Liège(Belgium), 24 – 28 September 2012.

[58] B. Končar, Thermal-hydraulic analyses report of alternative He-cooled divertor concepts, (Report, TA WP12-DAS02-T06), Ljubljana, Jožef Stefan Institute, 2012, pp. 17.

[59] S. Košmrlj, B. Končar, M. Leskovar, Simulation of helium cooled pebble bed test blanket module, (JSI work report, 10812, rev. 0), 2012.

[60] M. Leskovar, B. Končar, I. Lengar, S. Košmrlj, Assessment report on interface between MCNP and ANSYS CFX (blanket case) : report for TA WP12-DTM01 EFDA, Ljubljana: Jožef Stefan Institute, 2012, pp. 18.

[61] S. Košmrlj, B. Končar, M. Leskovar, Simulation of helium cooled pebble bed test blanket module, (JSI work report, 10812, rev. 0), 2012.

5   Conference abstracts

[62] M. Mozetič, A. Drenik, A. Vesel, D. Alegre, F. L. Tabarés, A. Kreter, Removal of a-C:H by RF discharge in ammonia, 20th International Conference on Plasma Surface Interactions 2012, Aachen, Germany, 21 -25 May 2012,

Forschungszentrum Jülich, GmbH Institute for Energy and Climate, 2012.

[63] A. Drenik, R. Zaplotnik, A. Vesel, M. Mozetič, Erosion of amorphous carbon layers in the afterglow of oxygen microwave plasma, 14th Joint Vacuum Conference, 12th European Vacuum Conference, 11th Annual Meeting of the German Vacuum Society, 19th Croatian-Slovenian Vacuum Meeting, 4 - 8 June 2012, Dubrovnik, Croatia, Programme and book of abstracts. Zagreb: Croatian Vacuum Society, 2012, pp. 35.

[64] R. Zaplotnik, M. Mozetič, A. Vesel. Carbon deposit removal by inductively coupled RF oxygen plasma, 14th Joint Vacuum Conference, 12th European Vacuum Conference, 11th Annual Meeting of the German Vacuum Society, 19th Croatian-Slovenian Vacuum Meeting, 4 - 8 June 2012, Dubrovnik, Croatia, Programme and book of abstracts, Zagreb: Croatian Vacuum Society, 2012, pp. 88.

[65] G. Primc, M. Mozetič. NH3, ICP plasma characterization using a floating double electrical probe, 14th Joint Vacuum Conference, 12th European Vacuum Conference, 11th Annual Meeting of the German Vacuum Society, 19th Croatian-Slovenian Vacuum Meeting, 4 - 8 June 2012, Dubrovnik, Croatia, Programme and book of abstracts, Zagreb: Croatian Vacuum Society, 2012, pp. 153.

[66] M. Oberkofler, A. Drenik. First nitrogen-seeding experiments in JET with the ITER-like wall, 20th International Conference on Plasma Surface Interactions 2012, Aachen, Germany, 21 – 25 May 2012, Forschungszentrum Jülich, GmbH Institute for Energy and Climate, 2012.

[67] A. Drenik, A. Tomeljak, A. Vesel, M. Čekada, A. Kreter, Recombination coefficient of fine-grain graphite for neutral oxygen atoms. IN: 20th International Conference on Plasma Surface Interactions 2012, Aachen, Germany, 21 – 25 May 2012, Forschungszentrum Jülich, GmbH Institute for Energy and Climate, 2012.

6   Theses

[68] R. Zaplotnik, Optimizacija sklopa med visokofrekvenčnim generatorjem in nizkotlačno plazmo: doktorska disertacija (= Optimization of coupling between high-frequency generator and low pressure plasma : doctoral dissertation), Ljubljana, 2012, pp. 121.

[69] S. Paskvale, Carbon based protective coatings prepared by physical vapour deposition technique, PhD thesis, Ljubljana (2012).

7   General publications

S. Novak, Na poti z evropsko razstavo o fuziji, Novice - IJS Printed version: 2012, **160**, pp. 14-17.

Annex 1

Association EURATOM-MESCS management structure

<table>
<tr>
<td>

EURATOM
European Fusion Programme
EU Commission
DG Research

</td>
<td>

MESCS
Ministry for Education, Science, Culture and Sport
Republic of Slovenia

</td>
</tr>
</table>

Steering Committee

EURATOM	MESCS
Ruggero Giannella	Tomaž Boh
Vito Marchese	Helena Brlan
Marc Cosyns	Simon Ošo

Research Unit
Head of Research Unit: Andrej Trkov
Assistants:
Technology – Jože Duhovnik
Emerging Technology – Saša Novak
Nuclear Technology – Igor Lengar
Public Information – Saša Novak
Secretary: Uršula Turšič

Institutions within the Research Unit

1. Jožef Stefan Institute,
Jamova 39, 1000 Ljubljana, Slovenia
Tel.: +386-1-5885-450   Fax.: +386-1-5885-377
Web: htpp://www.ijs.si
Andrej Trkov *andrej.trkov@ijs.si*
with

University of Nova Gorica	**University of Ljubljana,**
Vipavska 13, 5000 Nova Gorica, Slovenia	**Faculty for Electrical Engineering**
	Tržaška 25, 1000 Ljubljana, Slovenia

2. University of Ljubljana, Faculty for Mechanical Engineering,
LECAD Laboratory,
Aškrčeva 6, 1000 Ljubljana, Slovenia
Tel.: +386-1-4771-416   Fax.: +386-1-4771-156
Web: htpp://www.lecad.uni-lj.si
Jože Duhovnik *joze.duhovnik@lecad.uni-lj.si*

Annex 2

Slovenian representatives in the European committees relevant to fusion research and development

Consultative Committee for the EURATOM Specific Programme on Nuclear Energy Research – Fusion (CCE-FU)

Ivan Skubic   Ministry for Education, Science, Culture and Sport of Republic of Slovenia

Andrej Trkov   Head of Research Unit, Jožef Stefan Institute, Ljubljana

EFDA Steering Committee

Andrej Trkov   Head of Research Unit, Jožef Stefan Institute, Ljubljana

Public Information Group

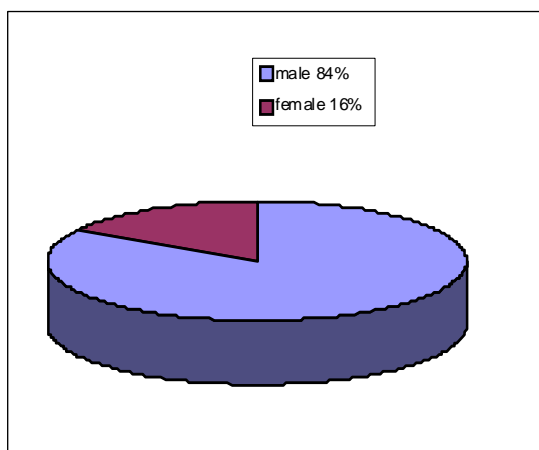Saša Novak   Jožef Stefan Institute, Ljubljana

Annex 3

Statistics

R&D projects in the Association EURATOM-MESCS for 2012

	JSI	ULJ	
Physics	12	1	**13**
JET	5	-	**5**
Fusion Expo	1	-	**1**
TOTAL	18	1	**19**

Manpower (ppy) for 2012

	Professional	**Non professional**	**TOTAL**
JSI	16,1	4,5	20.6
ULJ	1,4	0,4	1,8
	17,5	**4,9**	**22,4**

Association EURATOM-MESCS staff in 2012 by gender